2

RESEARCH AND DEVELOPMENT TECHNICAL REPORT

CECOM-TR-84-5

A THEORY OF MILLIMETER WAVE PROPAGATION IN VEGETATION

GERALD M. WHITMAN
FELIX K. SCHWERING
LI-WEN CHEN (NJIT)
CENTER FOR COMMUNICATION SYSTEMS

JULY 1984

DISTRIBUTION STATEMENT

Approved for public release;
distribution is unlimited.

CECOM

U S ARMY COMMUNICATIONS-ELECTRONICS COMMAND
FORT MONMOUTH, NEW JERSEY 07703

NOTICES

Disclaimers

The citation of trade names and names of manufacturers in this report is not to be construed as official Government indorsement or approval of commercial products or services referenced herein.

Disposition

Destroy this report when it is no longer needed. Do not return it to the originator.

UNCLASSIFIED

SECURITY CLASSIFICATION OF THIS PAGE *(When Data Entered)*

REPORT DOCUMENTATION PAGE		READ INSTRUCTIONS BEFORE COMPLETING FORM
1. REPORT NUMBER CECOM-TR-84-5	2. GOVT ACCESSION NO.	3. RECIPIENT'S CATALOG NUMBER
4. TITLE *(and Subtitle)* A THEORY OF MILLIMETER WAVE PROPAGATION IN VEGETATION		5. TYPE OF REPORT & PERIOD COVERED Technical Report June 1981 - May 1982 6. PERFORMING ORG. REPORT NUMBER
7. AUTHOR(s) Gerald M. Whitman Felix K. Schwering Li-Wen Chen (NJIT)		8. CONTRACT OR GRANT NUMBER(s)
9. PERFORMING ORGANIZATION NAME AND ADDRESS New Jersey Institute of Technology (NJIT) Newark, NJ (jointly with CECOM)		10. PROGRAM ELEMENT, PROJECT, TASK AREA & WORK UNIT NUMBERS 1L1 61102 AH 48 NM 11 01
11. CONTROLLING OFFICE NAME AND ADDRESS US Army Communications-Electronics Command (CECOM) Center for Communication Systems ATIN: DRSEL-COM-RM-4, Fort Monmouth, NJ 07703		12. REPORT DATE July 1984 13. NUMBER OF PAGES 157
14. MONITORING AGENCY NAME & ADDRESS *(if different from Controlling Office)*		15. SECURITY CLASS. *(of this report)* Unclassified 15a. DECLASSIFICATION/DOWNGRADING SCHEDULE

16. DISTRIBUTION STATEMENT *(of this Report)*

Approved for Public Release; Distribution Unlimited

17. DISTRIBUTION STATEMENT *(of the abstract entered in Block 20, if different from Report)*

18. SUPPLEMENTARY NOTES

19. KEY WORDS *(Continue on reverse side if necessary and identify by block number)*

Millimeter Waves; Propagation in Vegetation; Random Media; Transport Theory; Coherent and Incoherent Field Components

20. ABSTRACT *(Continue on reverse side if necessary and identify by block number)*

Millimeter-wave propagation in vegetation (forests) is studied using transport theory. A plane wave is assumed to enter a forest. The forest is modelled as a slab or half-space consisting of a random distribution of particles which scatter energy isotropically. The equation of radiative transfer in such a scattering and absorbing medium is solved by using Chebyshev polynomials as basis functions for series expansions of the diffuse or incoherent intensity. This choice of basis functions simplified considerably (cont)

DD FORM 1 JAN 73 1473 EDITION OF 1 NOV 65 IS OBSOLETE

UNCLASSIFIED

SECURITY CLASSIFICATION OF THIS PAGE *(When Data Entered)*

Block 20 - Abstract (contd)

the systems of linear equations which had to be solved numerically. Curves are presented which show the range dependency of both diffuse intensity and power flux density. Also drawn are figures depicting the directional spectrum of diffuse intensity.

TABLE OF CONTENTS

(page iv is blank)

FIGURES

FIGURES

FIGURES

FIGURES

FIGURES

FIGURES

FIGURES

FIGURES

FIGURES

TABLES

I. INTRODUCTION

The millimeter wave radios currently under development for use by US Army personnel may have to transmit information through groves of trees or be placed within a wooded area for camouflage purposes. Recent experimental results [VE,SJ] have indicated that such communication capability is feasible. To support this conclusion this study was initiated. A theory of millimeter-wave propagation in vegetation (forests) using transport theory evolved.

In the millimeter range a forest can be characterized as a random distribution of particles which absorb and scatter electromagnetic energy in all directions. Transport theory accounts for multiple scattering effects fully but neglects interference phenomena, which is justified by the experimental results. In transport theory the total field intensity is separated into two parts - the coherent intensity and the incoherent intensity. The polarization properties of the coherent component are the same as those of the incident field, which is taken to be a plane wave impinging upon the forest; the forest is assumed to be a slab or half-space region. The incoherent intensity, on the other hand, is described by using the four Stokes' parameters. The theory, thus, involves a system of four coupled integro-differential equations for the specific intensity of the incoherent component.

By making reasonable assumption concerning the statistical scattering characteristics of the forest medium, it was found that for the first of the Stokes' parameters a single, uncoupled equation is obtained which is identical to the conventional scalar transport equation. The first Stokes' parameter is the quantity of primary interest since it is, by definition, the total intensity of radiation, i.e., it represents the sum of the intensities of two orthogonal polarizations. This being the case, only the scalar transport equation was needed. The relevant equations are formulated in Section II for the case of planar geometry and plane wave incidence. These equations, subject to appropriate boundary conditions, are solved in Section III. Therein, Chebyshev polynomials are used as basis

functions for series expansions of the diffuse or incoherent intensity. This choice of basis functions reduced two of the three linear systems of equations which had to be solved to systems of two equations each. Legendre polynomials have been used in a similar fashion previously [ZSc]. The unknown expansion coefficients, however, are related by continued fractions, whereas the expansion coefficient associated with the Chebyshev polynomials are related more simply (see Equations (25) and (40)). In Section IV power flux density is defined in terms of intensity and is shown to reduce to truncated series expansions. Numerical results for intensity and flux are presented in Section V.

II. FORMULATION

A forest is modeled as a slab region (Fig. 1) confined within infinite planes $z = 0$ and $z = d$. Its vegetation is assumed to consist of a random distribution of particles which scatter and absorb the incident radiation. The vegetation medium is assumed to be statistically homogeneous and to be characterized by absorption (σ_a) and scatter (σ_s) cross sections per unit volume whose dimensions are meters^{-1}. Furthermore, we assume that the forest medium has an isotropic scatter characteristic, i.e., the average scatter current will radiate an equal amount of power into each spatial direction. A uniform plane wave is assumed to enter the forest from the direction $\hat{\Omega}_o$ defined by angles θ_o and ϕ_o of a spherical coordinate system (Fig. 1). The magnitude of the incident Poynting vector or power flux density is given as S_o in watts per meters squared and frequency is specified by ν_o in Hertz.

As energy enters the forest it is multiply scattered in all directions. To describe this phenomena we use the transport equation (also called the equation of radiative transfer). The transport equation is essentially a statement of conservation of energy and has as its dependent variable the quantity called spectral specific intensity $I_\nu(\underline{r};\hat{\Omega})$. It is written in this manner to indicate that it is both a function of position $\underline{r} = (x,y,z)$ and of direction as represented by the unit vector $\hat{\Omega}$; the subscript ν denotes its spectral nature. To define spectral specific intensity consider an element

of area dA (Fig. 2) whose orientation is defined by the unit normal vector $\hat{n}$. Assume that radiant power, i.e., energy per unit time dP flows in the direction specified by $\hat{\Omega}$ through the projected element of area $dA_1 = dA \cos\theta$. The spectral specific intensity at the point $\underline{r}$ in the direction $\hat{\Omega}$ is then defined by the relationship $I(\underline{r};\hat{\Omega}) = dP/dA_1 d\nu d\Omega$, i.e., to be the power per unit area in watts per meters squared, per frequency interval $d\nu$ in Hertz and per solid angle $d\Omega$ in steradians which flows in the direction $\hat{\Omega}$ normal to the projected element of area dA_1.

Since the planar geometry and incident plane wave problem depicted in Fig. 1 involves a medium (the forest) which scatters radiation isotropically, the spectral specific intensity depends only on the coordinate z and the directions θ and ϕ . Since the medium is linear the scatter field has the same frequency as the incident radiation. Hence[1]

$$I_\nu(r;\hat{\Omega}) = I(z;\theta,\phi)\delta(\nu-\nu_o), \tag{1}$$

and the transport equation becomes [OZ, CZ, ISl, Ch]

$$\cos\theta \frac{dI}{dz} + \sigma_t I = \frac{\sigma_s}{4\pi}\int_0^{2\pi}\int_0^{\pi} I(z;\theta',\phi') \sin\theta' d\theta' d\phi', \quad 0\le z\le d, \tag{2a}$$

where

$$\sigma_t = \sigma_a + \sigma_s \tag{2b}$$

is the total cross-section or extinction cross-section per unit volume. Introducing the normalized quantities

$$\tau = \sigma_t z, \quad \mu = \cos\theta \tag{3a}$$

and albedo

$$W = \sigma_s/\sigma_t \tag{3b}$$

allows us to rewrite Equation (2) as

$$\mu \frac{dI}{d\tau} + I = \frac{W}{4\pi}\int_0^{2\pi}\int_{-1}^{+1} I(\tau;\mu',\phi')d\mu' d\phi', \quad 0\le\tau\le\tau_o, \tag{4}$$

where $\tau_o = \sigma_t d$.

[1]Only the coherent component of the intensity depends on ϕ; the incoherent component depends on z and θ; see Equations (13) and (14).

For convenience we separate the intensity $I(\tau;\mu,\phi)$ into a sum of two terms (see Fig. 3 and [Isl])

$$I = I_d + I_{ri}. \tag{5}$$

After substituting Equation (5) into Equation (4) I_d is defined to satisfy the relationship

$$\mu \frac{dI_d}{d\tau} + I_d = \frac{W}{4\pi} \int_0^{2\pi} \int_{-1}^{1} (I_d + I_{ri})\, d\mu'\, d\phi' \tag{6}$$

and I_{ri} to satisfy the simpler relationship

$$\mu \frac{dI_{ri}}{d\tau} + I_{ri} = 0. \tag{7}$$

Integrating Equation (7) gives

$$I_{ri}(\tau;\mu,\phi) = I_{ri}(0;\mu,\phi)e^{-\tau/\mu}. \tag{8}$$

Comparing Equation (7) with Equation (4) we see that they would be identical if the integral term were zero. The integral term accounts for the multiscatter effects of the medium; without it the transport equation would simply describe the attenuation of energy as it flows in a particular direction through the medium due to absorption (σ_a) and scattering (σ_s) by particles along a given ray path. This effect is described by the solution given in Equation (8). Hence, we call I_{ri} the reduced incident or coherent intensity and we designate I_d, defined by Equation (6), the diffuse or incoherent intensity since it accounts for multiscatter effects.

To specify boundary conditions required by the slab geometry of Figure 1 it is convenient to separate the diffuse intensity into two components, a forward diffuse intensity I_d^+ and a backward diffuse intensity I_d^-, where

$$I_d = \begin{cases} I_d^+, & 0 \le \theta \le \pi/2 \quad \text{or} \quad 0 \le \mu \le 1 \qquad (9a) \\ I_d^-, & \frac{\pi}{2} \le \theta \le \pi \quad \text{or} \quad -1 \le \mu \le 0 \qquad (9b) \end{cases}.$$

Definition (9) is further clarified by Figure 3 wherein the forward diffuse constituent I_d^+ is confined to angles of scatter θ between zero and ninety degrees (representing energy transport in the positive τ direction) while the backward diffuse intensity I_d^- ranges over ninety to one hundred and eighty degrees (corresponding to energy flow in the negative τ direction). Since these components are generated within the forest we must have

$$I_d^+ = 0 \quad \text{at} \quad \tau = 0 \tag{10a}$$

and

$$I_d^- = 0 \quad \text{at} \quad \tau = \tau_o, \tag{10b}$$

i.e., diffuse intensity cannot enter the slab from the exterior regions.

Recall that we have assumed that a plane wave enters the forest in direction $\hat{\Omega}_o$ with a power density or Poynting vector magnitude of S_o watts per meters squared. The incident intensity in watts per meters squared per radians squared is then

$$I_o = S_o\, \delta(\hat{\Omega} - \hat{\Omega}_o) = S_o\, \frac{\delta(\theta-\theta_o)\delta(\phi-\phi_o)}{\sin\theta} = S_o\delta(\mu-\mu_o)\delta(\phi-\phi_0), \tag{11}$$

where $\delta(x)$ represents a Dirac delta function and (θ_o, ϕ_o) are the direction angles of the incident plane wave. From Equations (5), (9) and (10) we see that intensity in the forward direction satisfies the continuity condition

$$I_o = I_d^+ + I_{ri} = I_{ri} \quad \text{at } \tau = 0. \tag{12}$$

Using Equations (8), (11) and (12) we obtain for the reduced incident intensity

$$I_{ri}(\tau;\mu,\phi) = I_o e^{-\tau/\mu} = S_o\, \delta(\mu-\mu_o)\delta(\phi-\phi_o)e^{-\tau/\mu_o}. \tag{13}$$

Substituting Equation (13) into Equation (6) and integrating over ϕ yields transport equations for the diffuse intensity

$$\mu \frac{dI_d^{\pm}}{d\tau} + I_d^{\pm} = \frac{W}{2}\left[\int_0^1 I_d^{+}\, d\mu' + \int_{-1}^{0} I_d^{-}\, d\mu'\right] + \frac{WS_o}{4\pi} e^{-\tau/\mu_o}, \qquad (14)$$

$$\begin{matrix} 0\le\mu\le 1. \\ -1 \quad\quad 0 \end{matrix}$$

The superscript designations ($\pm$) identify the appropriate ranges of μ as defined in Equation (9). The two linear integrodifferential Equations (14) subject to the two boundary conditions, Equation (10), constitute a complete mathematical statement of the problem which will be treated in the succeeding sections.

III. REDUCTION OF THE TRANSPORT EQUATION TO SYSTEMS OF LINEAR EQUATIONS

The Transport equations (14) are solved by representing the diffuse intensities as truncated series expansions of half-range Chebyshev polynomials

$$I_d^{\pm}(\tau;\mu) = \sum_{n=0}^{N}{}' B_n^{\pm}(\tau)\, T_n^{\pm}(\mu), \quad \begin{matrix} 0 \le\mu\le 1, \\ -1 \quad 0 \end{matrix} \qquad (15a)$$

with

$$T_n^{\pm}(\mu) = T_n(2\mu \mp 1) \qquad (15b)$$

denoting two Chebyshev polynomials of order n which are complete orthogonal functions over the μ domains (0,1) and (-1,0), respectively. Substituting Equation (15) into Equation (14) gives

$$\sum_{n=0}^{N}{}' \left[\mu \frac{dB_n^{\pm}(\tau)}{d\tau} + B_n^{\pm}(\tau)\right] T_n^{\pm}(\mu) = \frac{W}{2} \sum_{n=0,2,4,\ldots}^{\le N} \left[B_n^{+}(\tau)+B_n^{-}(\tau)\right]\left[\frac{-1}{n^2-1}\right] + \frac{WS}{4\pi} e^{-\tau/\mu_o}, \quad \begin{matrix} 0\le\mu\le 1, \\ -1 \quad 0 \end{matrix} \qquad (16)$$

where use was made of the integral evaluations

$$\int_0^1 T_n^+(\mu)\,d\mu = \int_{-1}^0 T_n^-(\mu)d\mu = \tfrac{1}{2}\int_{-1}^1 T_n(x)dx = \begin{cases} \frac{-1}{n^2-1}, & n=0,2,4,\ldots \\ 0, & n=1,3,5,\ldots \end{cases} \tag{17}$$

Using the recursive formulas

$$2(2\mu\mp1)T_n(2\mu\mp1) = T_{n+1}(2\mu\mp1)+T_{n-1}(2\mu\mp1) \tag{18}$$

to replace the terms $\mu T_n(2\mu\mp1)$ in Equation (16) yields

$$\sum_{n=0}^{N}\left\{[T_{n+1}^{\pm}+T_{n-1}^{\pm}]\frac{dB_n^{\pm}}{d\tau} + T_n^{\pm}\left[\mp2\,\frac{dB_n^{\mp}}{d\tau} + 4B_n^{\pm}\right]\right\} = 2W \sum_{n=0,2,4..}^{\leq N}[B_n^+ + B_n^-]\left(\frac{-1}{n^2-1}\right) + \frac{WS_o}{\pi}\,e^{-\tau/\mu_o}, \quad \underset{-1}{0} \leq \mu \leq \underset{0}{1} \tag{19}$$

The orthogonality properties of the half-range Chebyshev polynomials $T_n^{\pm}(\mu) = T_n(2\mu\mp1)$ provide the means to obtain the following system of 2n+2 coupled first order differential equations for the τ-dependent expansion coefficients $B_n(\tau)$:

$$\frac{dB_1^{\pm}}{d\tau} \pm2\,\frac{dB_0^{\pm}}{d\tau} + 4B_0^{\pm} + 2W\sum_{n=0,2,4,\ldots}^{\leq N}[B_n^+ + B_n^-]\left(\frac{1}{n^2-1}\right) - \frac{WS_o}{\pi}\,e^{-\tau/\mu_o} = 0, \quad n=0, \tag{20a}$$

$$2\,\frac{dB_0^{\pm}}{d\tau} + \frac{dB_2^{\pm}}{d\tau} \mp2\,\frac{dB_1^{\pm}}{d\tau} + 4B_1^{\pm} = 0, \quad n = 1, \tag{20b}$$

$$\frac{dB_{n-1}^{\pm}}{d\tau} + \frac{dB_{n+1}^{\pm}}{d\tau} \pm 2\frac{dB_n^{\pm}}{d\tau} + 4B_n^{\pm} = 0, \quad n = 2,3,\ldots, N-1, \tag{20c}$$

$$\frac{dB_{N-1}^{\pm}}{d\tau} \mp 2\,\frac{dB_N^{\pm}}{d\tau} + 4B_N^{\pm} = 0, \quad n=N. \tag{20d}$$

In deducing the above use was made of the fact that $T_{-1} = T_1$ and that the truncated series representations Equation (15) require the coefficients $B_n(\tau)$ to be zero for n>N; the latter was used in writing Equation (20d).

Orthogonality of the $T_n(2\mu\mp1)$ functions is also used to obtain from Equations (10) and (15) the boundary conditions

$$B_n^+(0) = 0 \qquad \text{for all n} \qquad (21a)$$

$$B_n^-(\tau_o) = 0. \qquad (21b)$$

The total solution to Equation (20) subject to boundary conditions Equation (21) consists of homogeneous and particular solutions $B_n^{\pm h}(\tau)$ and $B_n^{\pm p}(\tau)$, respectively, i.e.,

$$B_n^{\pm}(\tau) = B_n^{\pm h}(\tau) + B_n^{\pm p}(\tau), \quad n = 0,\ldots,N. \qquad (22)$$

The coefficients $B_n^{\pm h}(\tau)$ satisfy the linear system of Equations (20) with S_o set equal to zero while $B_n^{\pm p}(\tau)$ satisfy the inhomogeneous system ($S_o \neq 0$) and have the same functional dependence on τ as the forcing function (see Equation (42b)).

A. Homogeneous Solution to Equation (20) ($S_o = 0$)

Since the system of equations (20) involves only first order derivatives in τ, homogeneous solutions must depend exponentially on τ. Hence, it may be assumed that, in general, the homogeneous solution to Equation (20) takes the form

$$B_n^{\pm h}(\tau) = \sum_{k=0}^{N} a_{n,k}^{\pm} \, e^{-\tau/s_k}, \qquad (23)$$

where $a_{n,k}^{\pm}$ and s_k are unknown constants and integer k accounts for all possible solutions. Substituting Equation (23) into Equations (20) and (21) gives the linear system of equations

$$a^{\pm}_{1,k} - 2(2s_k \mp 1)a^{\pm}_{0,k} - 2s_k \, W \sum_{n=0,2,\ldots}^{\leq N} \frac{a^{+}_{n,k} + a^{-}_{n,k}}{n^2-1} = 0, \quad n=0, \tag{24a}$$

$$2a^{\pm}_{0,k} - 2(2s_k \mp 1)a^{\pm}_{1,k} + a^{\pm}_{2,k} = 0, \quad n=1, \tag{24b}$$

$$a^{\pm}_{n-1,k} - 2(2s_k \mp 1)a^{\pm}_{n,k} + a^{\pm}_{n+1,k} = 0, \quad n=2,\ldots,N-1, \tag{24c}$$

and

$$a^{\pm}_{N-1,k} - 2(2s_k \mp 1)a^{\pm}_{N,k} = 0, \quad n=N. \tag{24d}$$

Using the definitions of the Chebyshev polynomials of the second kind [ASt], the three Equations (24b), (24c) and (24d) yield expressions for all coefficients in terms of the two coefficients $a^{\pm}_{N,k}$:

$$a^{\pm}_{n,k} = \frac{\varepsilon_n}{2} U_{N-n}(2s_k \mp 1)a^{\pm}_{N,k}, \quad n=0,1,2,\ldots,N, \tag{25a}$$

$$\varepsilon_n = \begin{cases} 1, & n=0 \\ 2, & n \neq 0 \end{cases}. \tag{25b}$$

Substituting Equation (25) into Equation (24a) and utilizing the relationships

$$U_{n+1}(x) = 2x\, U_n(x) - U_{n-1}(x) \tag{26a}$$

$$T_{N+1}(x) = x\, U_N(x) - U_{N-1}(x) \tag{26b}$$

result in the simpler system of equations

$$\underset{\sim}{A}(s_k)\underline{a}_k = 0, \tag{27a}$$

where

$$\underset{\sim}{A}(s_k) = \begin{pmatrix} a_1(s_k^+) & a_2(s_k^-) \\ a_2(s_k^+) & a_1(s_k^-) \end{pmatrix}, \quad \underline{a}_k = \begin{pmatrix} a_{N,k}^+ \\ a_{N,k}^- \end{pmatrix}, \tag{27b}$$

$$s_k^{\pm} = 2s_k \mp 1, \quad a_1(x) = \alpha(x) + s_k W\beta(x), \quad a_2(x) = s_k W\beta(x), \tag{27c}$$

$$\alpha(x) = T_{N+1}(x), \quad \beta(x) = -U_N(x) + 2S_e(x), \quad S_e(x) = \sum_{n=2,4,\ldots}^{\leq N} \frac{U_{N-n}(x)}{n^2-1}. \tag{27d}$$

For non-trivial solutions, $\det \underset{\sim}{A}(S_k) = 0$; yielding the characteristic equation

$$\begin{aligned} T_{N+1}(2s_k+1)T_{N+1}(2s_k-1) + s_k W \left[T_{N+1}(2s_k+1) \left\{ -U_N(2s_k-1) + 2S_e(2s_k-1) \right\} \right. \\ \left. + T_{N+1}(2s_k-1) \left\{ -U(2s_k+1) + 2S_e(2s_k+1) \right\} \right] = 0. \end{aligned} \tag{28}$$

This eigenvalue equation is a polynomial in s_k^2 with real coefficients of order N+1 and provides 2N+2 non-zero, distinct, real eigenvalues $s_k = \pm s_m$, $s_m > 0$, $m=0,\ldots,N$. Physically, real eigenvalues are to be expected since the associated eigenfunctions are orthogonal and their sum represents specific intensity or real power. Combining Equation (28) with one of the equations of Equation (27) yields for each eigenvalue s_k:

$$\frac{a_{N,k}^-}{a_{N,k}^+} = \frac{T_{N+1}(2s_k-1)}{T_{N+1}(2s_k+1)}, \quad k = \pm m, \; m=0,\ldots,N. \tag{29}$$

For k = m, i.e., for positive eigenvalues $s_k = s_m > 0$ assume that

$$a_{N,m}^+ = a_m \, T_{N+1}(2s_m+1), \quad a_m = \text{constant}. \tag{30}$$

It then follows using Equations (29) and (30) that

$$a_{N,m}^- = a_m \, T_{N+1}(2s_m-1). \tag{31}$$

Combining Equations (30) with (31) gives for $s_k = s_m > 0$

$$a^{\pm}_{N,m} = a_m \, T_{N+1}(2s_m \pm 1). \tag{32}$$

Similarly, for k = -m, i.e., for negative eigenvalues

$s_k = s_{-m} = - s_m$ it can be shown that

$$a^{\pm}_{N,-m} = a_{-m} \, T_{N+1}(2s_m \mp 1), \; a_{-m} = \text{constant}. \tag{33}$$

Using Equations (32) and (33) with (25) permits Equation (23) to be written in terms of positive eigenvalues only:

$$B_n^{\pm h}(\tau) = \frac{1}{2} \, \varepsilon_n \sum_{m=0}^{N} [a_m \, T_{N+1}(2s_m \pm 1) \, U_{N-n}(2s_m \mp 1) e^{-\tau/s_m} \tag{34}$$

$$+ (-1)^N b_m \, T_{N+1}(2s_m \mp 1) \, U_{N-n}(2s_m \pm 1) e^{\tau/s_m}].$$

In Equation (34) we have used the identity $U_n(-x) = (-1)^n U(x)$ and have set $b_m = (-1)^N a_{-m}$. Hence, with Equation (15) the most general homogeneous solution to Equation (14) is:

$$I_d^{\pm h} = \sum_{n=0}^{N} B_n^{\pm h}(\tau) \, T_n(2\mu \mp 1) \tag{35}$$

with $B_n^{\pm h}(\tau)$ given by Equation (34).

Simpler expressions for $I_d^{\pm h}$ are obtained by substituting Equation (34) into (35), interchanging the order of the summation operations and using a closed form expression to replace the series which is summed over the integer n. The result is

$$I_d^{\pm h} = \frac{1}{4} \sum_{m=0}^{N} a_m e^{-\tau/s_m} \, T_{N+1}(2s_m \pm 1) \left[\frac{T_{N+1}(2s_m \mp 1) - T_{N+1}(2\mu \mp 1)}{s_m - \mu} \right]$$

$$+ \; b_m e^{\tau/s_m} \, T_{N+1}(2s_m \mp 1) \left[\frac{T_{N+1}(2s_m \pm 1) + (-1)^N T_{N+1}(2\mu \mp 1)}{s_m - \mu} \right]. \tag{36}$$

B. Particular Solution

To obtain the particular solution we assume that $B_n^{\pm p}(\tau)$ has the same τ- dependence as the forcing term in Equation (20a), namely,

$$B_n^{\pm p}(\tau) = A_n^{\pm} e^{-\tau/\mu_o}. \tag{37}$$

Substituting into Equation (20) yields the following linear system of equations for the coefficients A_n:

$$A_1^{\pm} - 2(2\mu_o \mp 1) A_0^{\pm} - 2\mu_o W \sum_{\substack{n=0,2,4,\ldots \\ n=1}}^{N} \left(\frac{A_n^+ + A_n^-}{2}\right) + \mu_o \frac{WS_o}{\pi} = 0, \quad n = 0, \tag{38a}$$

$$2A_0^{\pm} - 2(2\mu_o \mp 1)A_1^{\pm} + A_2^{\pm} = 0 \quad , \quad n = 1, \tag{38b}$$

$$A_{n-1}^{\pm} - 2(2\mu_o \mp 1)A_n^{\pm} + A_{n+1}^{\pm} = 0 \quad , n = 2, \ldots, N-1, \tag{38c}$$

and

$$A_{N-1}^{\pm} - 2(2\mu_o \mp 1)A_N^{\pm} = 0 \, , \quad n = N \, . \tag{38d}$$

Since Equations (38) are identical in form to Equations (24) except for the forcing term $\mu_o S_o W/\pi$ they can be solved in like fashion to yield the system of two equations for the two unknowns $A_N^{\pm}$:

$$\underset{\sim}{A}(\mu_o)\underline{A} = \mu_o \frac{WS_o}{\pi} \underline{1} \, , \quad \underline{A} = \begin{pmatrix} A_N^+ \\ A_N^- \end{pmatrix} \, , \quad \underline{1} = \begin{pmatrix} 1 \\ 0 \end{pmatrix} , \tag{39}$$

where

$$A_n^{\pm} = \frac{1}{2} \varepsilon_n \, U_{N-n}(2\mu_o \mp 1) A_N^{\pm} \quad , \, n = 0,1,2,\ldots N \, , \tag{40}$$

with ε_n defined in Equation (25b).
The matrix $\underset{\sim}{A}(\mu_o)$ is identical to $\underset{\sim}{A}(s_k)$ in Equation (27b) but with s_k replaced by μ_o and $s_k^{\pm}$ by $\mu_o^{\pm} = 2\mu_o \mp 1$. The solution to Equation (39) involves a simple 2 x 2 matrix inversion from which it is found that

$$A_N^{\pm} = \mu_o \frac{WS_o}{\pi} \frac{T_{N+1}(2\mu_o \mp 1)}{\det \underset{\sim}{A}(\mu_o)} , \tag{41}$$

where $\det \underset{\sim}{A}(\mu_o)$ is identical to the left hand side of Equation (28) but with s_k replaced by μ_o.

Combining Equations (37) and (39) with Equation (41) gives the particular solution

$$I_d^{\pm p} = \sum_{n=0}^{N} B_n^{\pm p}(\tau)\ T_n(2\mu \mp 1) \tag{42a}$$

with

$$B_n^{\pm p}(\tau) = \varepsilon_n \frac{\mu_o WS_o}{2\pi} \frac{T_{N+1}(2\mu_o \pm 1)}{\det \underset{\sim}{A}(\mu_o)} U_{N-n}(2\mu_o \mp 1) e^{-\tau/\mu_o}. \tag{42b}$$

As was done for the homogeneous solution, the summation over n in Equation (42a) can be replaced by a closed form expression which results in

$$I_d^{\pm p} = \frac{A_N^{\pm}\ e^{-\tau/\mu_o}}{4} \left[\frac{T_{N+1}(2\mu_o \mp 1) - T_{N+1}(2\mu \mp 1)}{\mu_o - \mu} \right] \tag{43}$$

with $A_N^{\pm}$ given by Equation (41).

C. Total Solution

The complete solution for the diffuse intensity is the superposition of the homogeneous and particular solutions, given either by Equations (35) and (42) or (36) and (43). The unknown coefficients a_m and b_m are determined by application of the boundary conditions in Equation (21) which we write as

$$B_n^{+h} + B_n^{+p} = 0 \text{ at } \tau = 0 \text{ for } 0 \leq \mu \leq 1 \tag{44a}$$

and

$$B_n^{-h} + B_n^{-p} = 0 \text{ at } \tau = \tau_o \text{ for } -1 \leq \mu \leq 0 . \tag{44b}$$

Substitution of Equations (34) and (42b) into Equation (44) and equating coefficients of $T_n(2\mu\mp 1)$ to zero (these polynomials are complete for the μ-ranges involved) provide the following system of inhomogeneous linear equations from which to determine the 2N+2 unknown constants a_m and b_m:

$$\sum_{m=0}^{N}[a_m T_{N+1}(2s_m+1)U_{N-n}(2s_m-1)+b_m(-1)^n T_{N+1}(2s_m-1)U_{N-n}(2s_m+1)] = -A_N^+ U_{N-n}(2\mu_o-1), \quad (45a)$$

$$\sum_{m=0}^{N}[a_m T_{N+1}(2s_m-1)U_{N-n}(2s_m+1)e^{-\tau_o/s_m} + b_m(-1)^n T_{N+1}(2s_m+1)U_{N-n}(2s_m-1)e^{\tau_o/s_m} = -A_N^- e^{-\tau_o/\mu_o} U_{N-n}(2\mu_o+1) \quad (45b)$$

with $A_N^{\pm}$ given by Equation (41) and n = 0,...,N.

Although we have formally addressed only the slab problem, the above analysis applies in a simple fashion to the half space problem ($\tau_o = \infty$). From Equation (45b) we see that for $\tau_o \to \infty$ all coefficients b_m must be identically zero in order that the system of equations remain bounded. Equation (45a) alone yields enough relationships from which to determine the remaining nonzero coefficients a_m.

IV. FLUX DENSITY

A second fundamental quantity used in transport theory to describe power flow properties is the flux density. With reference to Figure 2 and the definition of specific intensity, the forward flux density $F^+(\underline{r};\hat{n})$ is defined [Isl] as the amount of power that flows through the area element dA in all directions $0 \leq \theta \leq \pi/2$ where θ is measured from the unit vector $\hat{n}$ normal to the area element, i.e.,

$$F^+(\underline{r};\hat{n}) = \int_0^{2\pi}\int_0^{\pi/2} I(\underline{r};\hat{\Omega})\hat{\Omega}.\hat{n}\, d\Omega\,, \quad \hat{\Omega}.\hat{n} = \cos\theta\,. \quad (46a)$$

Flux is in units of watts per meters squared and solid angle $d\Omega = \sin\theta d\theta d\phi$. In like fashion, we also define a backward flux density $F^-(\underline{r};\hat{n})$ in terms of power which flows through dA but in the $-\hat{n}$ direction, i.e.,

$$F^-(\underline{r};\hat{n}) = \int_0^{2\pi}\int_{\pi/2}^{\pi} I(\underline{r};\hat{\Omega})\hat{\Omega}.(-\hat{n})d\Omega \ . \tag{46b}$$

For the slab geometry and plane wave incidence of Figure 1, the above flux densities depend only on z (or τ) and can be written using Equations (8) and (15) as

$$F^+(\tau) = F^+_{ri}(\tau)+F^+_d(\tau),\ F^-(\tau) = F^-_d(\tau)\ , \tag{47a}$$

where

$$F^+_{ri}(\tau) = \int_0^{2\pi}\int_0^1 \mu I_{ri}(\tau;\phi,\mu)d\mu d\phi = S_o e^{-\tau/\mu_o}\int_0^{2\pi}\delta(\phi-\phi_o)d\phi\int_0^1\delta(\mu-\mu_o)\mu d\mu$$

$$= \mu_o S_o e^{-\tau/\mu_o}\ , \tag{47b}$$

$$F^+_d(\tau) = \int_0^{2\pi}\int_0^1 \mu I^+_d(\tau;\mu)d\mu d\phi = \sum_{n=0}^{N} B^+_n(\tau)\left[2\pi\int_0^1 \mu T_n(2\mu-1)d\mu\right], \tag{47c}$$

and

$$F^-_d(\tau) = -\int_0^{2\pi}\int_{-1}^0 \mu I^-_d(\tau;\mu)d\mu d\phi = -\sum_{n=0}^{N} B^-_n(\tau)\left[2\pi\int_{-1}^0 \mu T_n(2\mu+1)d\mu\right], \tag{47d}$$

where μ has been substituted for θ.

Evaluations of the above integrals can be shown to yield

$$2\pi\int_0^1 \mu T_n(2\mu-1)d\mu = \begin{cases} J^e_n \equiv -\dfrac{\pi}{n^2-1}, & n = 0,2,4,\ldots \\ J^o_n \equiv \dfrac{-\pi}{n^2-4}, & n = 1,3,5,\ldots \end{cases} \tag{48}$$

$$2\pi\int_{-1}^0 \mu T_n(2\mu+1)d\mu = \begin{cases} -J^e_n, & n = 0,2,4,\ldots \\ J^o_n, & n = 1,3,5,\ldots \ . \end{cases} \tag{49}$$

Hence,

$$F_d^{\pm}(\tau) = -\pi\left[\sum_{n=0,2,4,\ldots}^{\leq N} \frac{1}{n^2-1} B_n^{\pm}(\tau) \pm \sum_{n=1,3,5,\ldots}^{\leq N} \frac{1}{n^2-4} B_n^{\pm}(\tau)\right], \tag{50}$$

where the summations terminate at N or N-1, N being either even or odd and $B_n^{\pm}(\tau)$ is given by Equation (22) with $B_n^{\pm h}(\tau)$ available from Equation (34) and $B_n^{\pm p}(\tau)$ from Equation (42b).

A convenient way to express the above result after interchanging the order of the summation is to use the quantities defined in Equation (27d), namely $\alpha(x)$, $\beta(x)$ and $S_e(x)$ along with the odd summation term

$$S_o(x) = \sum_{n=1,3,5,\ldots}^{\leq N} (n^2-4)^{-1} U_{N-n}(x) \tag{51}$$

so that Equation (50) becomes

$$F^{\pm}(\tau) = -\frac{\pi}{2}\sum_{m=0}^{N} [a_m \alpha(x_m^{\mp})\{\beta(x_m^{\pm}) \pm 2 S_o(x_m^{\pm})\}e^{-\tau/s_m}$$

$$+ b_m \alpha(x_m^{\pm})\{\beta(x_m^{\mp}) \mp 2 S_o(x_m^{\mp})\}e^{\tau/s_m}] \tag{52a}$$

$$- \frac{\mu_o W S_o}{2 \det \underset{\sim}{A}(\mu_o)} \alpha(y_o^{\mp})\{\beta(y_o^{\pm}) \pm 2 S_o(y_o^{\pm})\}e^{-\tau/\mu_o},$$

where

$$x_m^{\pm} = 2s_m \mp 1, \quad y_o^{\pm} = 2\mu_o \mp 1. \tag{52b}$$

V. NUMERICAL RESULTS

Based on the Chebyshev method, data is obtained for the diffuse intensities and the power fluxes for both the half-space ($\tau_o = \infty$) and slab configurations. Selected numerical results for flux incorporate a comparison with calculations using first order theory expressions (see [Isl]).

As can be seen from Equation (4) or (14) the forest is characterized by the single parameter W called the albedo, which is defined in Equation (3b). In general, it can vary from zero (no scattering) to unity (no absorption). We have chosen W to range from a low of 0.25 to a high of 0.95; the former describes a medium which mostly absorbs energy whereas the latter characterizes a predominantly scattering environment. A plane wave is assumed to enter the forest at incidence angles of $\theta_o = 0^o$, 30^o and 60^o for the half-space geometry and at $\theta_o = 0^o$ for the slab geometry. The normalized slab thickness τ_o varies from 0.2 to 20. All intensity curves are normalized by setting $S_o/4\pi$ equal to unity while all power flux curves are normalized with S_o set to unity. These normalizations were chosen to be compatible with the units of specific intensity which is power per unit area, per unit solid angle and of power flux which is power per unit area.

In Figures 4 and 5, the forward $I_d^+(\tau; 0^o)$ and backward $I_d^-(\tau; 180^o)$ diffuse intensities in the $\theta = 0^o$ and 180^o directions, respectively, are plotted for the three angles of incidence $\theta_o = 0^o$, 30^o and 60^o as a function of penetration depth τ for albedos W = 0.25, 0.50, 0.75, 0.90 and 0.95. For very small τ values the effect of multiscattering is small. The flow of energy is mainly confined to the coherent (reduced incident) intensity (not shown). Soon, however, multiscattering of the energy takes place. Energy transfers into the diffuse or incoherent state. It quickly builds up to a maximum, having started from zero, but then decreases with τ due to absorption loss along the longer multiscatter path lengths traversed in going from $\tau = 0$ to an observation point τ. Meanwhile, the coherent energy decreases more rapidly (see e.g. curve 5 in Fig. 15.c) since it loses energy both due to scattering out of the direction of flow as well as to absorption losses along the prescribed path. Furthermore, the maximum forward diffuse intensity is larger and occurs deeper inside the half-space region for stronger scattering (larger W) media. It also takes longer for intensity to attenuate and its rate of attenuation is smaller when W is larger.

Observe further that the forward diffuse intensity in the $\theta = 0^o$ direction is larger for smaller incidence angles. This can

be explained by noting that at a given value of τ more energy is available from the coherent intensity I_{ri} to be multiscattered when θ_o is smaller. For larger τ values, the rate of decrease of $I_d^+(\tau;0^o)$ depends only on the albedo. This follows from the asymptotic solution (see [CZ]) or from the curves in Figure 4 for W = 0.9 and 0.95 which have constant slopes near $\tau = 10$ (the asymptotic τ range is not reached for curves with smaller values of W). However, for smaller τ values, incidence angle does influence the rate of attenuation. The curves in Figure 4 indicate that smaller rates of attenuation are associated with smaller incidence angles. This also follows from Equation (43) where the exponential attenuation $(\exp(-\tau/\mu_o))$ is a dominant decay factor; for μ_o equal to unity, i.e., for normal incidence $(\theta_o = 0^o)$, the attenuation rate in the τ direction is smaller than when μ_o is smaller.

Figures 5 depict the τ dependence of the normalized $(S_o/4\pi = 1)$ backward diffuse intensity (in decibels) which flows in the $\theta = 180^o$ direction. Again we see that the larger the albedo the stronger the incoherent intensity which is characteristic of increased scattering taking place in the forest. Note that the strongest backward diffuse intensity occurs at the air-forest interface $\tau = 0$. This was anticipated because only the region to the right of a particular value of τ contributes to the backward intensity I_d^- at the value τ; hence, since every particle in the entire half-space $(\tau>0)$ scatters energy, a portion of which can be assumed to reach the interface, maximum backscatter intensity occurs there. As in the case of forward scatter, the angle of incidence θ_o also affects the amount of energy which backscatters. We see that for larger θ_o less energy travels in the $\theta = 180^o$ direction; this is due to the fact that a larger θ_o results in a smaller coherent intensity reaching the depth τ in the half-space region; hence, a smaller coherent intensity penetrates the region to the right of τ. With less energy available from the coherent energy state and thus for larger θ_o less scatter energy flows in the backward direction.

Figures 6 through 8 are plots of the normalized diffuse intensity (in decibels) versus scatter angle θ for albedos W = 0.25, 0.50, 0.75, 0.90 and 0.95 and for different penetration depths τ. In

Figure 6, $I_d^+(\tau;\theta)/I_d^+(\tau;90^o)$ is plotted for the smaller depths (τ=0.05, 0.1, 0.2, 0.5 and 1.0) while in Figure 7, $I_d^+(\tau;\theta)/I_d^+(\tau;0^o)$ versus θ is plotted for the larger depths (τ = 1, 2, 5, 10, 20). In Figure 8, $I_d^-(\tau;\theta)/I_d^-(\tau;90^o)$ versus θ is plotted for the three representative values τ = 0.1, 1.0 and 10. Also drawn are curves for different incidence angles (θ = 0^o, 30^o and 60^o).

Consider first Figure 6. It is immediately seen that for small penetration depths, maximum intensities flow in directions near θ = 90^o. As τ increases, the maxima shift toward the θ = 0^o direction. Furthermore, for larger albedos the relative peak intensity values diminish and occur at larger θ values (compare, for example, curve 5 in Figure 6.a to curve 5 in Figure 6.m). Note also in each figure, and for the larger τ values particularly, that the difference in intensity, as measured from one curve to the next at a given value of θ, decreases for larger albedos, i.e., the curves become more compressed (compare the curves of Figure 6.a to the curves of Figure 6.m to see this effect). Furthermore, at a given observation point τ we see that as θ_o increases the relative peak intensity rises and shifts further away from the vertical; for illustration refer to the τ=1, θ_o=0^o *and* 60^o *curves of Figures 6.m and 6.o*, respectively. Likewise, for a given incidence angle θ_o, as τ increases this same shift occurs as is vividly portrayed in the curves of Figures 7.a through 7.o where the relative maximum are seen to shift to the θ=0^o direction.

Changing θ_o seems to have a minor effect on this shift in maximum intensity, but an increase in τ plays a significant role. Recall that a major portion of the energy which scatters in a particular direction θ through the observation point τ comes from the more direct or shorter paths traversed between a scatterer (hit by the incident radiation) and the observation point. Evidently, for small τ and no matter whether θ_o be small or large, maximum intensity flows in directions near the vertical (θ = 90^o). This results because contributions to the energy flow through the point τ near the air-forest interface in directions θ_o are overwhelmed by the numerous energy contributions coming from the many scatterers in the infinite domain of the thin slab region between the interface (τ = 0) and the observation point τ; the bulk of the energy must travel in directions near

$\theta = 90^{o}$ in order to pass through τ. For fixed τ and for increasing θ_o more energy transfers into the diffuse intensity sooner (i.e., at smaller depths τ). Hence, more energy is now available to be scattered into the $\theta \Rightarrow 0^{o}$ direction to counteract the energy contribution which enhances vertical flow. However, the contributions in the normal direction for small τ values are small and the effect of shifting the intensity away from the vertical direction is not strongly felt until τ becomes larger.

For larger values of τ, Figures 7.a through 7.o show that the angular distribution of intensity evolves into a narrow beam of radiation directed in the $\theta = 0^{o}$ direction. This can be understood by again considering a point on the τ-axis, but this time far from the air-forest interface. The strongest scattered radiation to reach the observation point τ is now seen to come from the region adjacent to the τ-axis. This occurs because energy originating there suffers the least loss (due to absorption) as paths leading to the observation point from this region are smaller than from elsewhere. In Figures 7 it is seen that for the smaller albedo cases, indicative of larger absorption losses, beam narrowing occurs at shorter penetration depths when compared to the larger albedo cases. Hence, the forward diffuse intensity exhibits focusing into the $\theta = 0^{o}$ direction at large τ values regardless of the direction of the incident radiation.

In Figures 8, the relative backward diffuse intensity $I_d^-(\theta;\tau)/I_d^-(90^{o};\tau)$ versus scatter angle θ for the half-space problem is seen to display a maximum intensity flowing in the $\theta = 90^{o}$ direction (except for the $\tau = 0.1$, $\theta_o = 0^{o}$ curves of Figures 8.j ($W = 0.9$) and 8.m ($W = 0.95$) and the $\tau = 0.1$, $\theta_o = 30^{o}$ ($W = 0.95$) curve of Figure 8.n) and to decrease monotonically to a minimum value in the $\theta = 180^{o}$ direction. Also, for the small albedo case ($W = 0.25$) and for incidence angles $\theta_o = 0^{o}$ and 30^{o} (Figs. 8.a and 8.b, respectively) the relative backward diffuse intensity is shown to be essentially independent of τ; this is also true for the $\tau = 0.10$ and 1.0, $\theta_o = 60^{o}$ curves of Figure 8.c and for the $\theta_o = 60^{o}$ curves of Figures 8.f, 8.i, 8.l and 8.o.

The curves show that as energy progresses through the forest it, at first, scatters predominantly in the vertical direction and

eventually proceeds in the forward normal direction, losing energy all the time. Backscatter at τ comes from the entire region to the right of τ. In a small layer to the right of τ, energy is the strongest and provides the most significant backscatter contribution. This contribution flows predominantly in the near vertical direction. As θ increases from 90^{o} to 180^{o}, the backscatter diffuse intensity falls because energy contributions in these directions (from successive layers to the right of the initial layer) are relatively weaker. Hence, in these directions, the intensity is less than in the vertical direction as most figures show and the τ-dependence is essentially that of the vertical direction.

For small θ_o observe that the relative backward diffuse intensity at small penetration depths is larger than at large penetration depths. However, at larger incidence angles θ_o the reverse occurs; less relative energy flows in the $\theta = 180^{o}$ direction at smaller τ values than at larger τ values. At larger angles θ_o more energy is lost from the coherent intensity due to absorption and scatter over a small distance τ than occurs at the smaller angles θ_o (note that if ℓ is the path length, $\tau = \ell \cos \theta_o$; hence, if τ is fixed, ℓ is larger when θ_o is larger). Therefore, less energy is available to be scattered into the backward direction when θ_o is large. For small τ, most of the energy remains still with the coherent intensity and the diffuse intensity strongly scatters near the vertical direction regardless of θ_o. Therefore, for small τ we expect the same for the back diffuse intensity. However, for small angles considerable energy enters the region to the right of τ; the smaller τ, the more energy enters the larger region to the right of τ and, therefore, contributes more scatter energy backward. For sufficiently large τ, the forward energy flow becomes essentially forward diffuse energy. It is a beam of radiation centered around the τ-axis. The strongest backscatter intensity now travels near the τ-axis but in the $\theta = 180^{o}$ as path lengths are smallest in this direction. For larger θ_o this effect is reached sooner in the forest than when θ_o is smaller. Hence, we see a stronger relative diffuse intensity at larger τ values when θ_o is large.

In Figures 9 through 12 intensity curves are drawn for the slab problem. All curves are very similar to those we have already

discussed for the half-space problem. Note in Figure 10 that I_d^- goes to zero as τ approaches τ_o as boundary condition, Equation (10b), requires.

Power flux density is plotted versus τ in Figures 13 through 20 (using the Chebyshev method). Curves for the half-space problem are given in Figure 13; the remaining figures depict results for the slab problem. Values for albedo range from 0.5 to 0.95. A normalization of incident power flux S_o equal to unity is chosen for all flux curves. In Figures 13-17, normal incidence ($\theta_o = 0^o$) is chosen. In the remaining three flux figures, Figures 18-20, θ_o is taken to be forty-five degrees.

In Figure 13.a, the normalized forward diffuse flux is seen to quickly reach a maximum and then to decay exponentially with τ. The flux is larger and its rate of decay with τ slower when the albedo is bigger. This is also true for the backward diffuse density curves in Figure 13.b. Such behavior is characteristic of flux density curves for the slab problem as well, but a dependence on τ_o enters the problem. In particular, for small τ the flux F_d^+ monotonically increases from zero to a peak value at τ_o (see Figs. 14.a and 15.a for τ_o = 0.25 and 1.0, respectively). For larger values of τ_o (see Fig. 16.a ($\tau_o = 5$) and Figure 17.a ($\tau_o = 20$)), a maximum is reached and exponential decay then follows. For the slab case, the backward diffuse flux density F_d^- monotonically increases from zero at τ_o to a peak value at the air-forest interface ($\tau = 0$). This latter effect is reasonable since it shows the flux density to be a maximum in the backward direction when the entire forest region is involved.

For the normal incidence case we see in Figures 14.c, 15.c, 16.c, and 17.c the exponential attenuation of both the coherent flux densities F_{ri} and total forward flux densitities $F_{ri} + F_d^+$ for different albedos. The former (F_{ri}) curve 5 in all the figures exponentially attenuates the most rapidly. This occurs because the coherent flux density always loses energy due to absorption and out-scattering whereas the incoherent flux density F_d^+, which also loses energy due to these effects, gains energy due to in-scattering and hence does not attenuate as rapidly as F_{ri}. Note that the results for the thick

slab $\tau_o = 20$) drawn in Figure 17 are very similar to the results for the half-space problem presented in Figure 13; of course, the backward diffuse flux density F_d^- is zero at $\tau = \tau_o$ for the slab problem whereas it monotonically goes to zero as $\tau \to \infty$ for the half-space problem.

For forty-five degree incidence angles, it is seen from Figure 18 that for small τ_o the coherent flux density is almost constant over the slab width. In addition, forward and backward flux densities are nearly identical for the two different incidence angle cases $\theta_o = 0^o$ and 45^o (compare curves of Figure 14 to those of Figure 18). Hence, for thin slabs the incidence angle does not affect flux density very much. For larger vales of τ_o (compare Figure 17 to Figure 20) the effect of changing θ_o is noticeable, but again, not significantly. Observe further that this effect is more pronounced when W is smaller. This is also true for intensity as can be seen by comparing Figure 7.a with 7.e. Recall that a smaller W means less scattering and more absorption. F_d^+ and F_d^- are then smaller at larger θ_o since path length is larger and attenuation stronger when θ_o is larger.

Flux curves are drawn in Figure 21 from calculations based on the first order theory [Isl]. In this theory the forward flux is independent of slab width τ_o. Hence, Figures 21.a and 21.b remain valid for both the half-space and slab problems. However, slab thickness does affect the calculation of backward flux density. This is evident by comparing Figure 21.c to 21.d and 21.e. The former shows F_d^- curves for the half-space problem with W = 0.5, 0.75, 0.90, 0.95 and $\theta_o = 0^o$ whereas the latter depicts backward flux curves for two slabs ($\tau_o = 1$ and 20, respectively) with W = 0.5, 0.9 and $\theta_o = 0^o$. Figure 21.f depicts the coherent flux density (curve 5) as well as the total forward flux densities as a function of τ, valid for both the half-space and slab configurations. Evidently, F_{ri} dominates. The general characteristics of these first order flux curves agree with the more accurate ones presented previously using the Chebyshev method and give additional support to the latter theory. Note that the Chebyshev method yields a more distinctive effect of varying albedo values than does first order theory (as can be seen by comparing Figure 17 to Figure 21).

In Tables 1, 2 and 3, all positive eigenvalues of the characteristic equation are listed. They occur between 0 and 1 except for the largest one which is larger than unity. For larger W, the largest eigenvalue is closer to the root of the asymptotic eigenvalue equation, i.e., tanh (1/Ws) = 1/s (see [CZ] or [Oz]). The larger the value of W, the larger the value of the largest eigenvalue. The largest eigenvalue approaches infinity when W is equal to unity. The smallest eigenvalue approaches zero as N approaches infinity.

VI. CONCLUSIONS

Diffuse intensity curves in the forward and backward directions were presented for various values of albedo (from a low of 0.25 to a high of 0.95). A plane wave was assumed to enter the forest at incidence angles of $\theta_o = 0^o$, 30^o and 60^o for the half-space configuration and $\theta_o = 0^o$ for the slab geometry. The normalized slab thickness τ_o varied from 0.2 to 20. All intensity curves were normalized by setting $S_o/4\pi$ equal to unity.

Forward and backward diffuse intensities decayed slower when the albedo was larger and incidence angle smaller. The strongest diffuse intensity in the forward direction occurred near τ equal to unity while in backward direction the strongest intensity occurred at the air-forest interface $\tau = 0$. The maximum forward diffuse intensities flowed in directions near $\theta = 90^o$ for small τ. As τ and θ_o increased the maximum forward diffuse intensities shifted away from the vertical. The τ dependence was much more significant than the θ_o dependence. We found that for small τ, incidence angle θ_o did not affect the maximum forward diffuse intensity. At larger values of τ we found that the angular distribution of intensity evolved into a narrow beam of radiation directed in the $\theta = 0^o$ direction. For smaller albedos, beam narrowing occurred at shorter penetration depths when compared to larger values of W.

With regard to the backward diffuse intensity, a maximum occurred in the $\theta = 90^o$ direction and decreased to a minimum value in the $\theta = 180^o$ direction. For small τ and small θ_o the relative backward diffuse intensity was seen to be essentially independent of

τ. For small θ_o the relative backward diffuse intensity at small τ was stronger than at large τ. However, at large θ_o, the reverse occurred.

Power flux density curves in the forward and backward directions were presented for various values of albedo (from a low of 0.5 to a high of 0.95) and for two angles of incidence ($\theta_o = 0^o$ and 45^o). Characteristic of such curves was that for sufficiently wide slabs ($\tau_o > 1$) the forward flux density F_d^+ quickly reached a maximum value at $\tau \simeq 1$) and thereafter exponentially decayed as τ became larger. Larger albedos (stronger scattering) were seen to yield slower attenuation rates for F_d^+. The backward flux density was observed to reach its maximum at $\tau = 0$ as expected. Dependence of flux on incidence angles was also examined. Its effect was shown to be pronounced for smaller albedos.

VII. REFERENCES

ASt Abramowitz, M. and Stegun, I.A. (eds.) "Handbook of Mathematical Functions," Dover Publications, Inc., NY, 1965.

CZw Case, K. and Zweifel, P., "Linear Transport Theory," Addison-Wesley, 1969.

CH Chandrasekhar, S., "Radiative Transfer," Dover Publications, 1960.

Isl Ishimaru, A., "Wave Propagation and Scattering in Random Media," Vol. 1 (Single Scattering and Transport Theory), Academic Press, 1978

Oz Ozisik, M.N., "Radiative Transfer and Interactions with Conduction and Convection," John Wiley and Sons, 1973.

VE Violette, E.J., Espeland, R.H., Schwering, F.K., Whitman, G.M., "Millimeter Wave Propagation in Vegetation," The Ninth DARPA Tri-Service Millimeter-Wave Conference, Huntsville, AL, 20-22 Oct 1981.

SJ Schwering, F.K., Johnson, R.A., Rokkos, N., Whitman, G.M., "Effects of Vegetation and Battlefield Obscurants on Point-to-Point Transmission in the Lower Millimeter Wave Region (30-60 GHz)," US Army Science Conference, West Point, NY, 15-18 Jun 1982.

ASc Ziering, S. and Schiff, D., "Yvon's Method for Slabs," Nuclear Science and Engineering, Vol. 3, pp. 635-647.

Sny Snyder, M.A., "Chebyshev Methods in Numerical Approximation."

BFR Burden, L.R., Faires, J.D., Reynolds, C.A., "Numerical Analysis," Prindle, Wieber and Schmidt, Boston, 1981.

VIII. ACKNOWLEDGEMENT

This study was conducted jointly by the Center for Communication Systems of the US Army Communications-Electronics Command and the New Jersey Institute of Technology.

During the summers of 1980 and 1981 Professor Whitman worked under the Laboratory Research Cooperative Program with Dr. F. Schwering of the Command's Millimeter Wave and Secure Fiber Team. Mr. Li-Wen Chen received his MSEE degree from NJIT in October 1982 based on this research and is currently a professor at Koashung College, Taiwan.

The authors wish to express their gratitude to Dr. J. Robert Christian, Leader of the Millimeter Wave Team and Dr. Larry Dworkin, Chief of the Multichannel Transmission Division, for their encouragement and support.

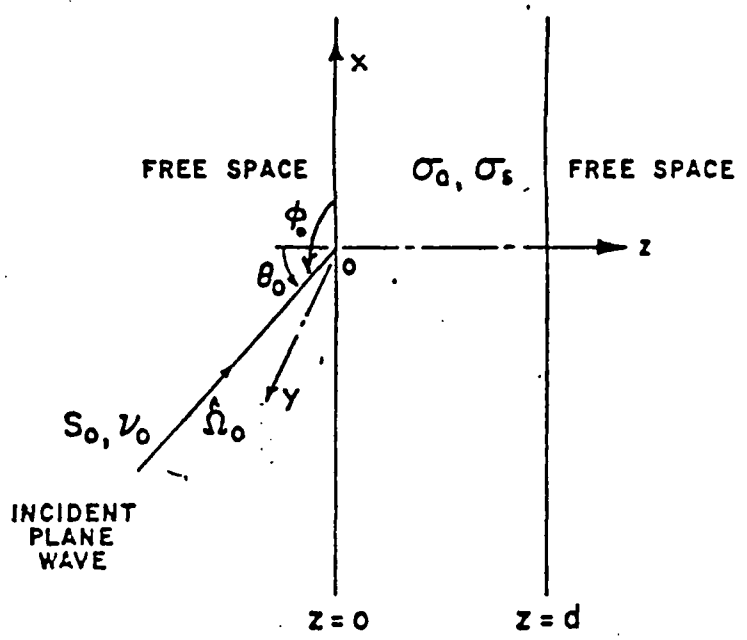

Figure 1.
SLAB MODEL OF A FOREST ILLUMINATED BY A PLANE WAVE.

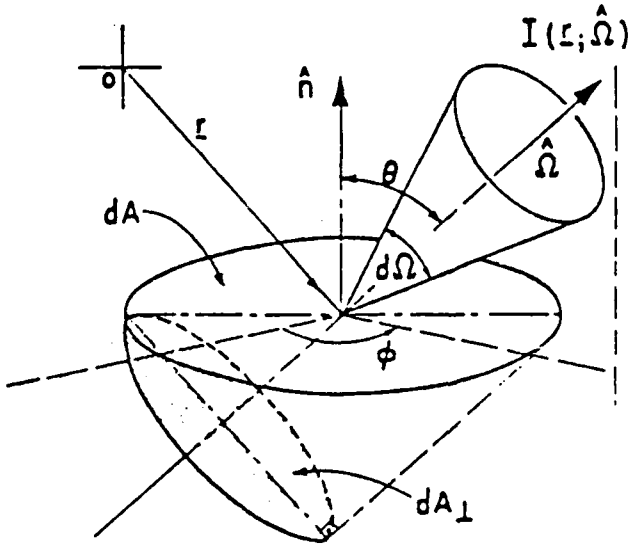

Figure 2.
SPECIFIC INTENSITY $I(\underline{r};\hat{\Omega})$ FLOWING THROUGH AREA ELEMENT dA_1

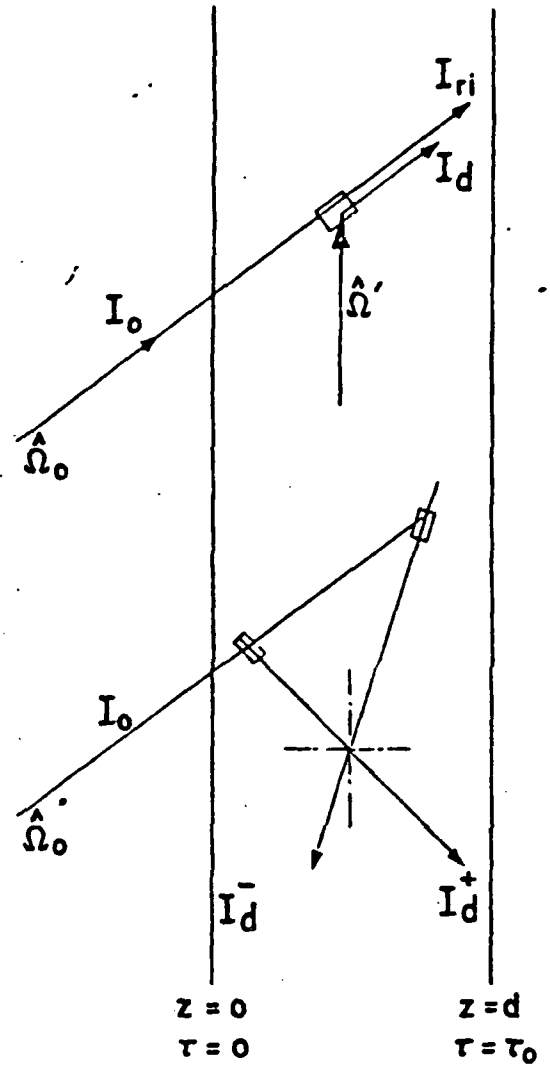

Figure 3.
TYPES OF INTENSITIES: REDUCED INCIDENT, I_{ri}; DIFFUSE, I_d; FORWARD DIFFUSE, I_d^+; BACKWARD DIFFUSE, I_d^-.

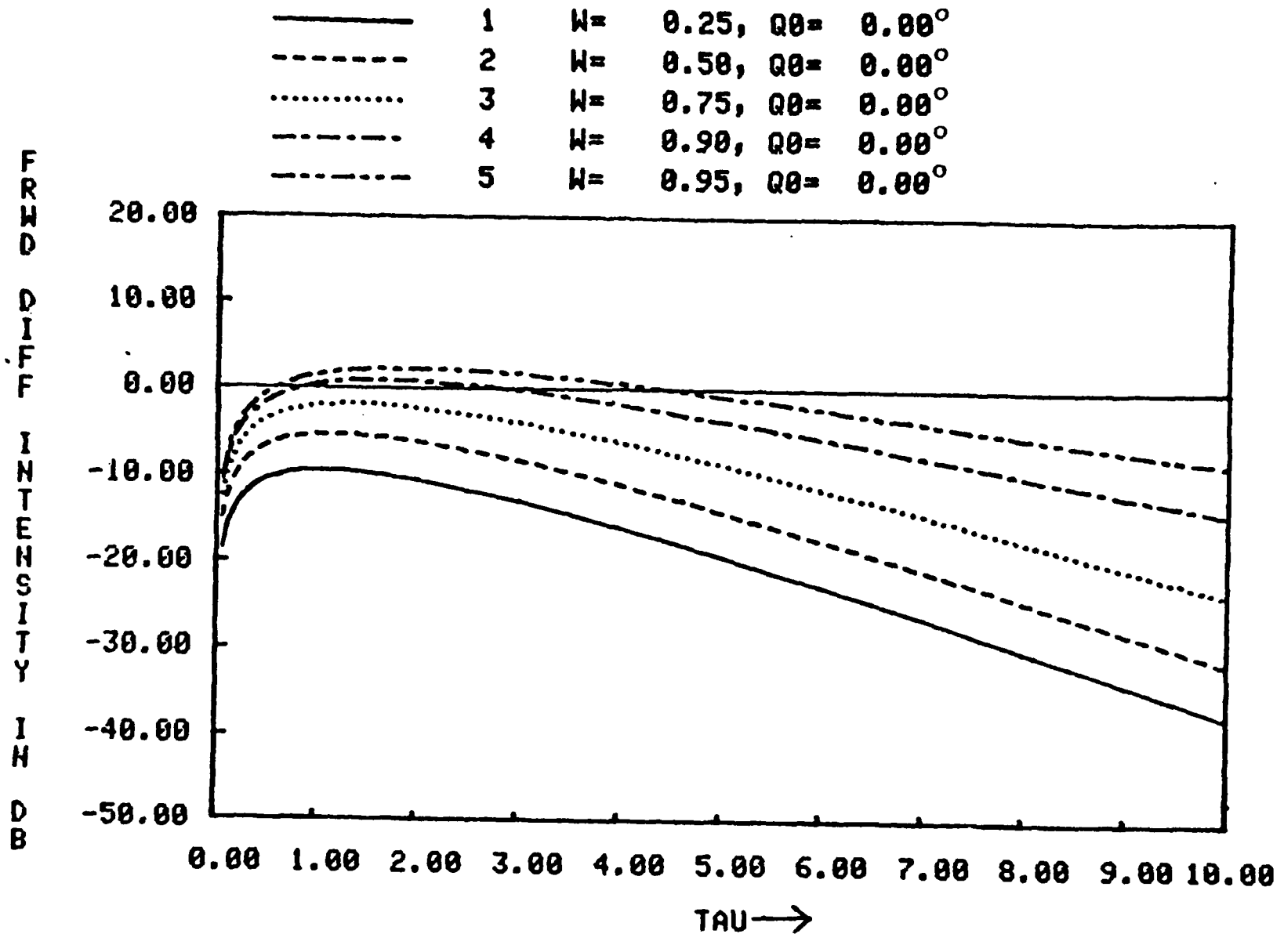

Figure 4.a. FORWARD DIFFUSE INTENSITY VS. DISTANCE FOR 1/2 SPACE WITH Q=0°

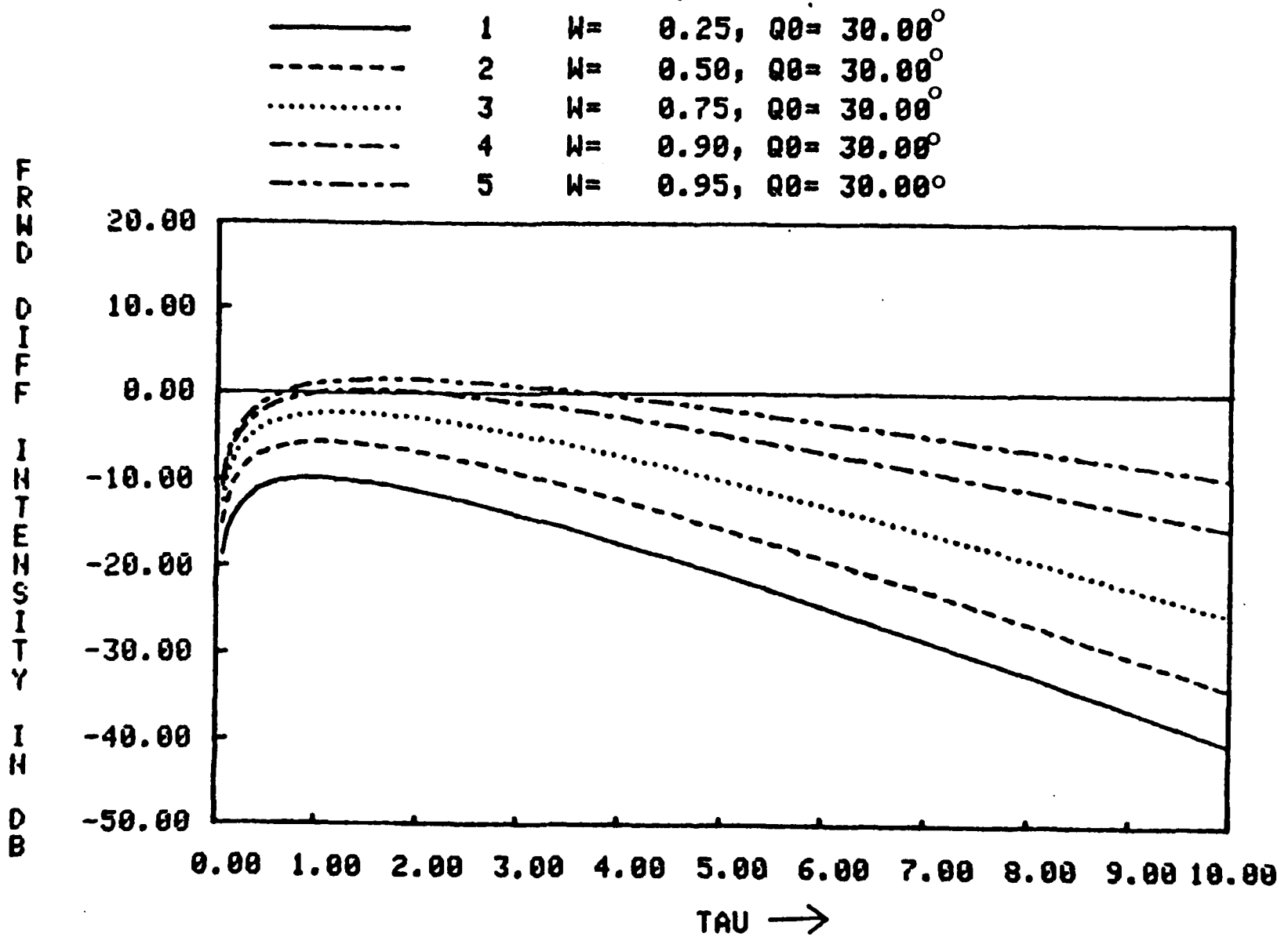

Figure 4.b. FORWARD DIFFUSE INTENSITY VS. DISTANCE FOR 1/2 SPACE WITH Q=0°

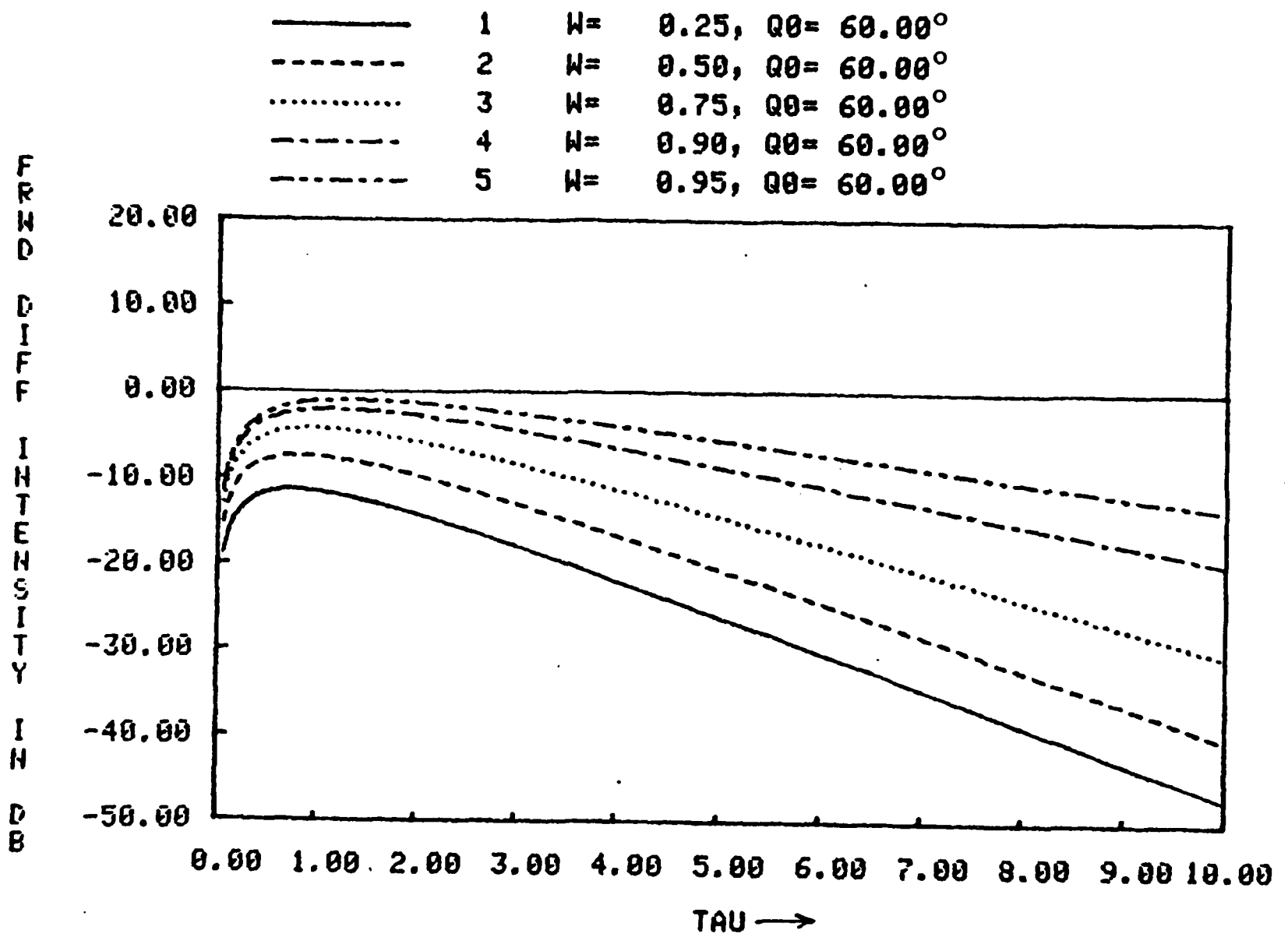

Figure 4.c. FORWARD DIFFUSE INTENSITY VS. DISTANCE FOR 1/2 SPACE WITH Q=0°

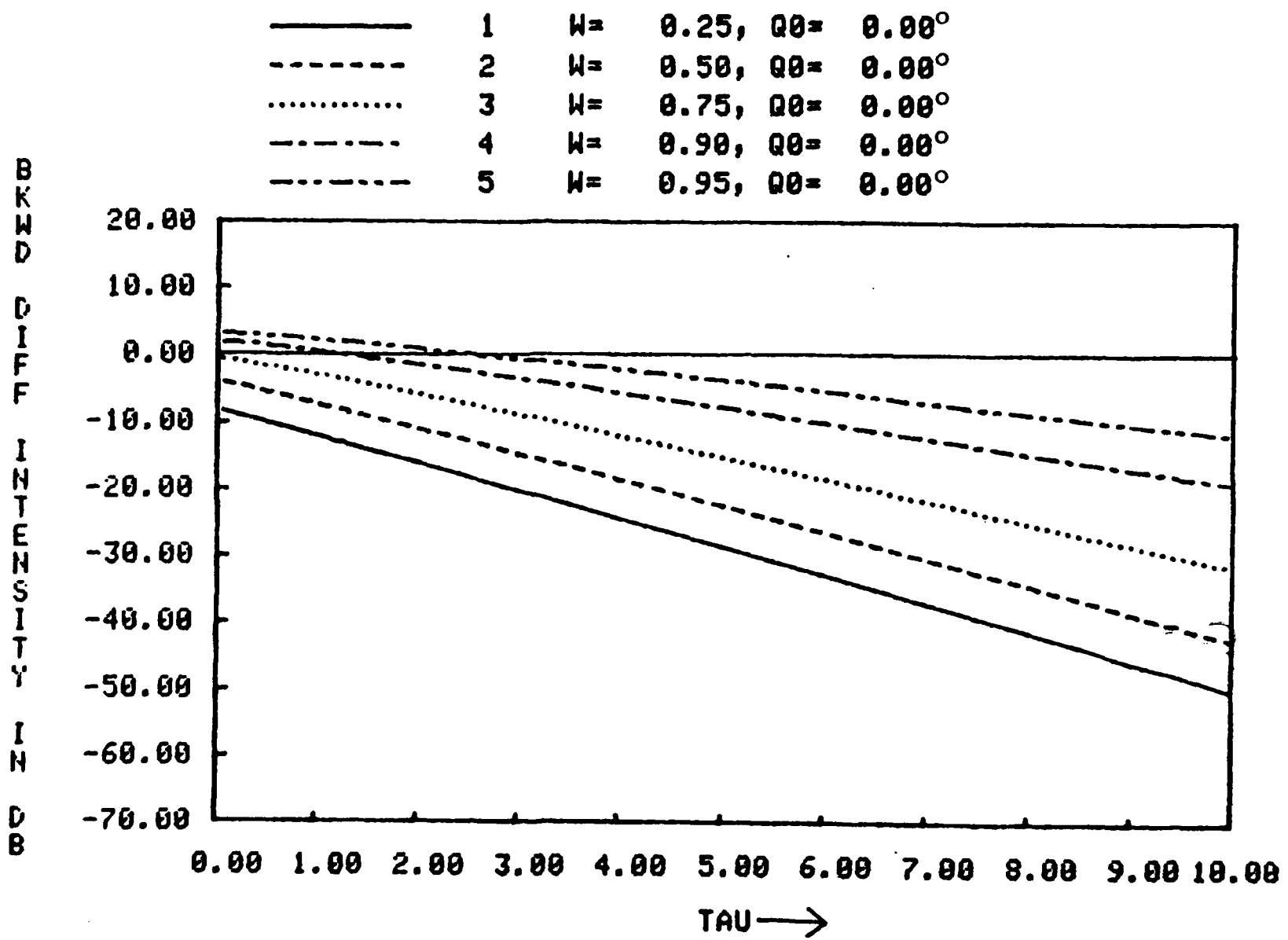

Figure 5.a. BACKWARD DIFFUSE INTENSITY VS. DISTANCE FOR 1/2 SPACE WITH Q=180°

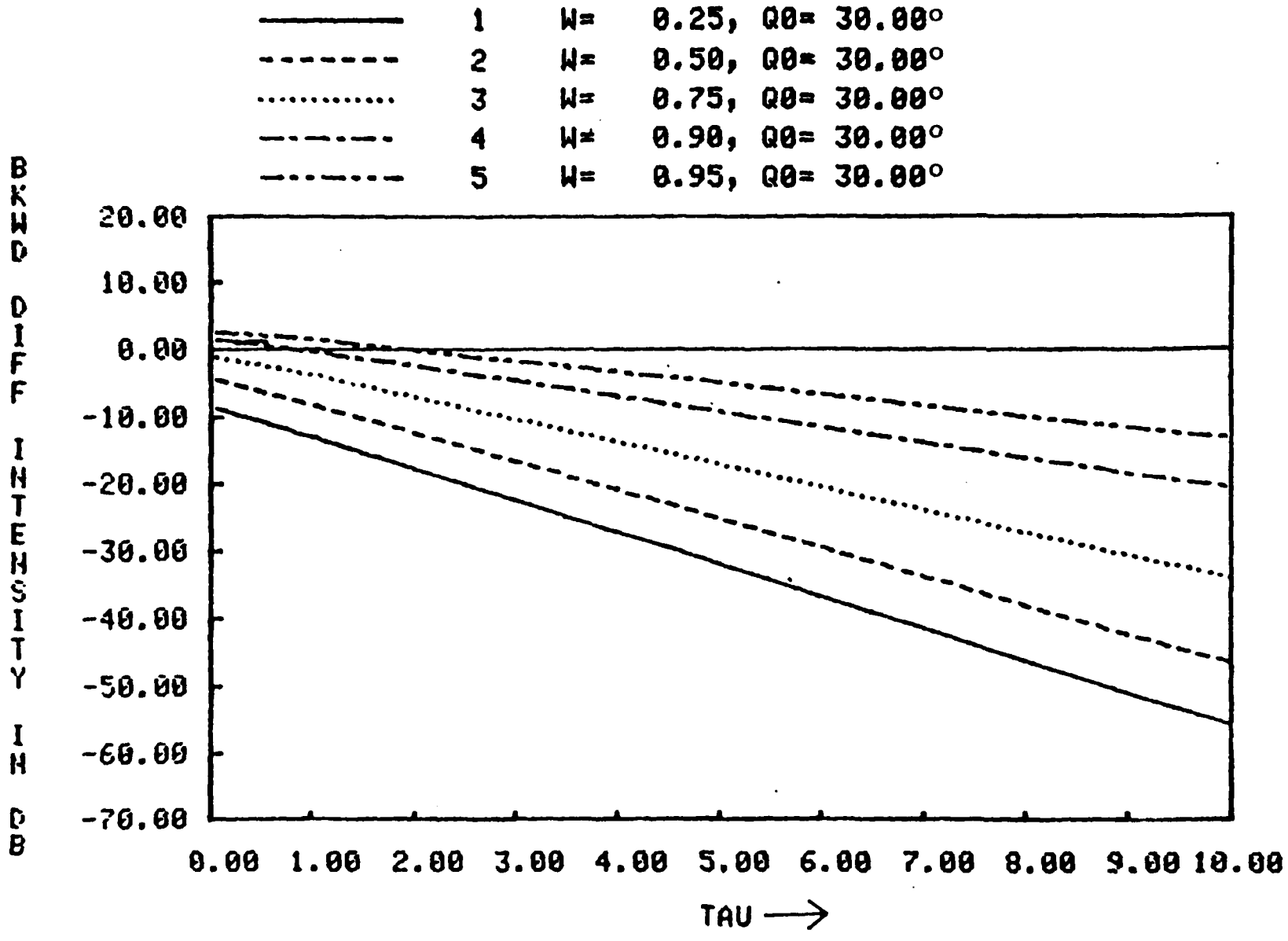

Figure 5.b. BACKWARD DIFFUSE INTENSITY VS. DISTANCE FOR 1/2 SPACE WITH Q=18A°

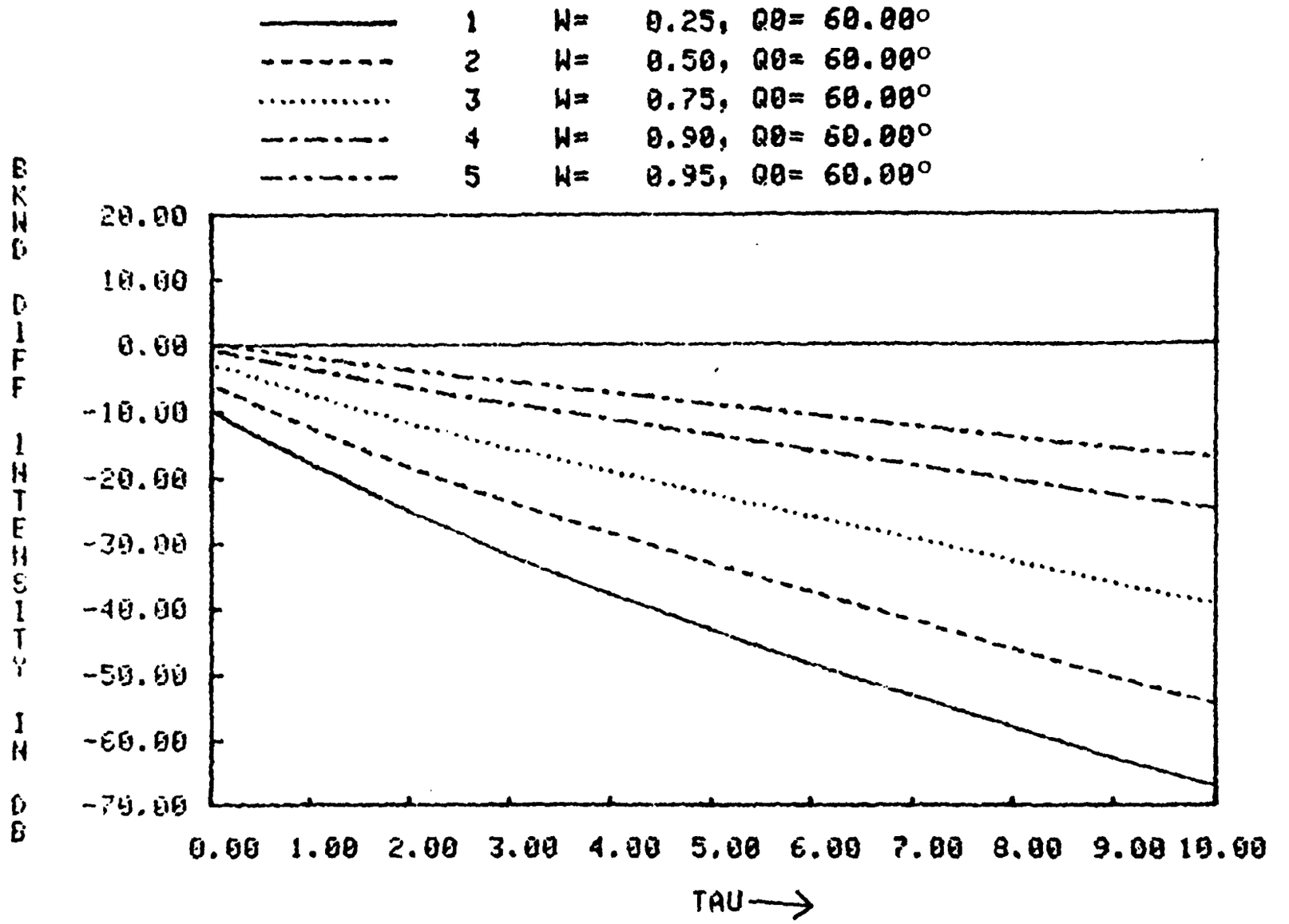

Figure 5.c. BACKWARD DIFFUSE INTENSITY VS. DISTANCE FOR 1/2 SPACE WITH Q=180°

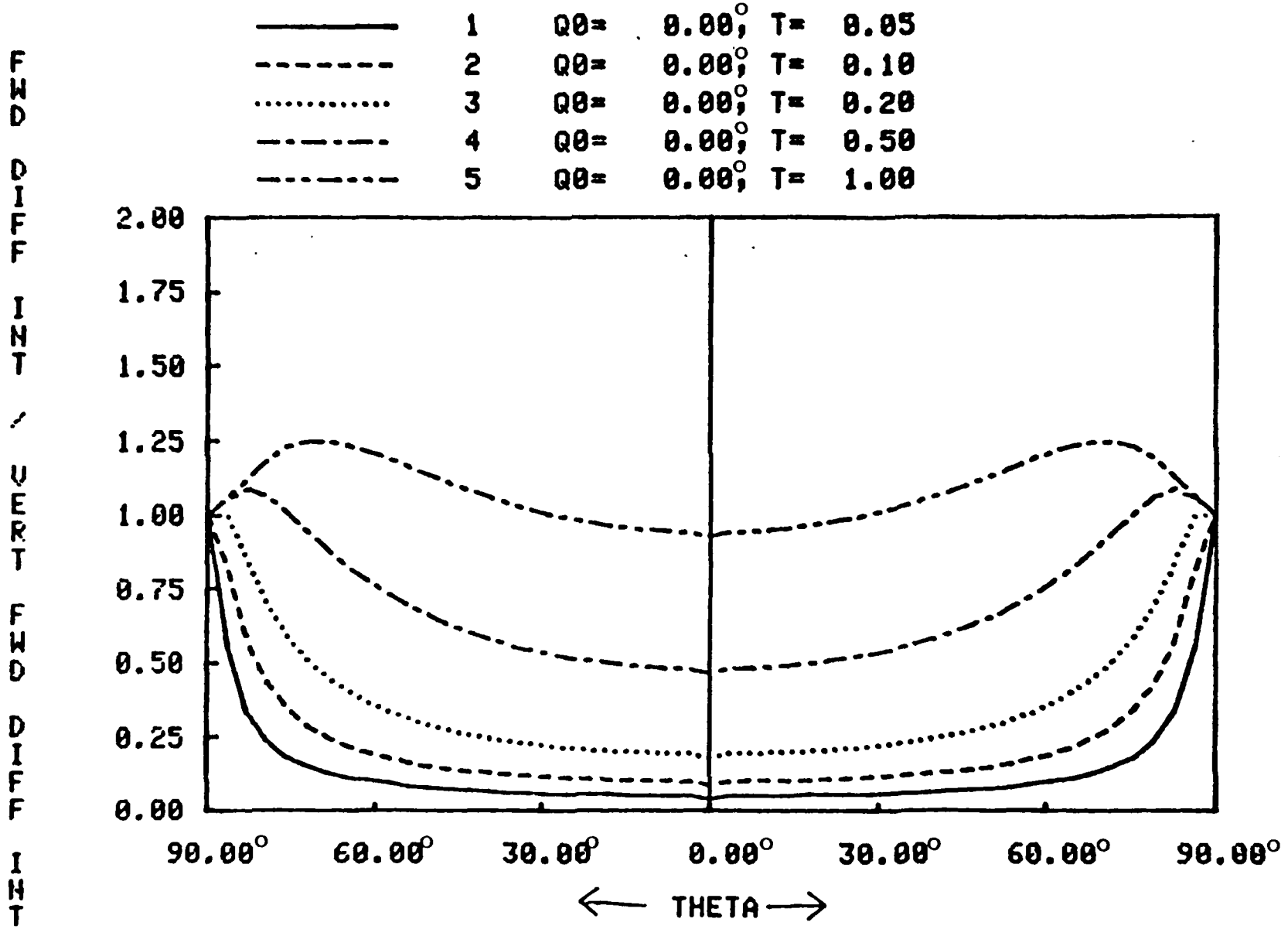

Figure 6.a RELATIVE FRWD DIFF INTENSITY VS. SCATTER ANGLE FOR 1/2 SPACE, W=0.25

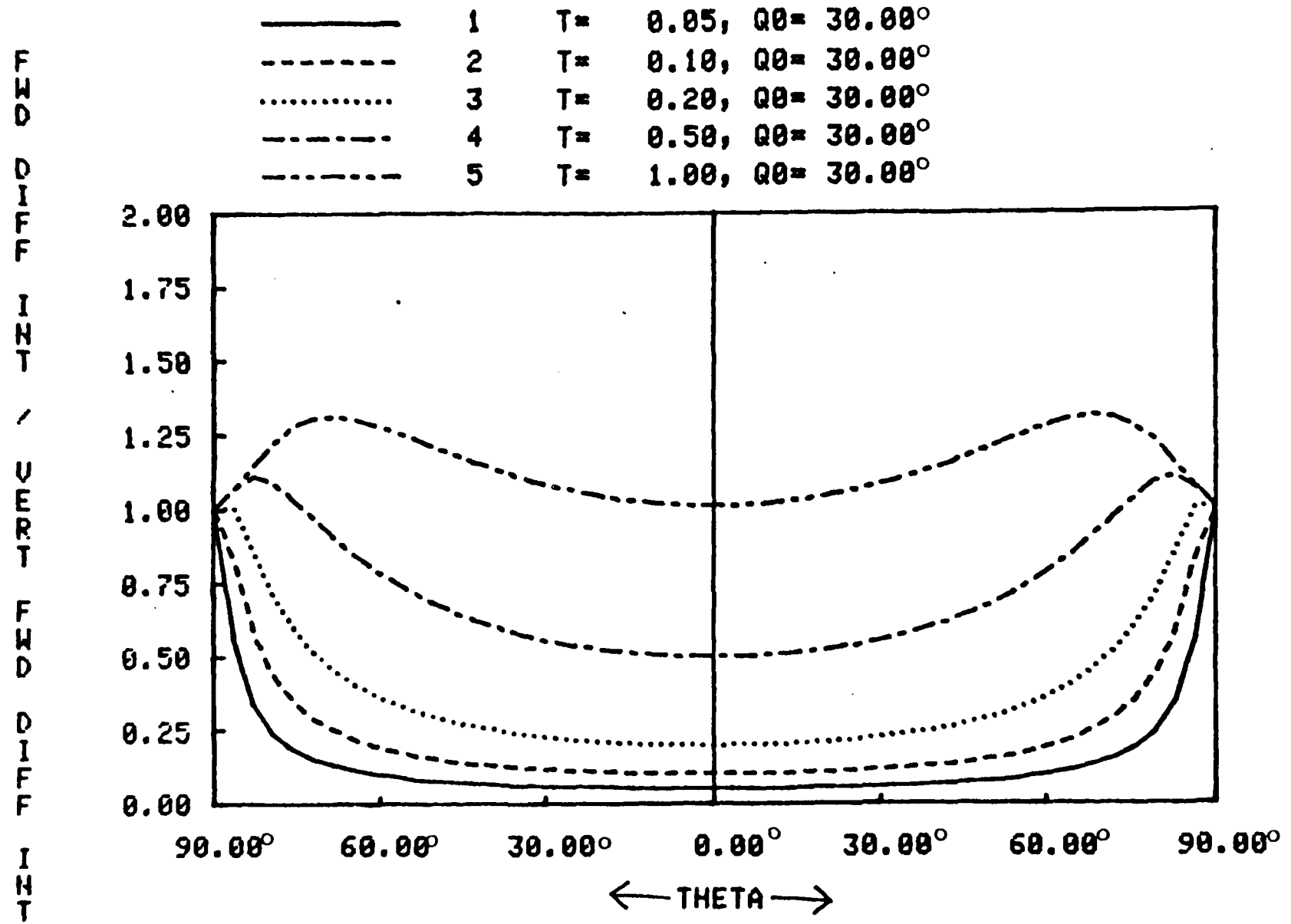

Figure 6.b. RELATIVE FRWD DIFF INTENSITY VS. SCATTER ANGLE FOR 1/2 SPACE, W=0.25

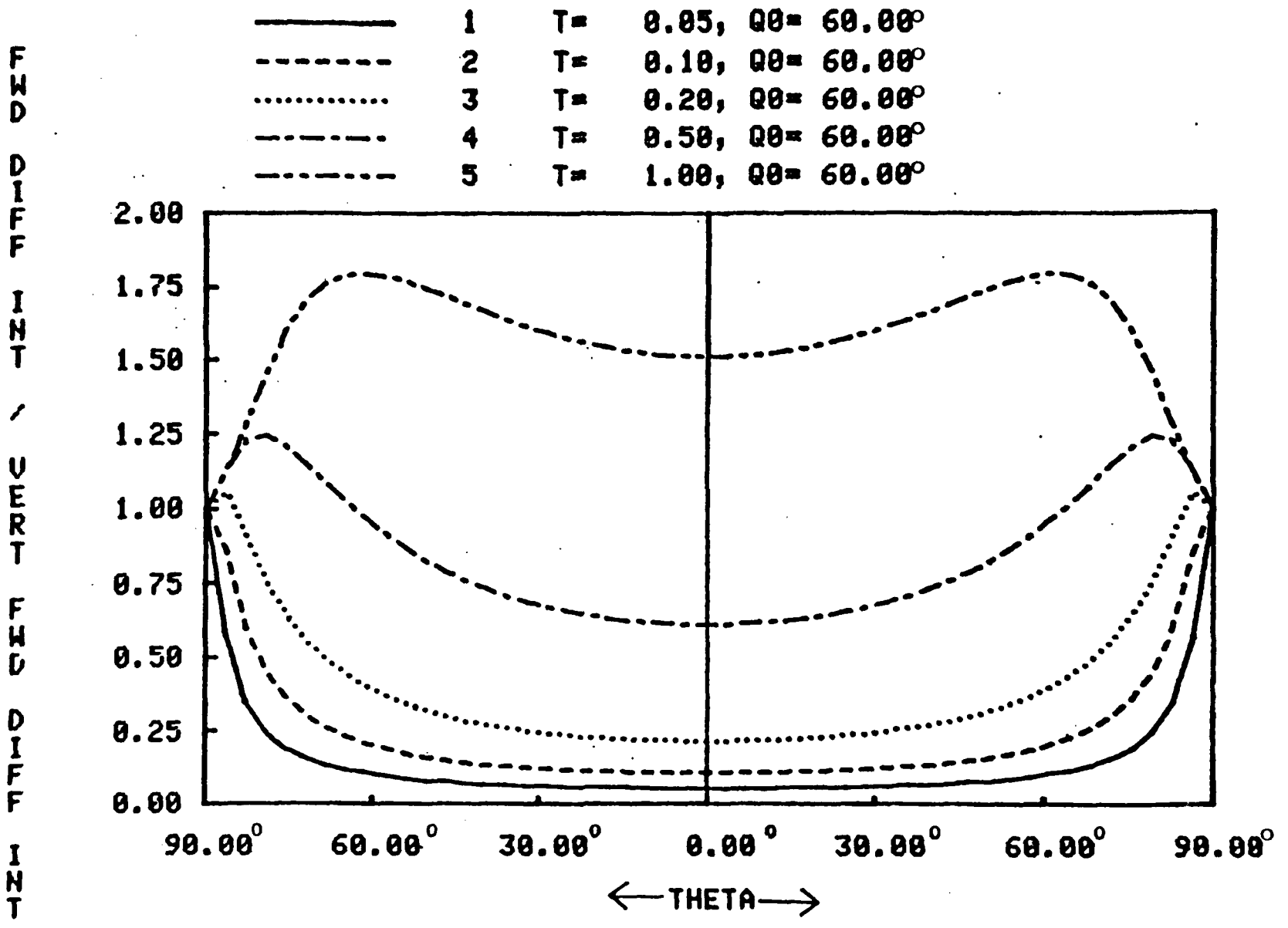

Figure 6.c RELATIVE FRWD DIFF INTENSITY VS. SCATTER ANGLE FOR 1/2 SPACE, W=0.25

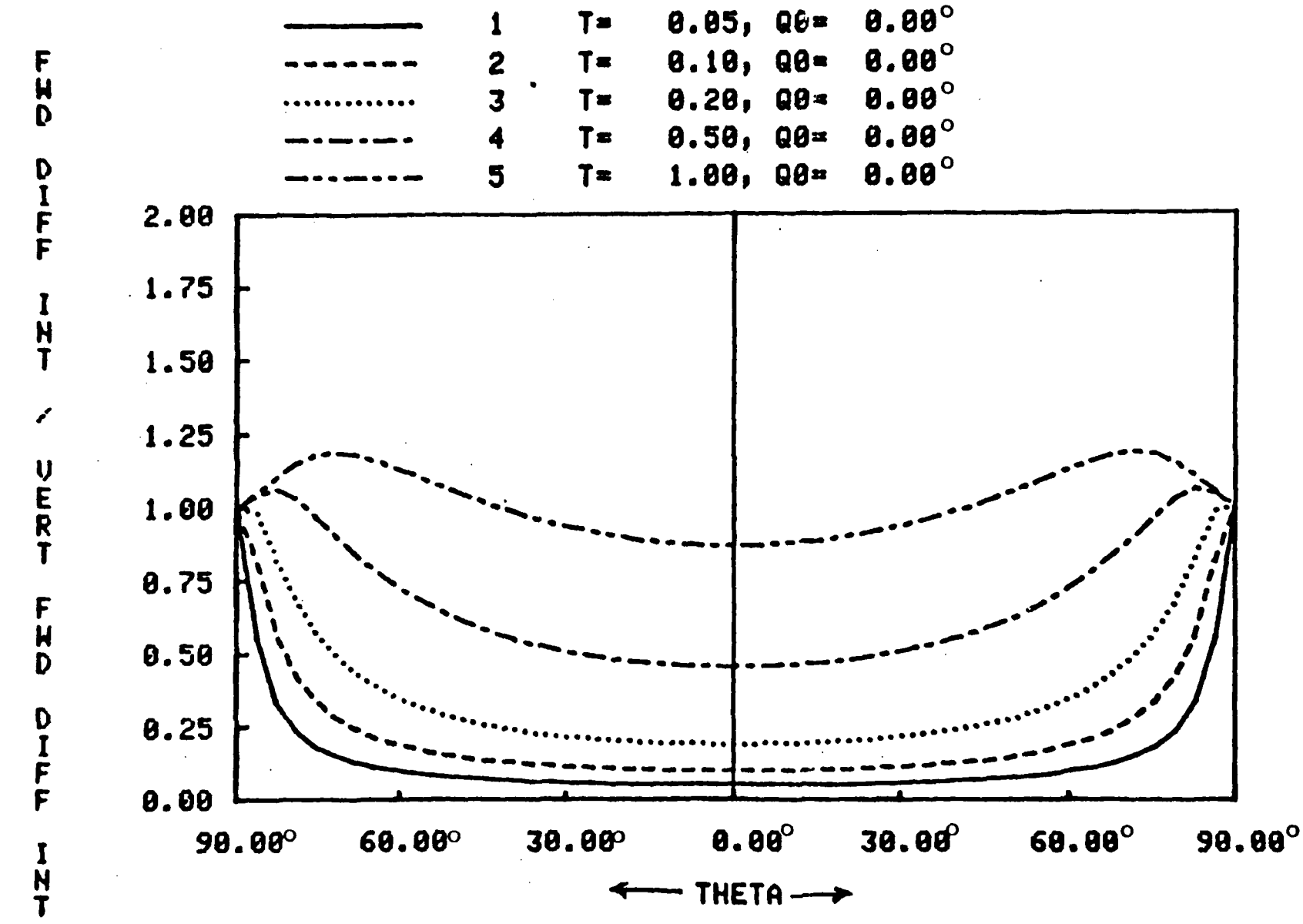

Figure 6.d, RELATIVE FRWD DIFF INTENSITY VS. SCATTER ANGLE FOR 1/2 SPACE, W=0.50

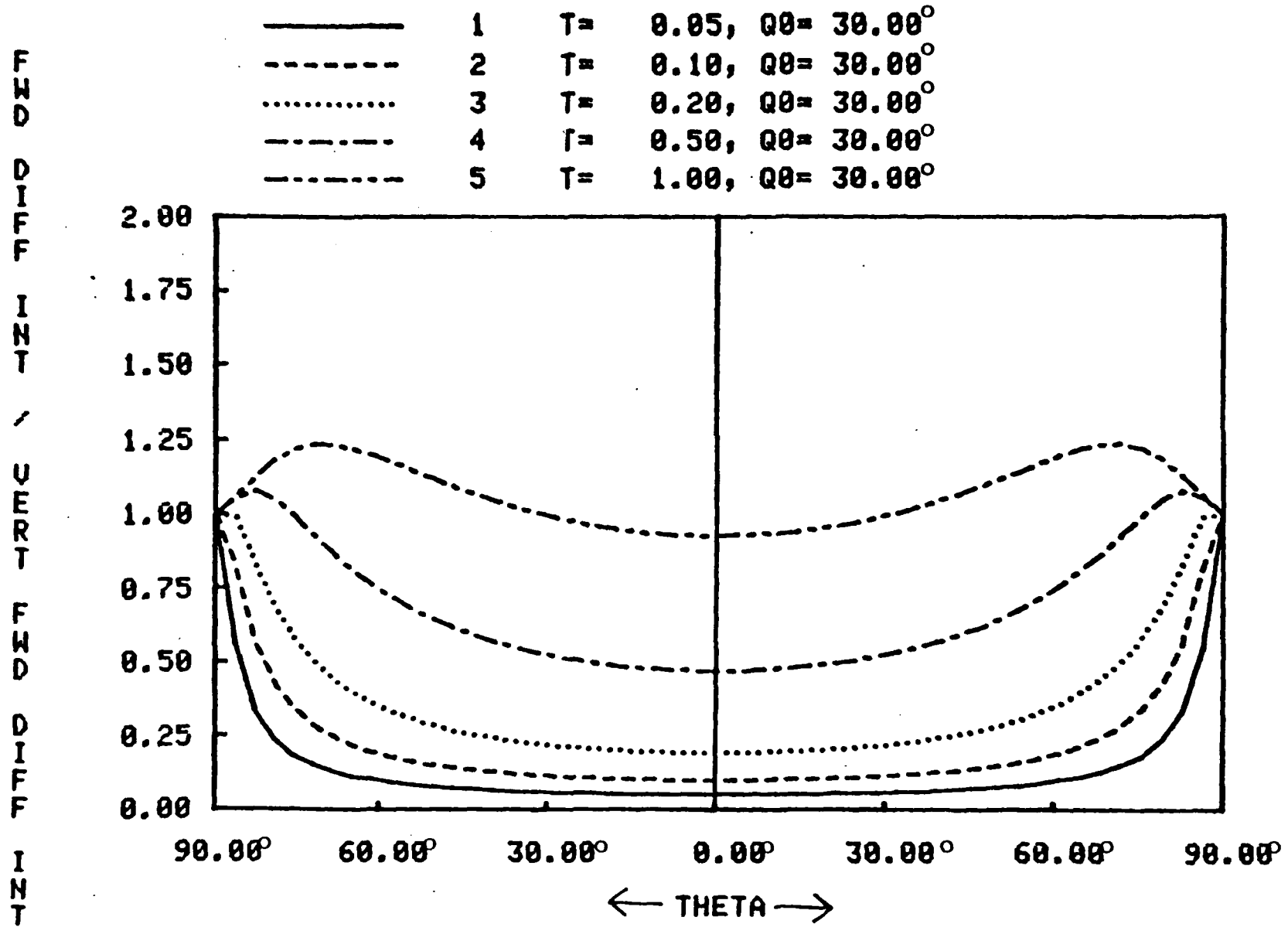

Figure 6.e. RELATIVE FRWD DIFF INTENSITY VS. SCATTER ANGLE FOR 1/2 SPACE, W=0.50

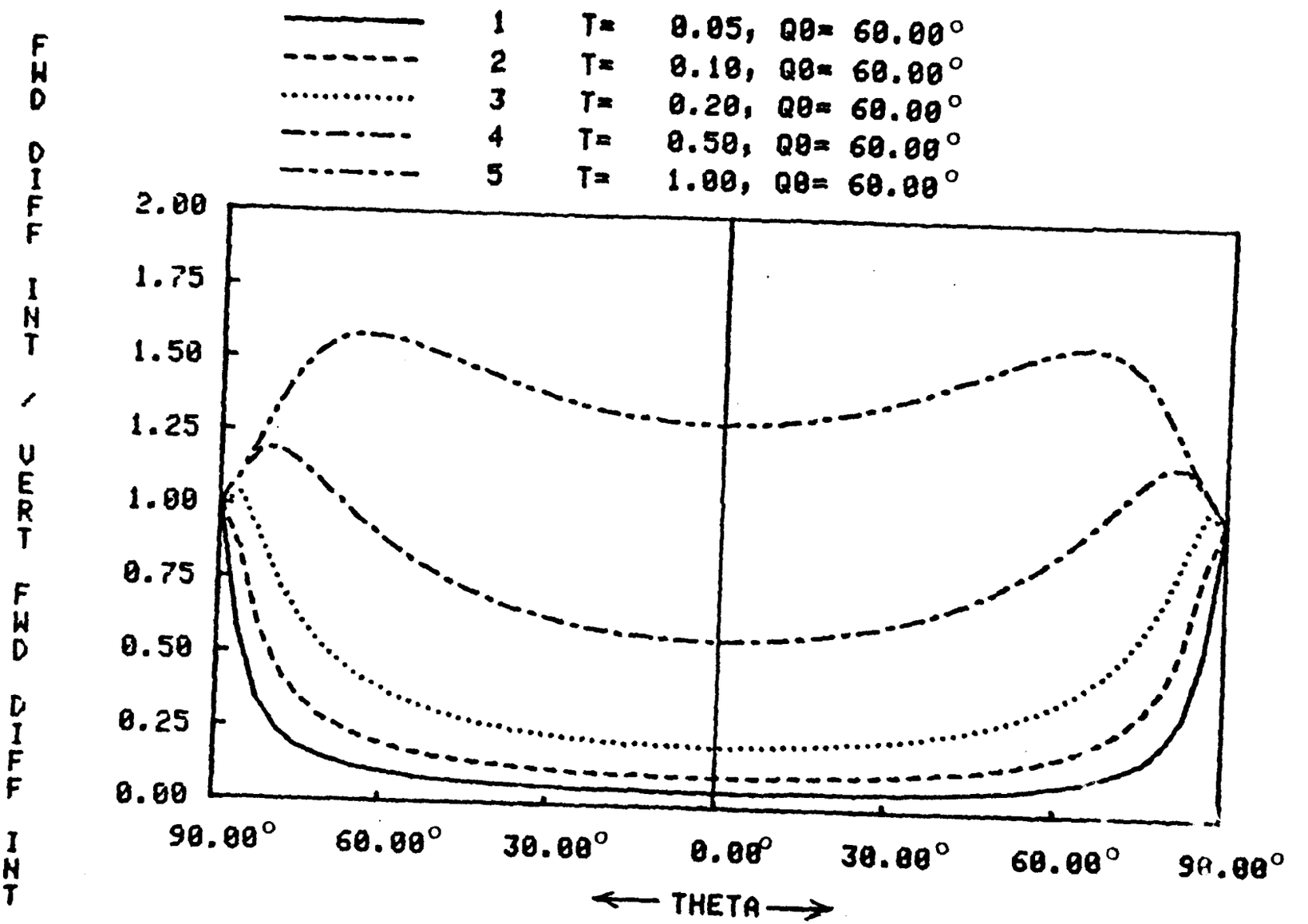

Figure 6.f. RELATIVE FRWD DIFF INTENSITY VS. SCATTER ANGLE FOR 1/2 SPACE, W=0.50

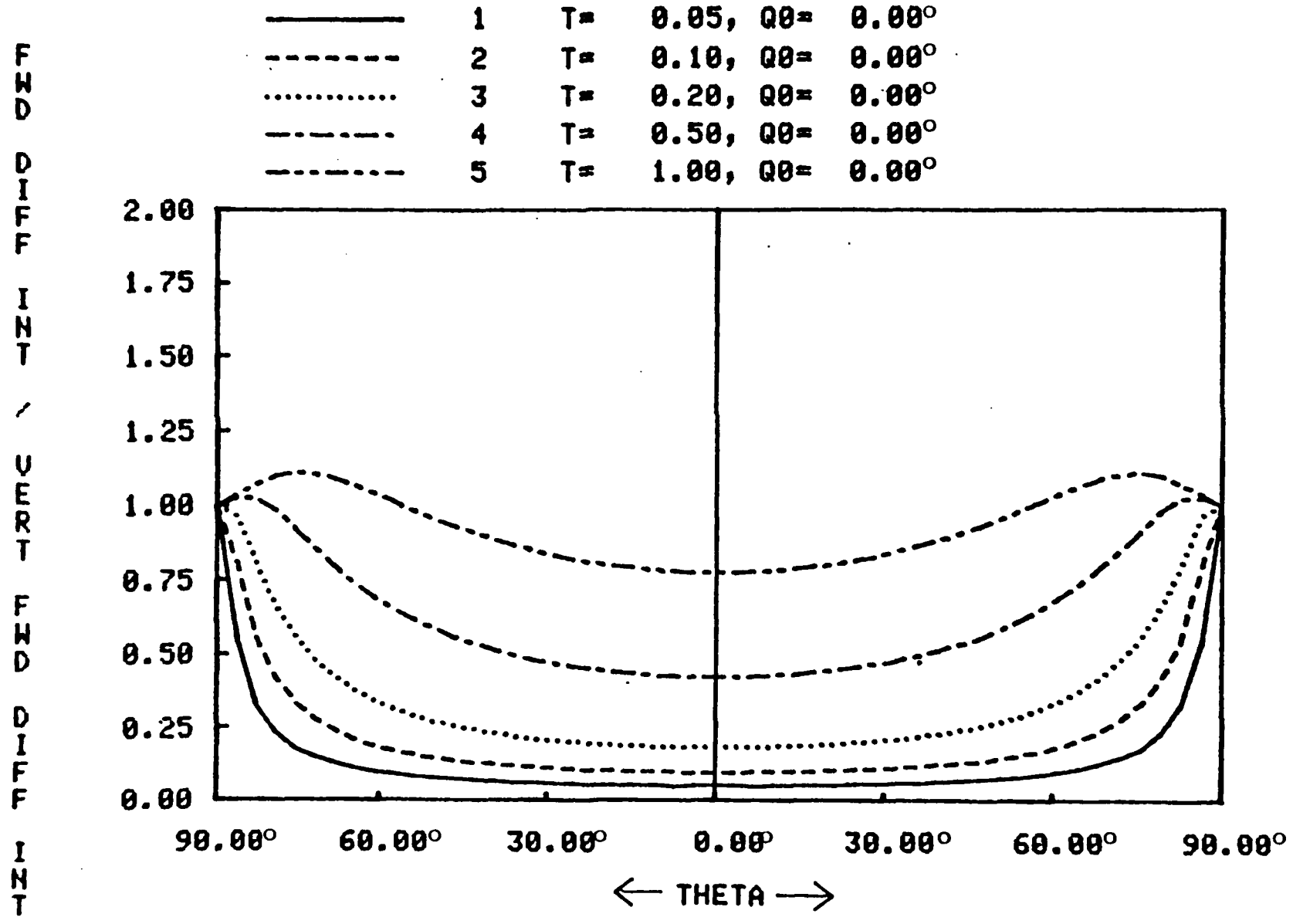

Figure 6.g. RELATIVE FRWD DIFF INTENSITY VS. SCATTER ANGLE FOR 1/2 SPACE, W=0.75

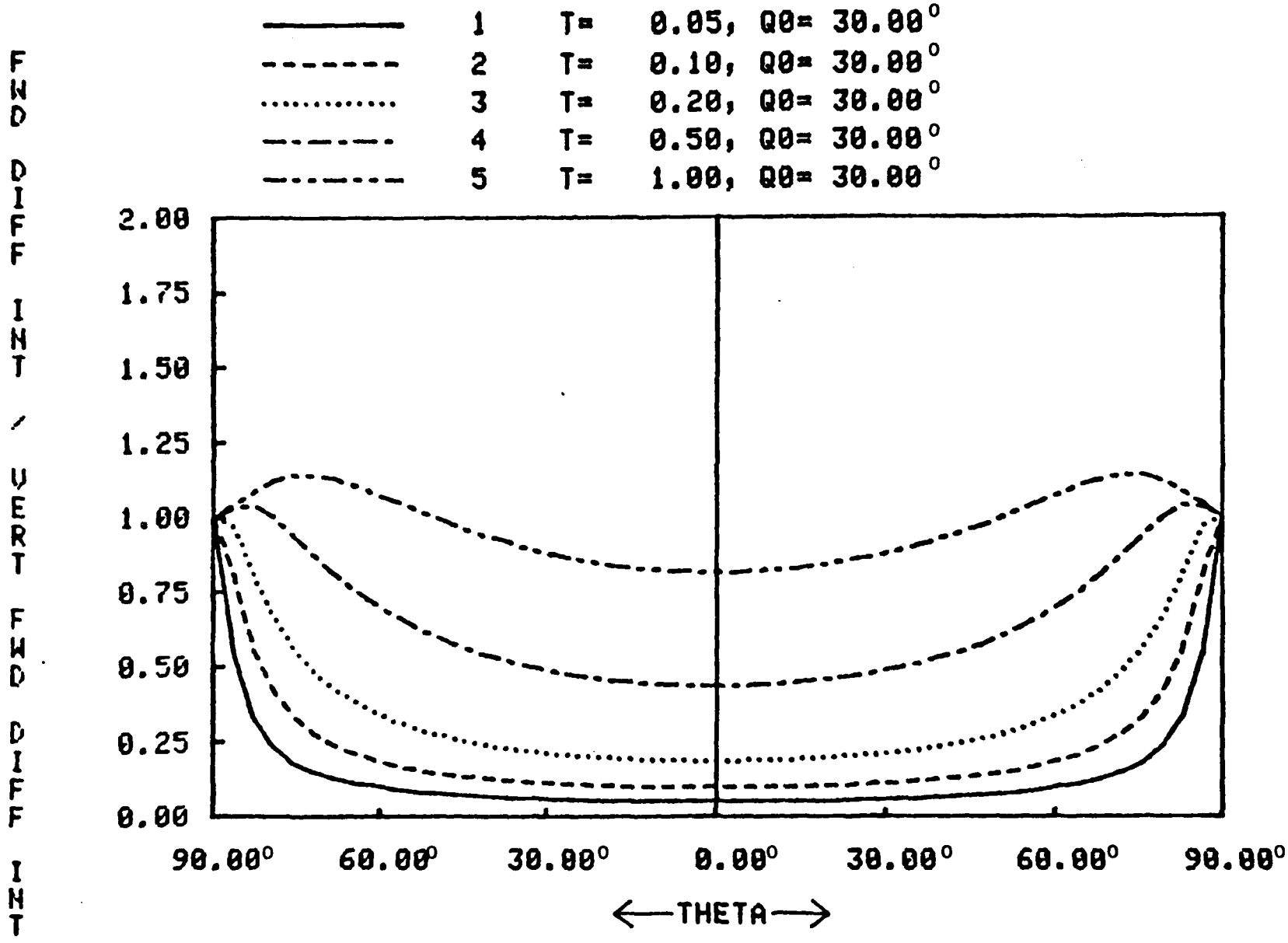

Figure 6.h. RELATIVE FRWD DIFF INTENSITY VS. SCATTER ANGLE FOR 1/2 SPACE, W=0.75

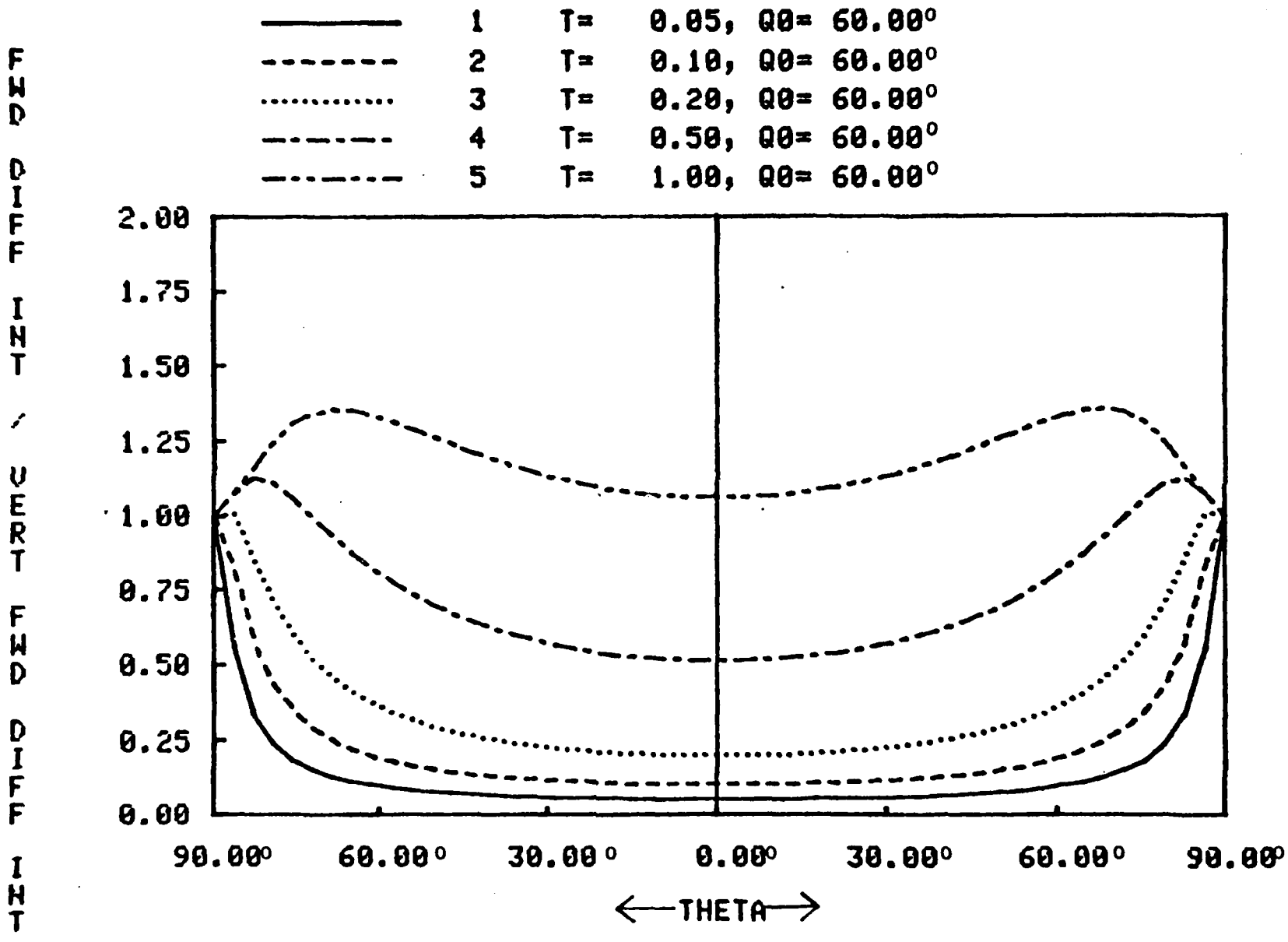

Figure 6.i. RELATIVE FRWD DIFF INTENSITY VS. SCATTER ANGLE FOR 1/2 SPACE, W=0.75

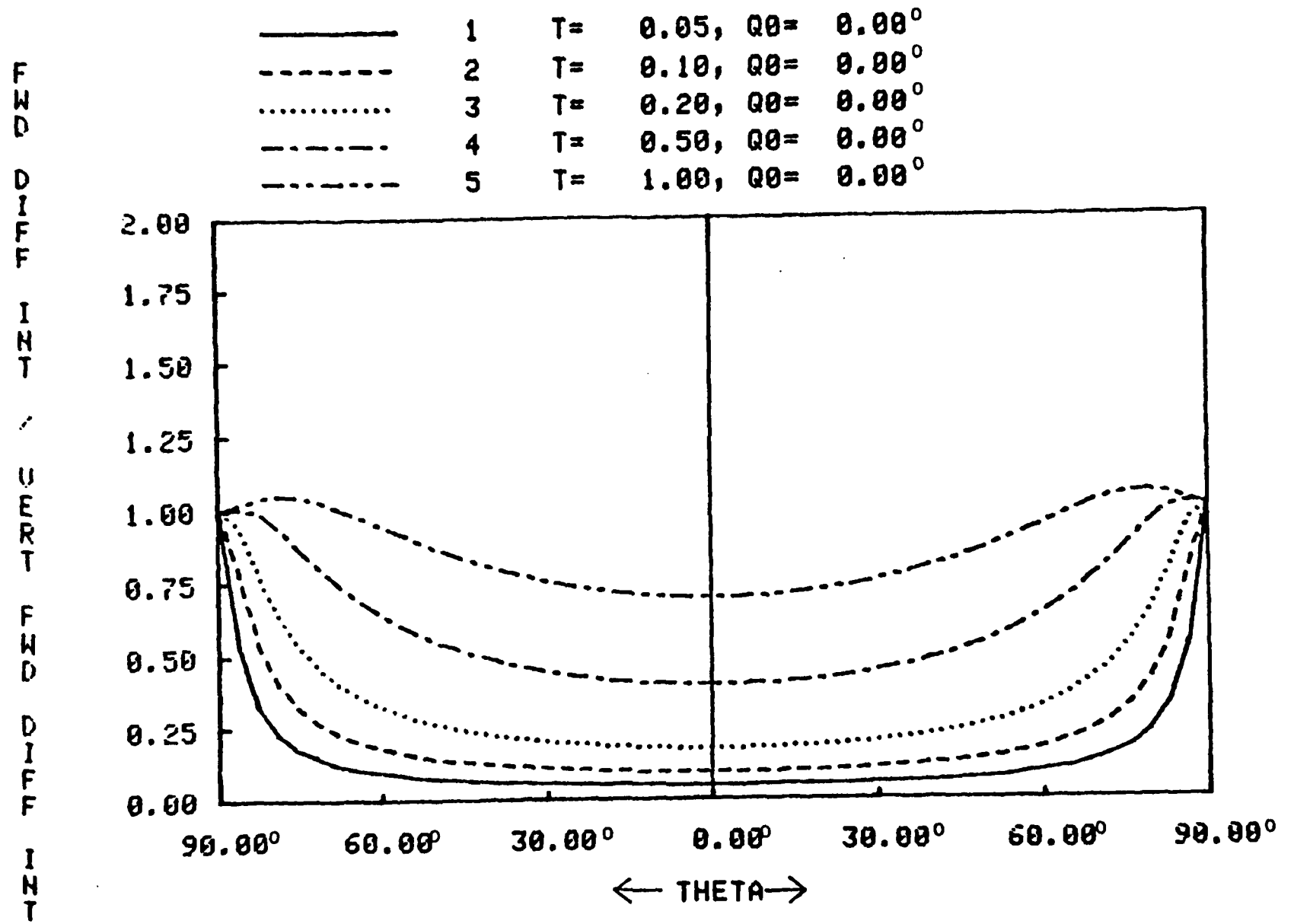

Figure 6.j. RELATIVE FRWD DIFF INTENSITY VS. SCATTER ANGLE FOR 1/2 SPACE, W=0.90

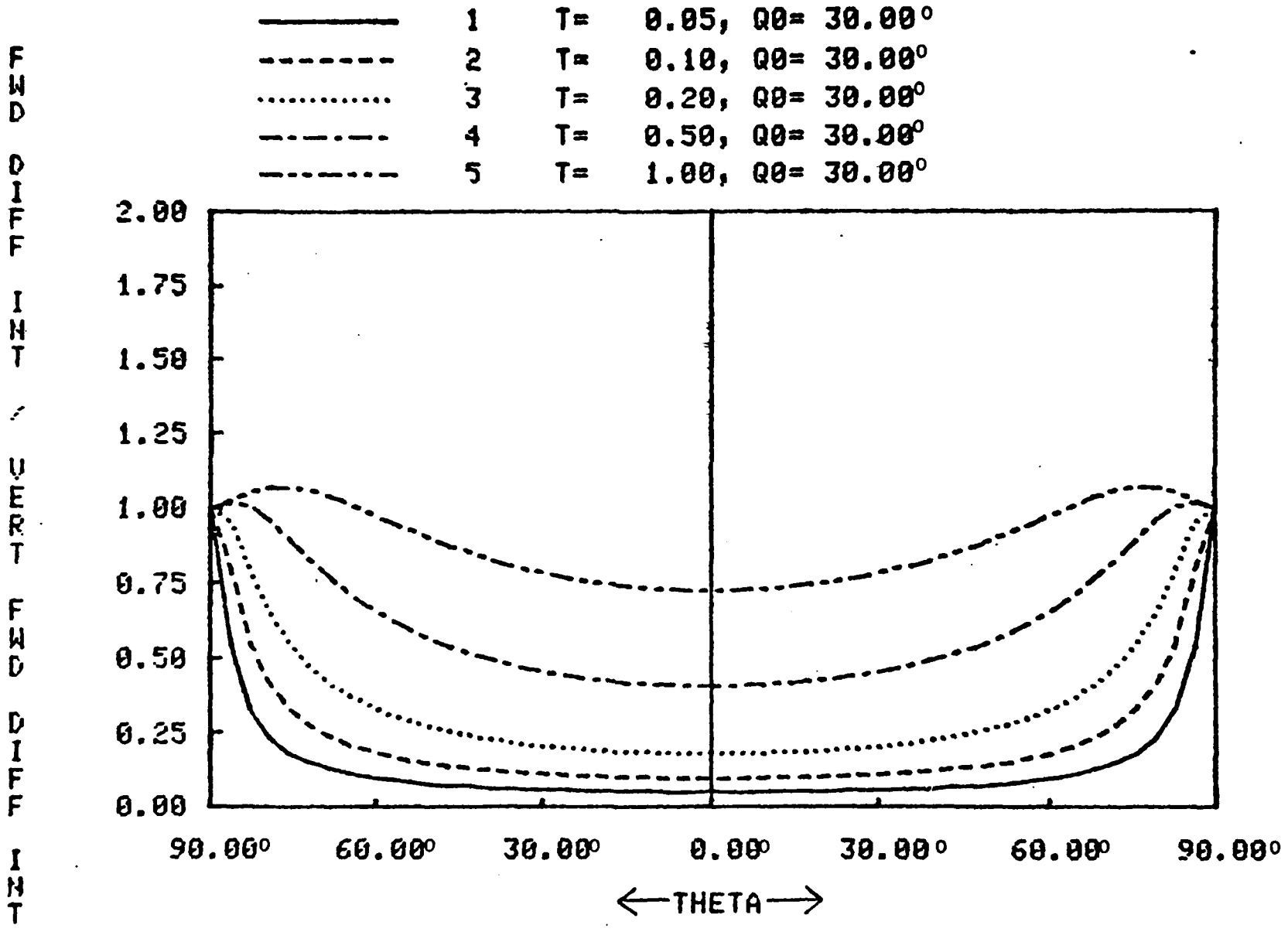

Figure 6.k. RELATIVE FRWD DIFF INTENSITY VS. SCATTER ANGLE FOR 1/2 SPACE, W=0.90

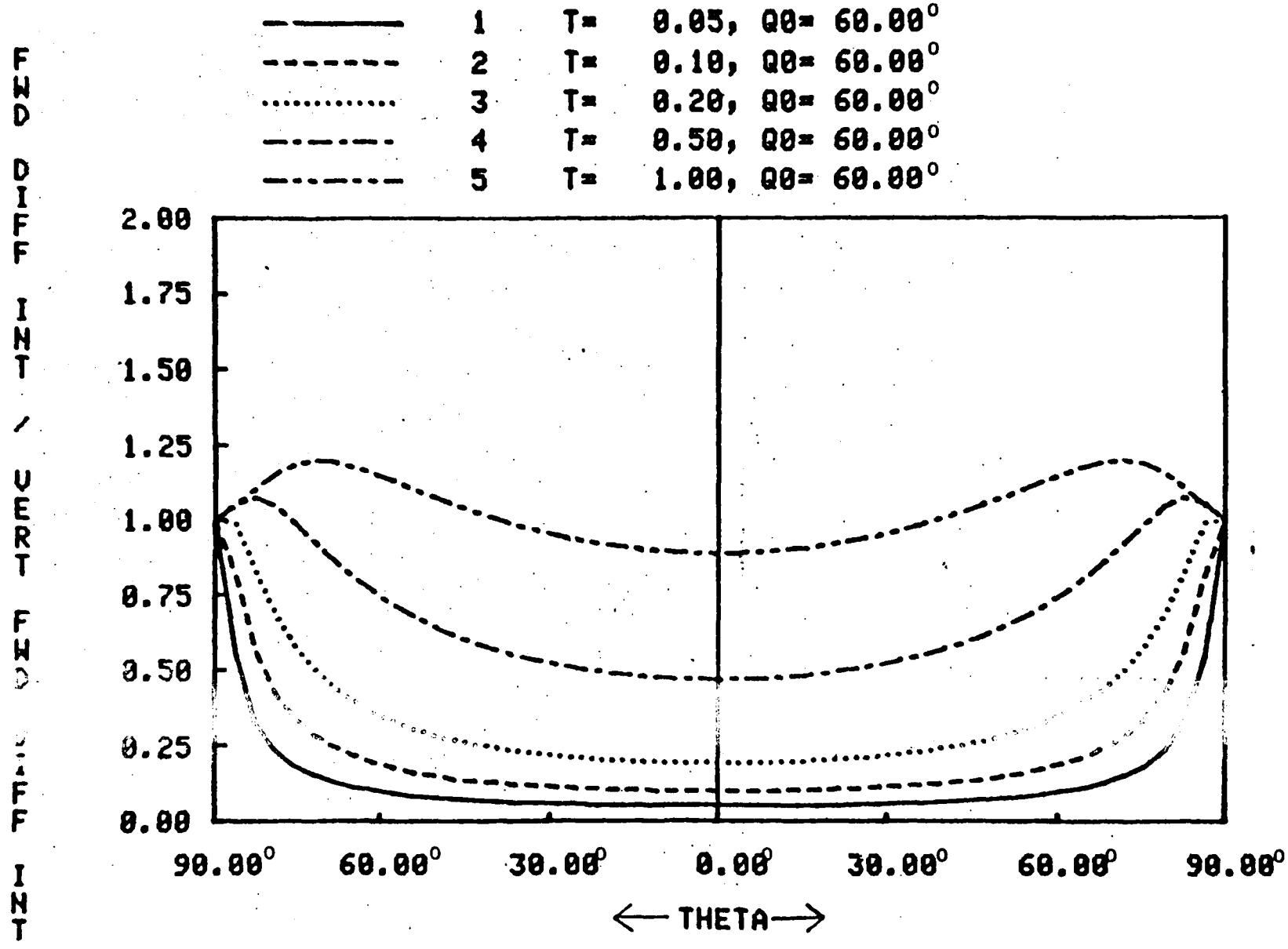

Figure 6.1. RELATIVE FRWD DIFF INTENSITY VS. SCATTER ANGLE FOR 1/2 SPACE, W=0.90

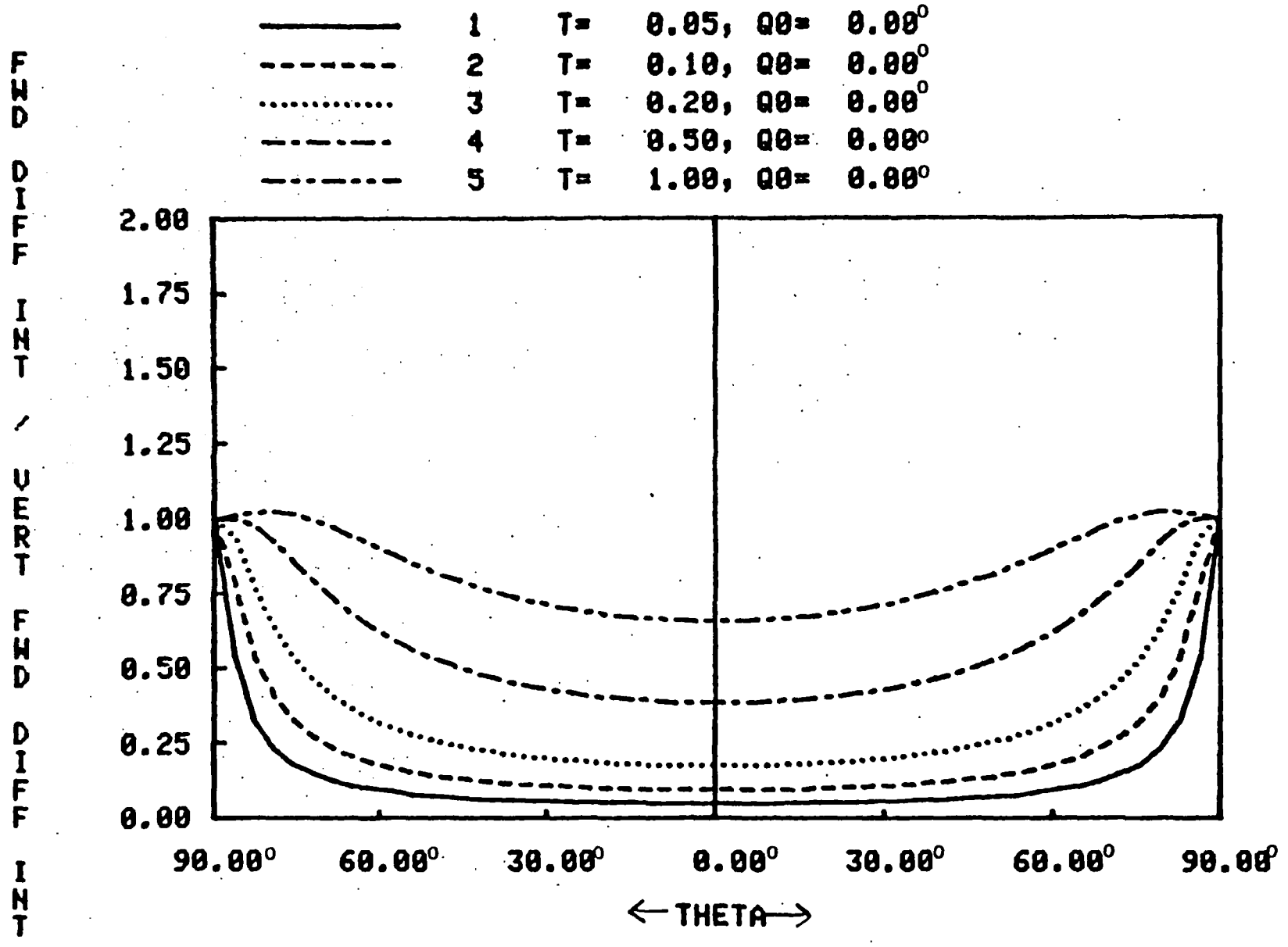

Figure 6.m RELATIVE FRWD DIFF INTENSITY VS. SCATTER ANGLE FOR 1/2 SPACE, W=0.95

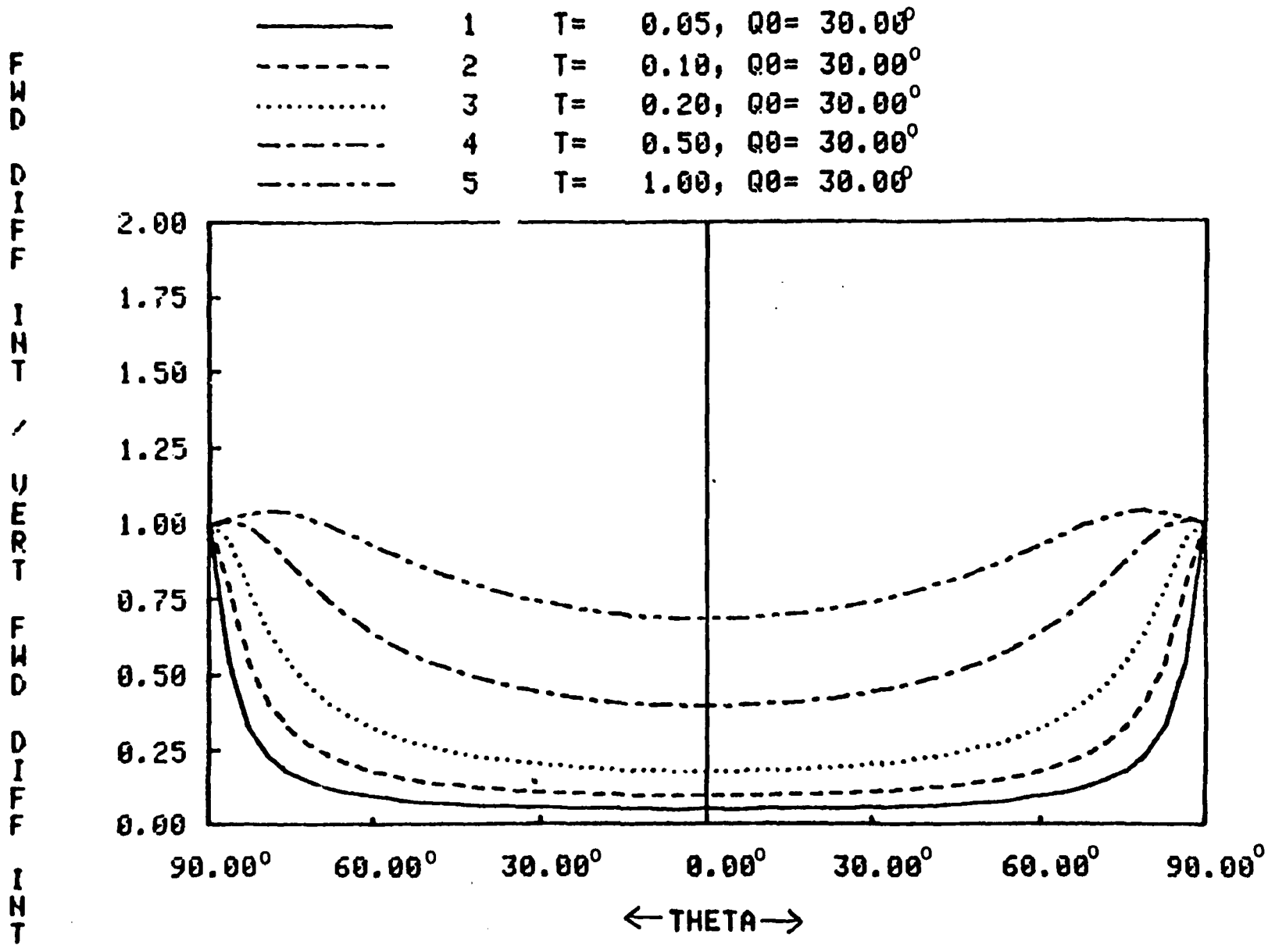

Figure 6.n. RELATIVE FRWD DIFF INTENSITY VS. SCATTER ANGLE FOR 1/2 SPACE, W=0.95

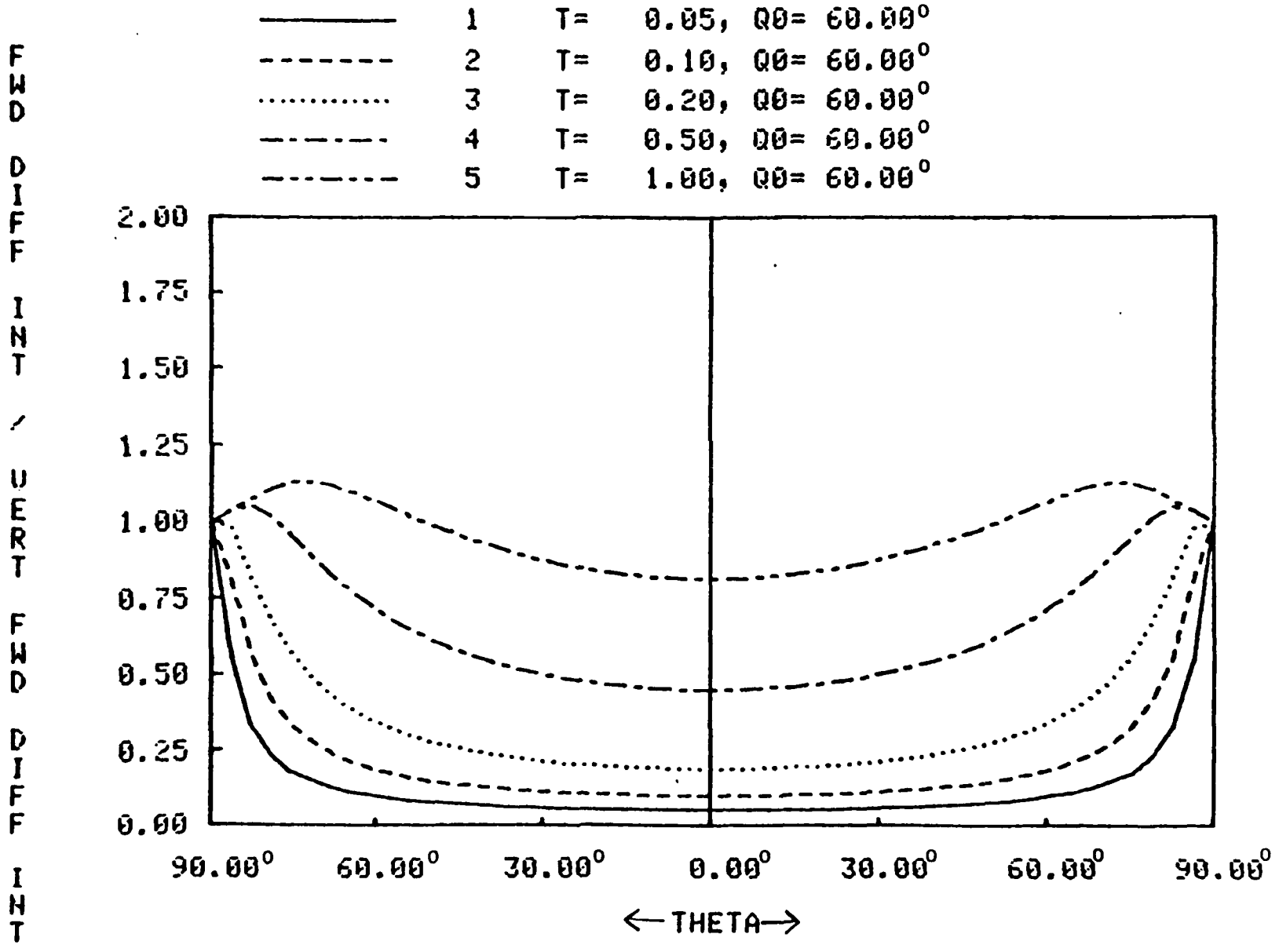

Figure 6.o. RELATIVE FRWD DIFF INTENSITY VS. SCATTER ANGLE FOR 1/2 SPACE, W=0.95

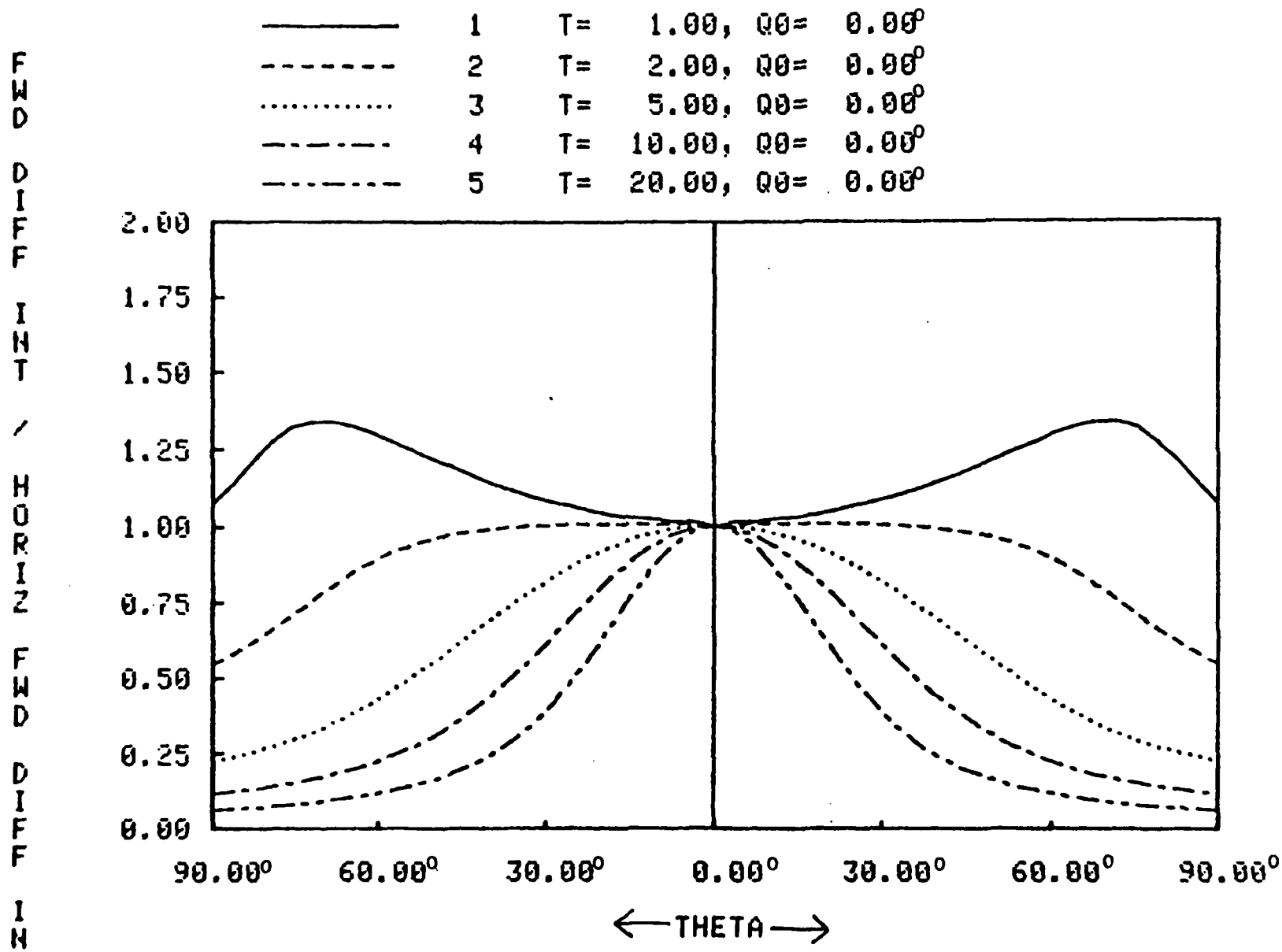

Figure 7.a RELATIVE FRWD DIFF INTENSITY VS. SCATTER ANGLE FOR 1/2 SPACE, W=0.25

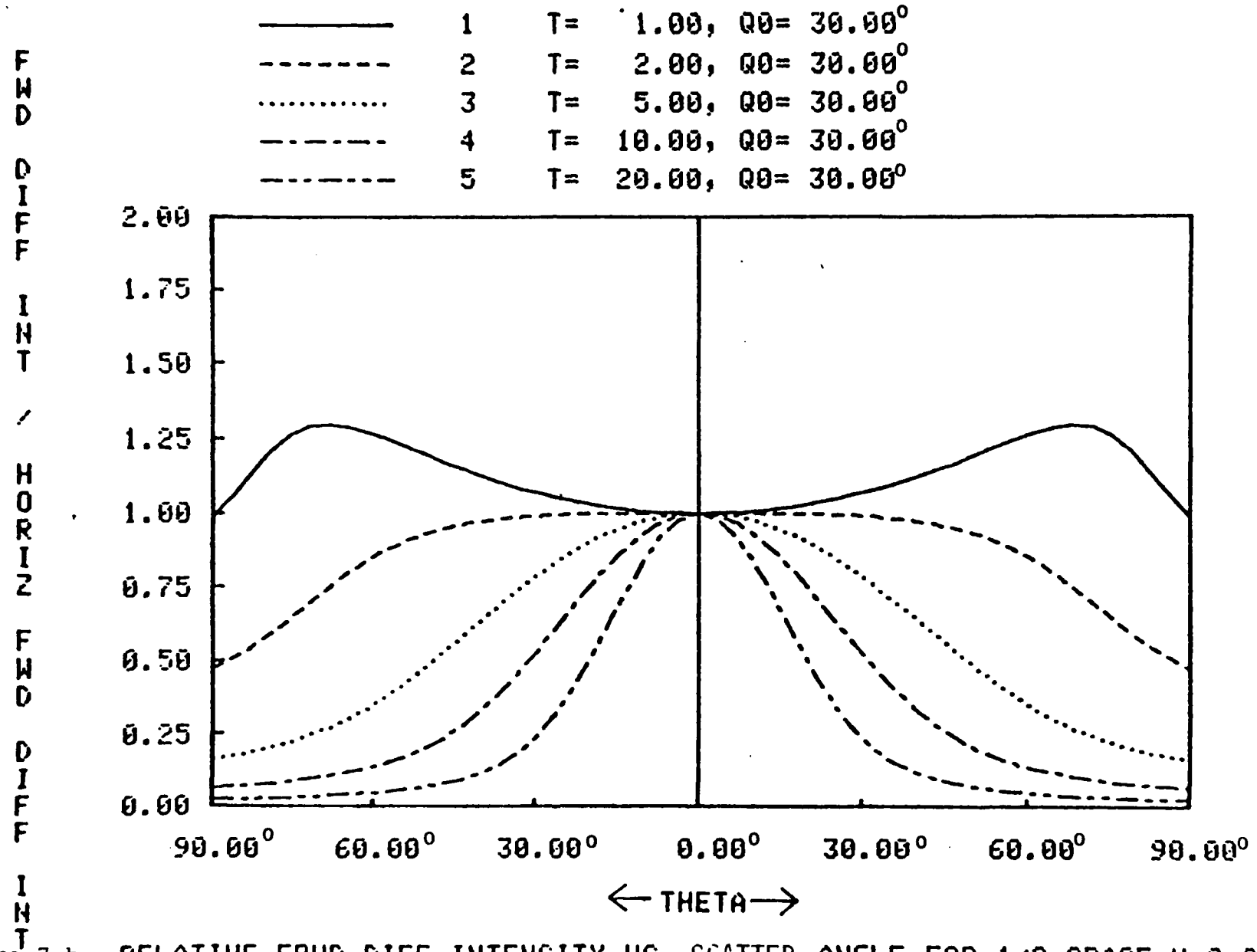

Figure 7.b. RELATIVE FRWD DIFF INTENSITY VS. SCATTER ANGLE FOR 1/2 SPACE, W=0.25

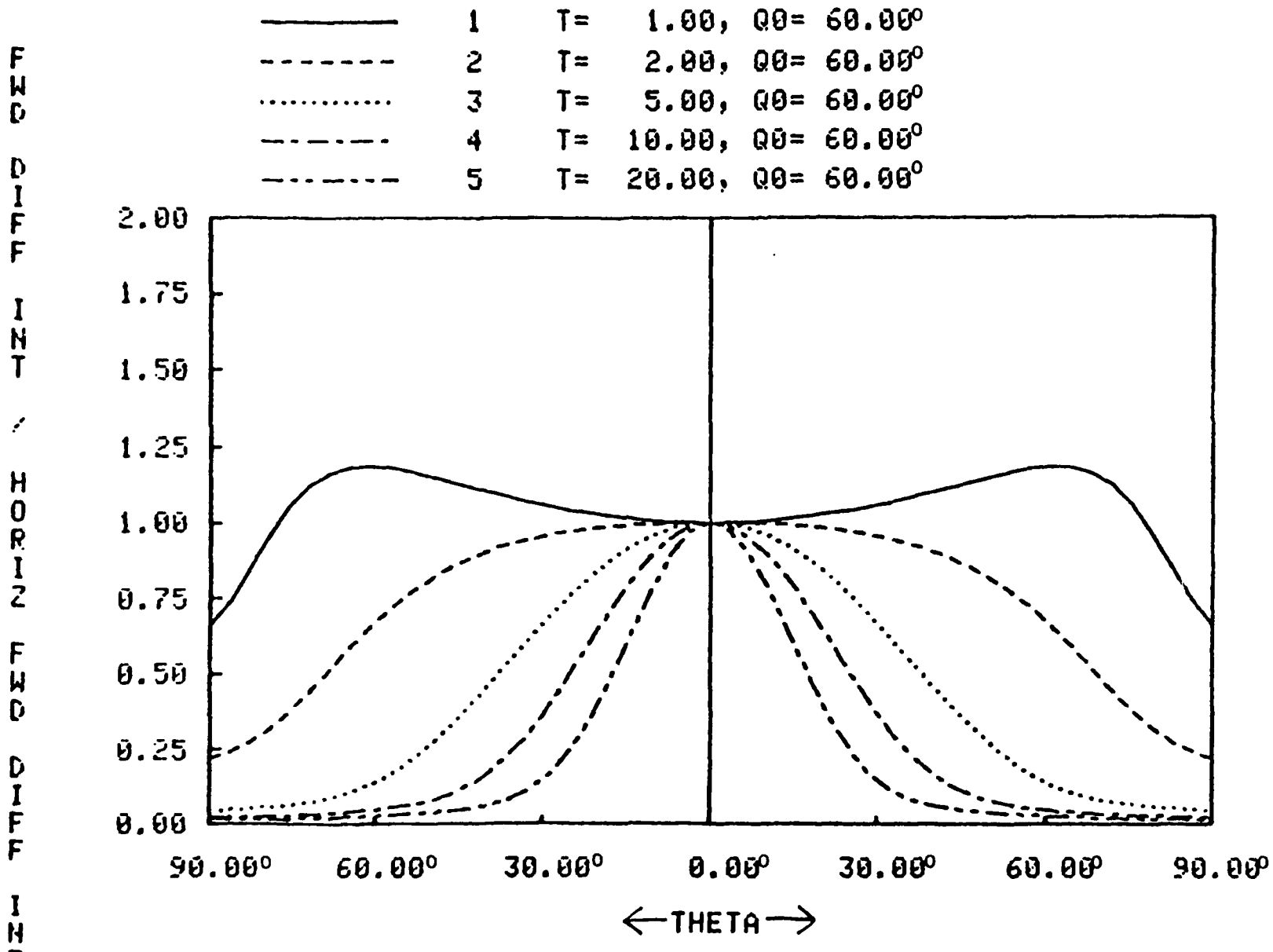

Figure 7.c. RELATIVE FRWD DIFF INTENSITY VS. SCATTER ANGLE FOR 1/2 SPACE, W=0.25

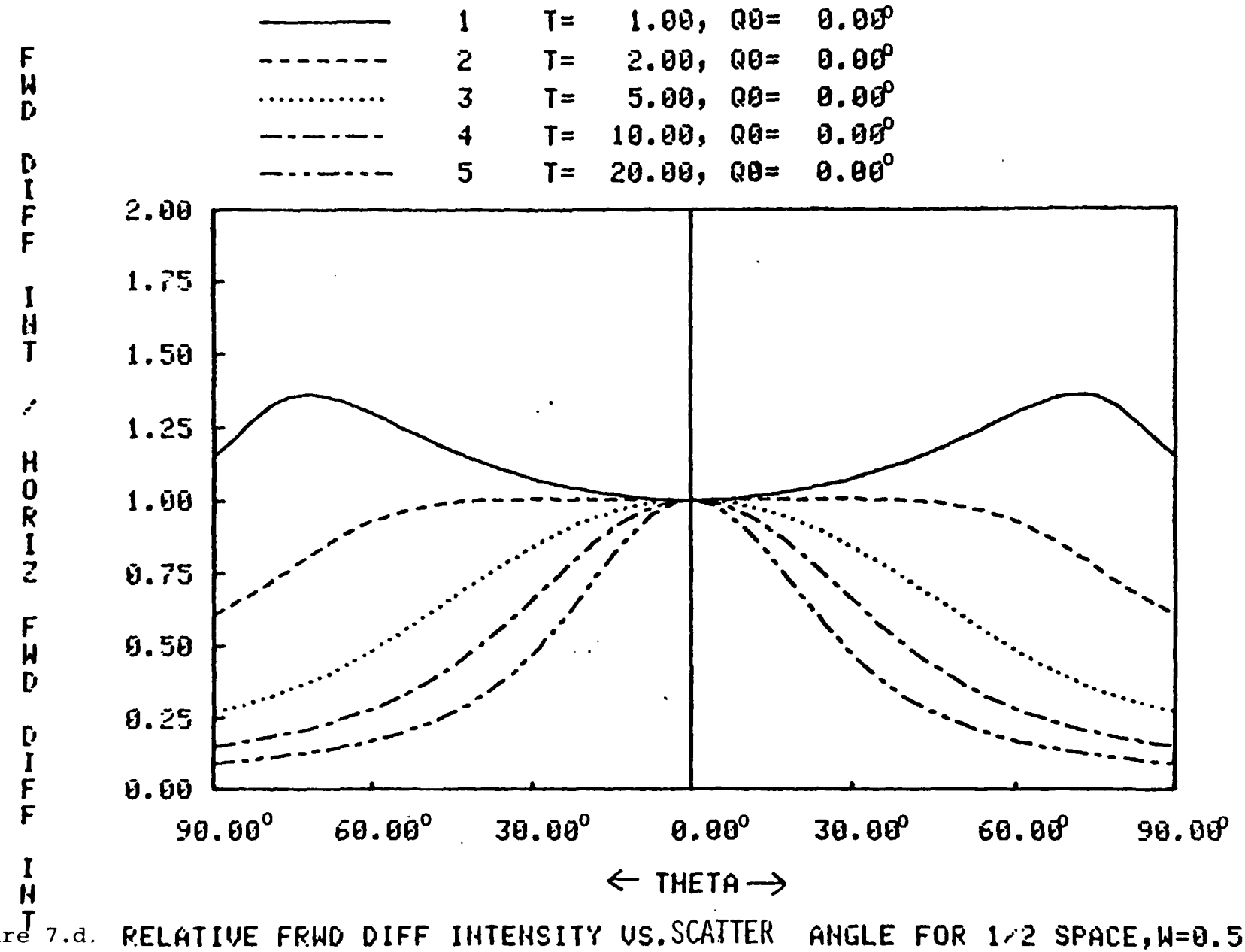

Figure 7.d. RELATIVE FRWD DIFF INTENSITY VS.SCATTER ANGLE FOR 1/2 SPACE,W=0.50

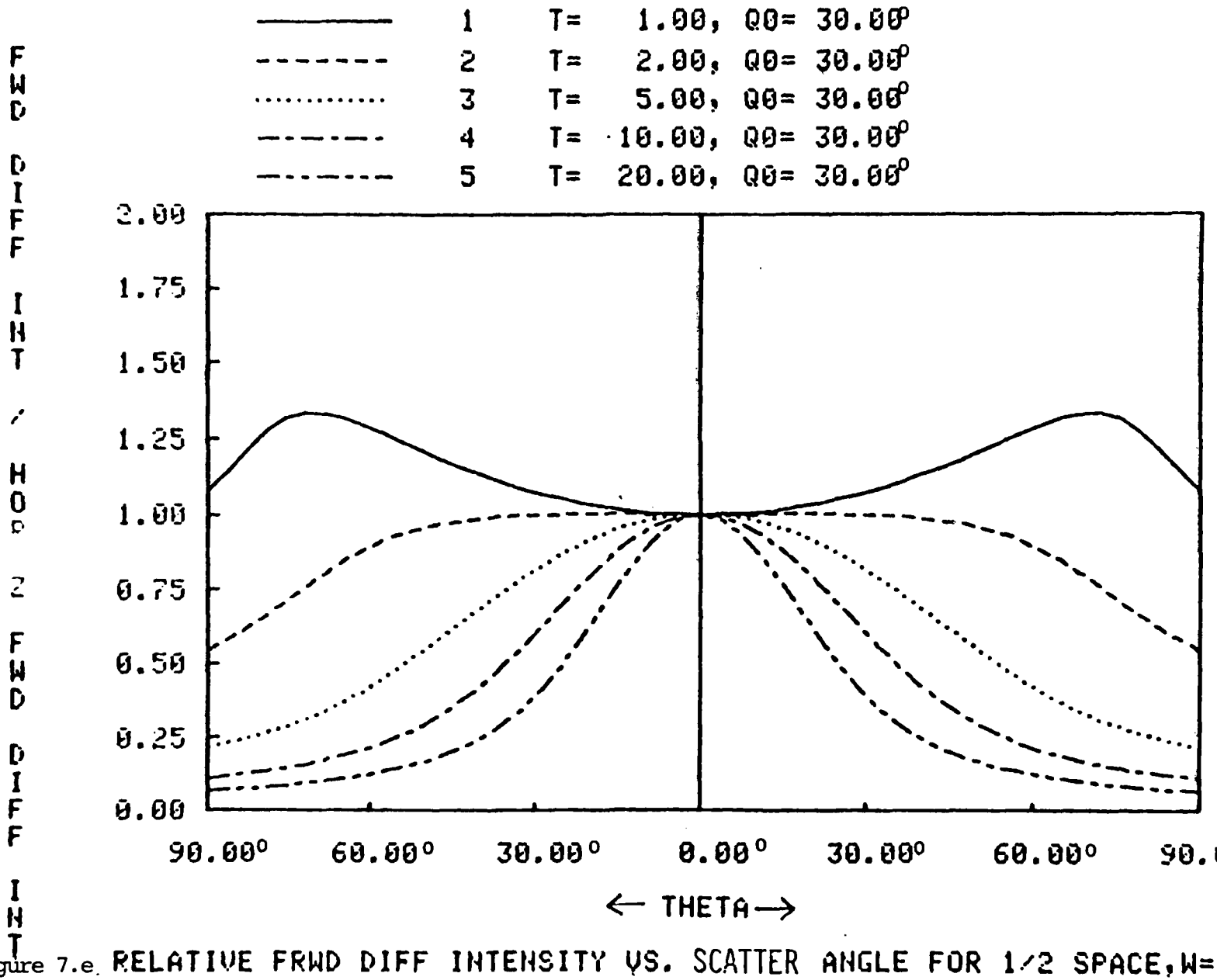

Figure 7.e. RELATIVE FRWD DIFF INTENSITY VS. SCATTER ANGLE FOR 1/2 SPACE, W=0.50

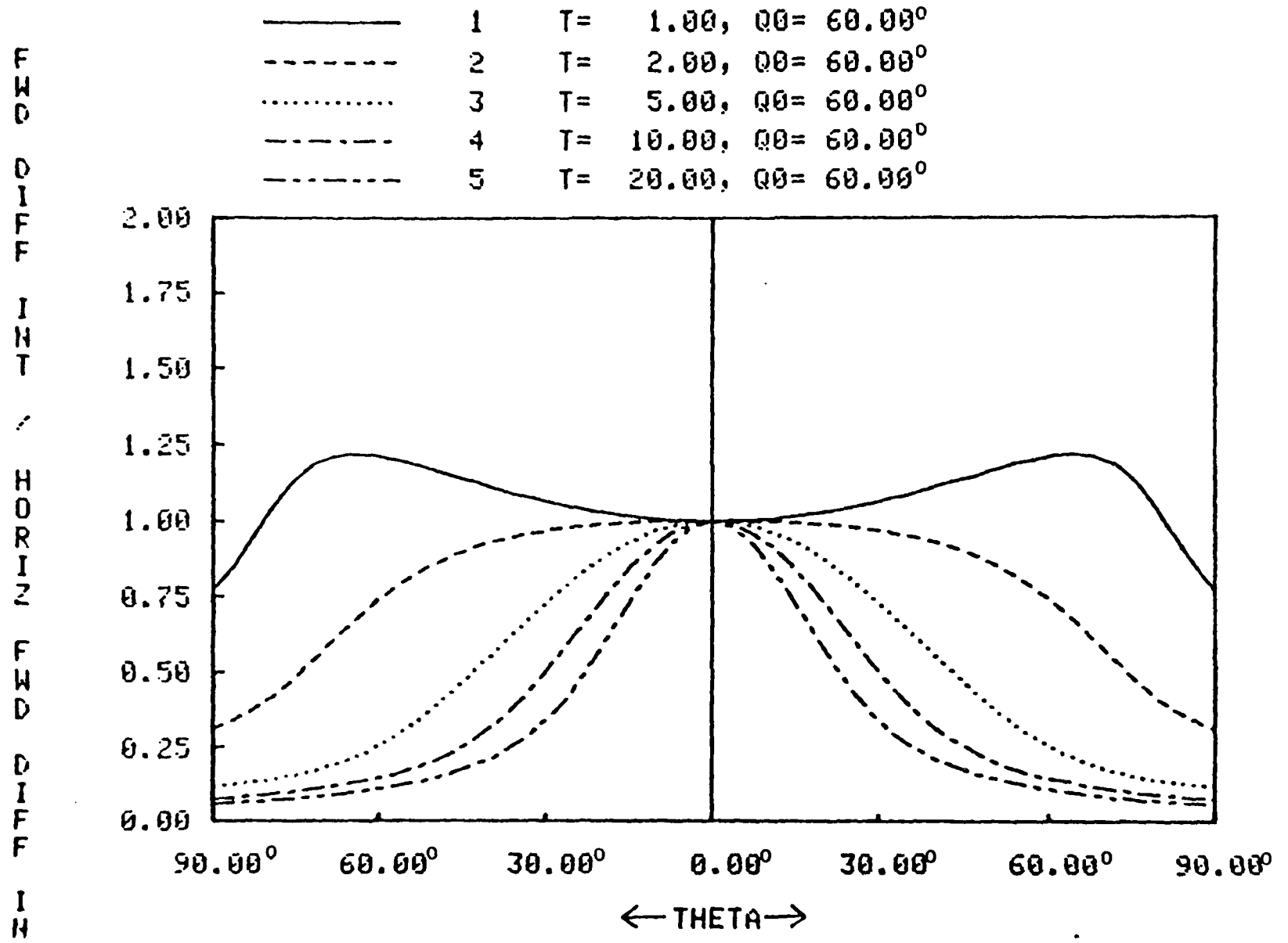

Figure 7.f. RELATIVE FRWD DIFF INTENSITY VS. SCATTER ANGLE FOR 1/2 SPACE, W=0.50

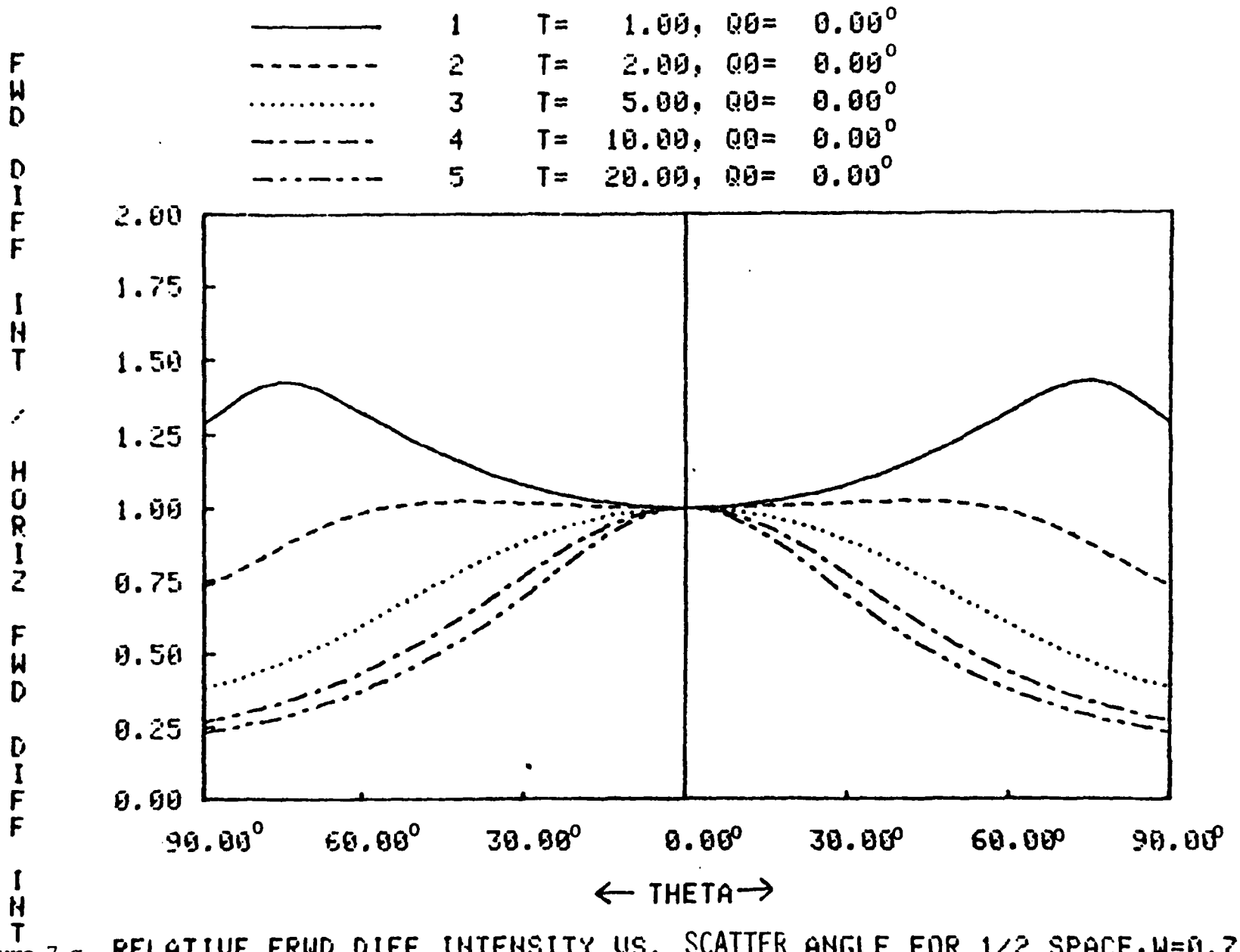

Figure 7.g. RELATIVE FRWD DIFF INTENSITY VS. SCATTER ANGLE FOR 1/2 SPACE, W=0.75

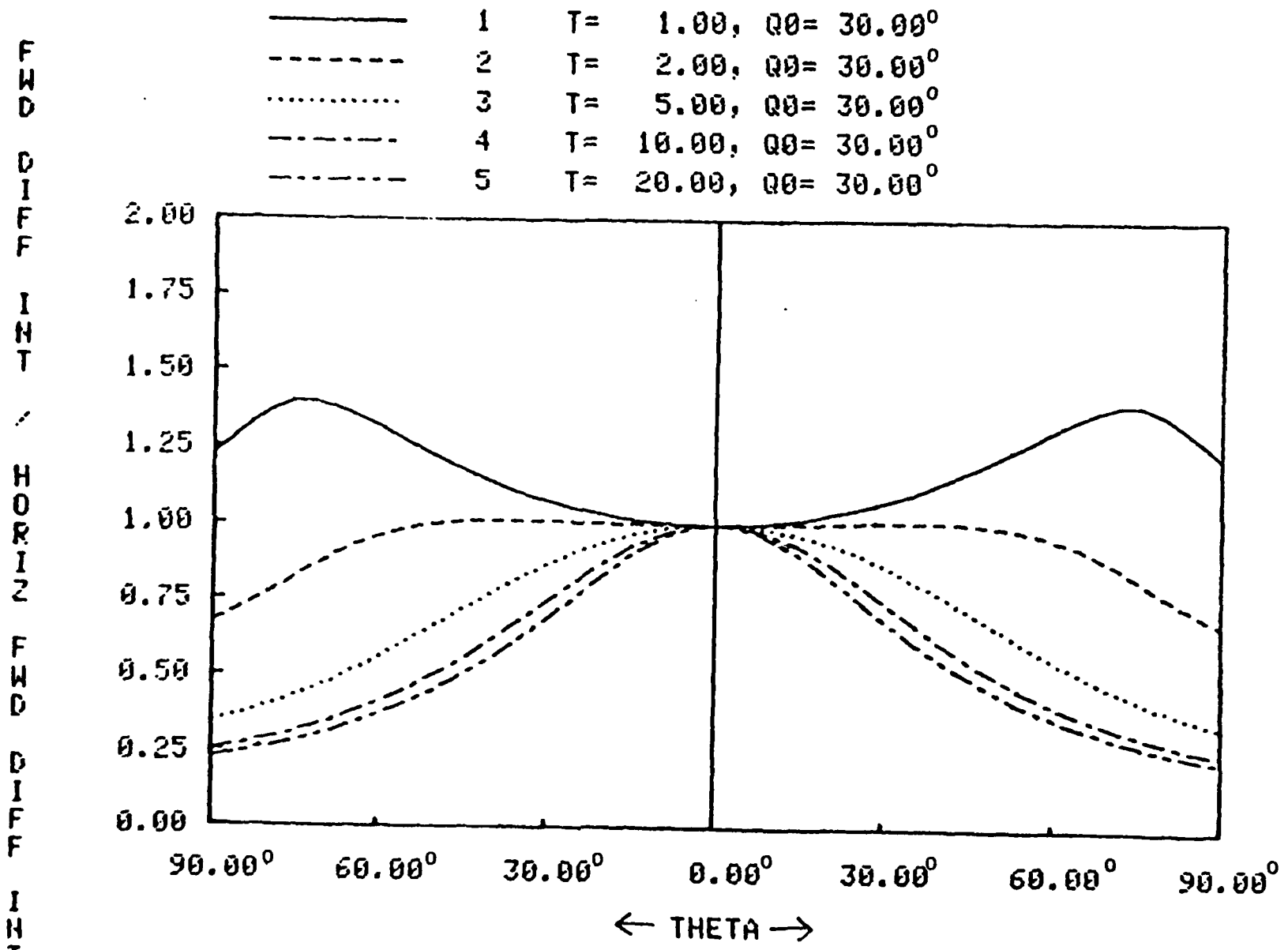

Figure 7.h RELATIVE FRWD DIFF INTENSITY VS. SCATTER ANGLE FOR 1/2 SPACE, W=0.75

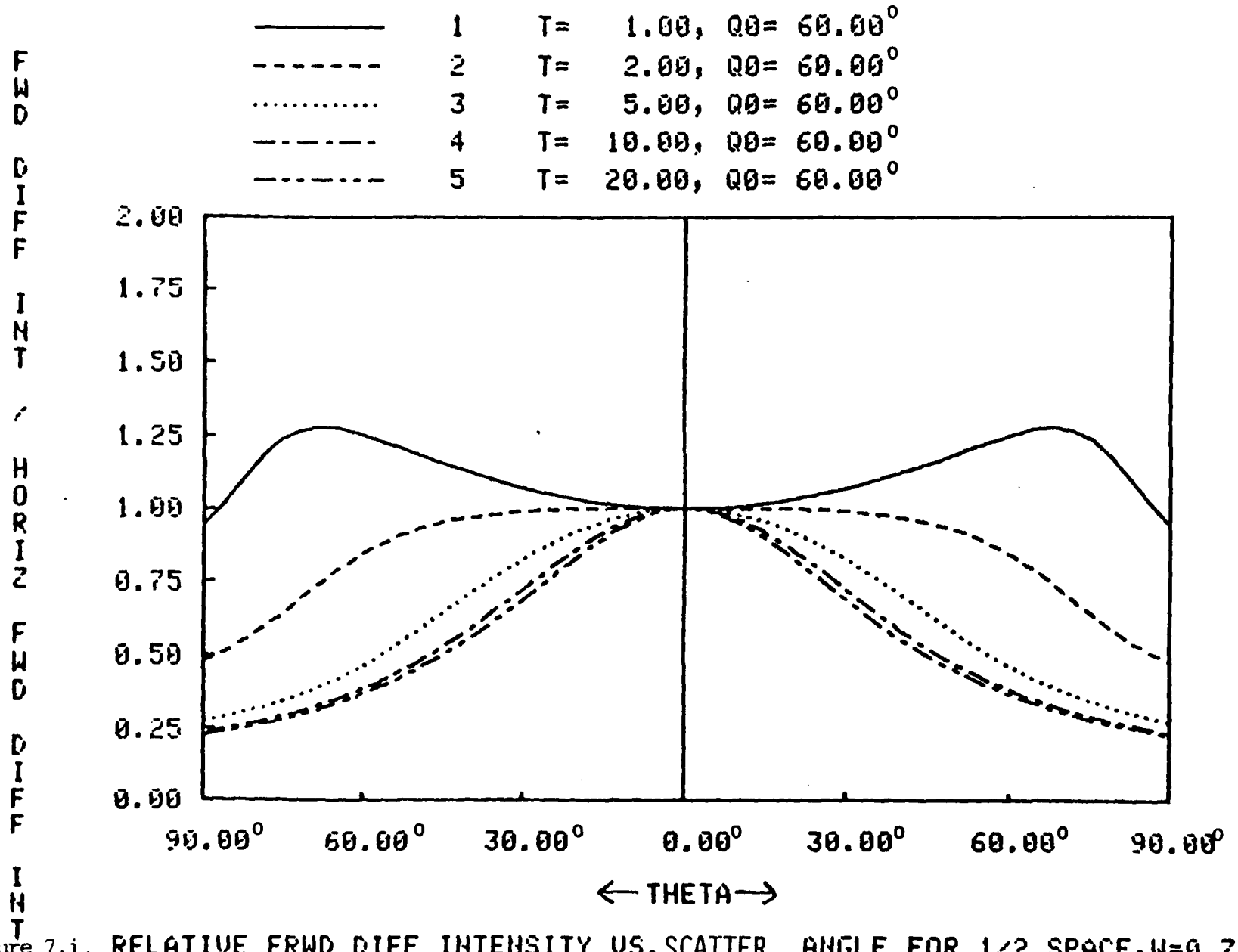

Figure 7.i. RELATIVE FRWD DIFF INTENSITY VS. SCATTER ANGLE FOR 1/2 SPACE, W=0.75

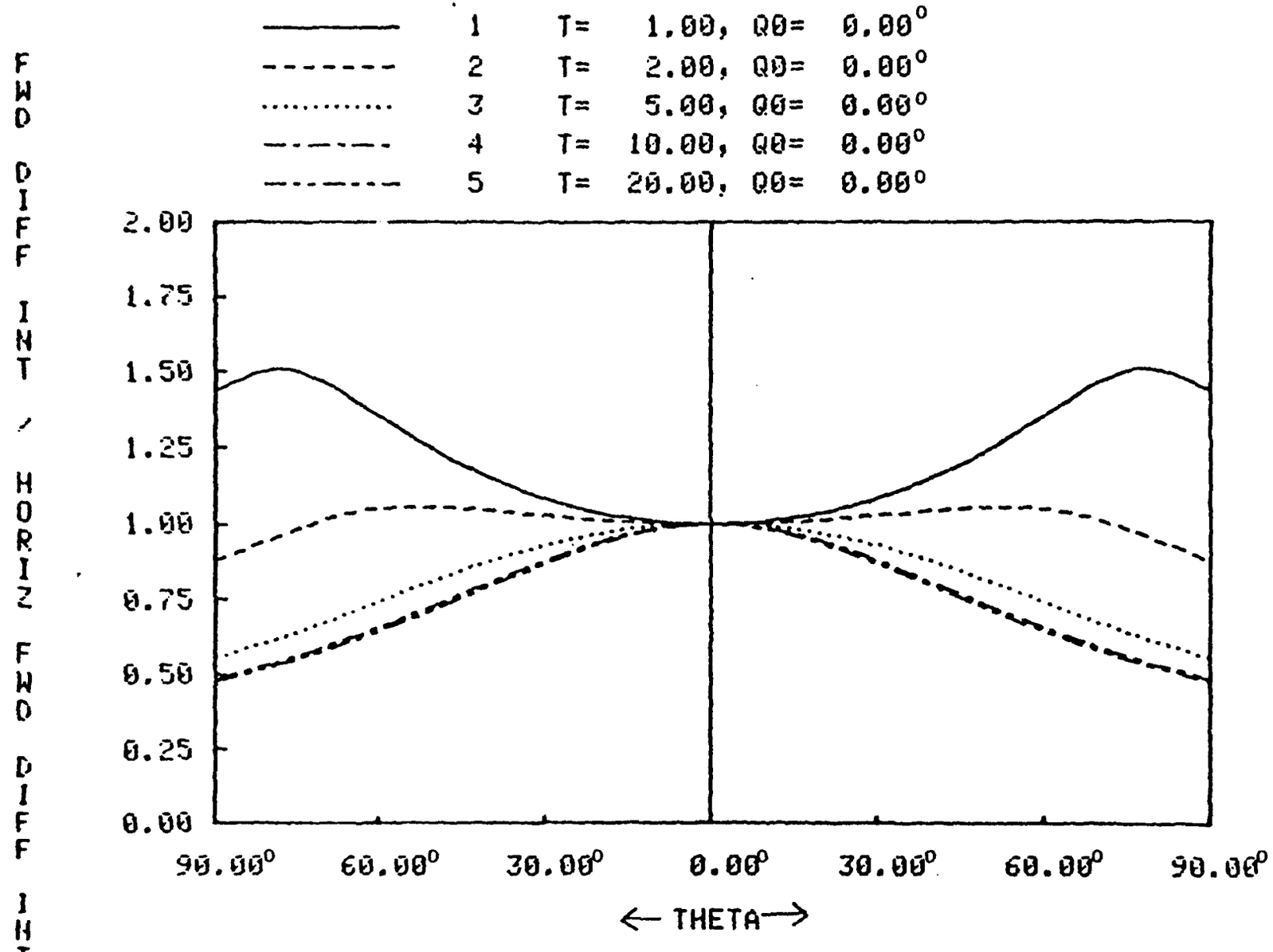

Figure 7.j. RELATIVE FRND DIFF INTENSITY VS. SCATTER ANGLE FOR 1/2 SPACE, W=0.90

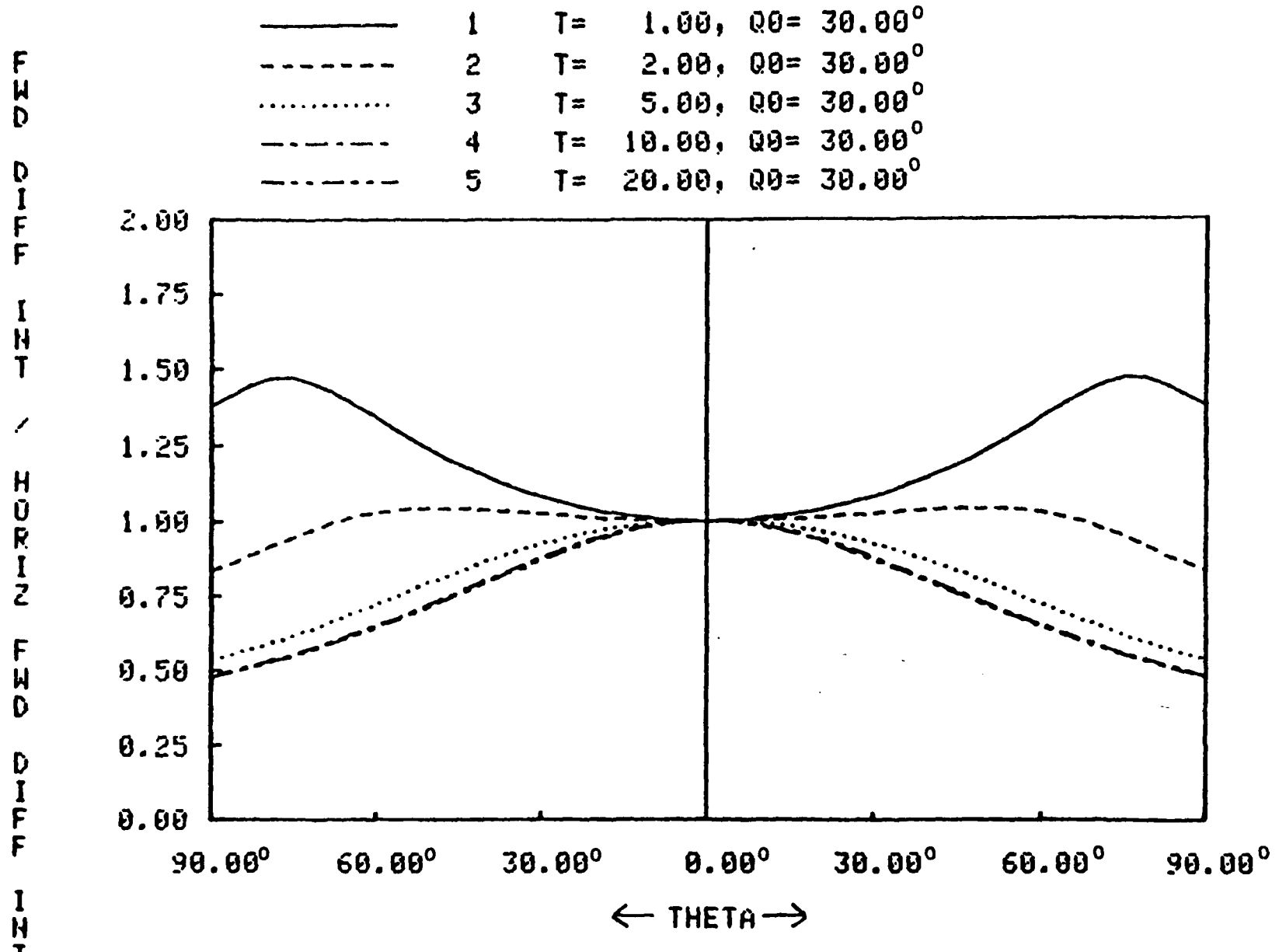

Figure 7.k RELATIVE FRWD DIFF INTENSITY VS. SCATTER ANGLE FOR 1/2 SPACE, W=0.90

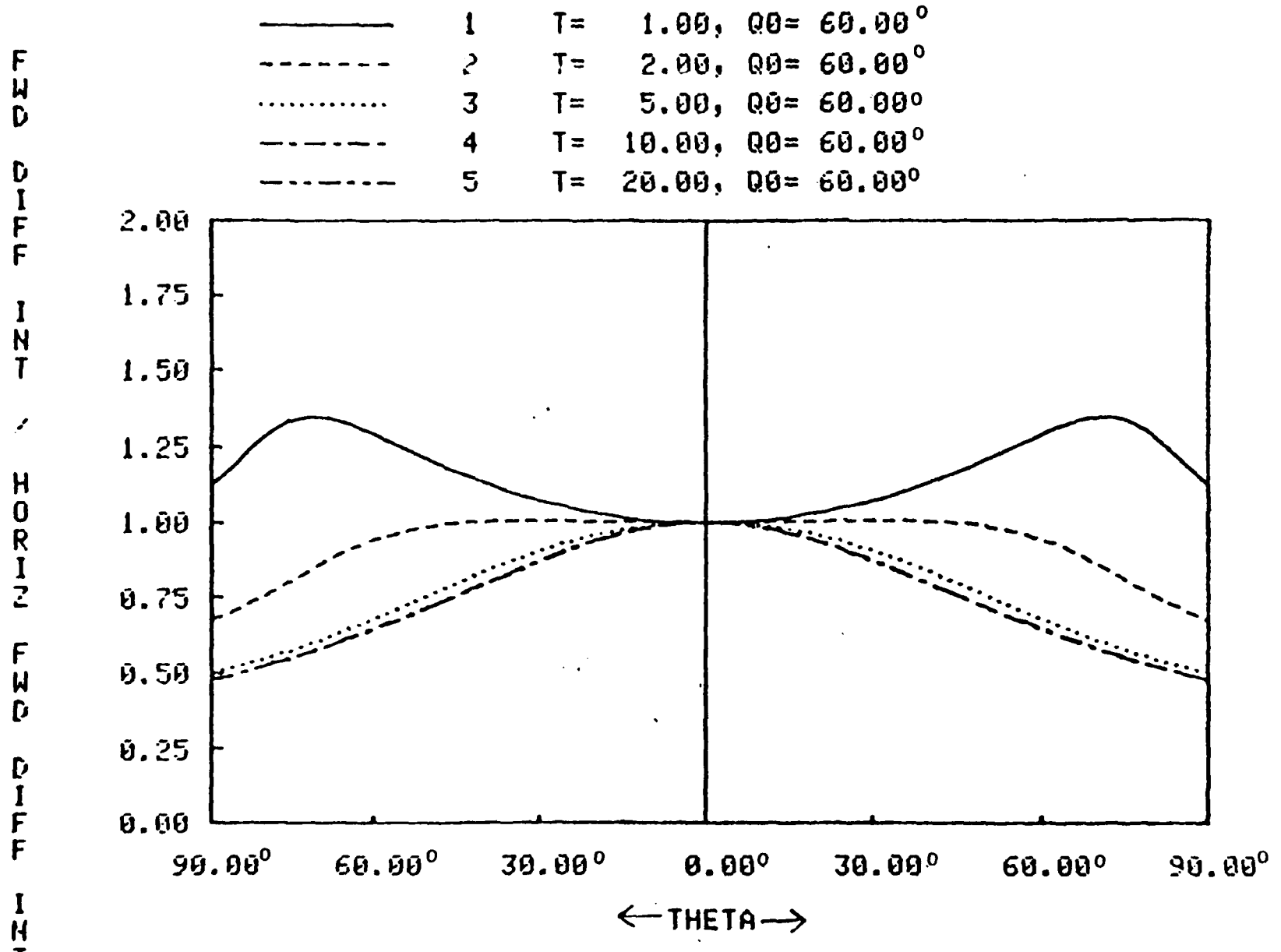

Figure 7.1 RELATIVE FRWD DIFF INTENSITY VS. SCATTER ANGLE FOR 1/2 SPACE, W=0.90

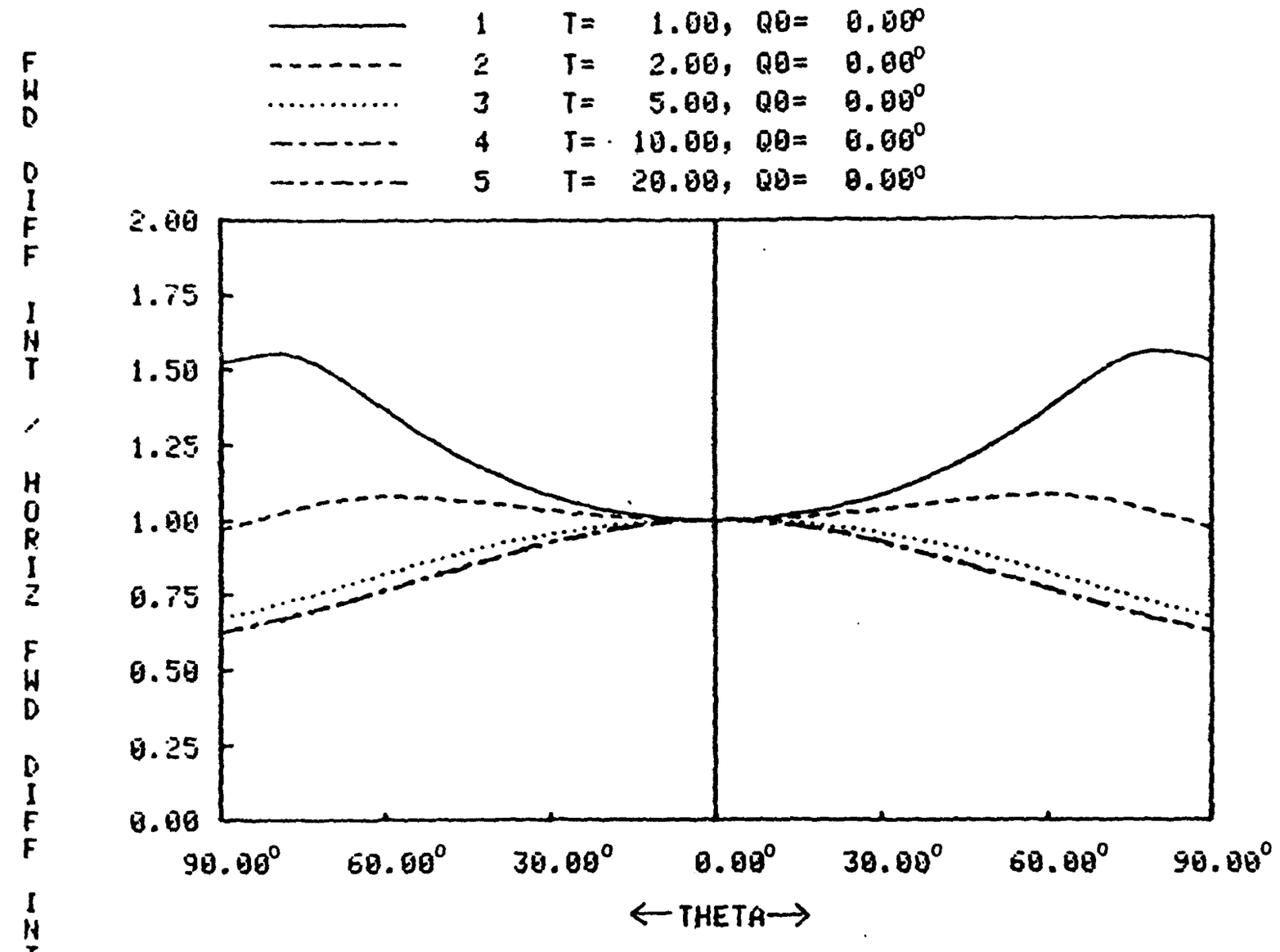

Figure 7.m. RELATIVE FRWD DIFF INTENSITY VS. SCATTER ANGLE FOR 1/2 SPACE, W=0.95

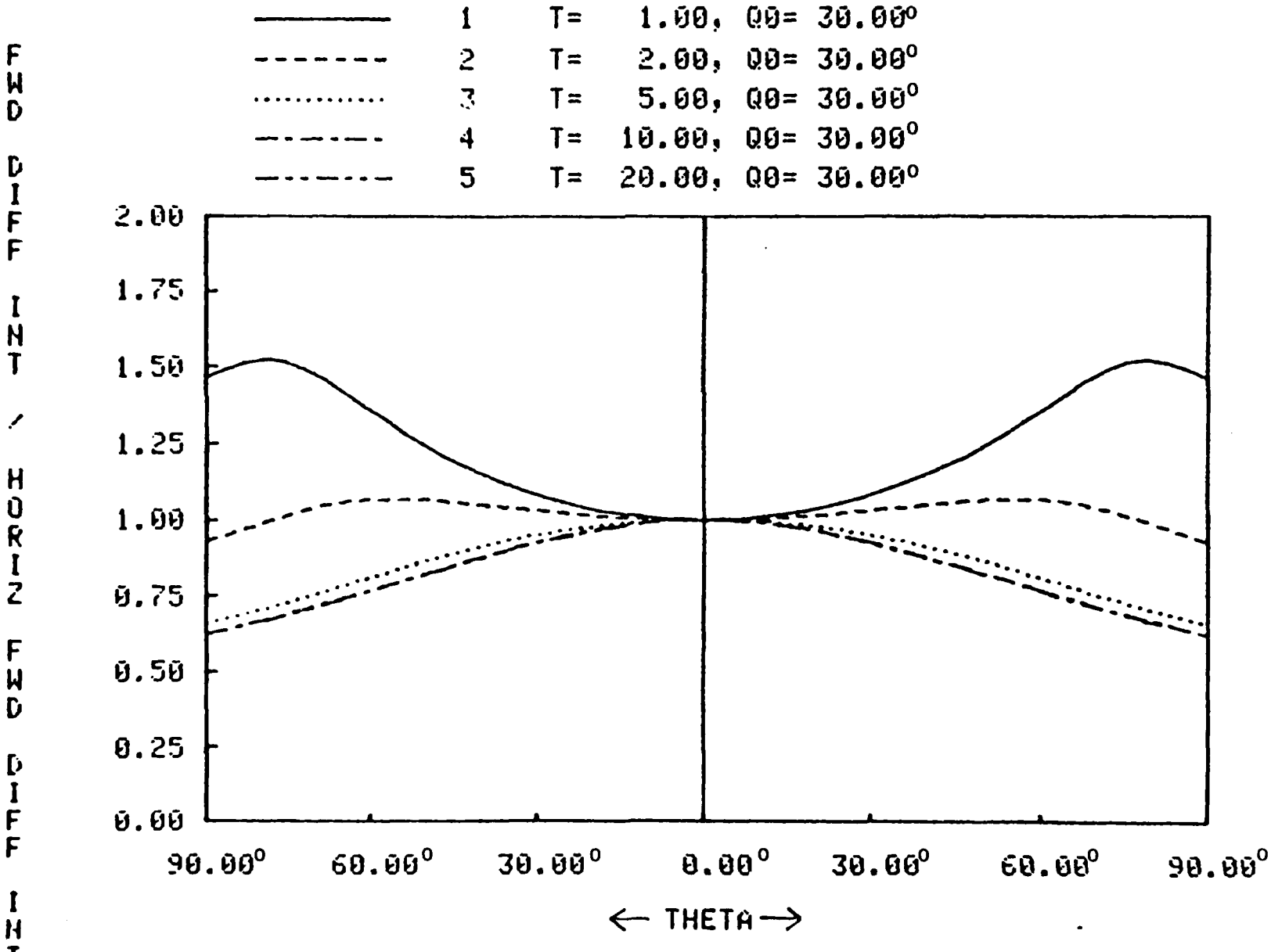

Figure 7.n RELATIVE FRWD DIFF INTENSITY VS. SCATTER ANGLE FOR 1/2 SPACE, W=0.95

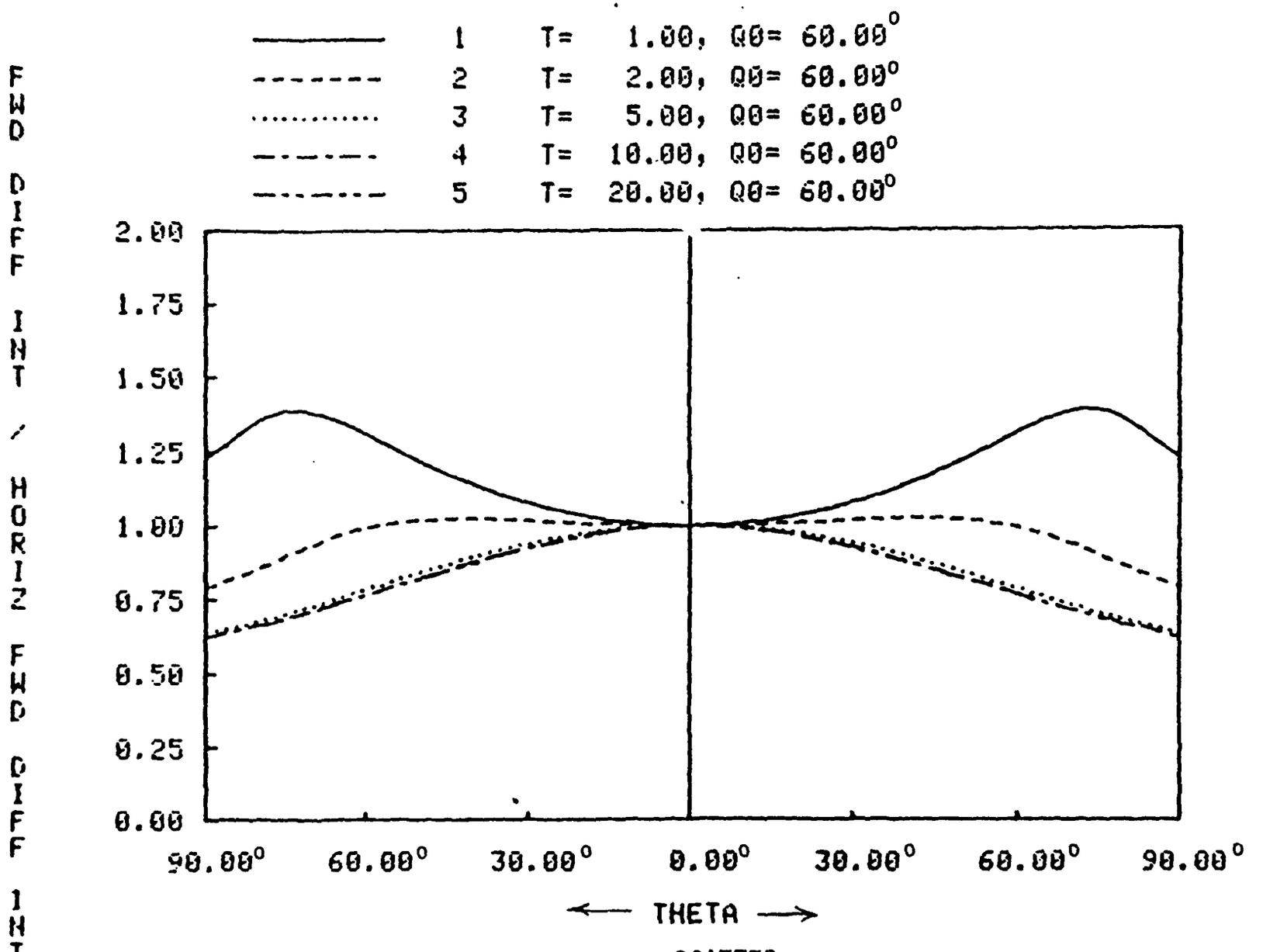

Figure 7.o RELATIVE FRWD DIFF INTENSITY VS. SCATTER ANGLE FOR 1/2 SPACE, W=0.95

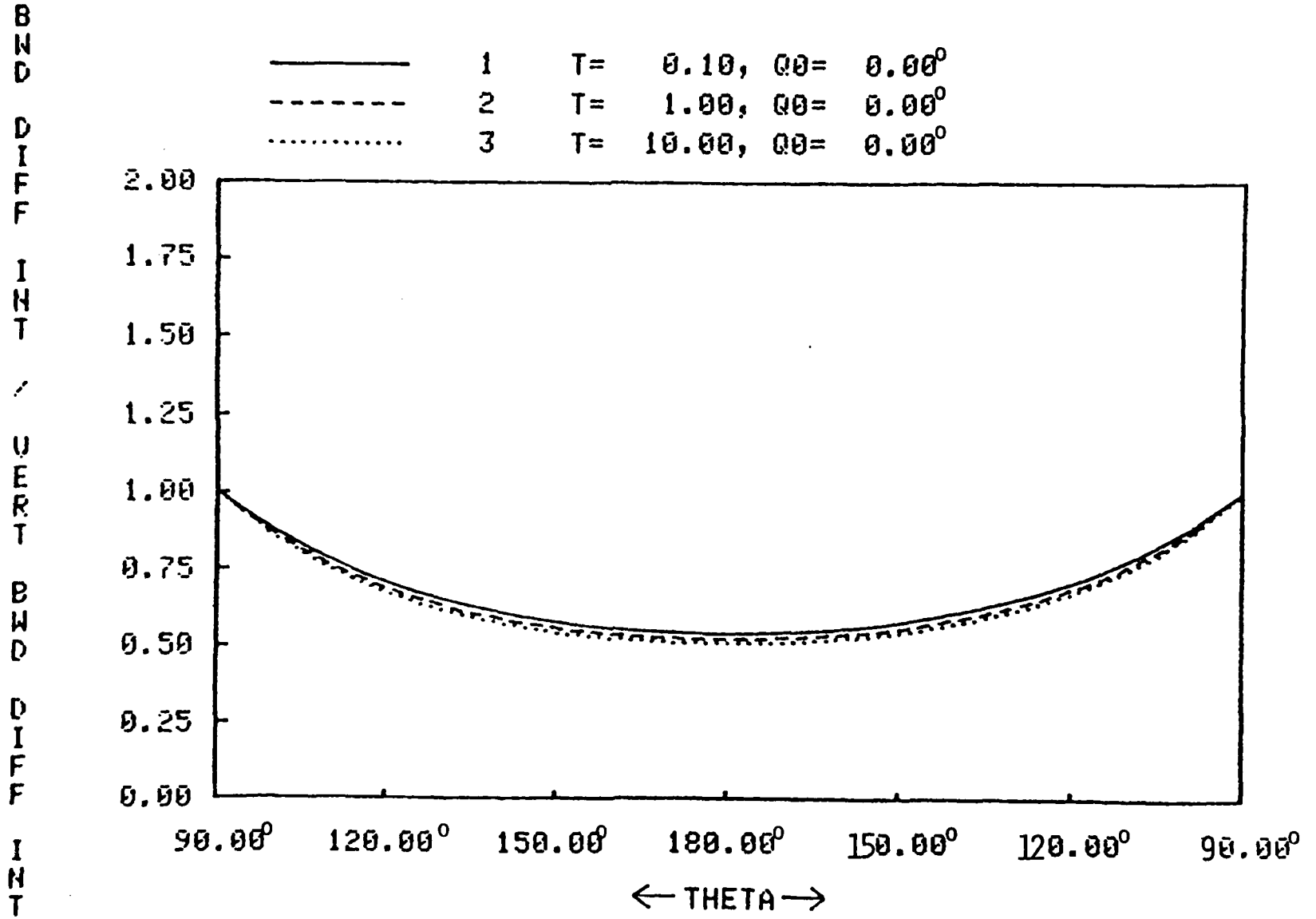

Figure 8.a. RELATIVE BWD DIFF INTENSITY VS. SCATTER ANGLE FOR 1/2 SPACE, W=0.25

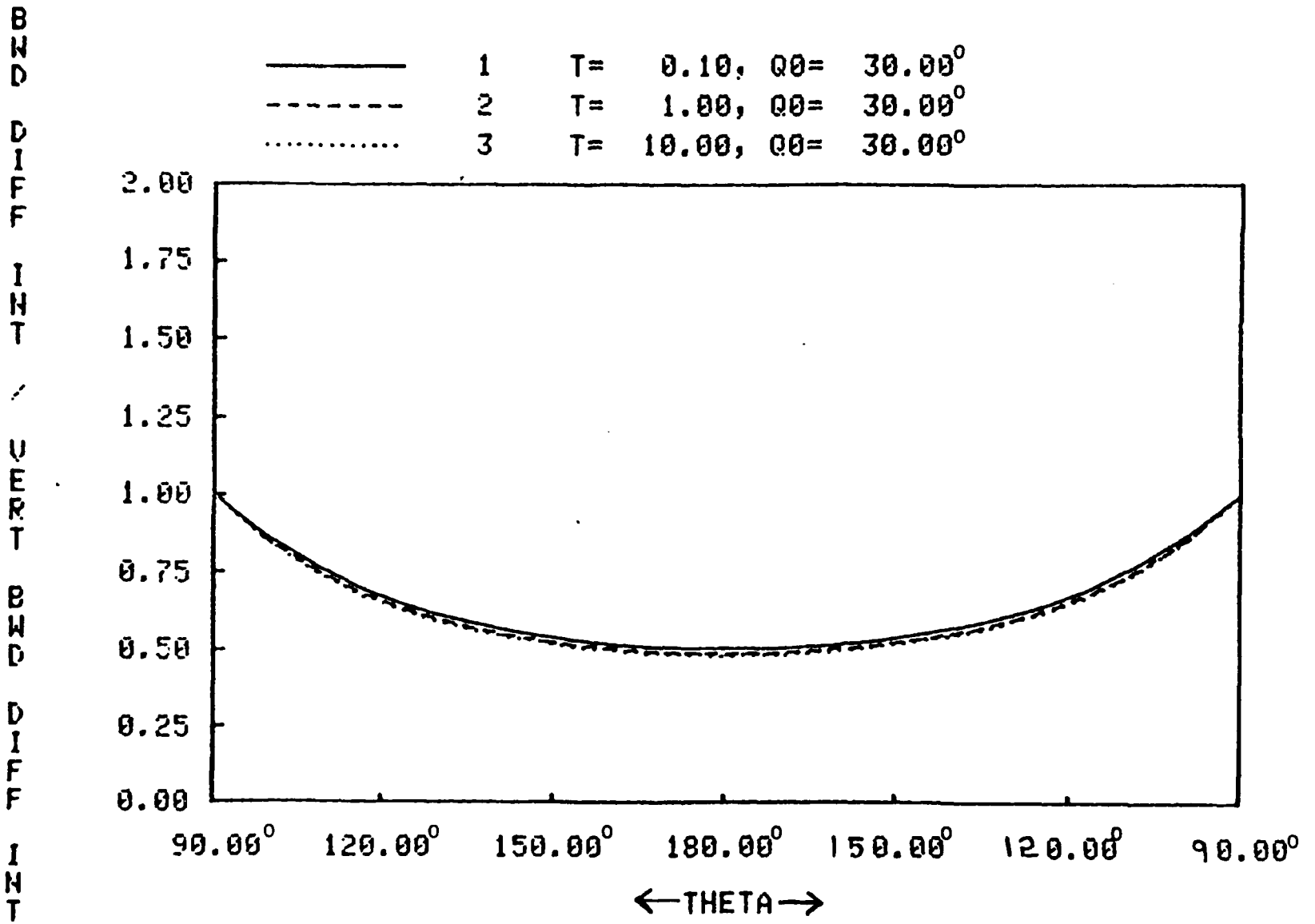

Figure 8.b. RELATIVE BWD DIFF INTENSITY VS. SCATTER ANGLE FOR 1/2 SPACE, W=0.25

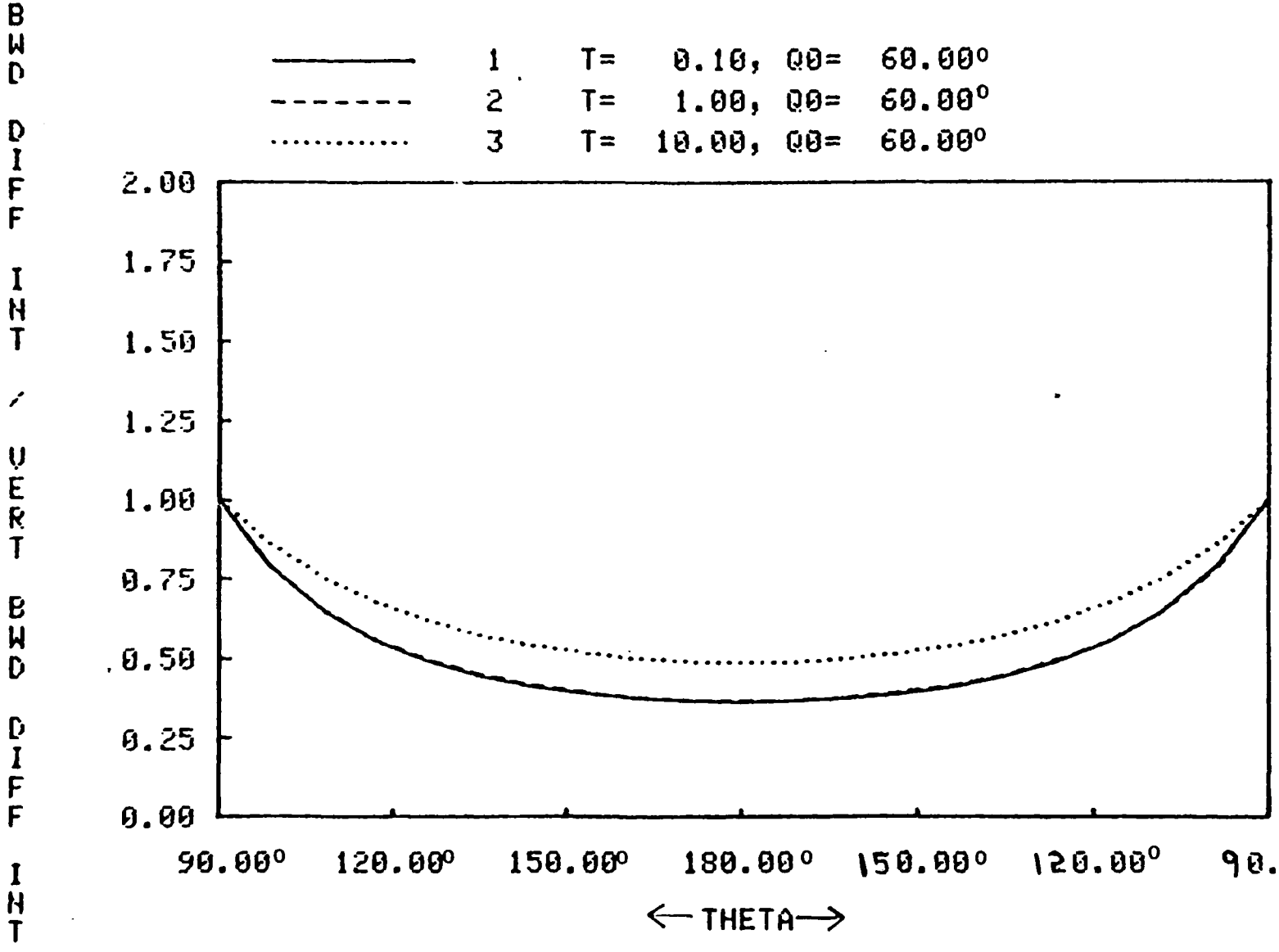

Figure 8.c. RELATIVE BWD DIFF INTENSITY VS. SCATTER ANGLE FOR 1/2 SPACE, W=0.25

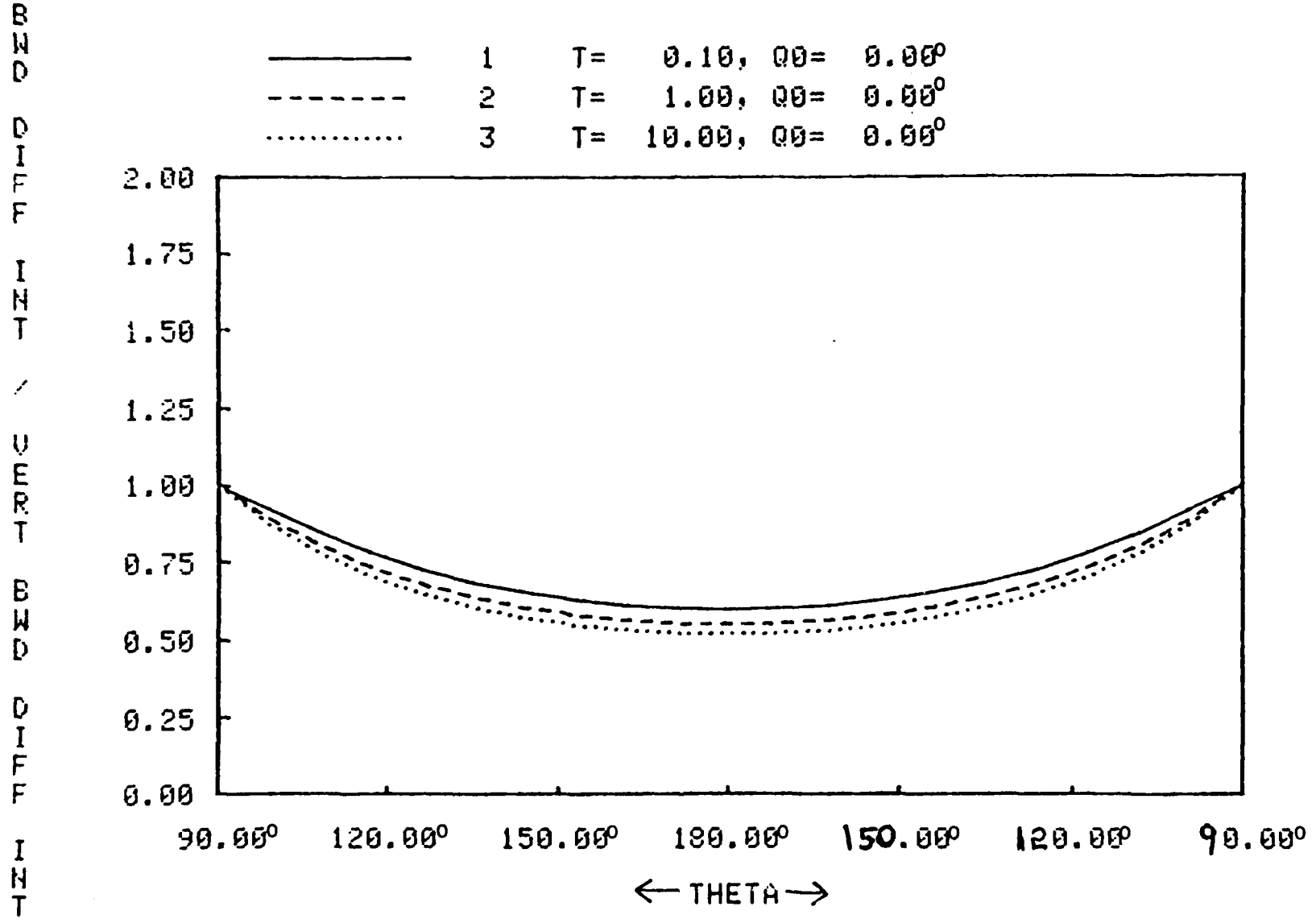

Figure 8.d RELATIVE BWD DIFF INTENSITY VS. SCATTER ANGLE FOR 1/2 SPACE, W=0.50

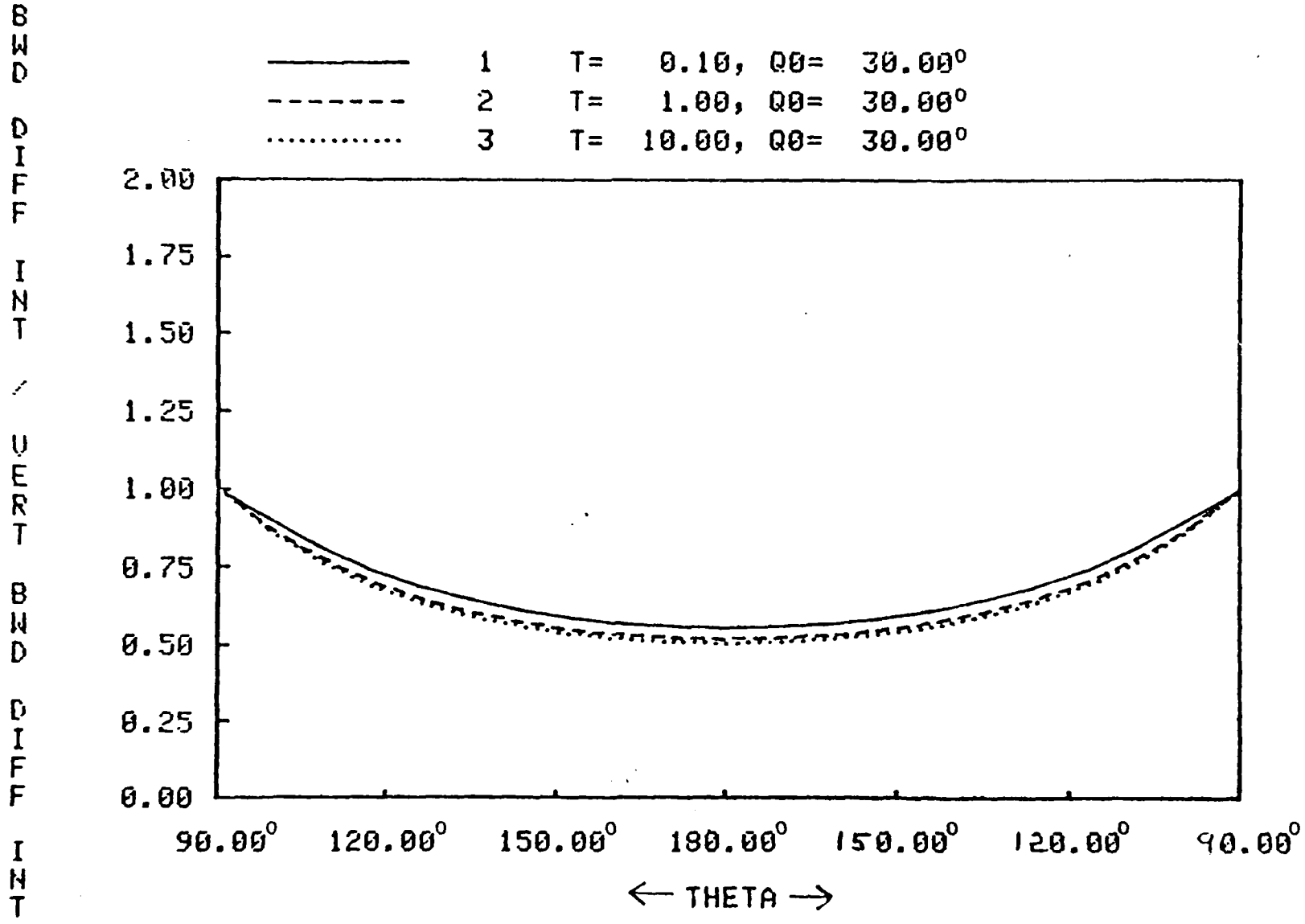

Figure 8.e. RELATIVE BWD DIFF INTENSITY VS. SCATTER ANGLE FOR 1/2 SPACE, W=0.50

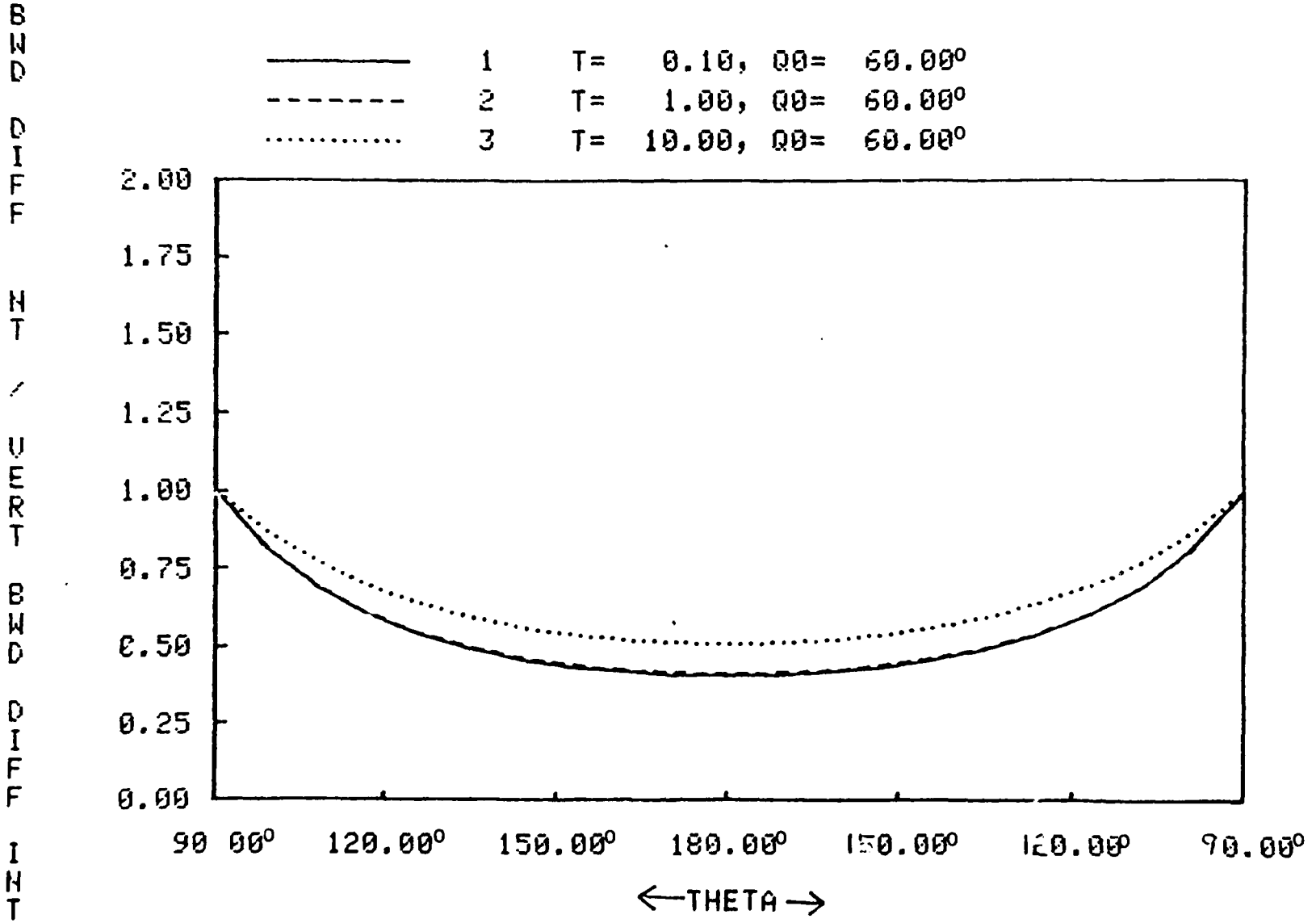

Figure 8.f RELATIVE BWD DIFF INTENSITY VS. SCATTER ANGLE FOR 1/2 SPACE, W=0.50

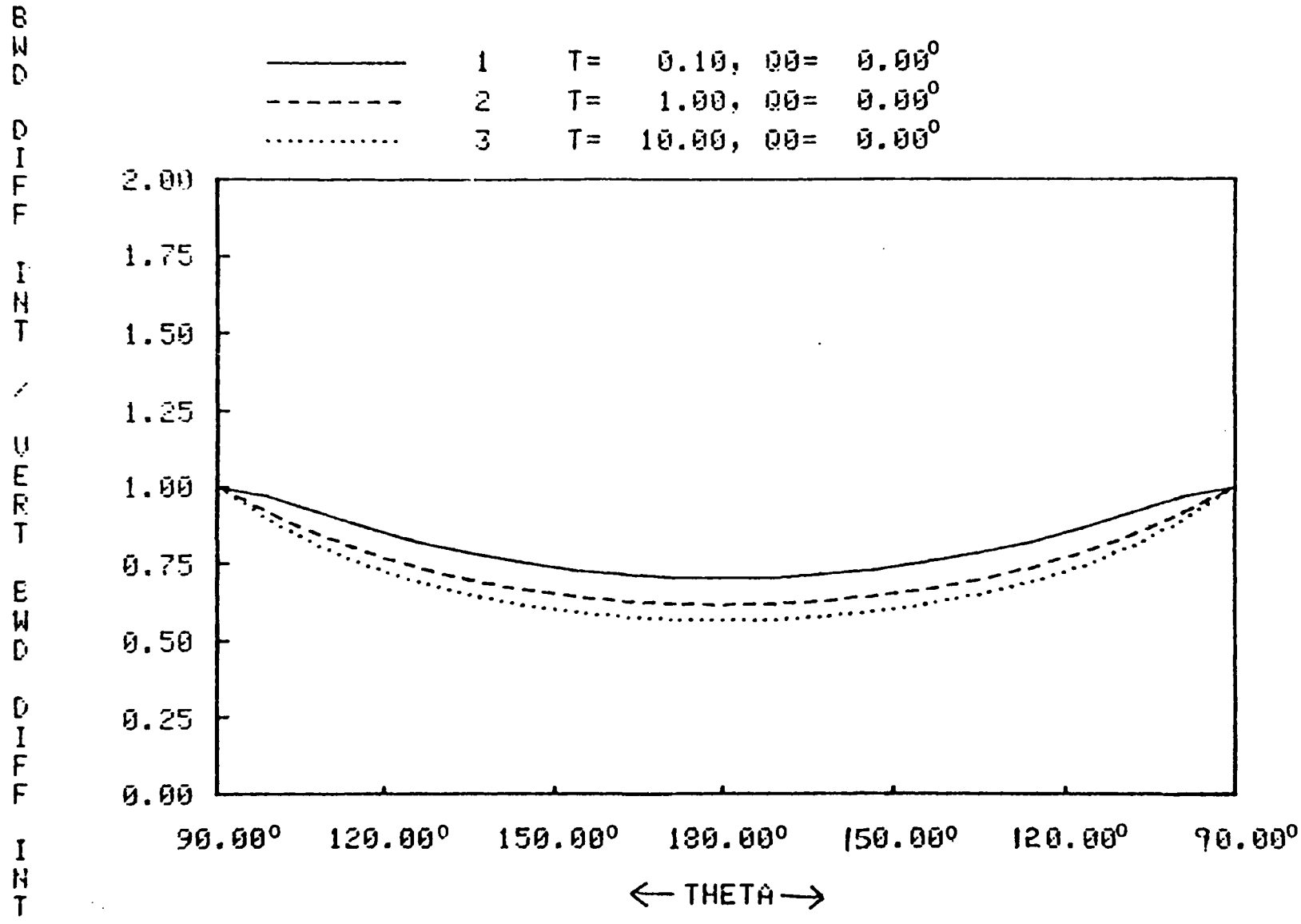

Figure 8.g RELATIVE BWD DIFF INTENSITY VS. SCATTER ANGLE FOR 1/2 SPACE, W=0.75

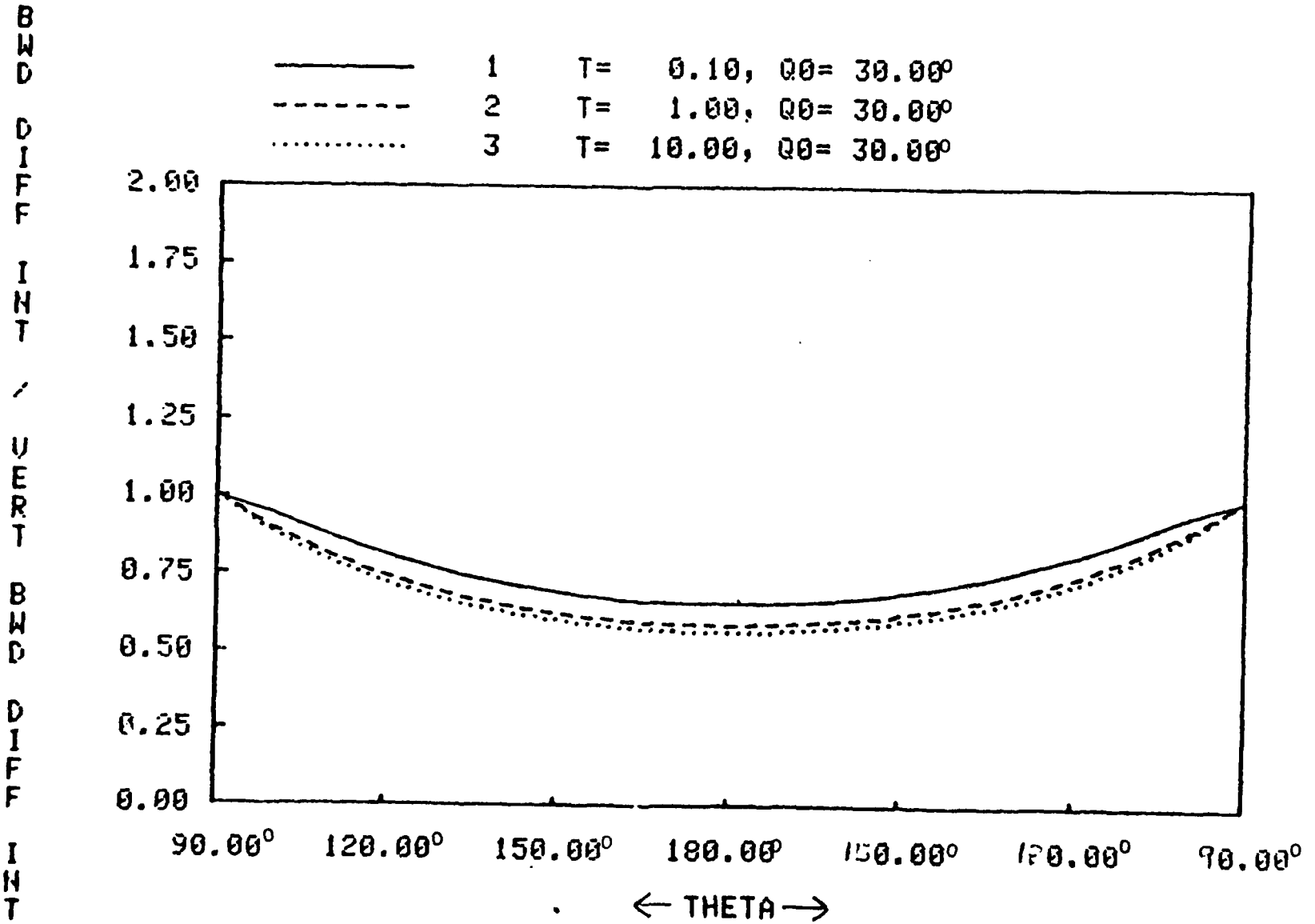

Figure 8.n. RELATIVE BWD DIFF INTENSITY VS. SCATTER ANGLE FOR 1/2 SPACE, W=0.75

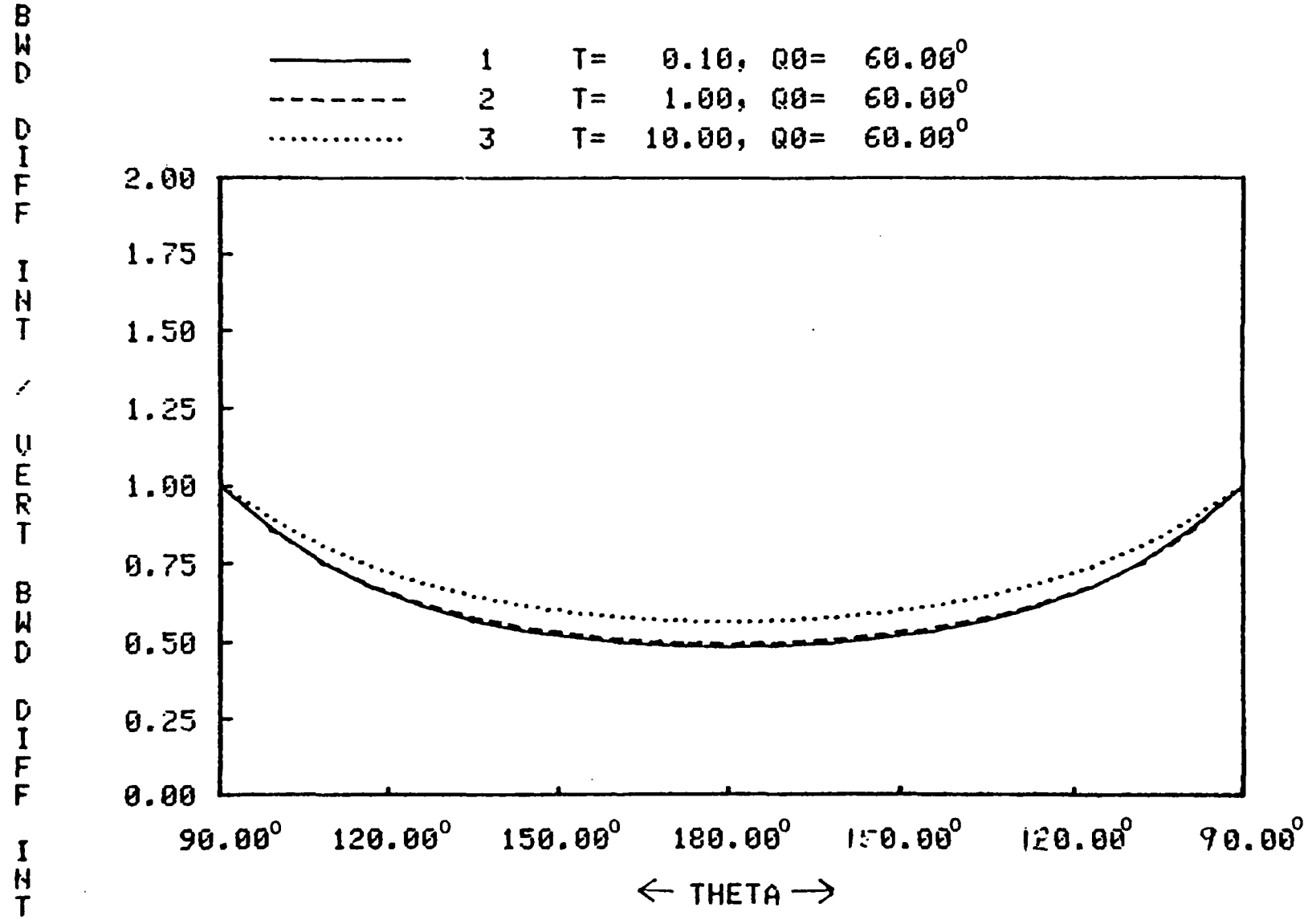

Figure 8.i RELATIVE BWD DIFF INTENSITY VS. SCATTER ANGLE FOR 1/2 SPACE, W=0.75

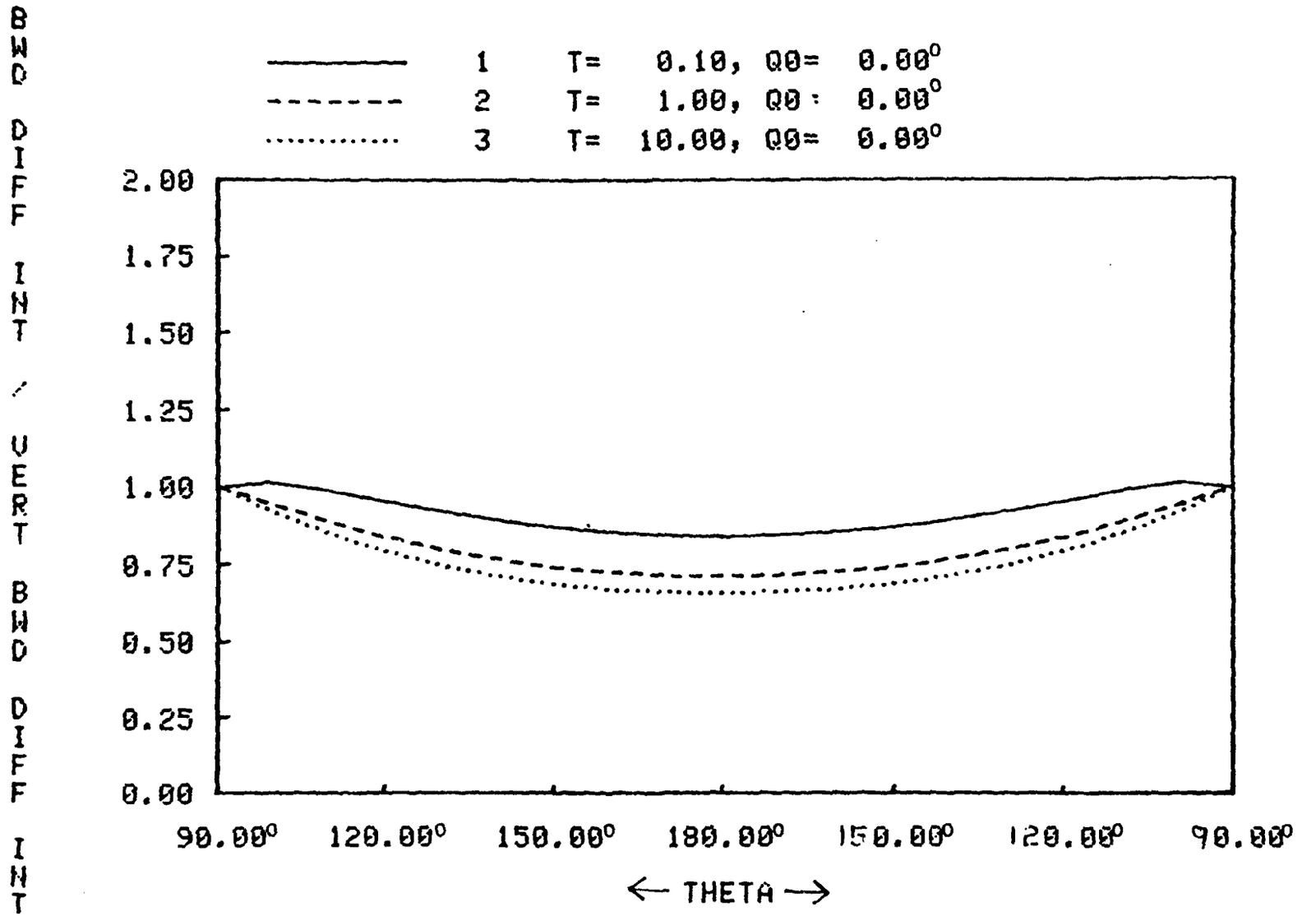

Figure 8.j. RELATIVE BWD DIFF INTENSITY VS. SCATTER ANGLE FOR 1/2 SPACE, N=0.90

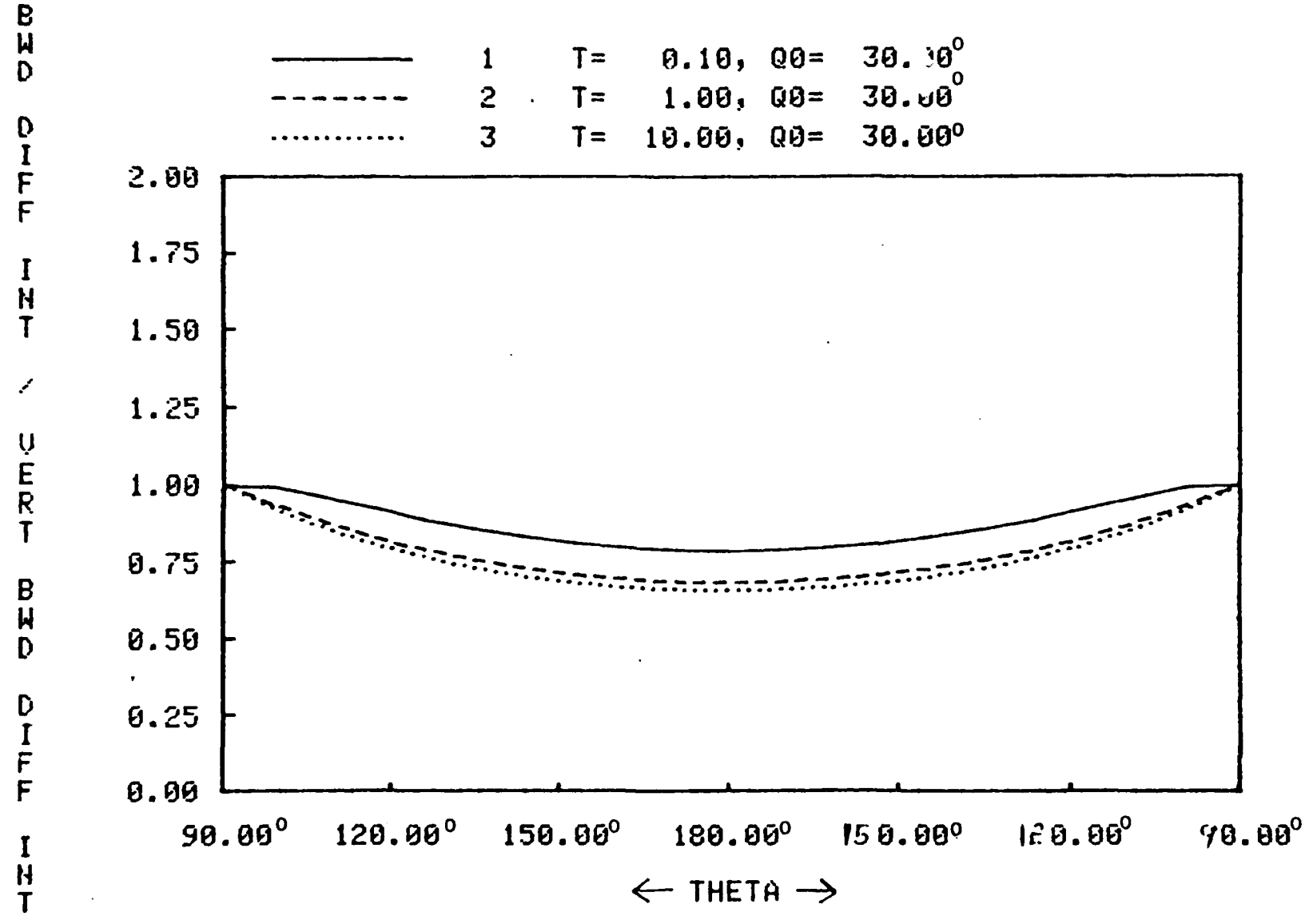

Figure 8.k. RELATIVE BWD DIFF INTENSITY VS. SCATTER ANGLE FOR 1/2 SPACE, W=0.90

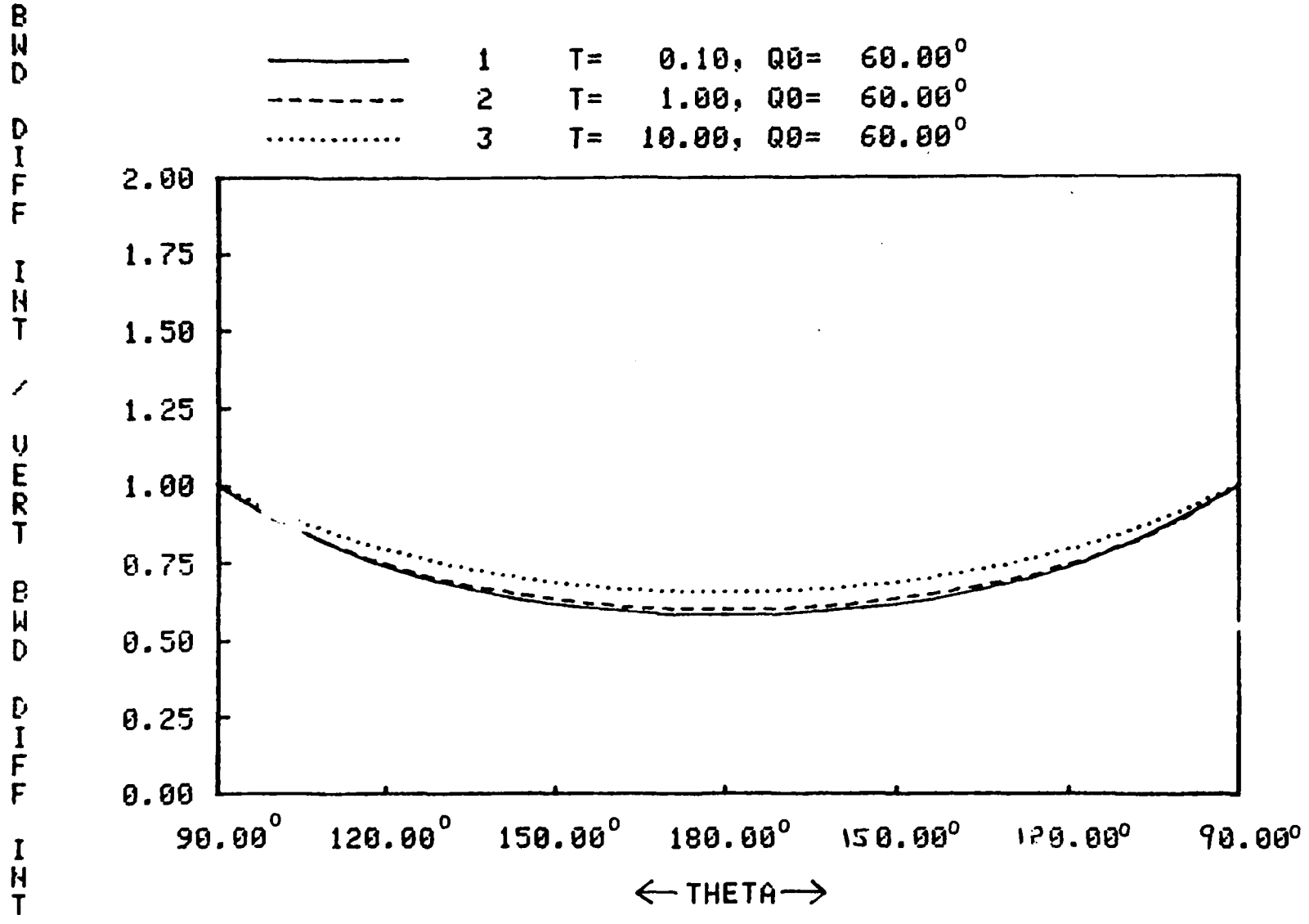

Figure 8.1 RELATIVE BWD DIFF INTENSITY VS. SCATTER ANGLE FOR 1/2 SPACE, W=0.90

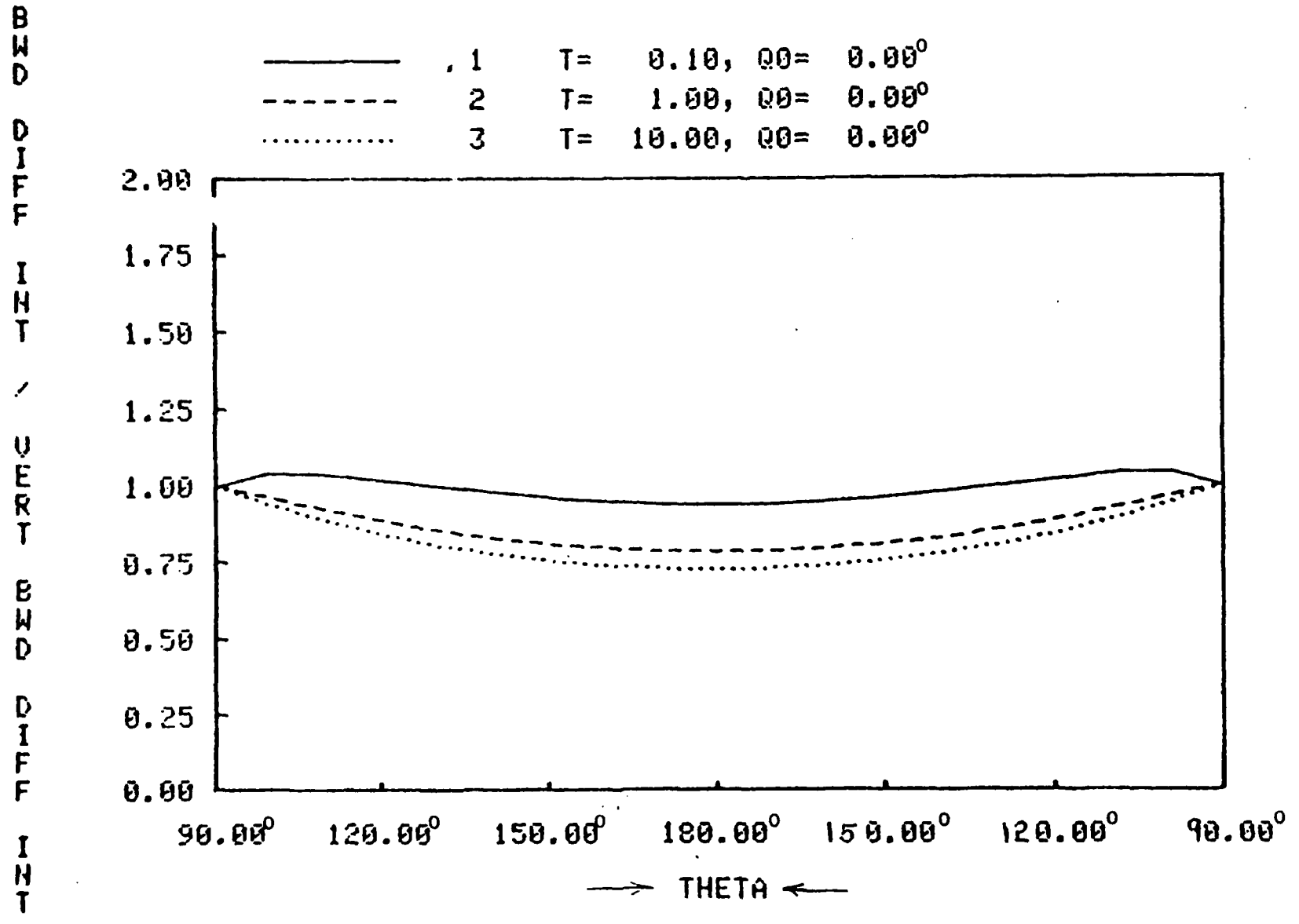

Figure 8.m RELATIVE BWD DIFF INTENSITY VS. SCATTER ANGLE FOR 1/2 SPACE, W=0.95

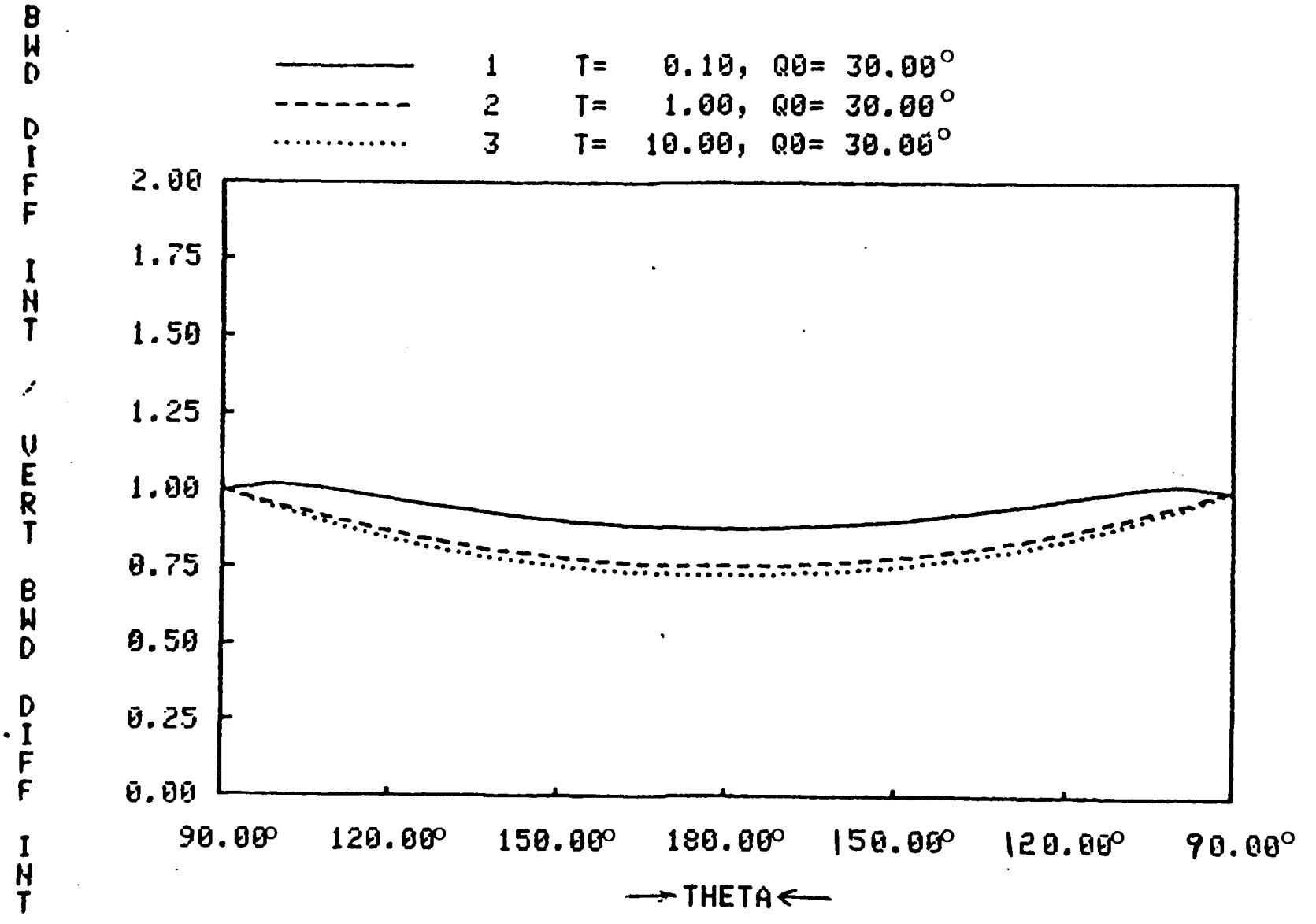

Figure 8.n. RELATIVE BWD DIFF INTENSITY VS. SCATTER ANGLE FOR 1/2 SPACE, N=0.95

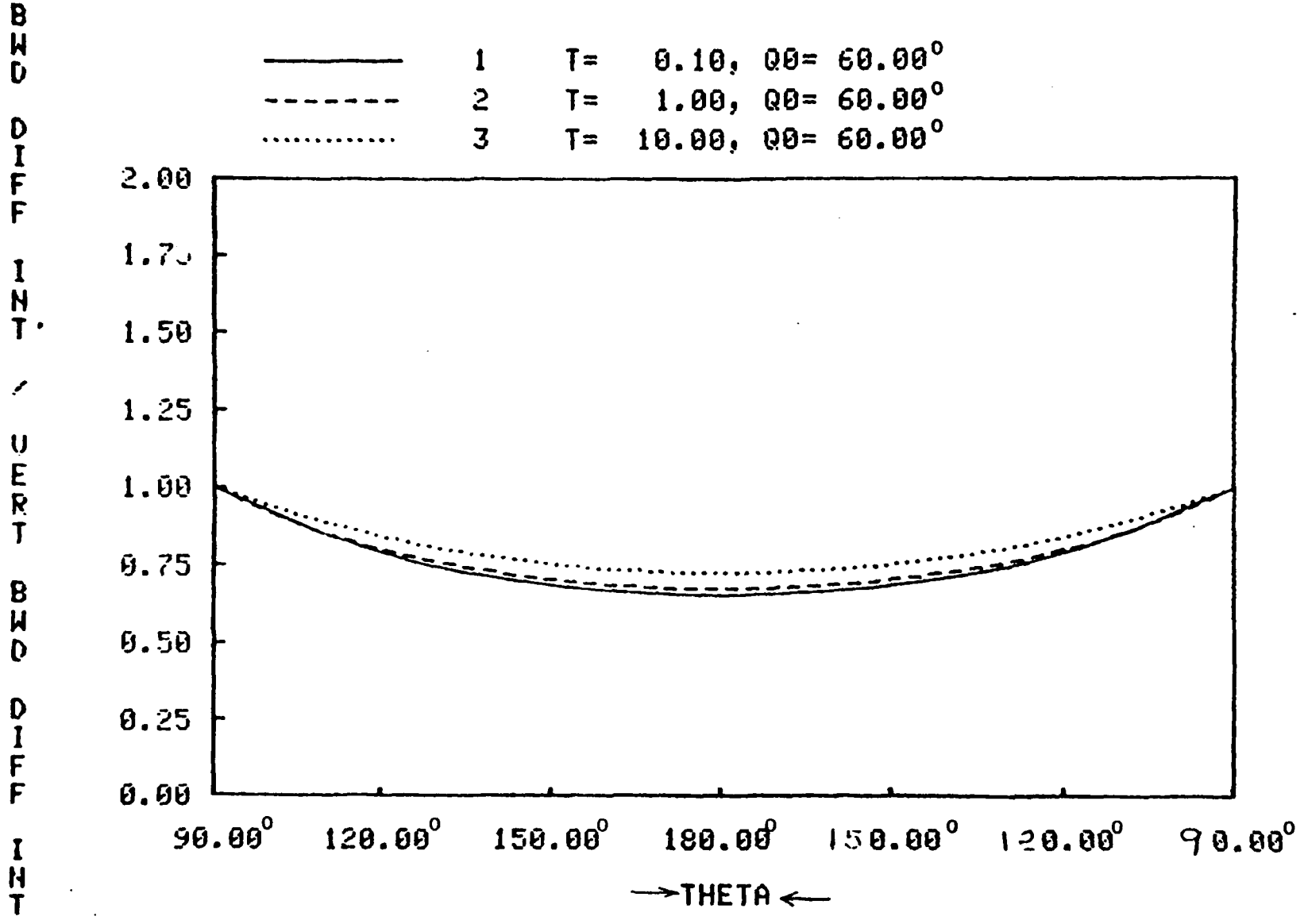

Figure 8.o. RELATIVE BWD DIFF INTENSITY VS. SCATTER ANGLE FOR 1/2 SPACE, W=0.95

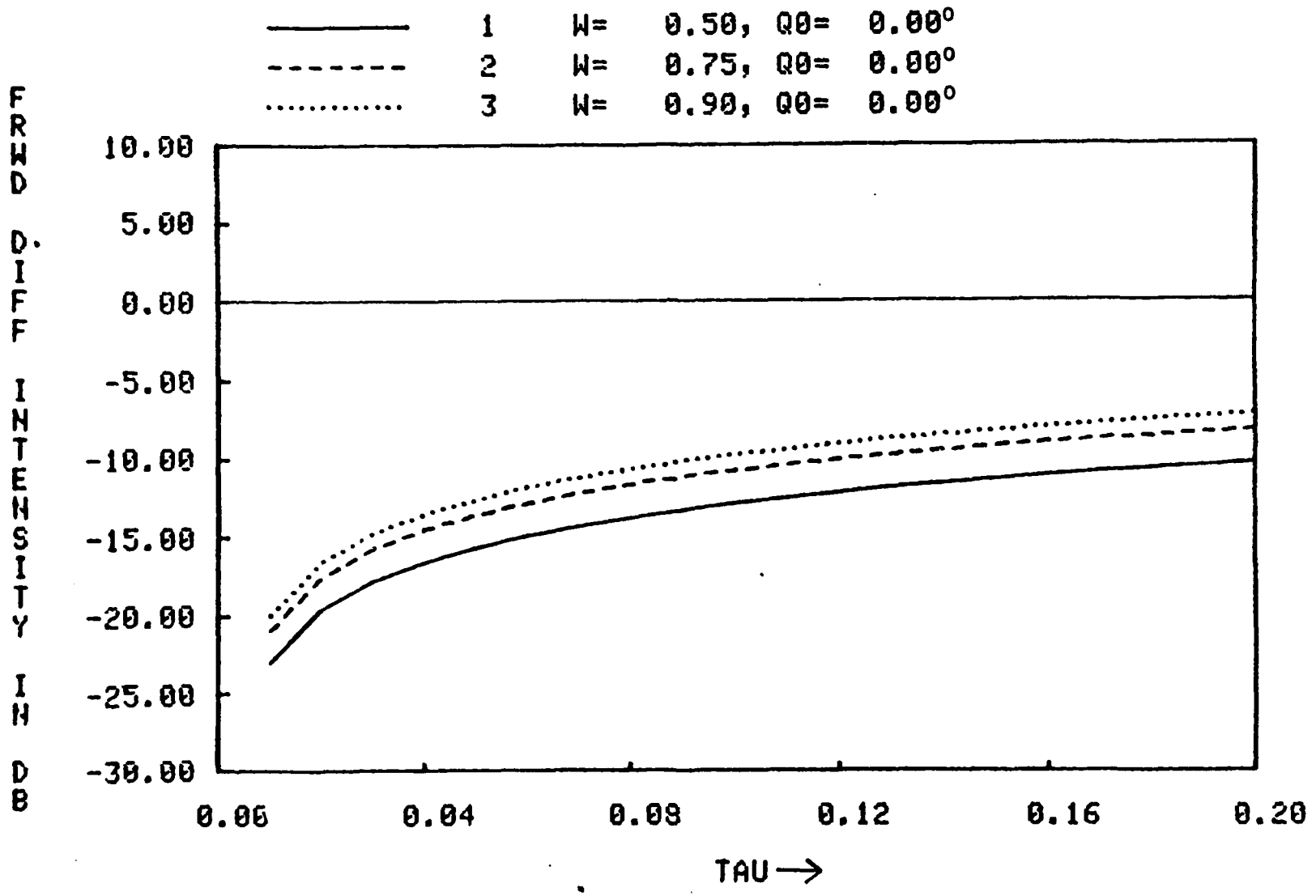

Figure 9.a. FORWARD DIFFUSE INTENSITY VS. DISTANCE FOR SLAB, $Q=0^{0}, \tau_{0}=0.2$

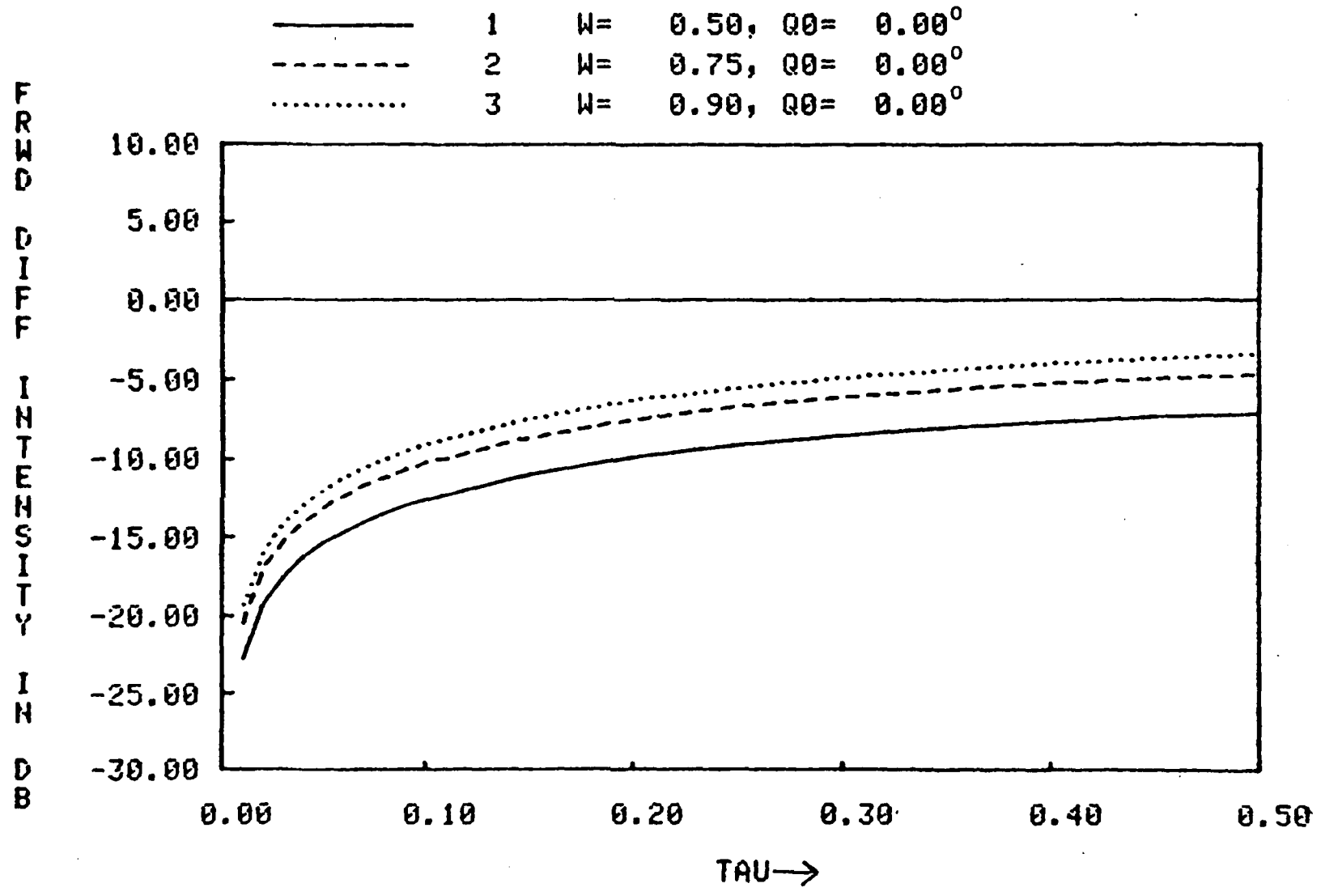

Figure 9.b FORWARD DIFFUSE INTENSITY VS. DISTANCE FOR SLAB, $Q=0^{0}$, $\tau_0=0.5$

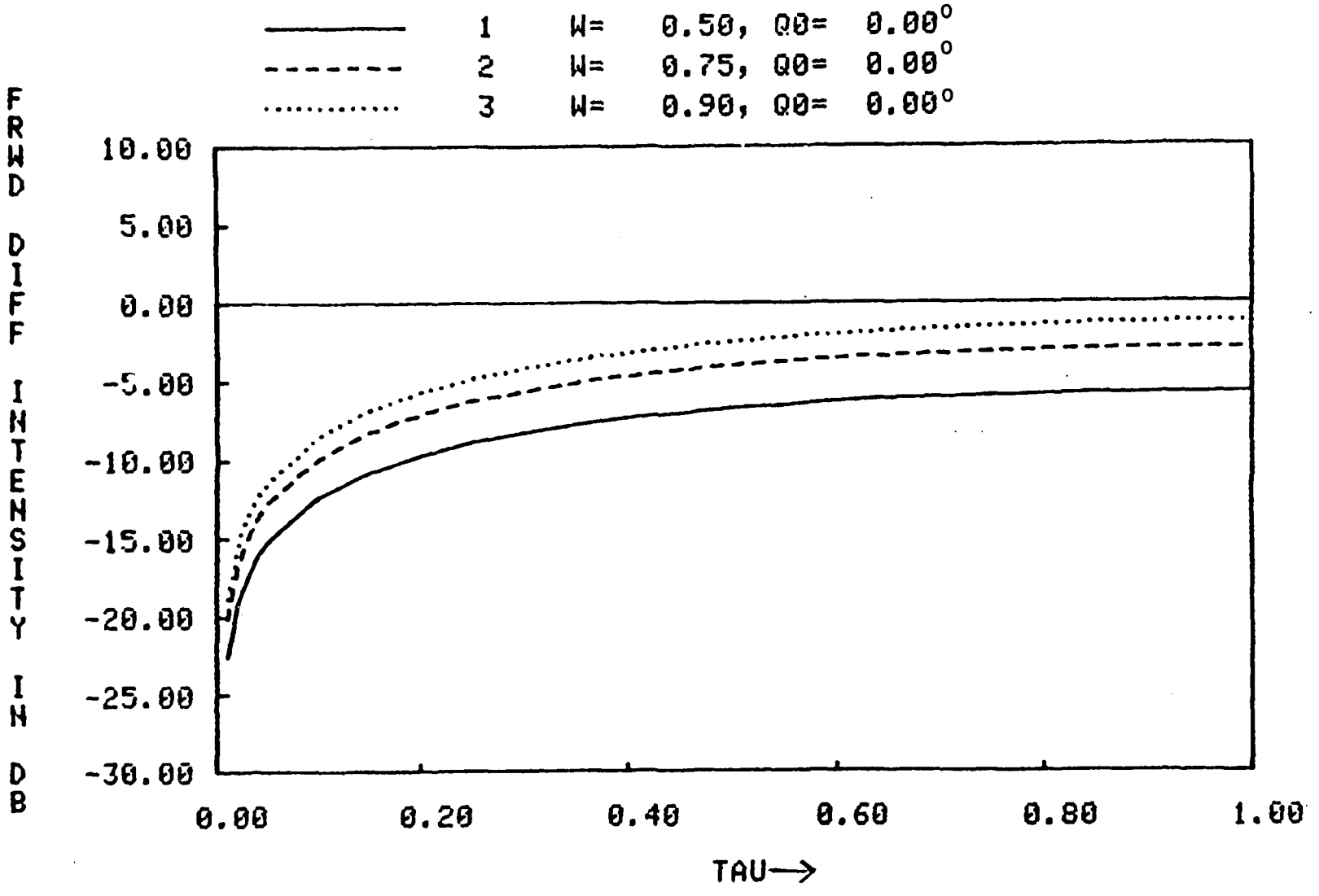

Figure 9.c. FORWARD DIFFUSE INTENSITY VS. DISTANCE FOR SLAB, $Q=0^{o}$, $\tau=1.0$

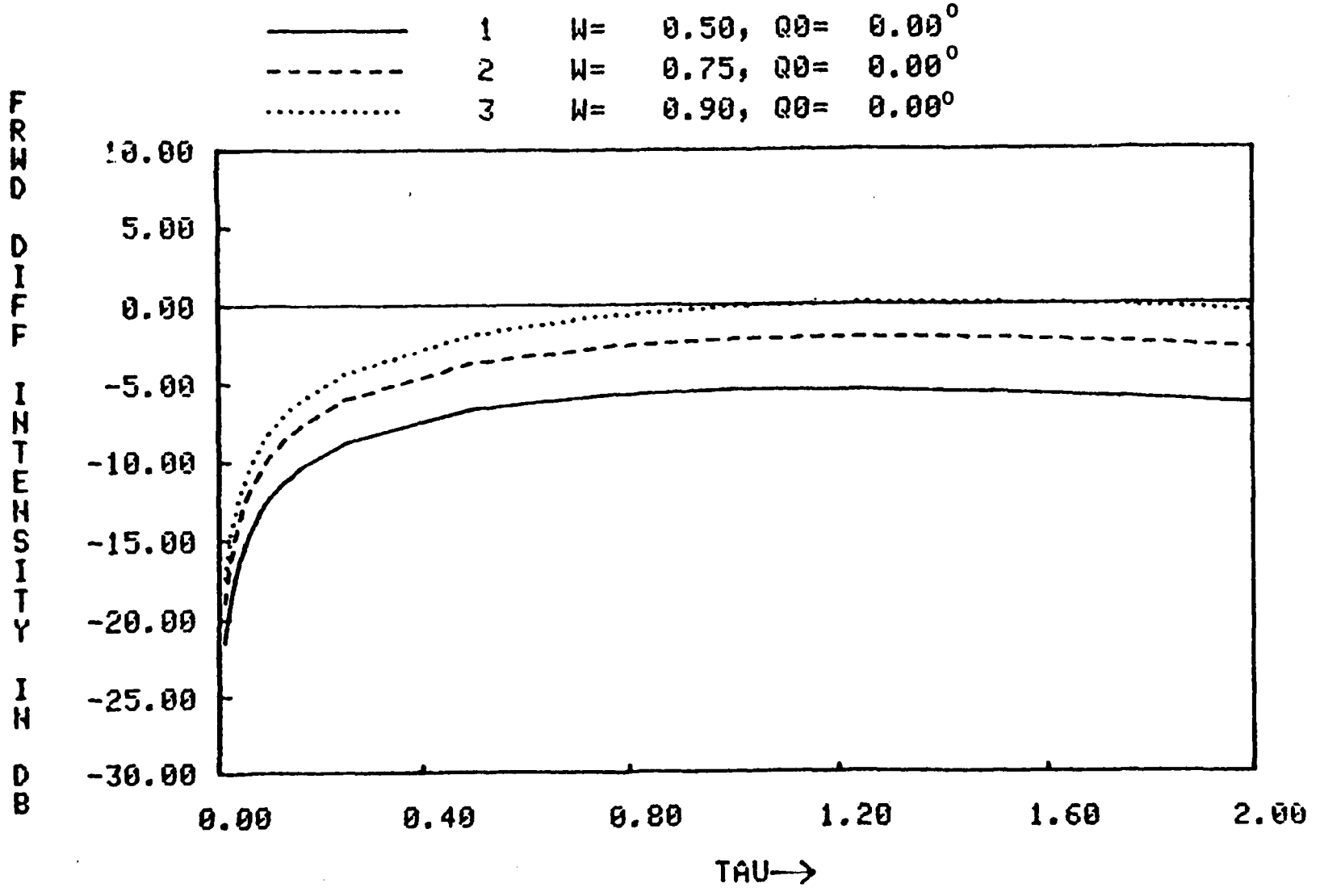

Figure 9.d FORWARD DIFFUSE INTENSITY VS. DISTANCE FOR SLAB, $\theta=0^{\circ}$, $\tau_o=2.0$

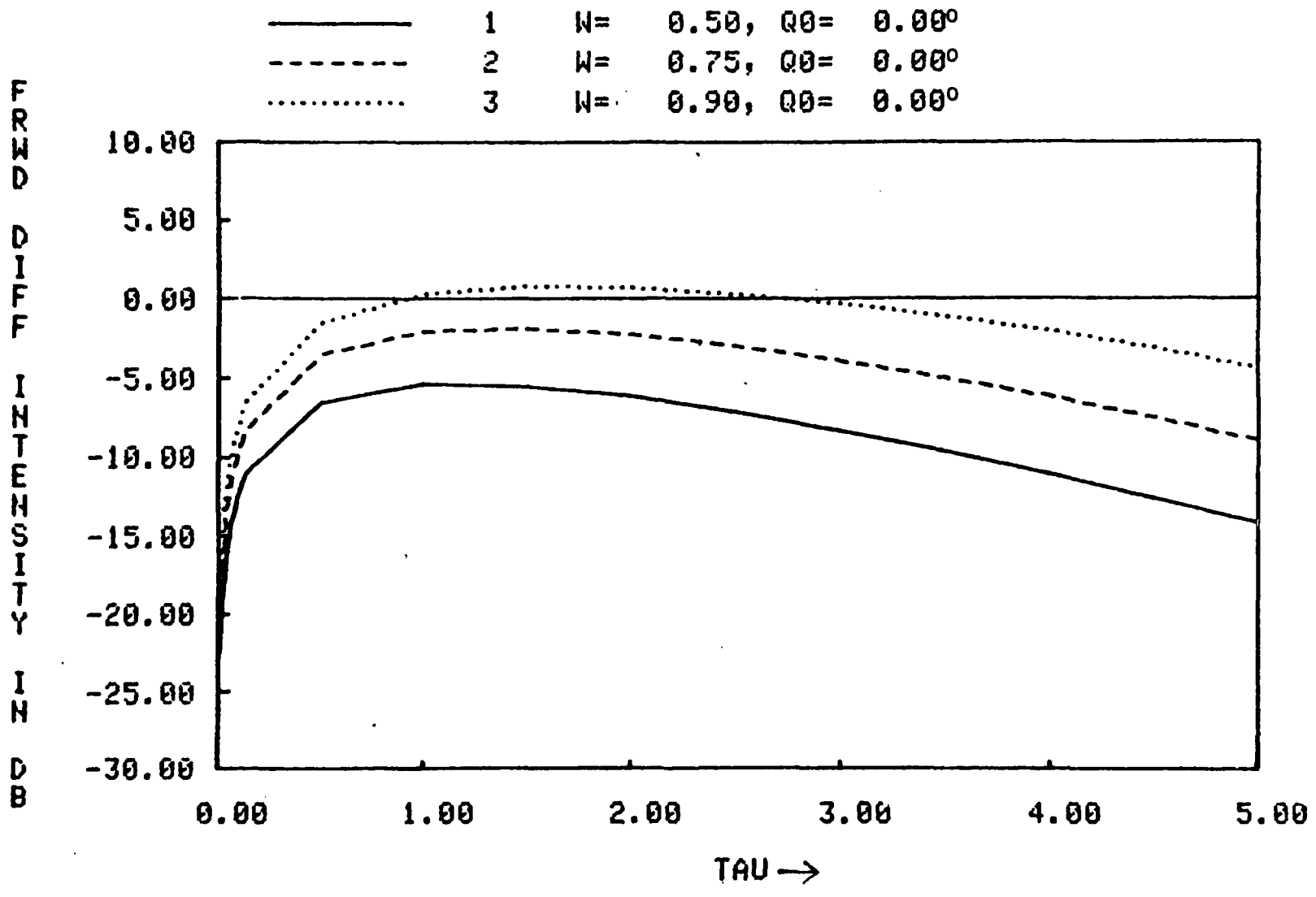

Figure 9.e FORWARD DIFFUSE INTENSITY VS. DISTANCE FOR SLAB, $Q=0^{o}, \tau_{o}=5.0$

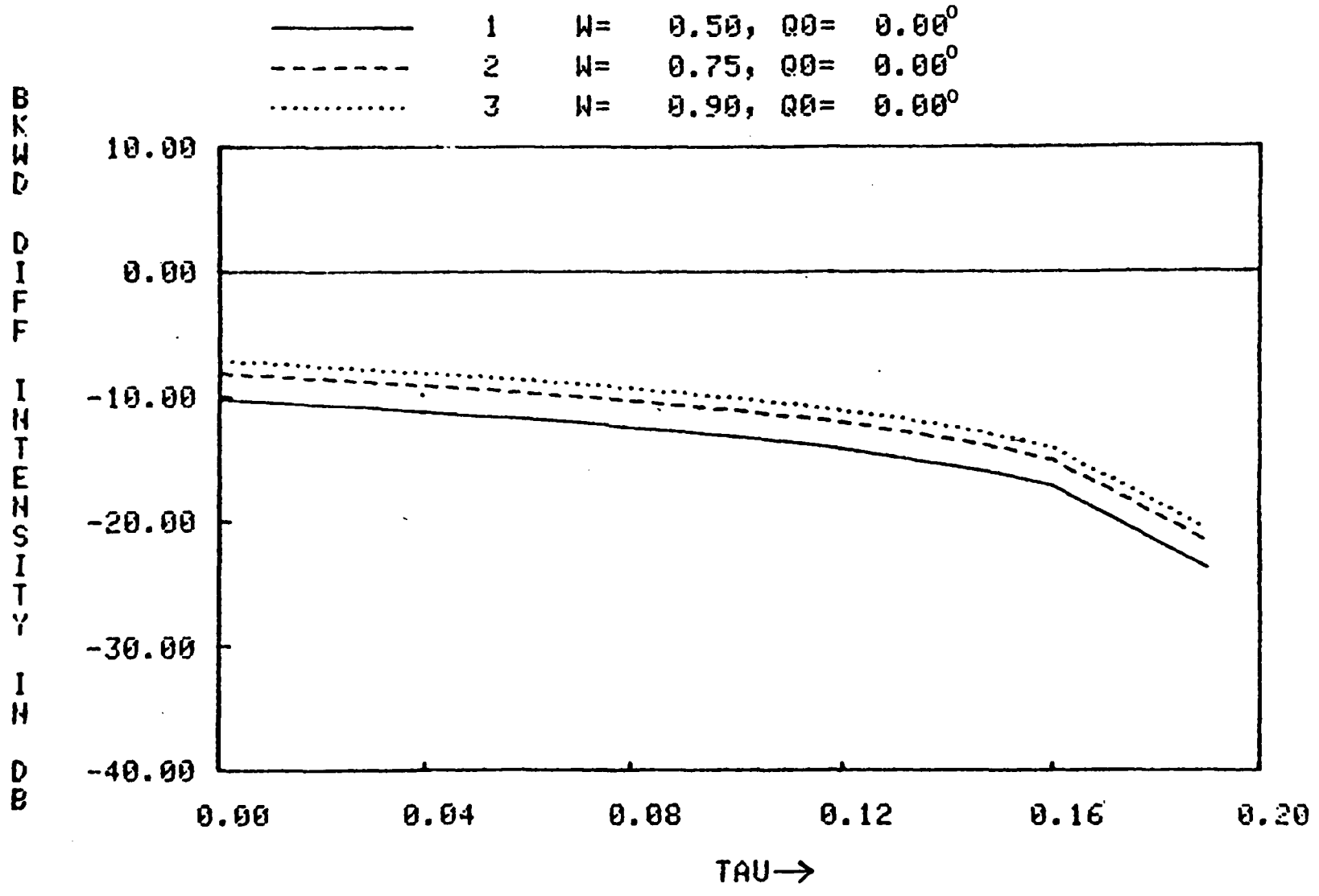

Figure 10.a BACKWARD DIFFUSE INTENSITY VS. DISTANCE FOR SLAB, $\Theta=180^{0}$, $\tau_{0}=0.2$.

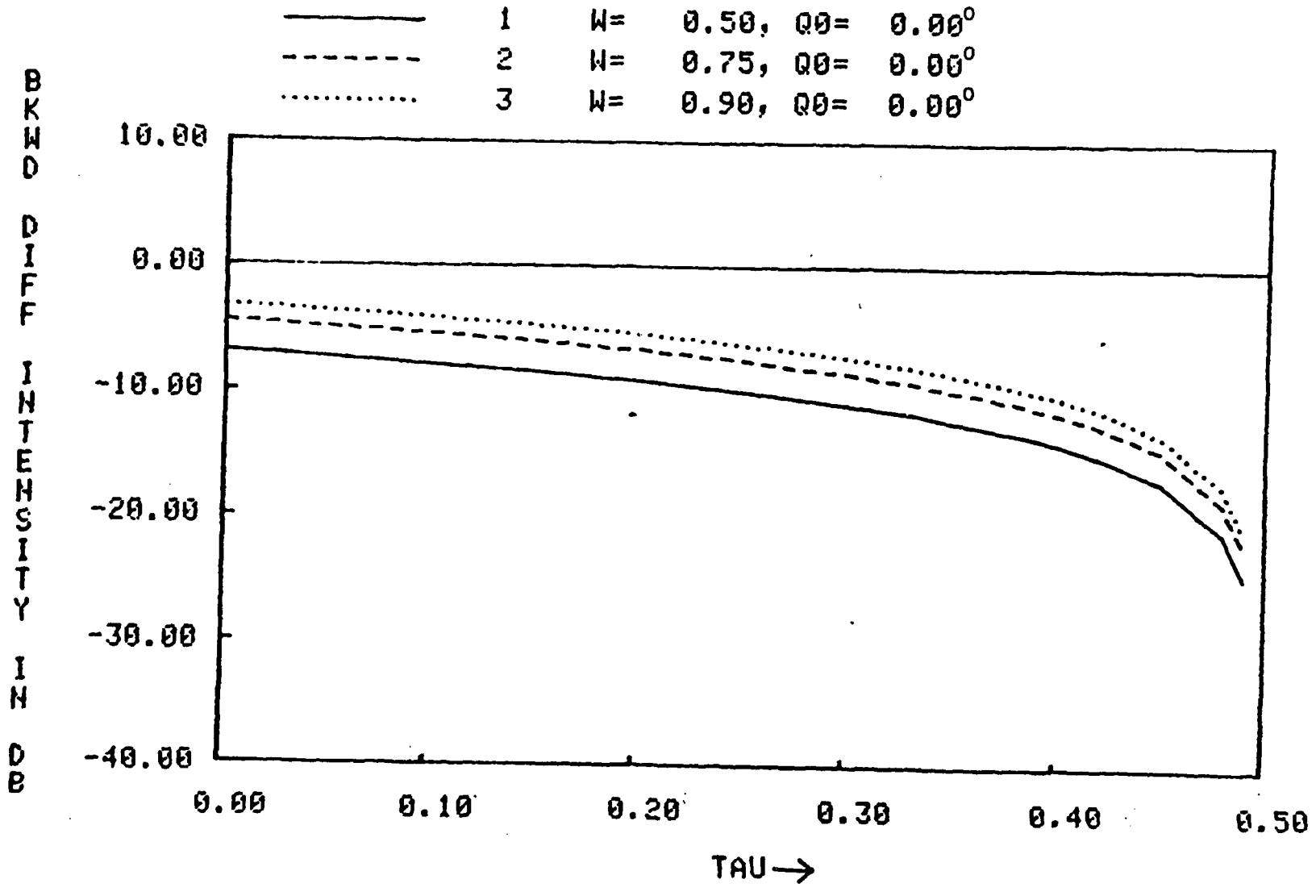

Figure 10.b. BACKWARD DIFFUSE INTENSITY VS. DISTANCE FOR SLAB, $Q=180^{0}, \tau_{0}=0.5$

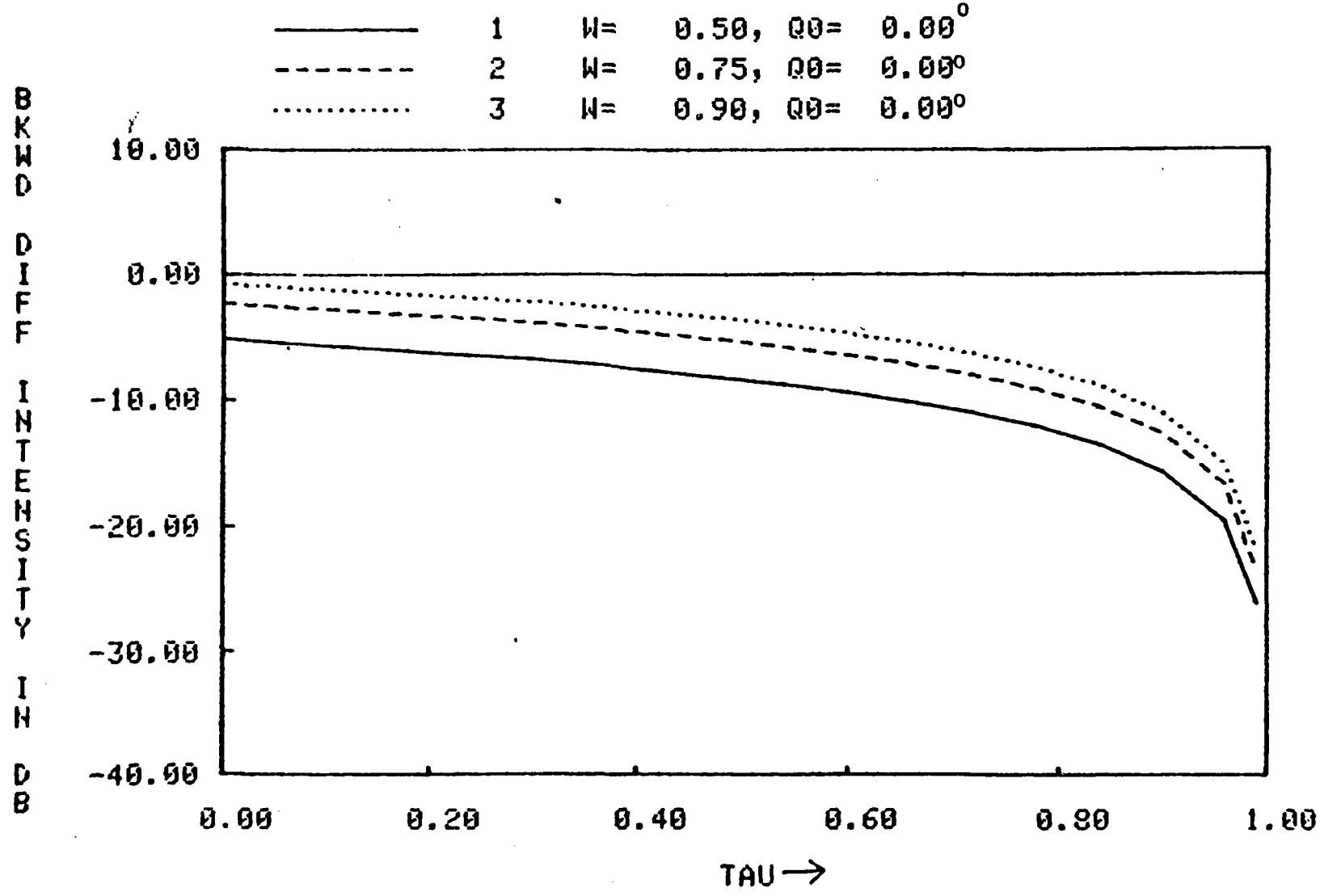

Figure 10.c. BACKWARD DIFFUSE INTENSITY VS. DISTANCE FOR SLAB, $\theta=180^{\circ}$, $\tau_0=1.0$

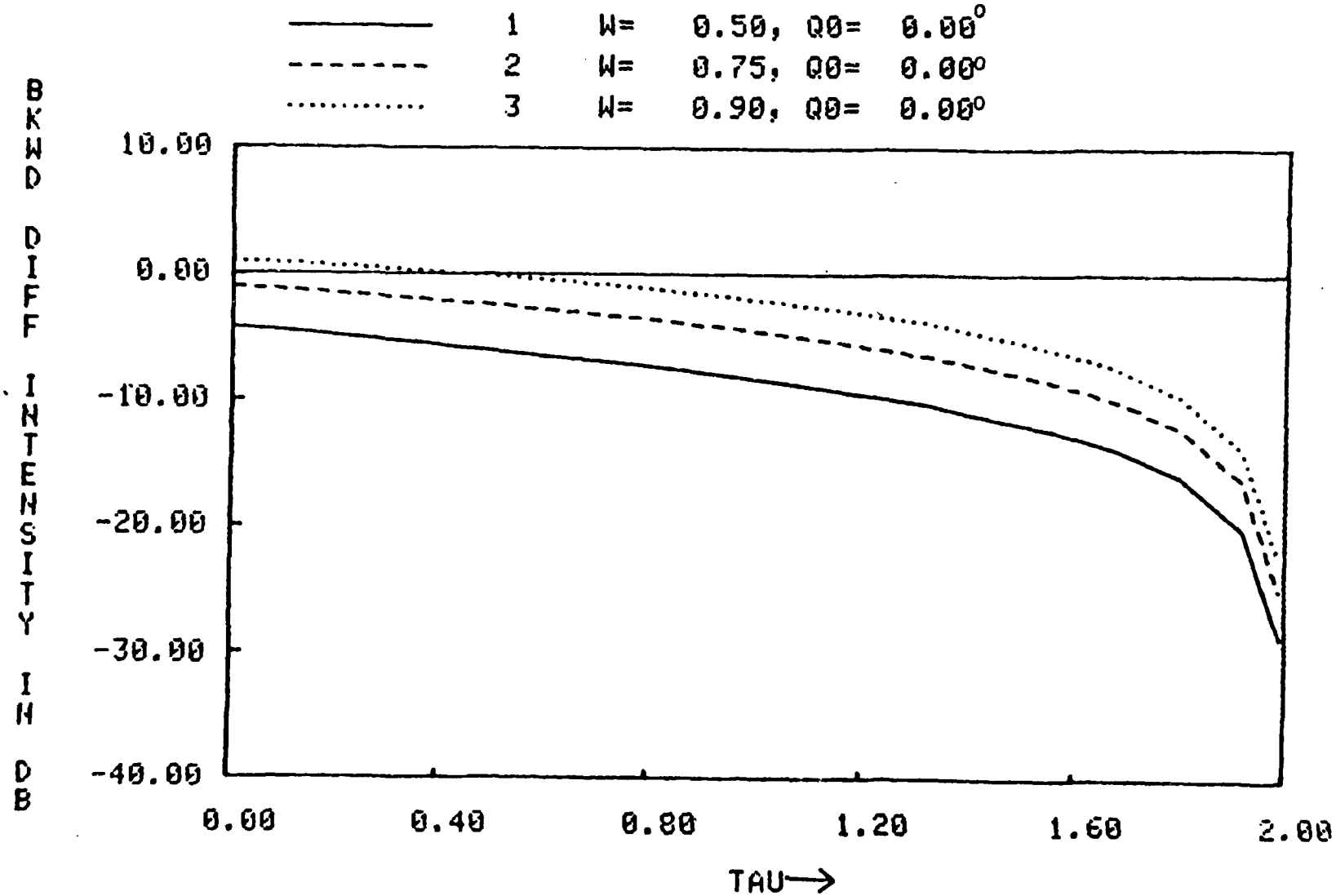

Figure 10.d BACKWARD DIFFUSE INTENSITY VS. DISTANCE FOR SLAB, $Q=180^{0}, \tau_{0}=2.0$

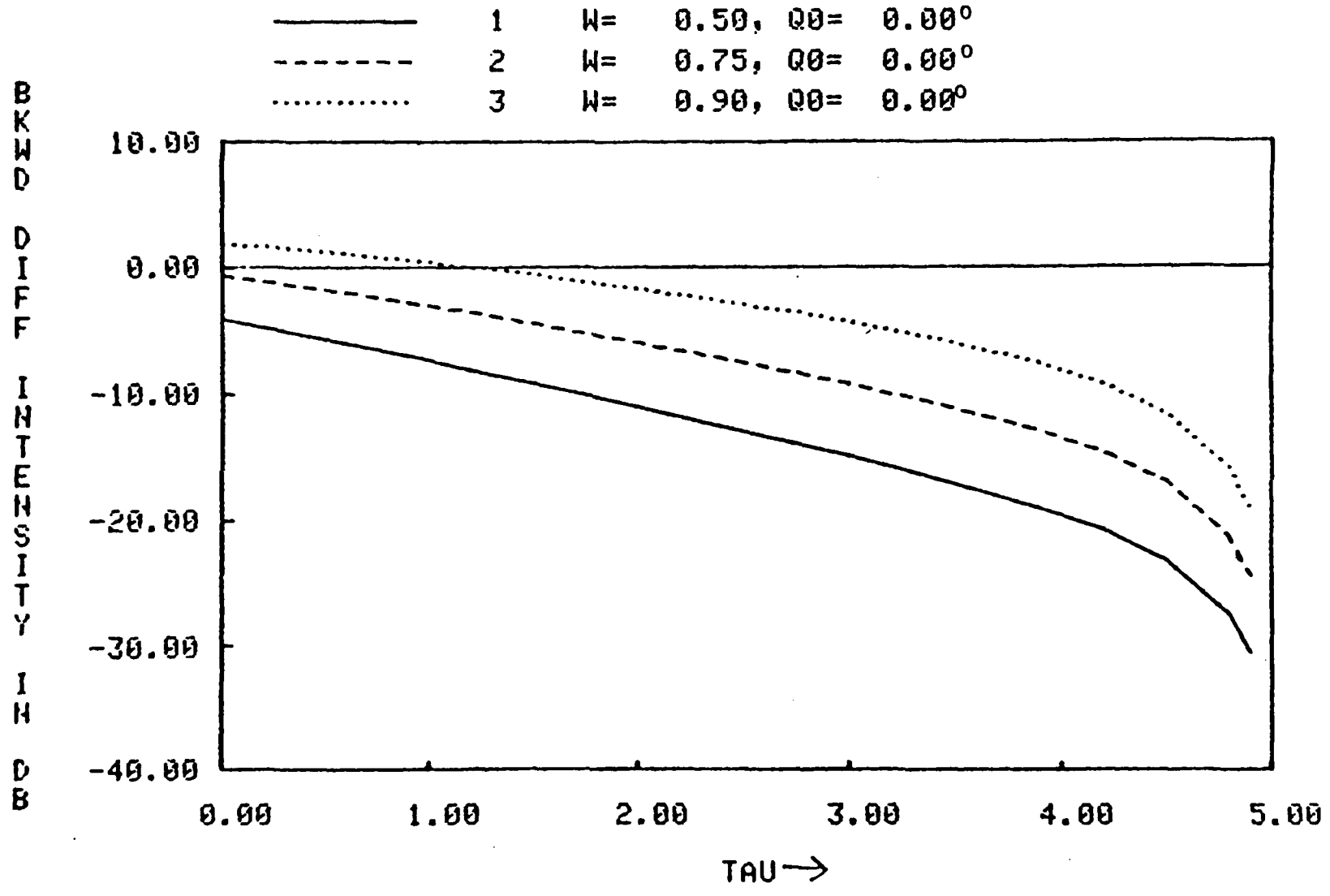

Figure 10.e. BACKWARD DIFFUSE INTENSITY VS. DISTANCE FOR SLAB, $Q=180^{0}, \tau_{0}=5.0$

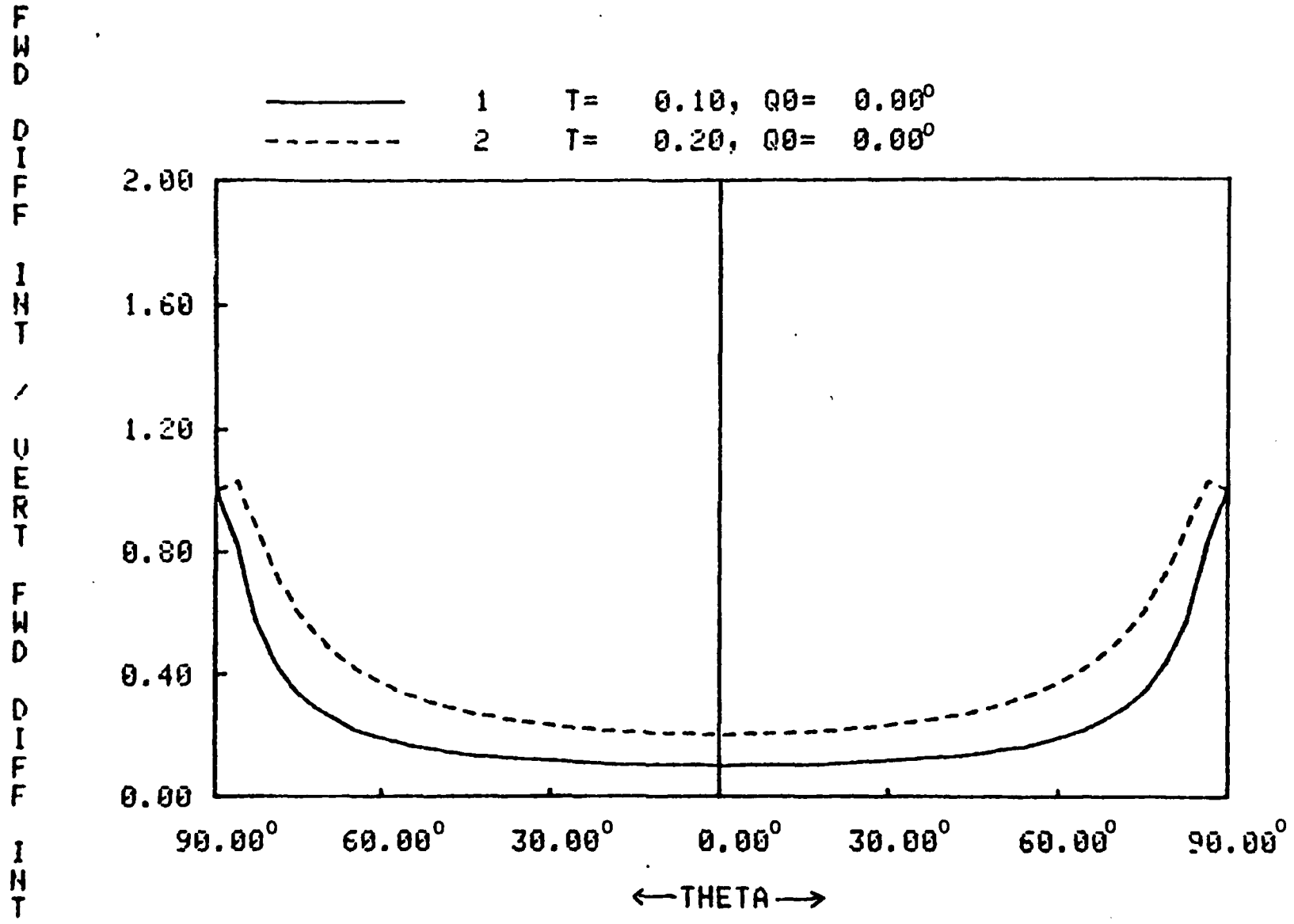

Figure 11.a. RELATIVE FWD DIFF INTENSITY VS. SCATTER ANGLE FOR SLAB, W=0.50 , τ_0=0.2

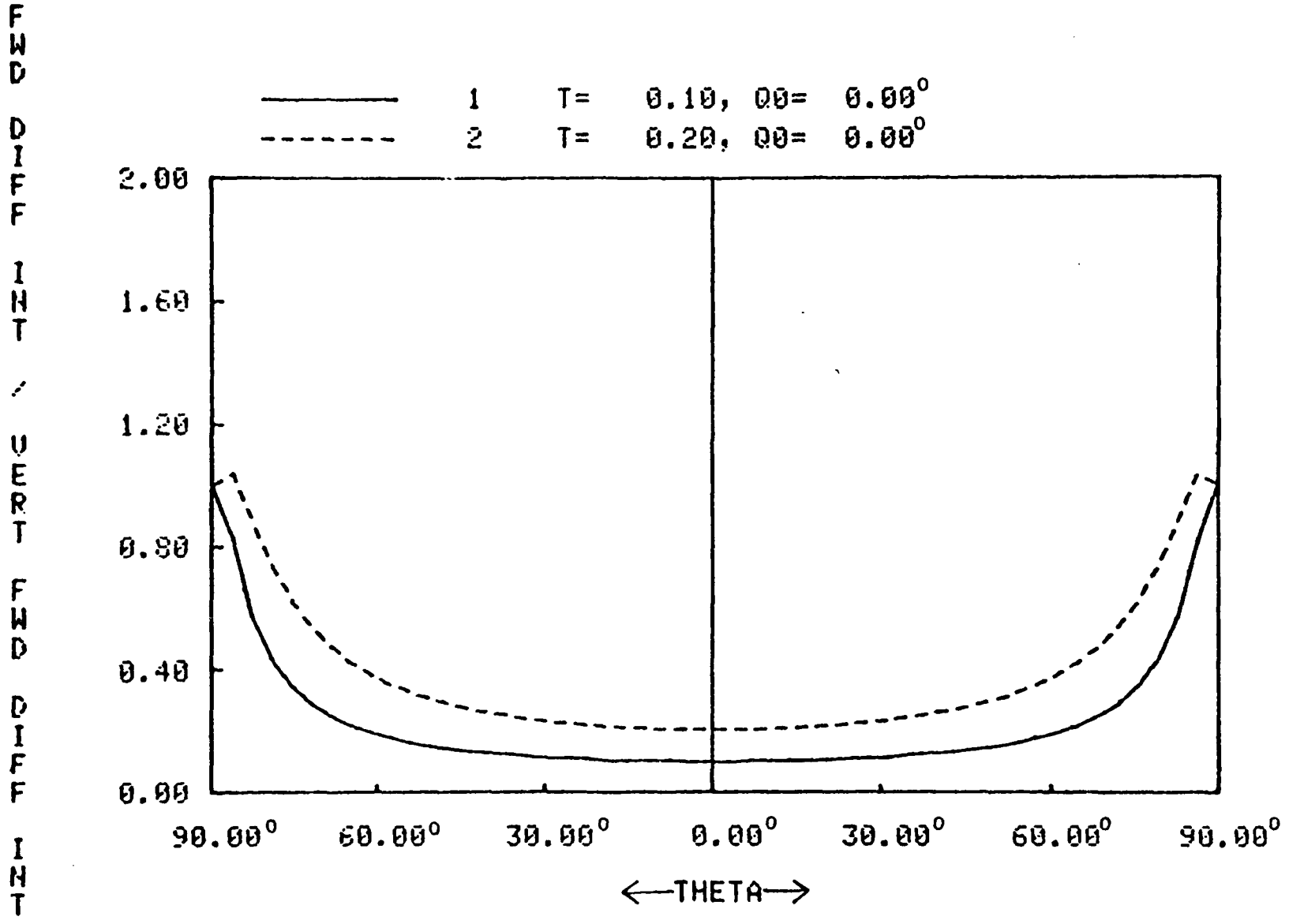

Figure 11.b. RELATIVE FWD DIFF INTENSITY VS. SCATTER ANGLE FOR SLAB, W=0.75, τ_0=0.2

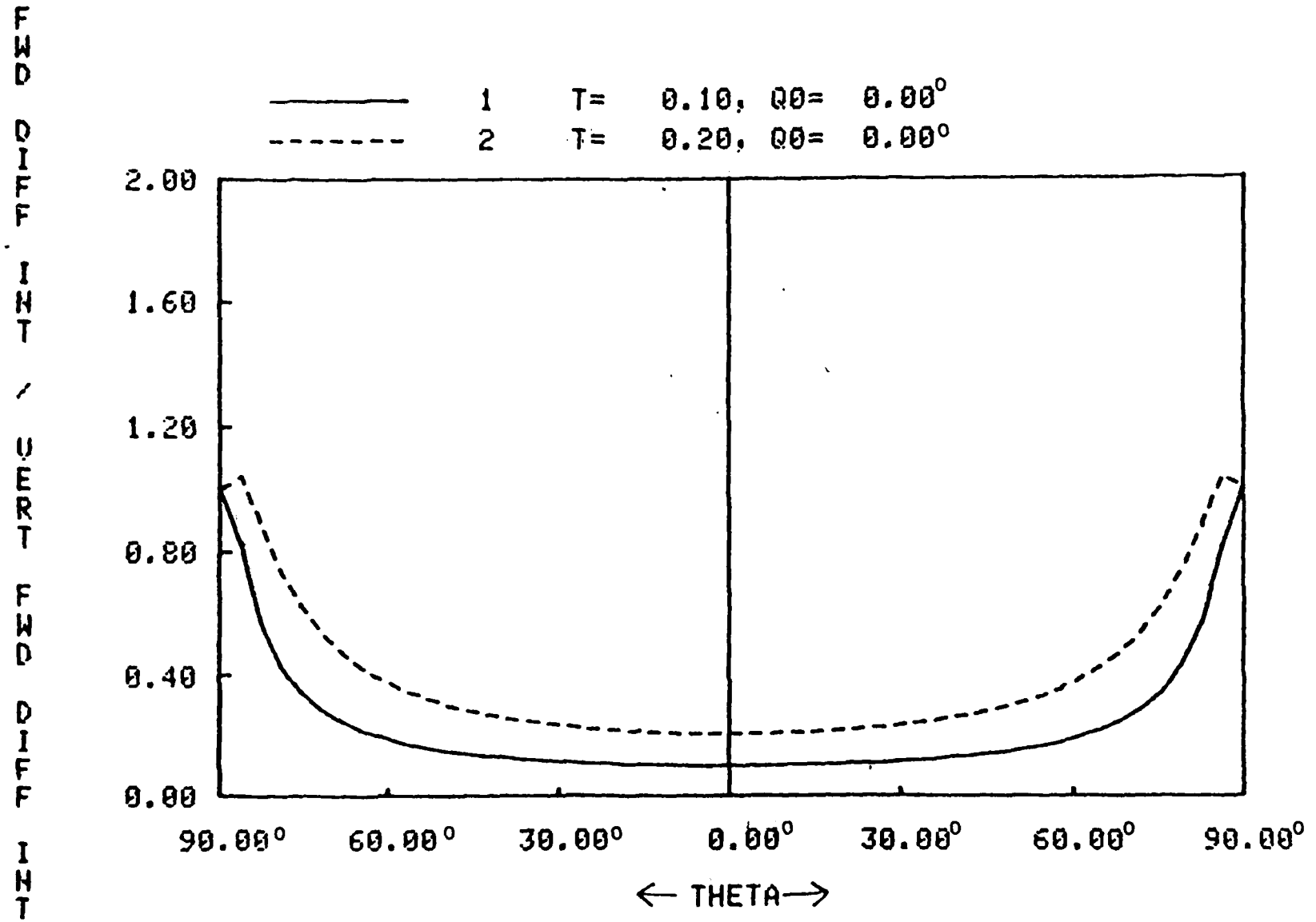

Figure 11.c. RELATIVE FWD DIFF INTENSITY VS. SCATTER ANGLE FOR SLAB, W=0.90 , τ_0=0.2

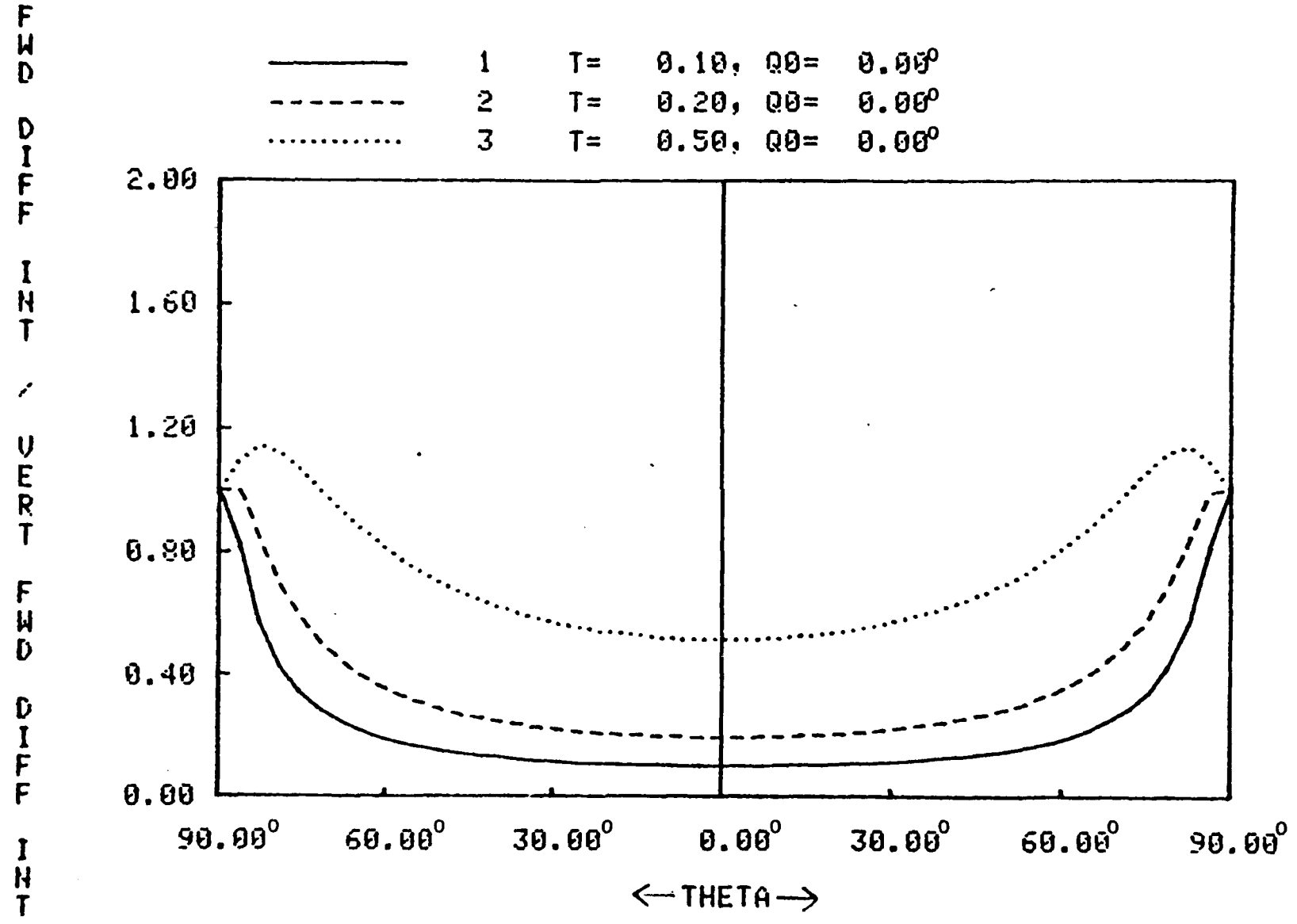

Figure 11.d. RELATIVE FWD DIFF INTENSITY VS. SCATTER ANGLE FOR SLAB, W=0.50, τ_0=0.5

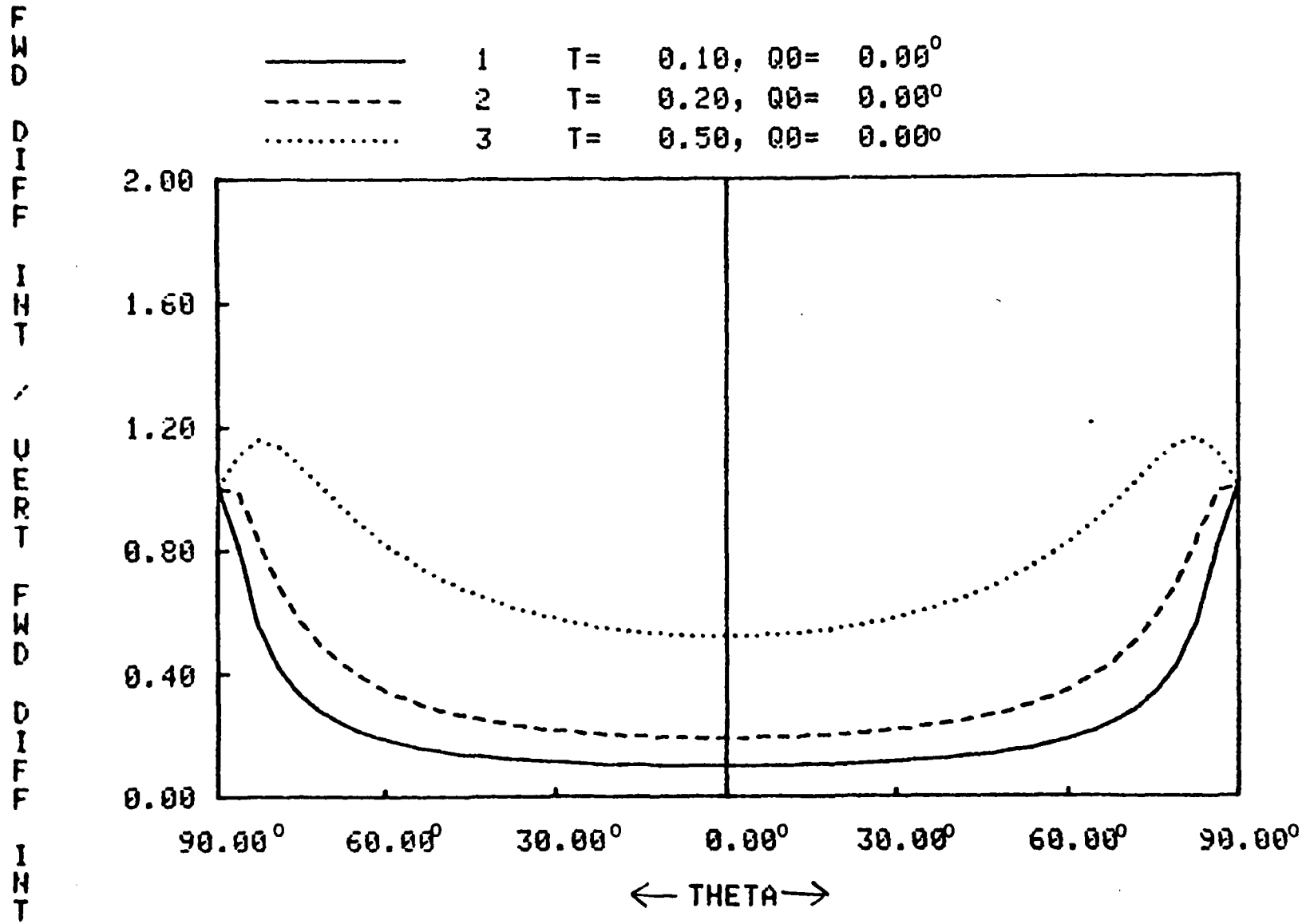

Figure 11.e RELATIVE FWD DIFF INTENSITY VS. SCATTER ANGLE FOR SLAB, W=0.75 , τ_0=0.5

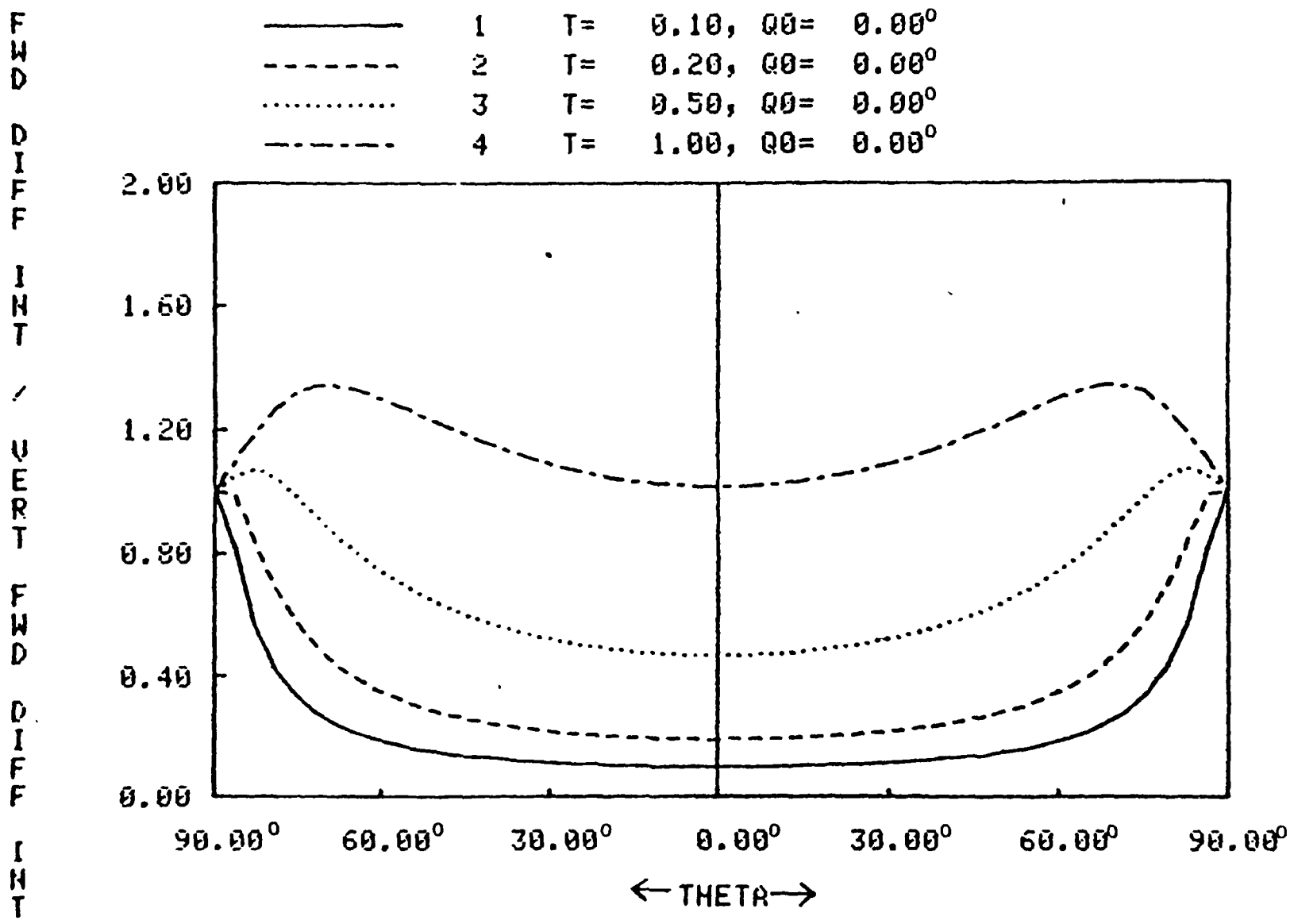

Figure 11.f RELATIVE FWD DIFF INTENSITY VS. SCATTER ANGLE FOR SLAB, W=0.50, τ_0=1.0

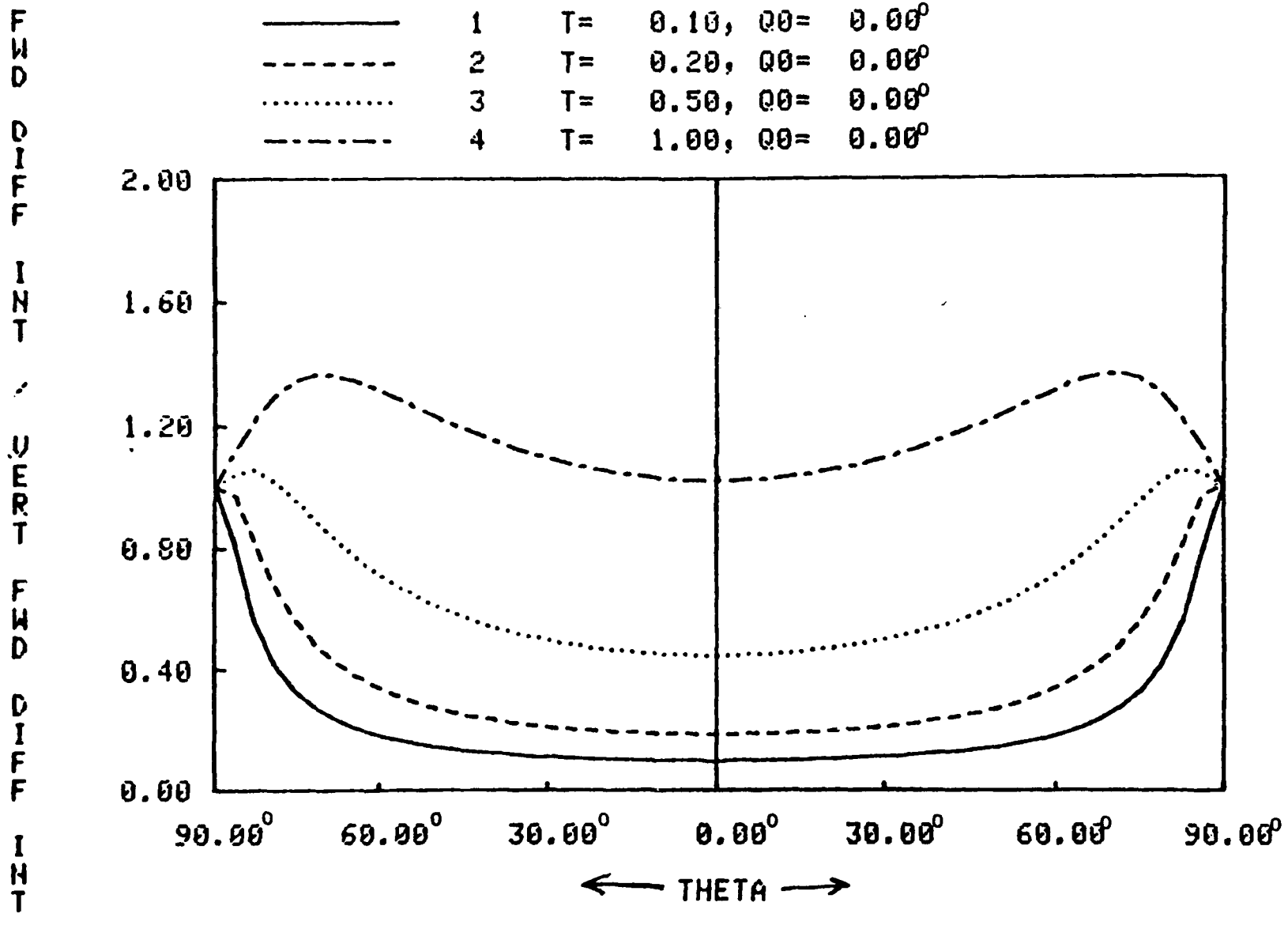

Figure 11.g. RELATIVE FWD DIFF INTENSITY VS. SCATTER ANGLE FOR SLAB, W=0.75, τ_0=1.0

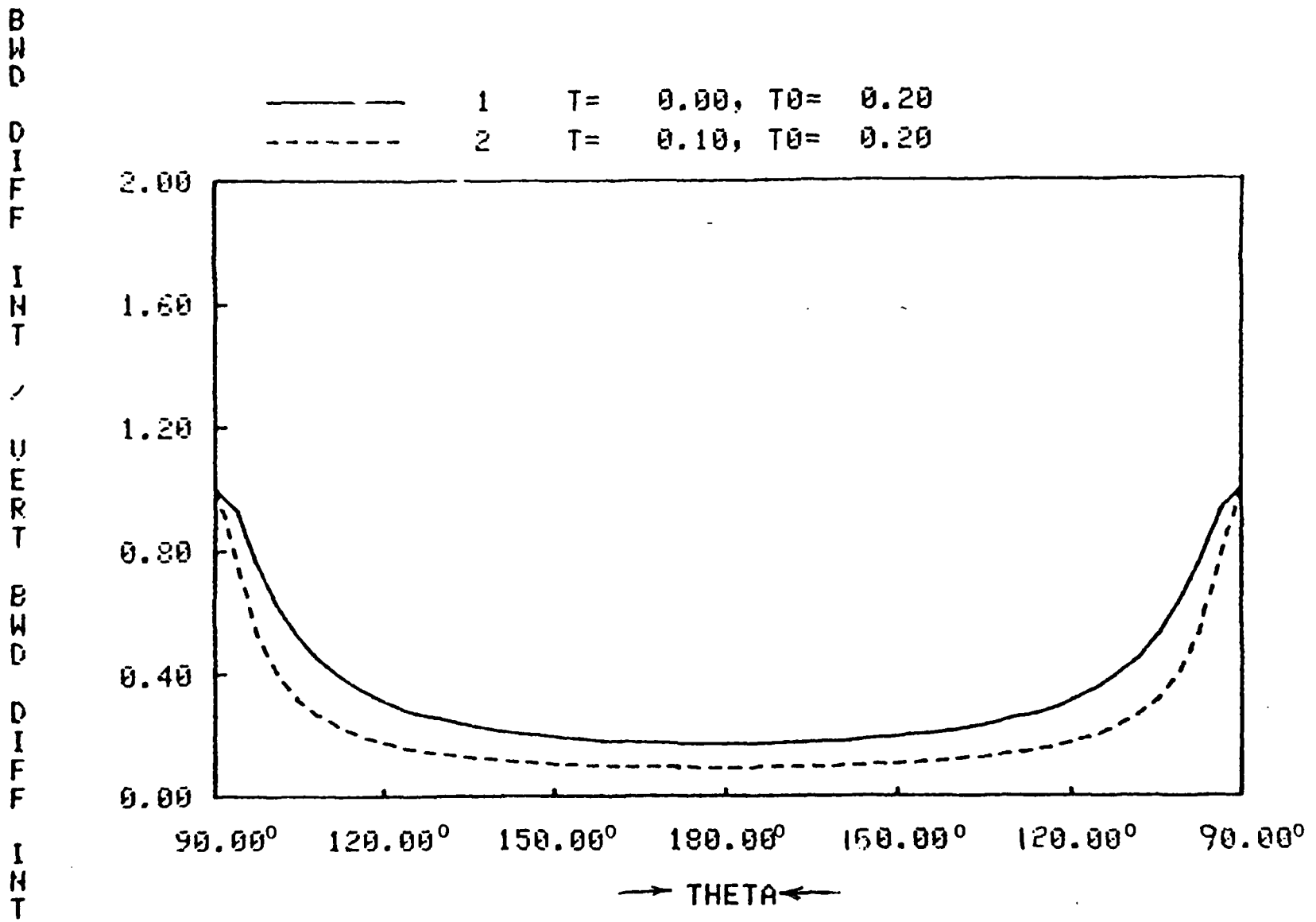

Figure 12.a RELATIVE BWD DIFF INTENSITY VS. SCATTER ANGLE FOR SLAB, Q0=0°, W=0.50

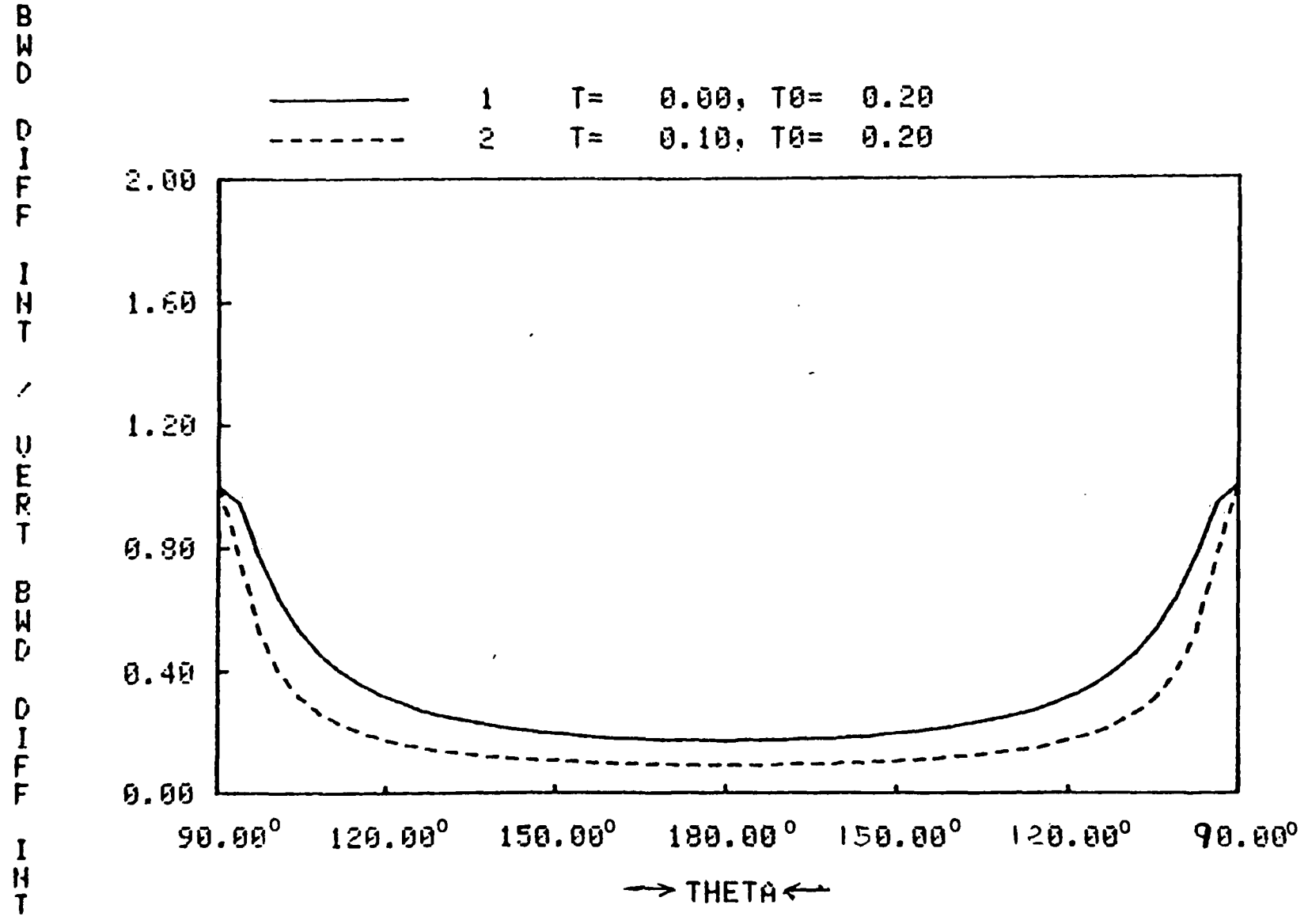

Figure 12.b. RELATIVE BWD DIFF INTENSITY VS. SCATTER ANGLE FOR SLAB, $\theta_0 = 0^\circ$, W=0.75

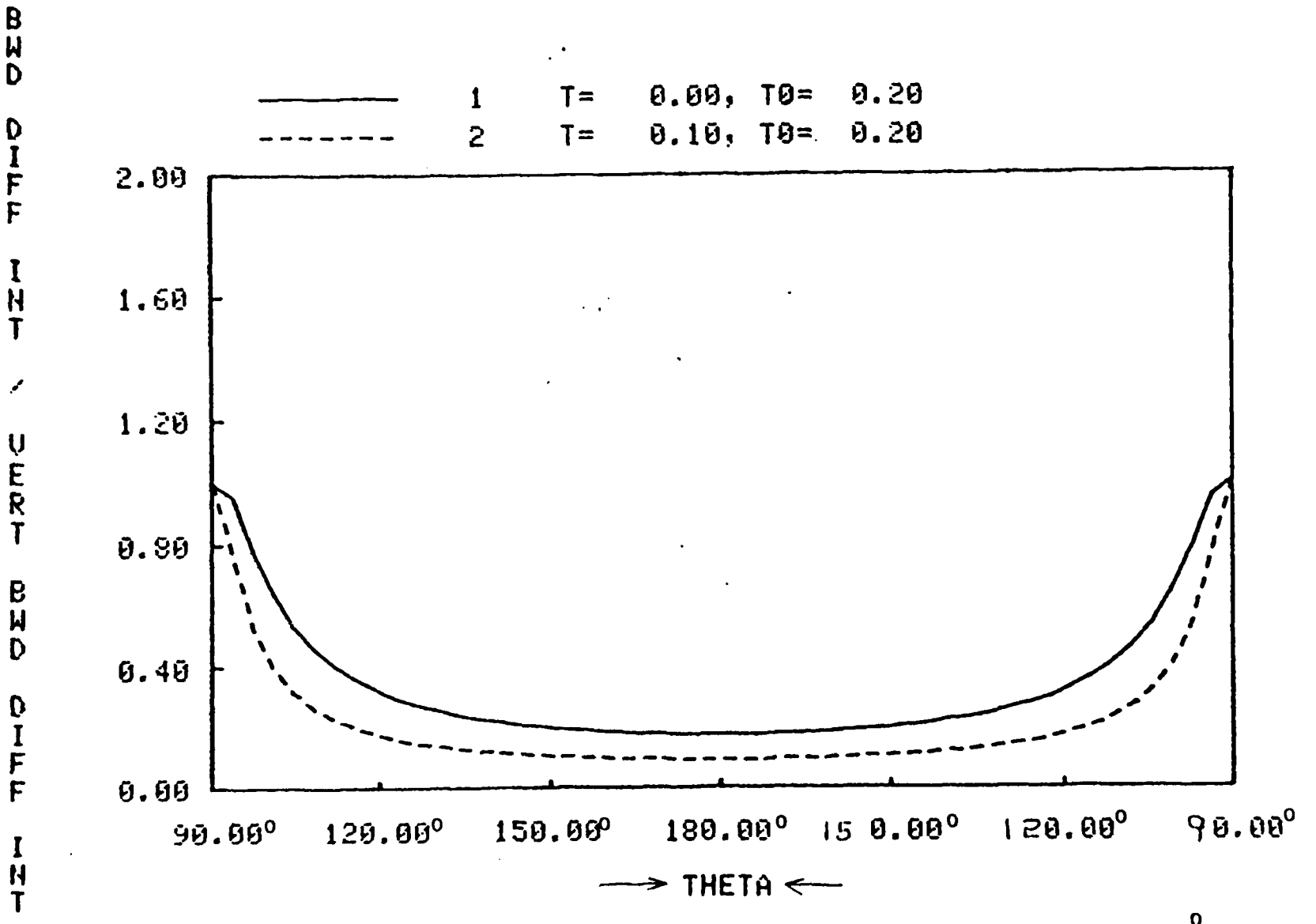

Figure 12.c. RELATIVE BWD DIFF INTENSITY VS. SCATTER ANGLE FOR SLAB, $Q0=0^{\circ}$, W=0.90

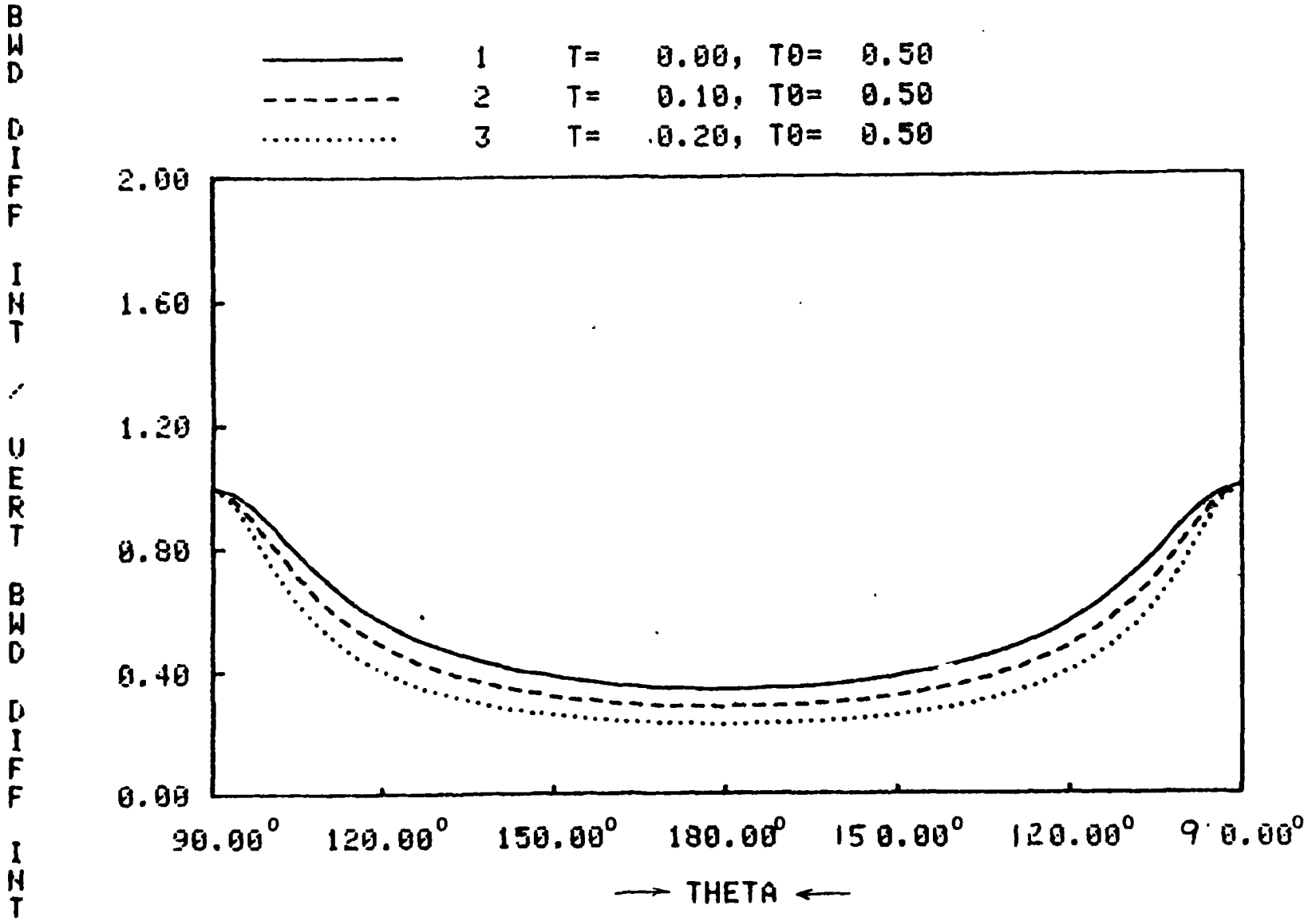

Figure 12.d. RELATIVE BWD DIFF INTENSITY VS. SCATTER ANGLE FOR SLAB, Q0=0°, W=0.50

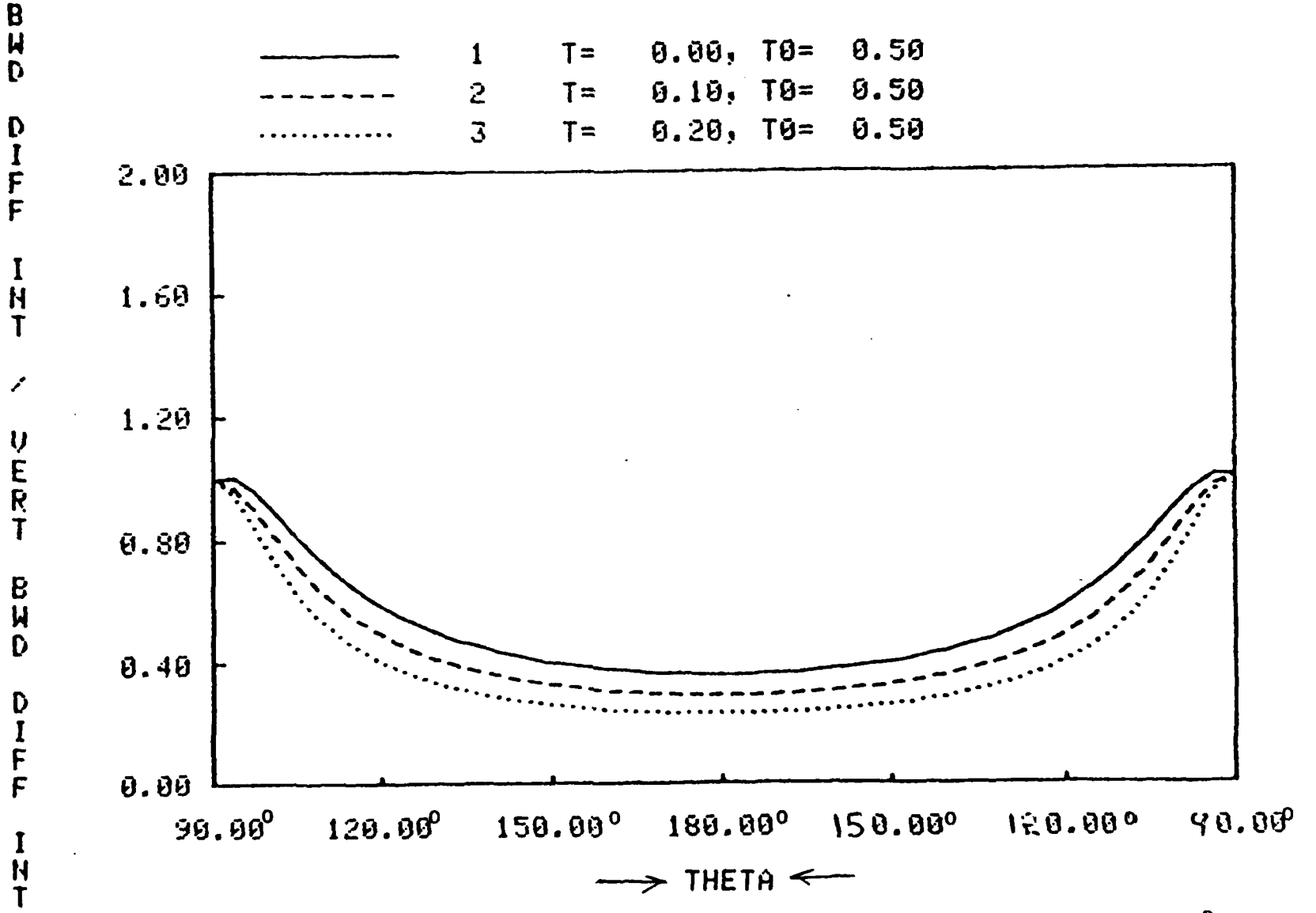

Figure 12.e RELATIVE BWD DIFF INTENSITY VS. SCATTER ANGLE FOR SLAB, $\theta_0 = 0^\circ$, W=0.75

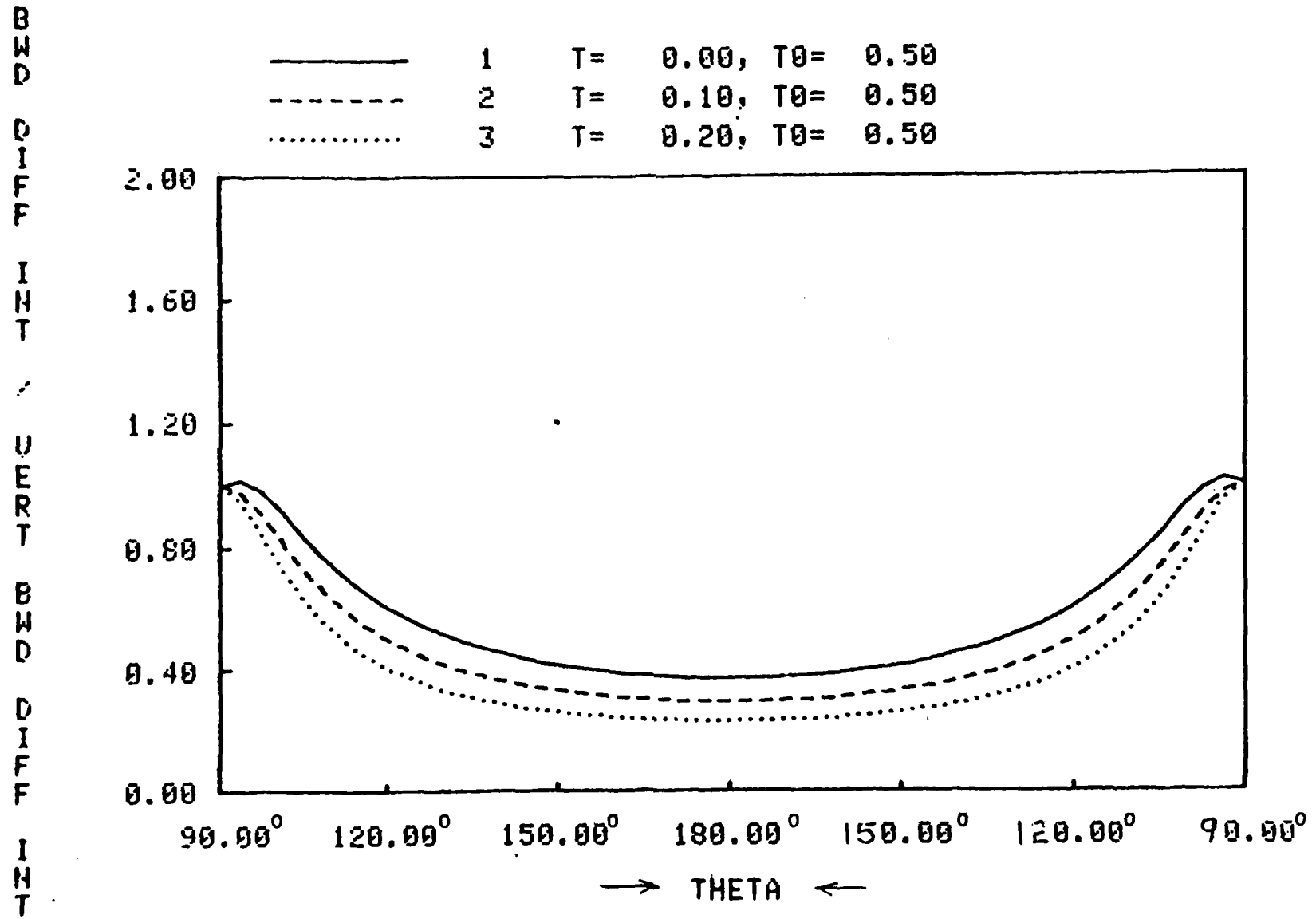

Figure 12.f. RELATIVE BWD DIFF INTENSITY VS. SCATTER ANGLE FOR SLAB, $Q0=0^{\circ}$, W=0.90

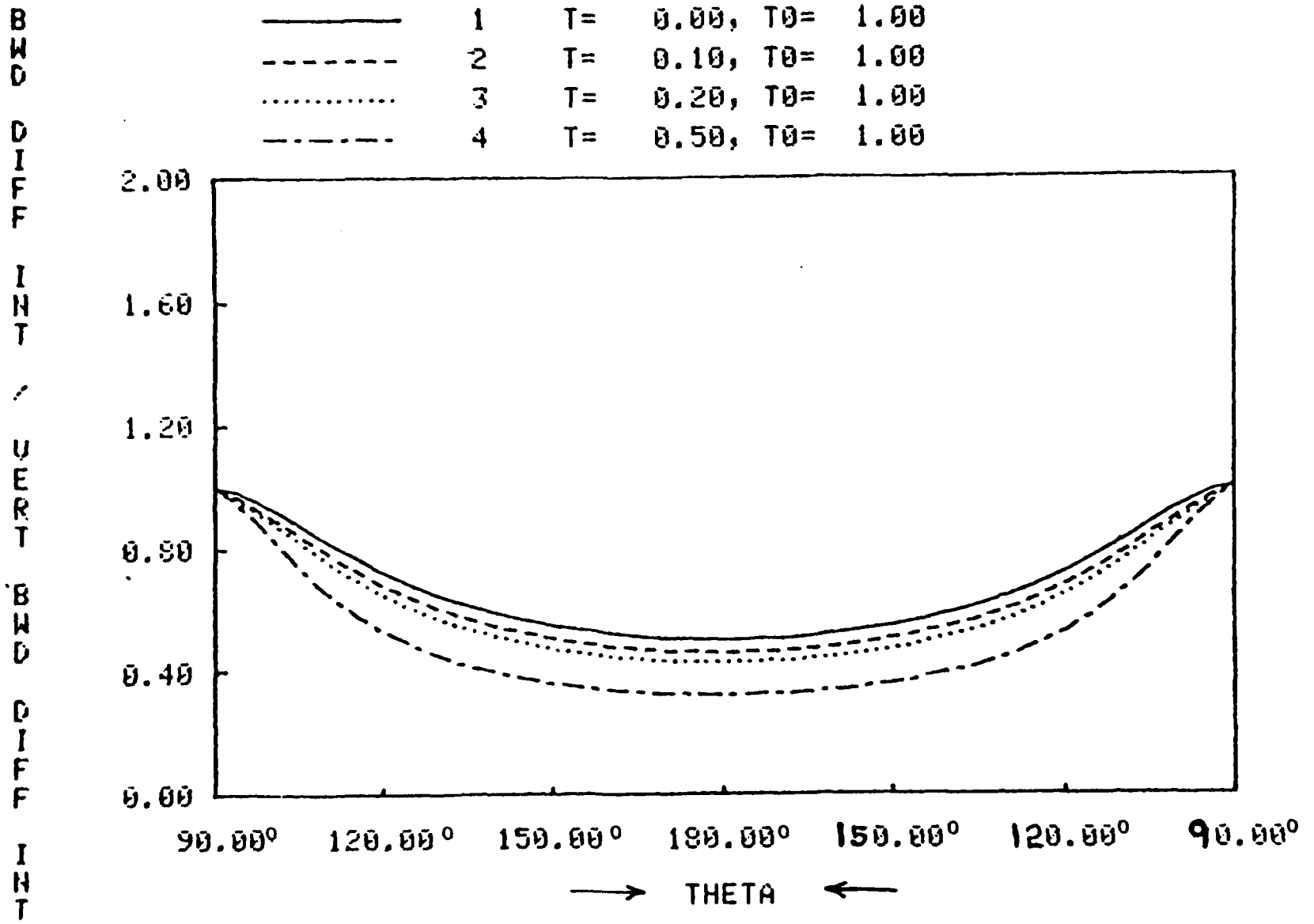

Figure 12.g. RELATIVE BWD DIFF INTENSITY VS. SCATTER ANGLE FOR SLAB, $\theta_0 = 0^\circ$, W=0.50

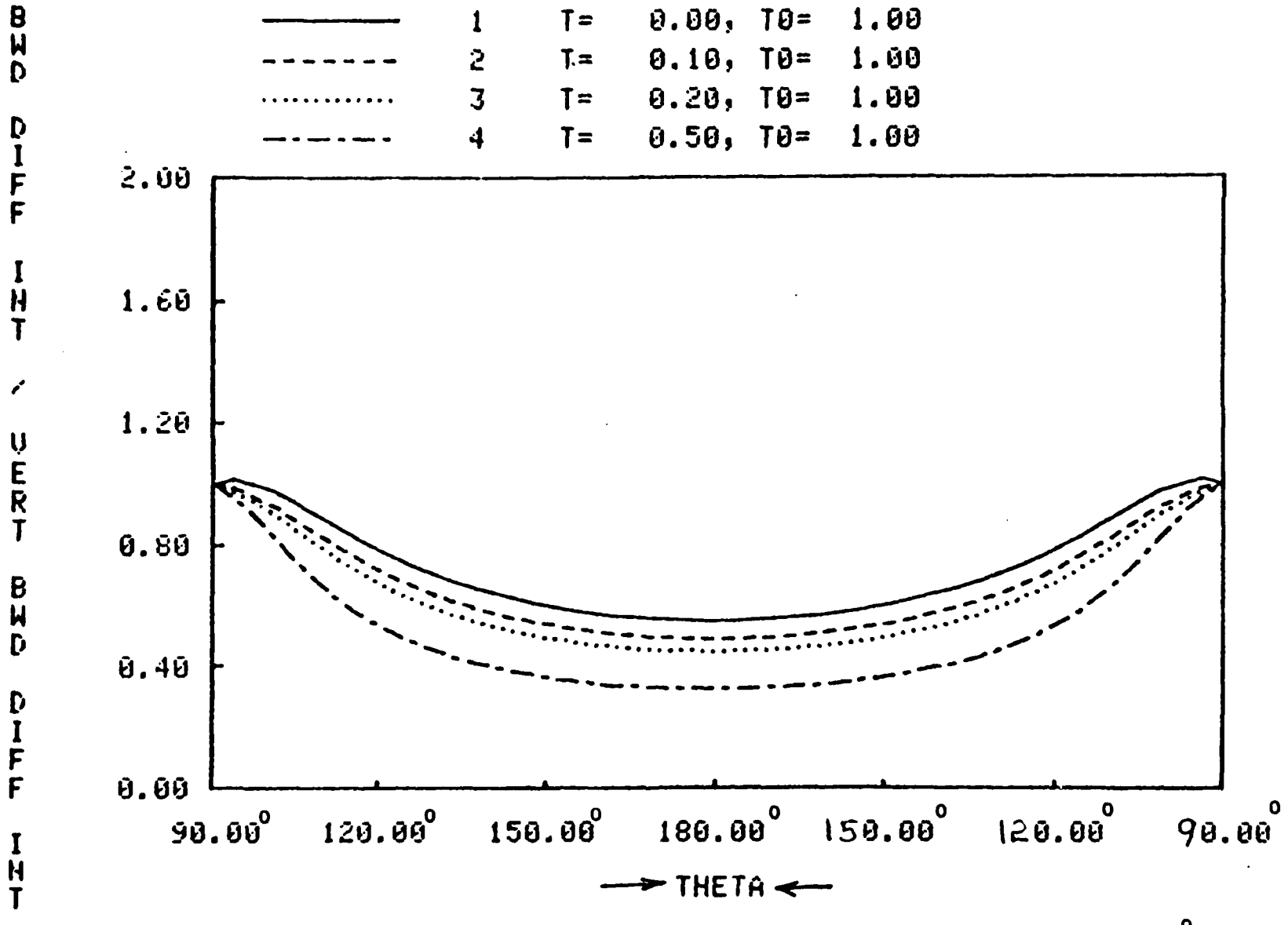

Figure 12.h. RELATIVE BWD DIFF INTENSITY VS. SCATTER ANGLE FOR SLAB, $Q0=0^{\circ}$, W=0.75

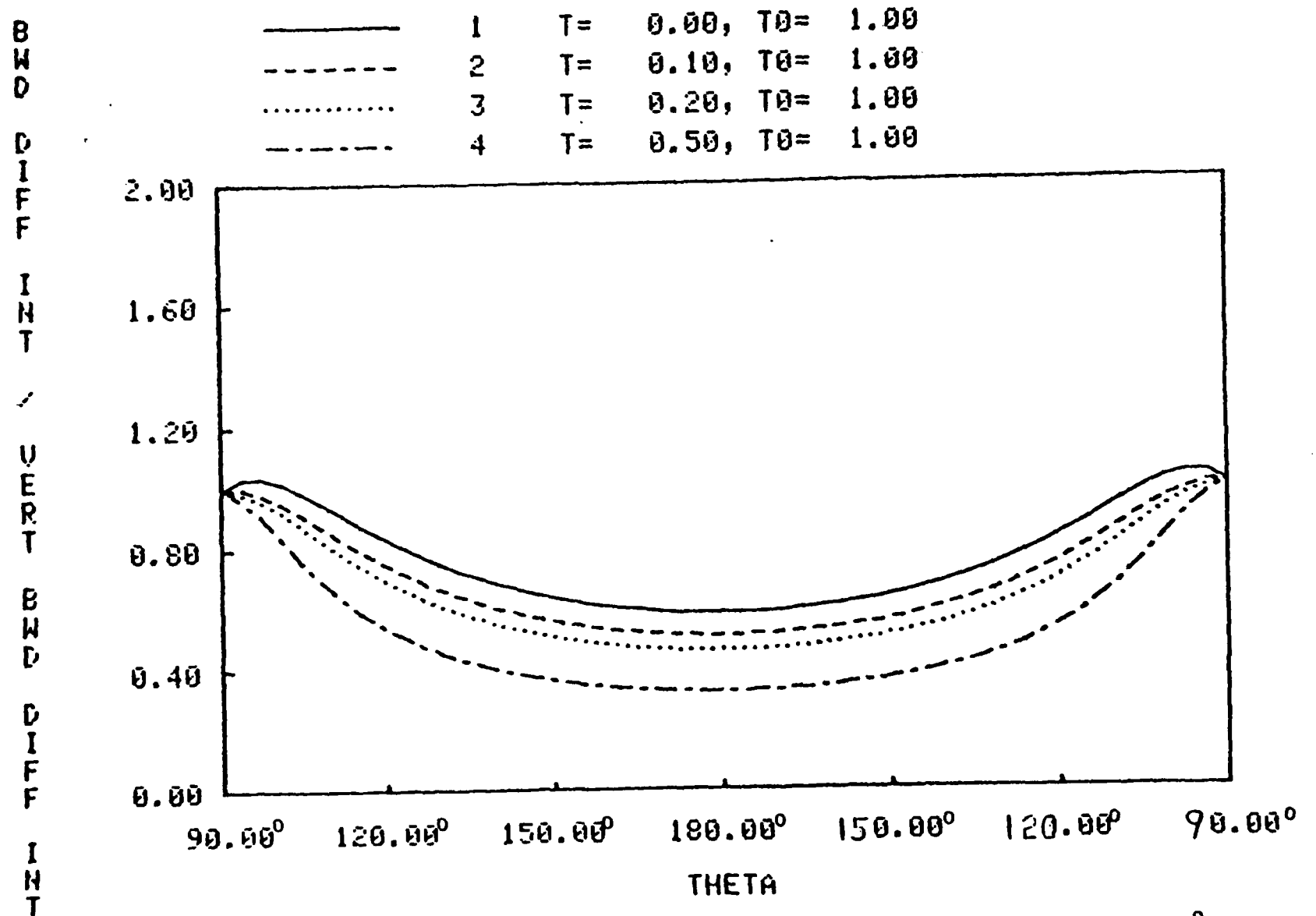

Figure 12.i. RELATIVE BWD DIFF INTENSITY VS. SCATTER ANGLE FOR SLAB, $\theta_0 = 0^\circ$, W=0.90

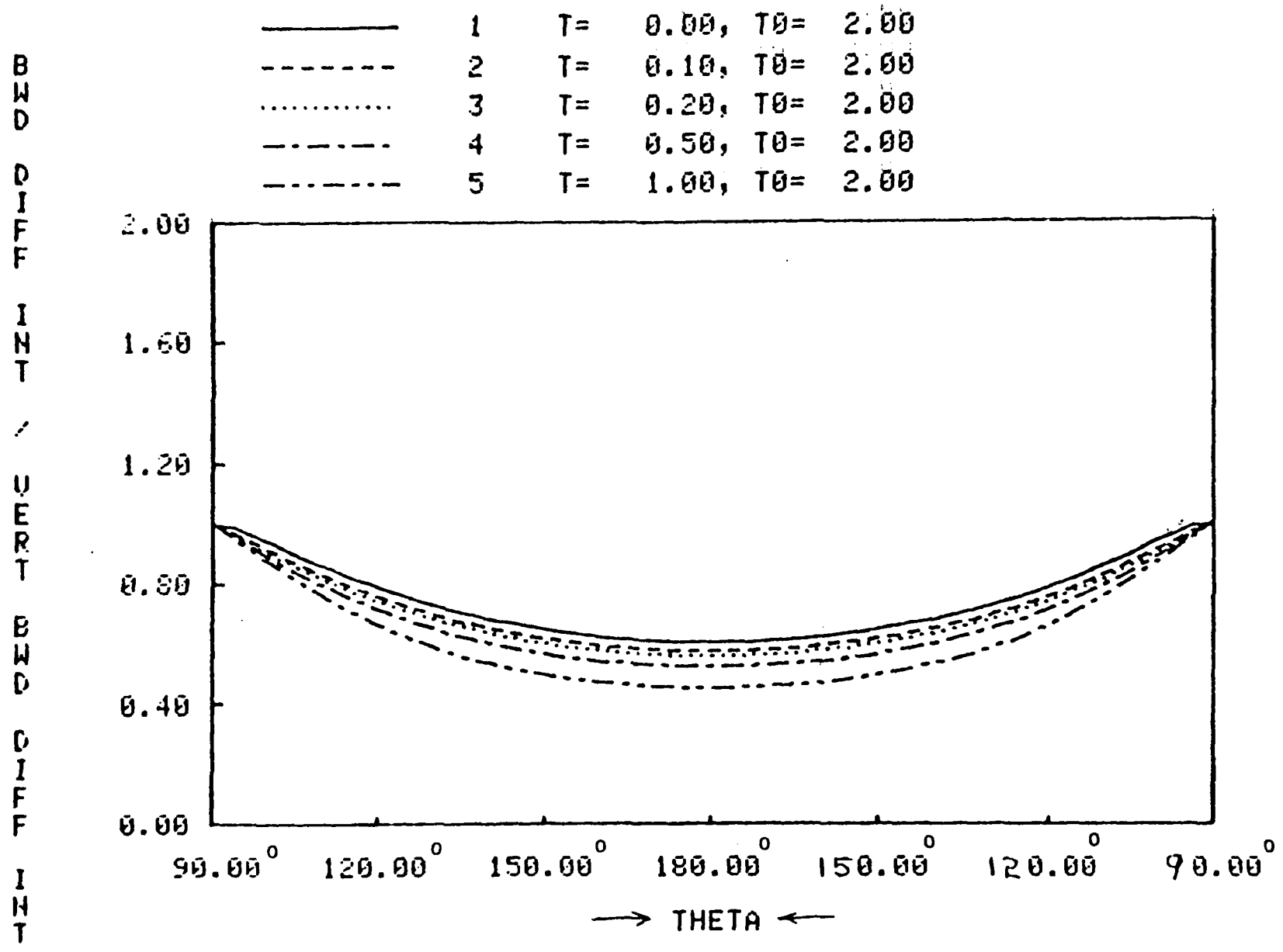

Figure 12.j RELATIVE BWD DIFF INTENSITY VS. SCATTER ANGLE FOR SLAB, Q0=0°, N=0.50

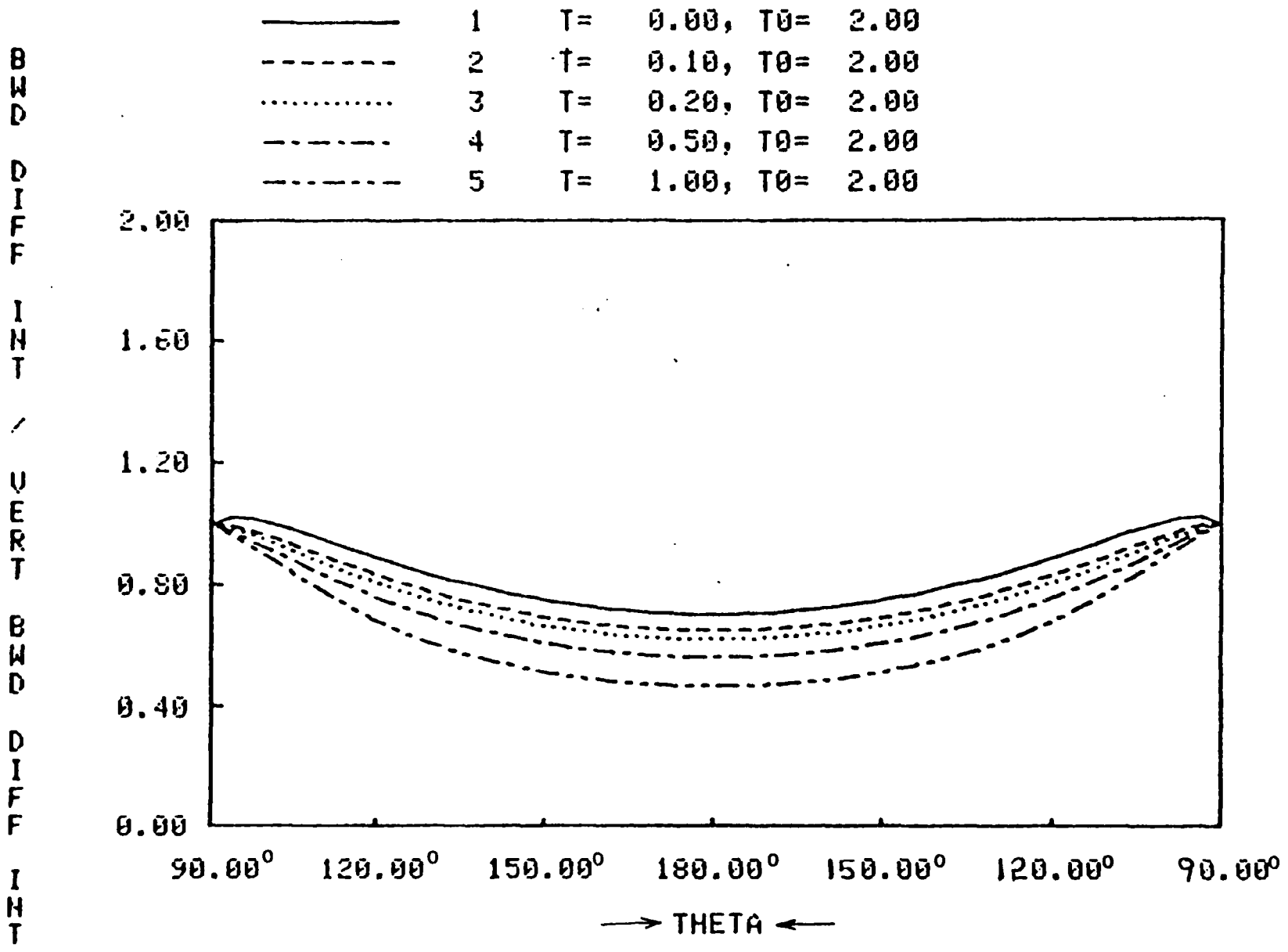

Figure 12.k RELATIVE BWD DIFF INTENSITY VS. SCATTER ANGLE FOR SLAB, $\theta_0 = 0^\circ$, W=0.75

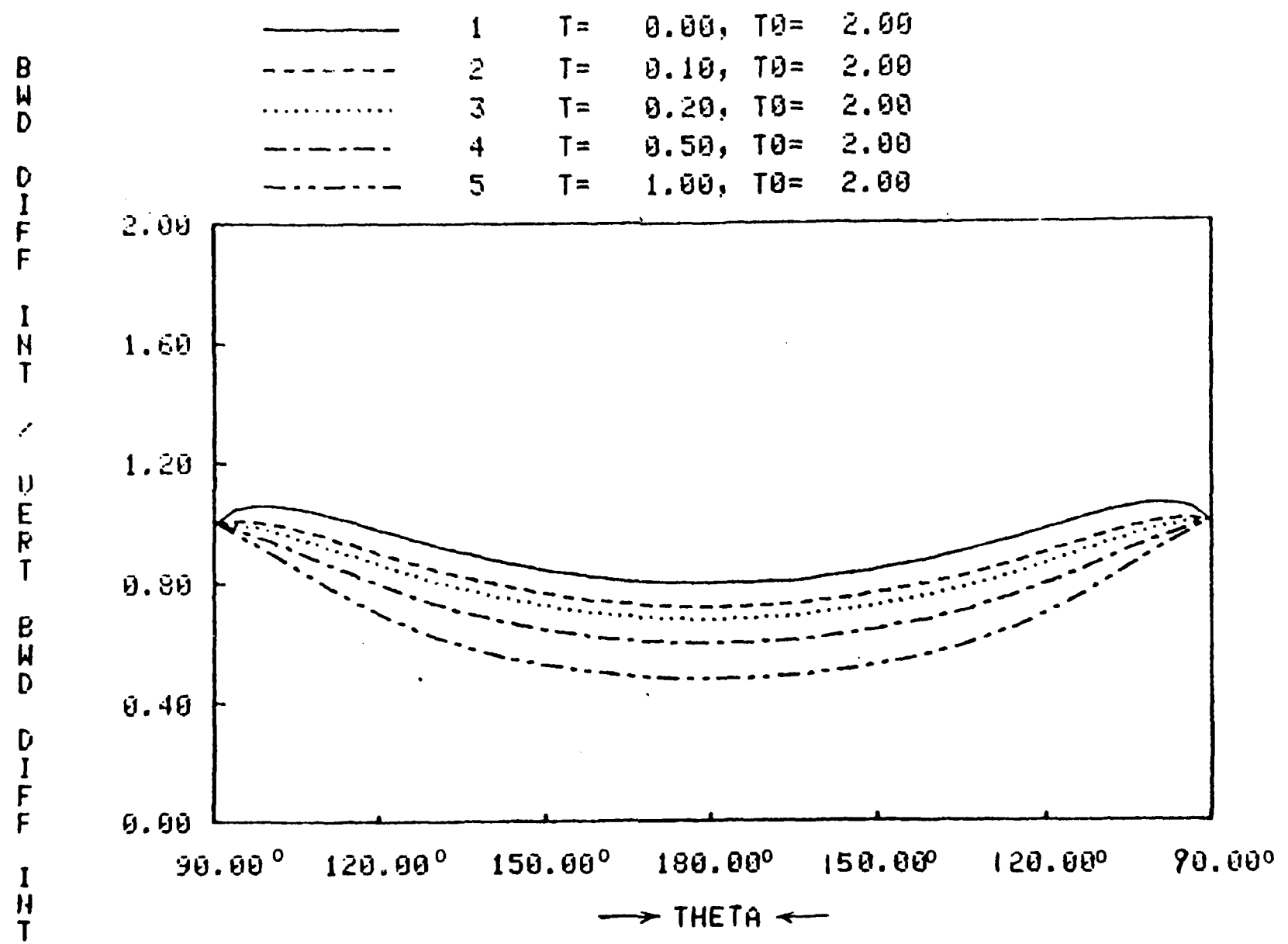

Figure 12.1. RELATIVE BWD DIFF INTENSITY VS. SCATTER ANGLE FOR SLAB, $\theta_0 = 0^\circ$, W=0.90

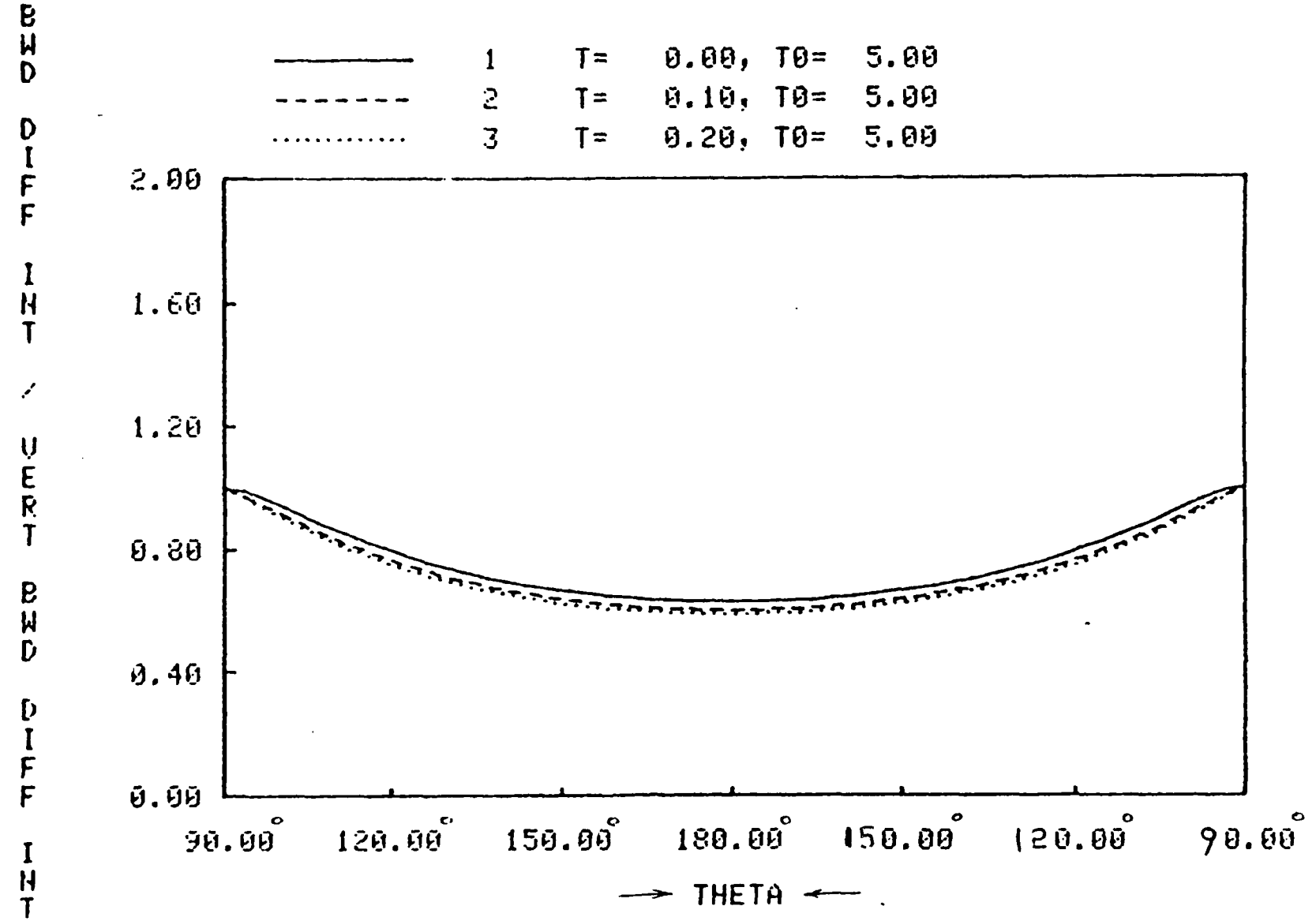

Figure 12.m RELATIVE BWD DIFF INTENSITY VS. SCATTER ANGLE FOR SLAB, Q0=0°, W=0.50

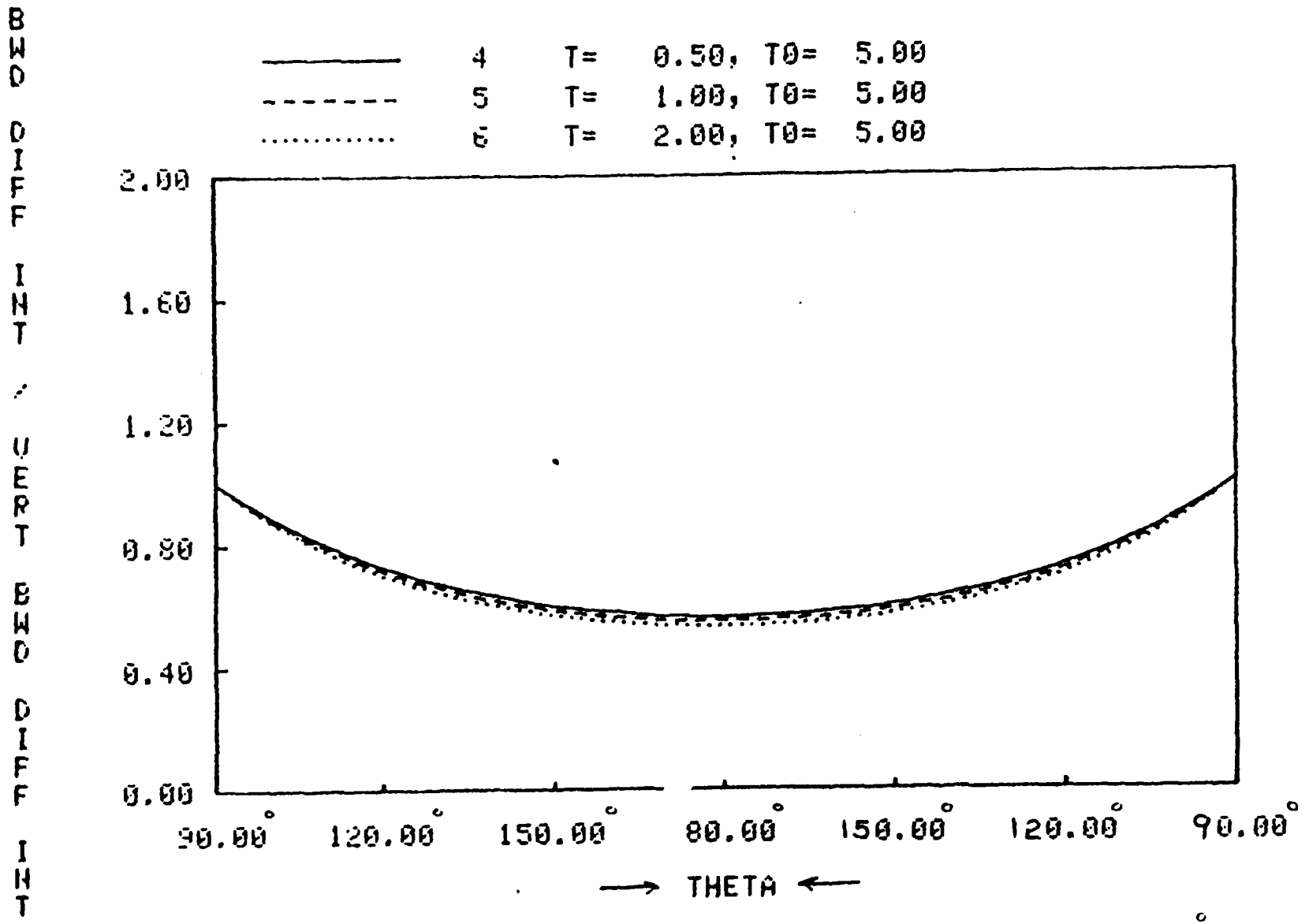

Figure 12.n RELATIVE BWD DIFF INTENSITY VS. SCATTER ANGLE FOR SLAB, Q0=0°, W=0.50

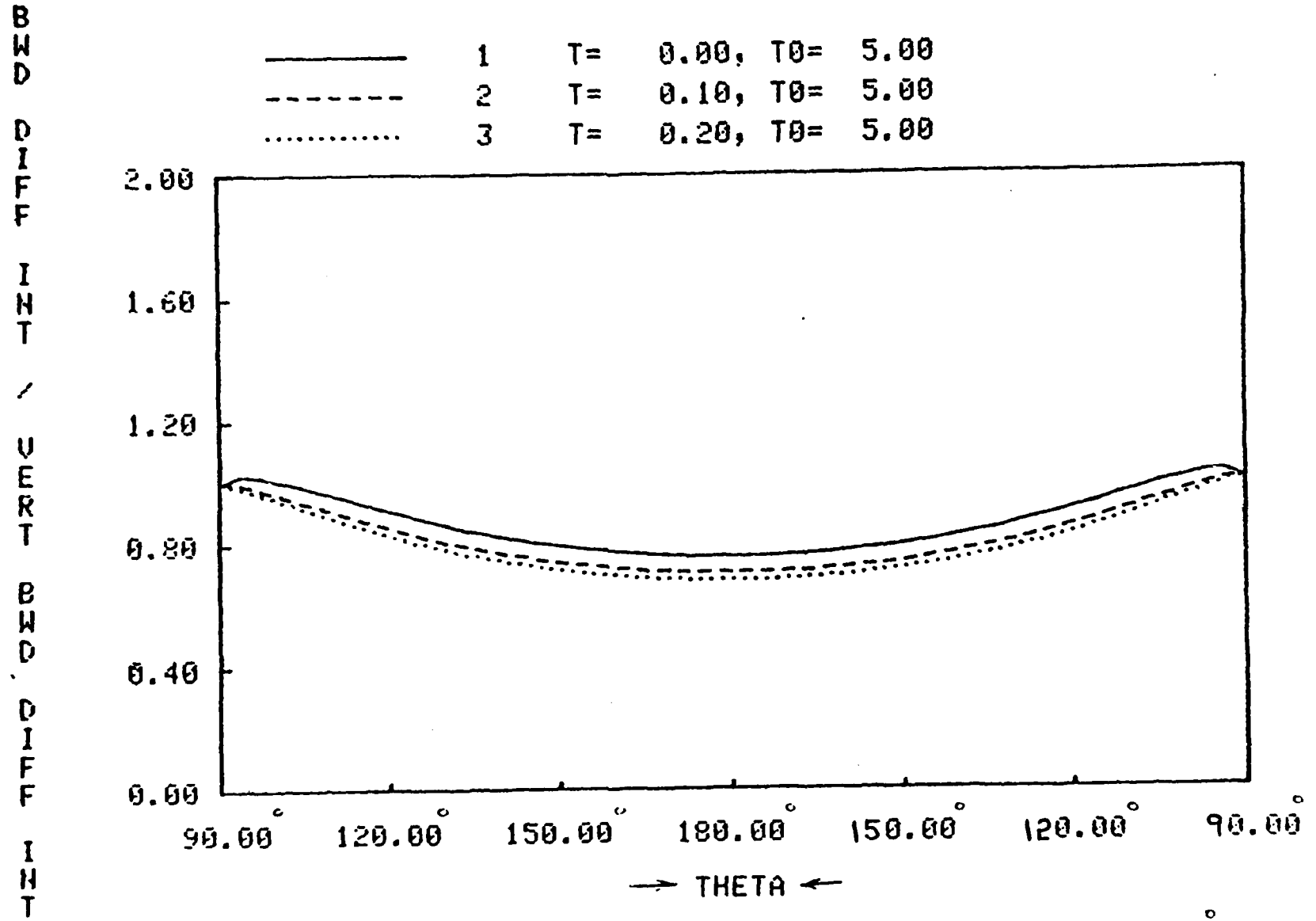

Figure 12.o. RELATIVE BWD DIFF INTENSITY VS. SCATTER ANGLE FOR SLAB, θ_0=0°, W=0.75

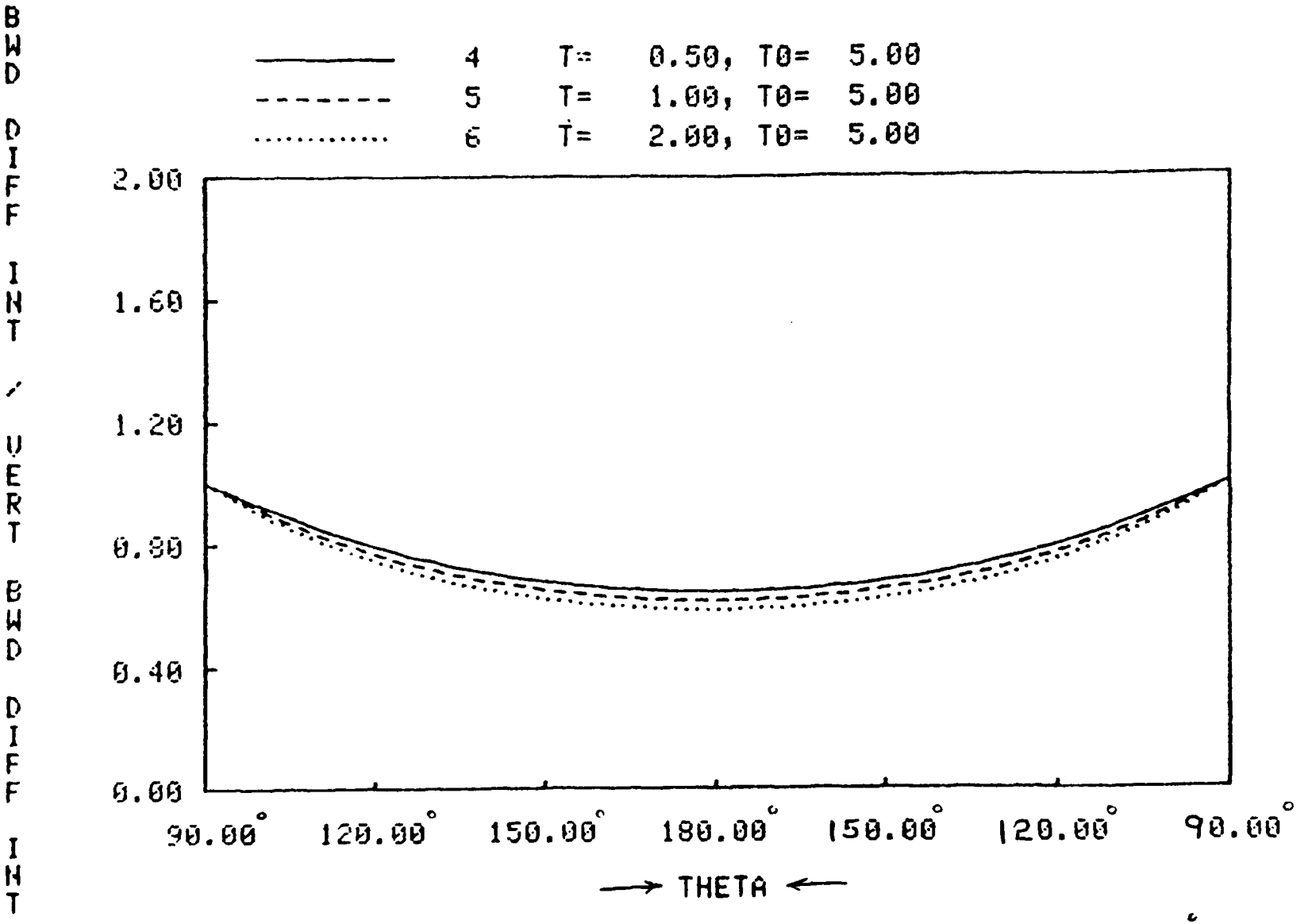

Figure 12.p RELATIVE BWD DIFF INTENSITY VS. SCATTER ANGLE FOR SLAB, Q0=0°, W=0.75

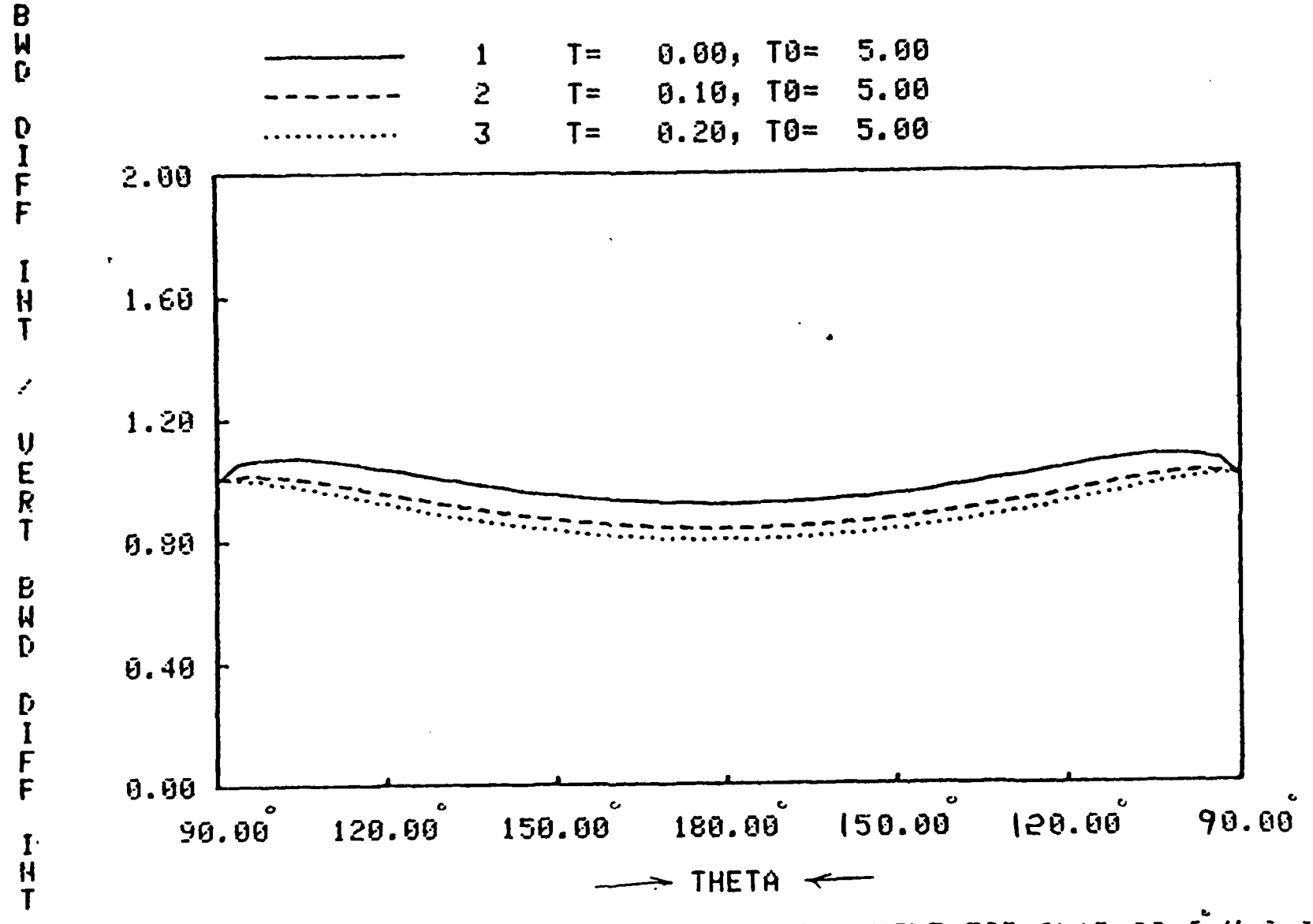

Figure 12.q. RELATIVE BWD DIFF INTENSITY VS. SCATTER ANGLE FOR SLAB, Q0=0°, W=0.90

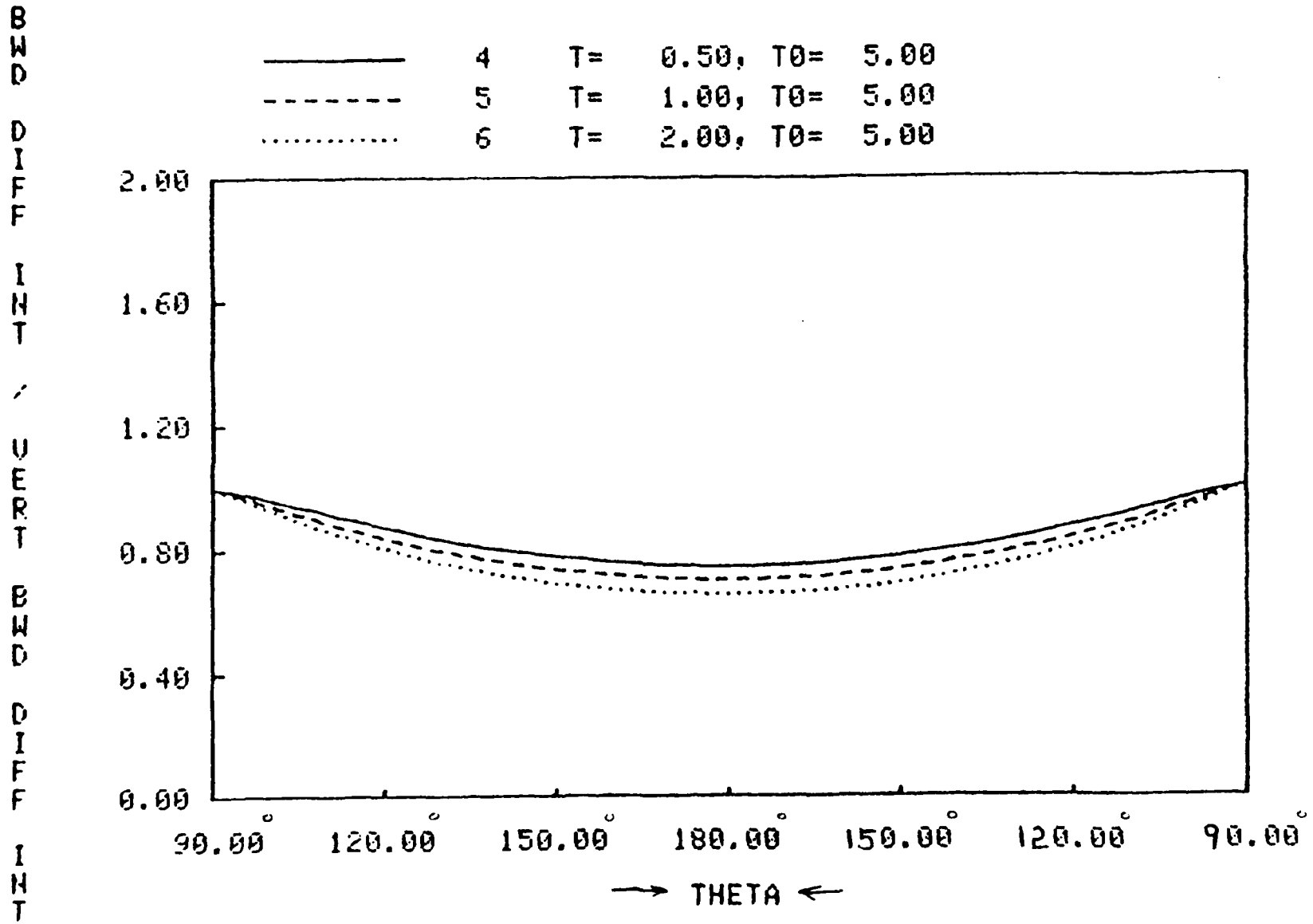

Figure 12.r RELATIVE BWD DIFF INTENSITY VS. SCATTER ANGLE FOR SLAB, Q0=0°, W=0.90

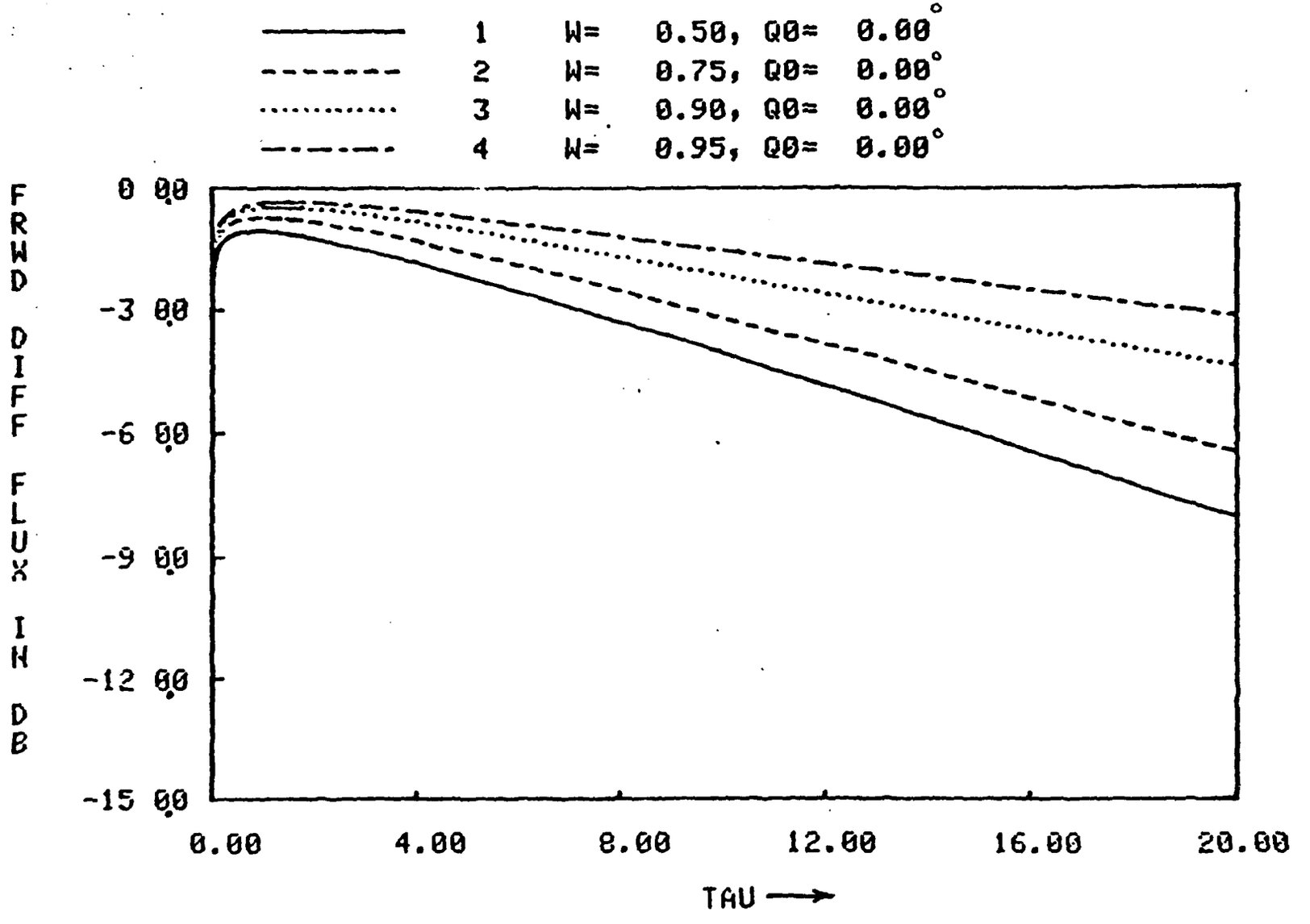

Figure 13.a. FORWARD DIFFUSE FLUX VS. DISTANCE FOR 1/2 SPACE, S_0=1

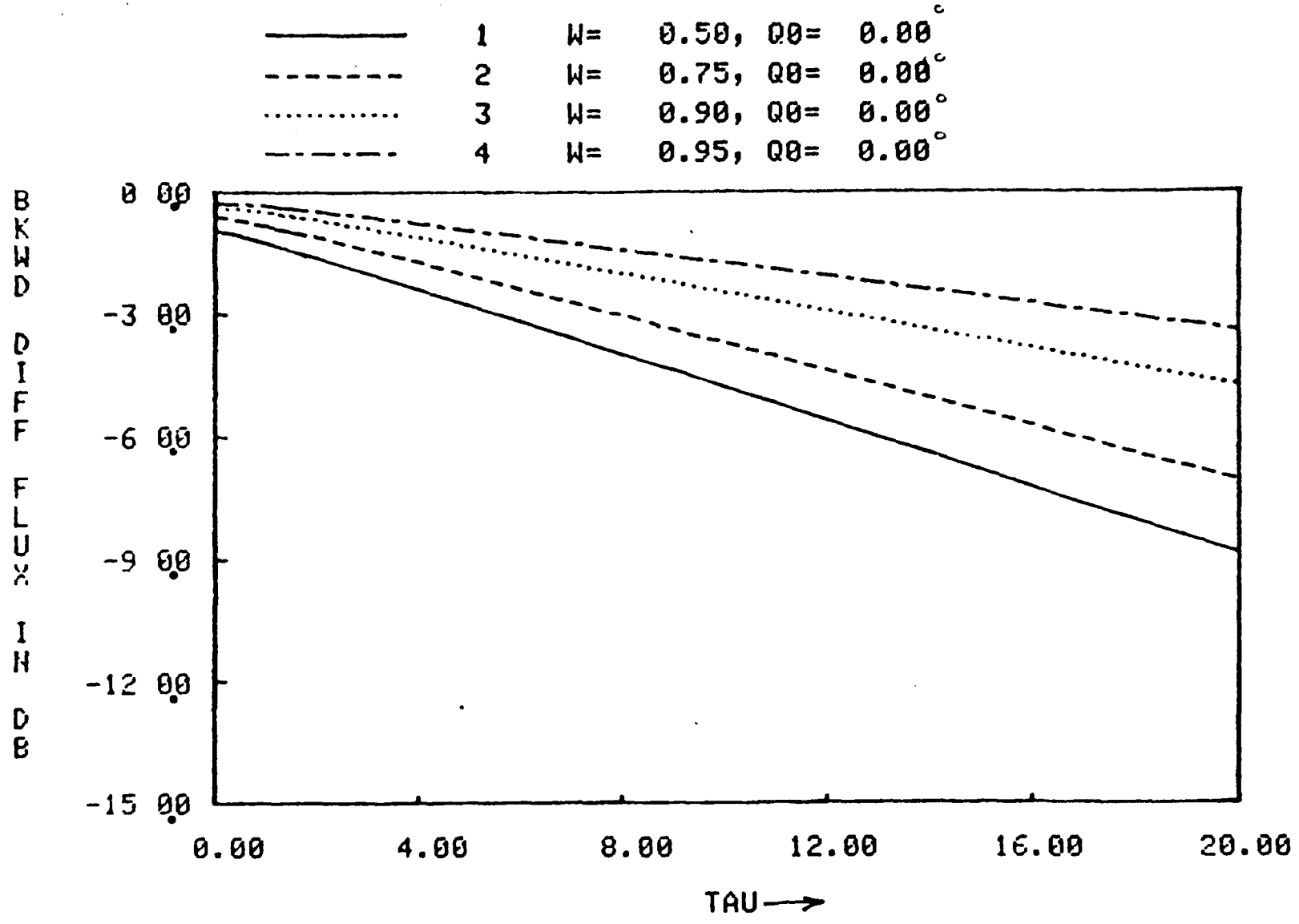

Figure 13.b. BACKWARD DIFFUSE FLUX VS. DISTANCE FOR 1/2 SPACE, S_o=1

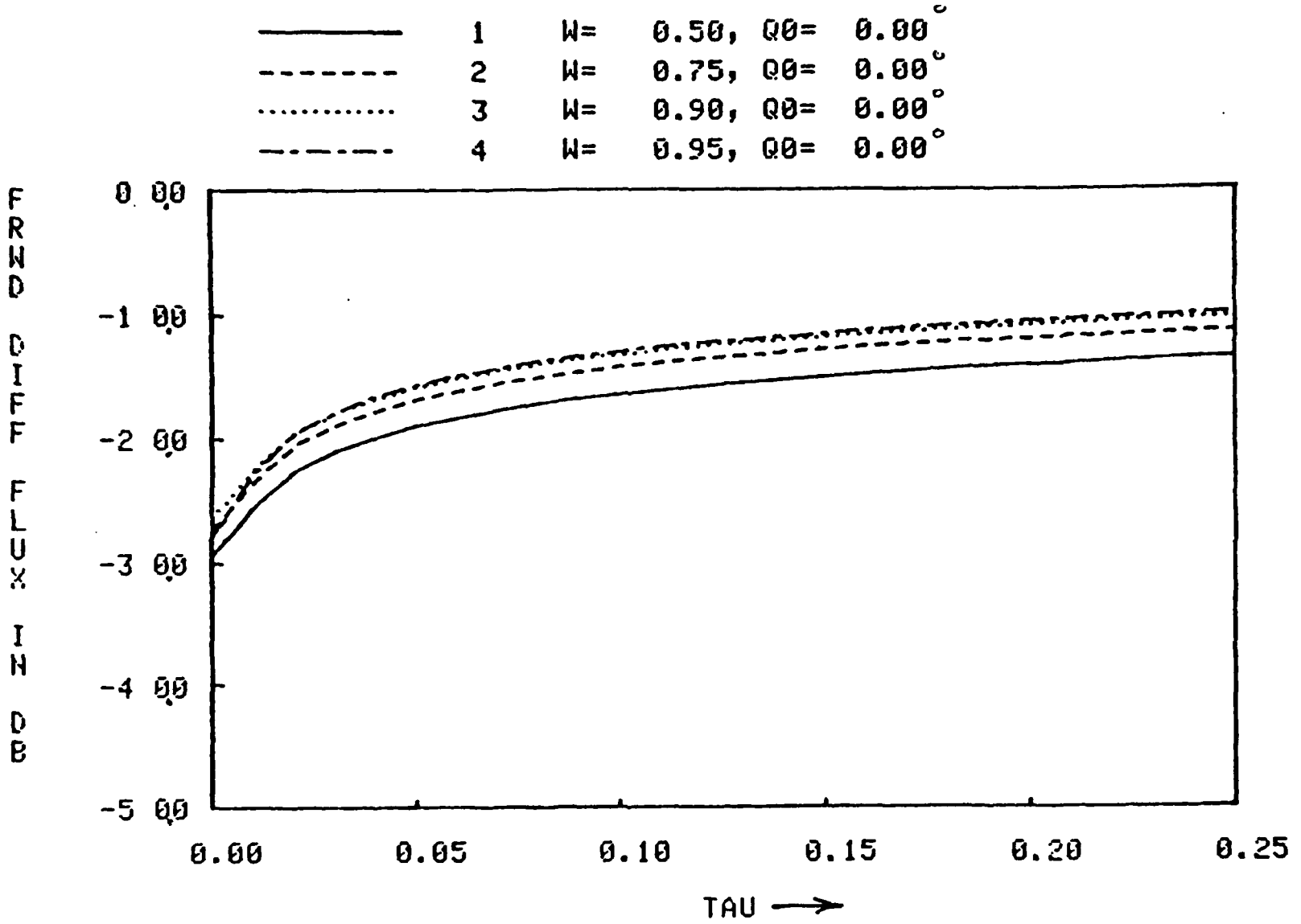

Figure 14.a. FORWARD DIFFUSE FLUX VS. DISTANCE FOR SLAB, T0= 0.25, S=1.0

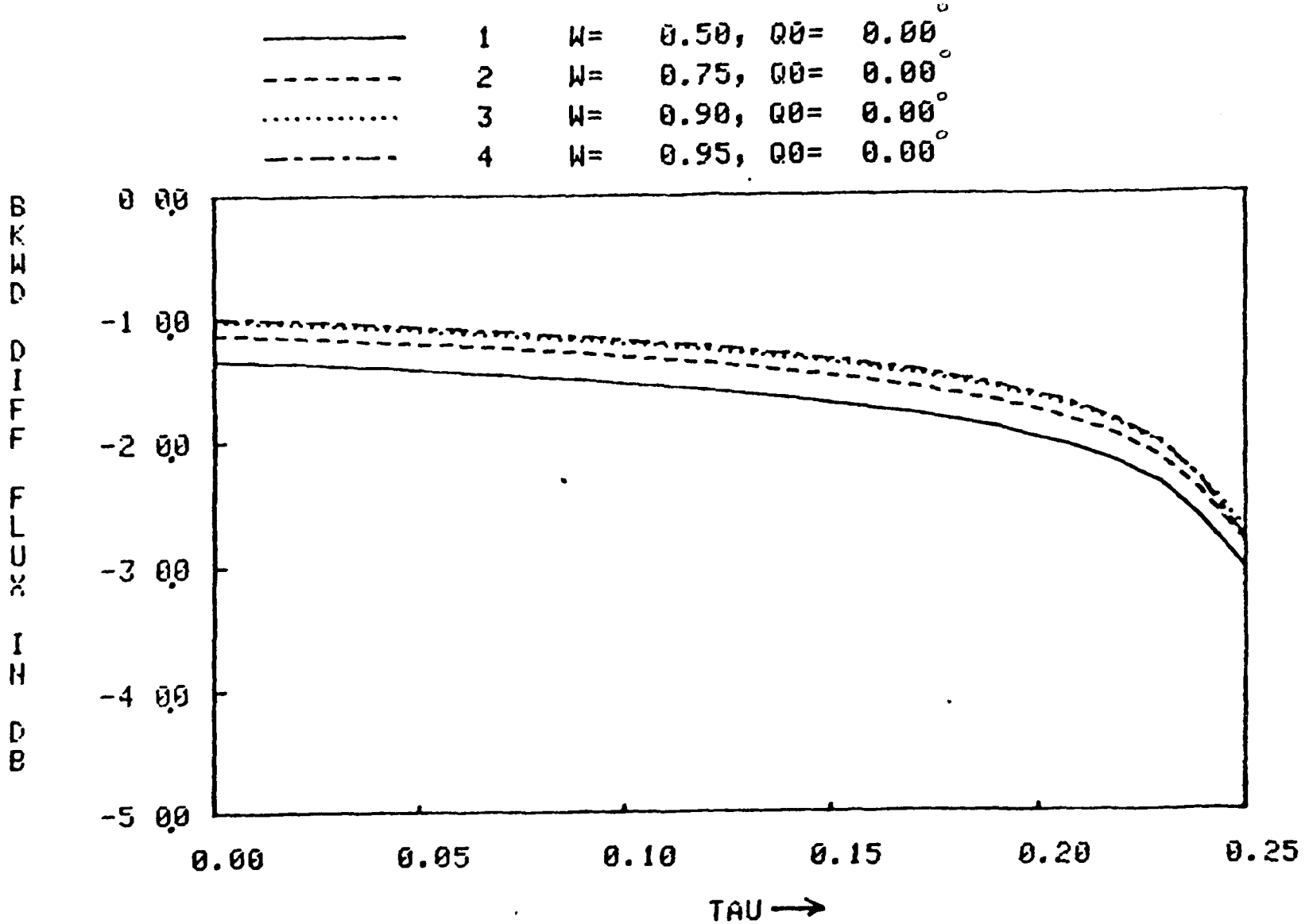

Figure 14.b. BACKWARD DIFFUSE FLUX VS. DISTANCE FOR SLAB, T0= 0.25, S=1.0

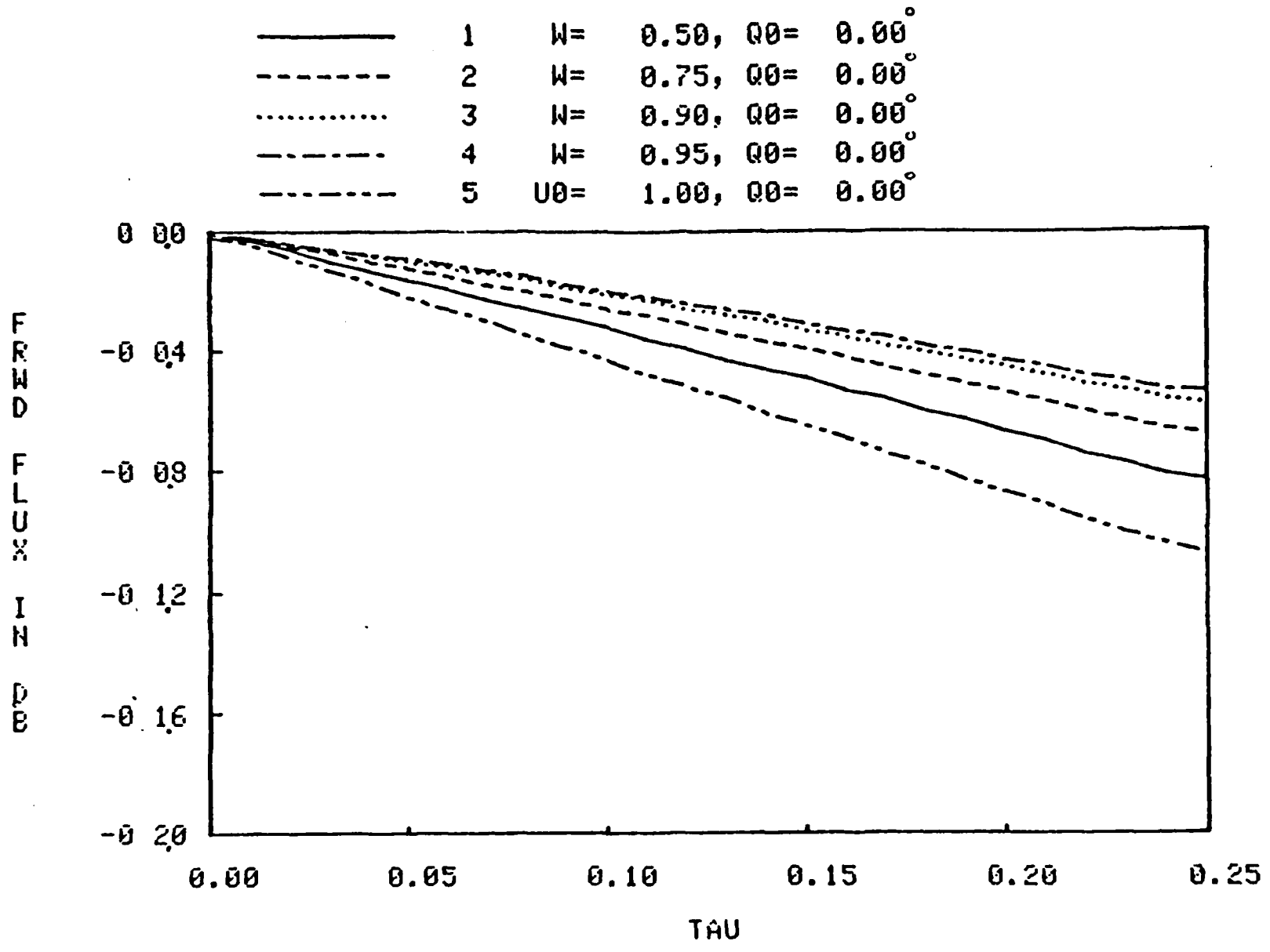

Figure 14.c. FORWARD FLUX VS. DISTANCE FOR SLAB, T0= 0.25, Ω=1.0

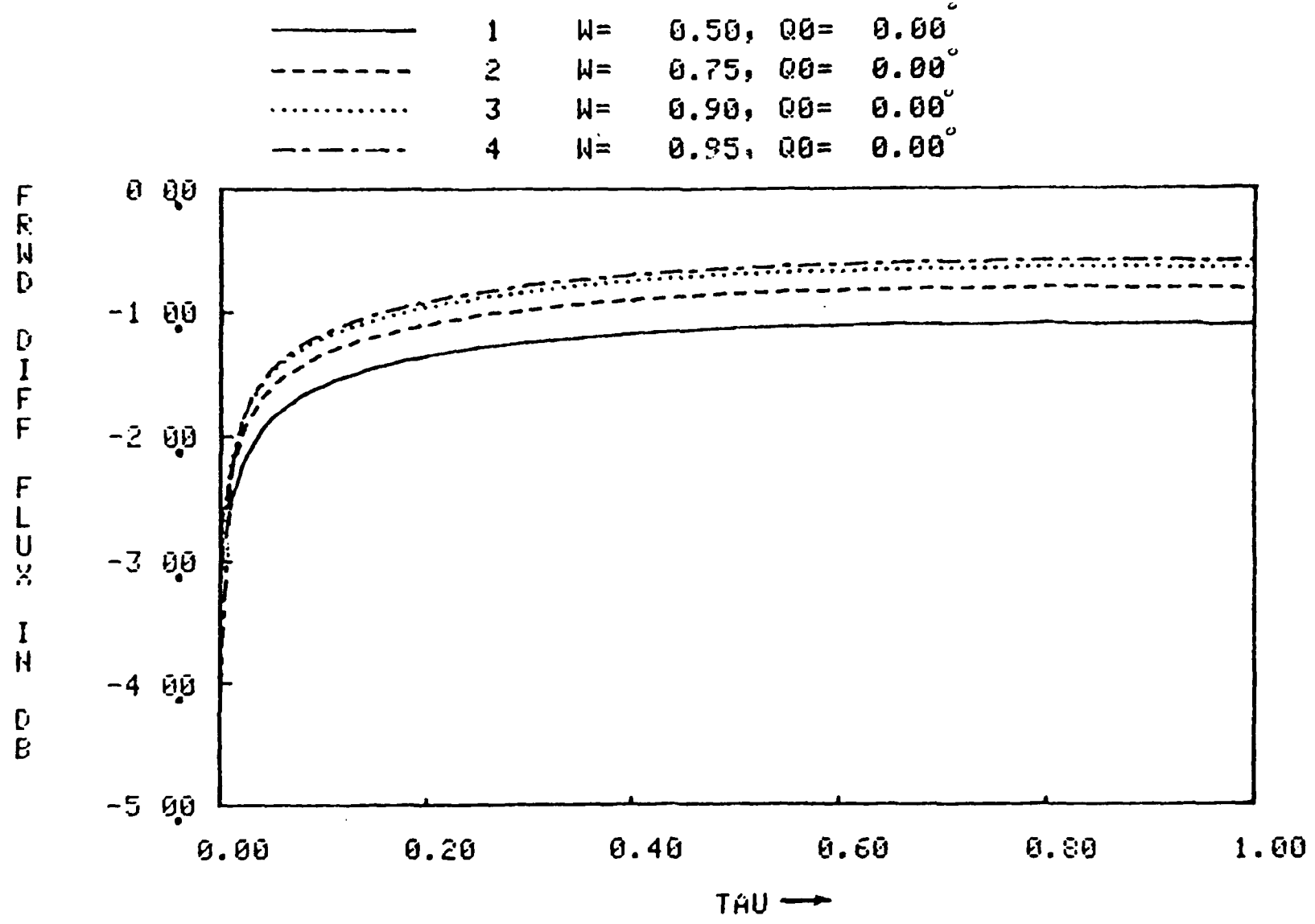

Figure 15.a. FORWARD DIFFUSE FLUX VS. DISTANCE FOR SLAB, T0= 1.00, S_o=1

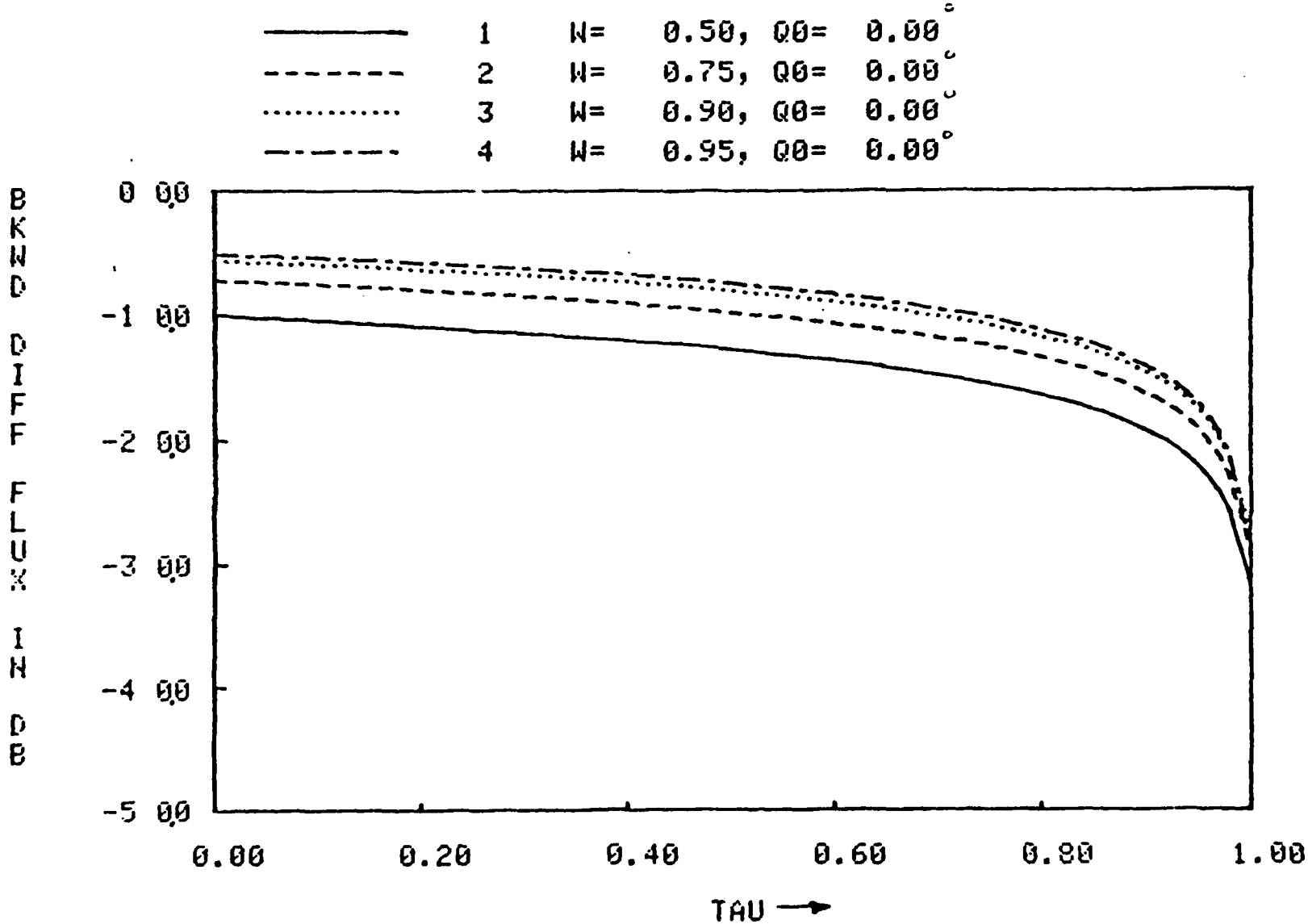

Figure 15.b. BACKWARD DIFFUSE FLUX VS. DISTANCE FOR SLAB, T0= 1.00, S=1

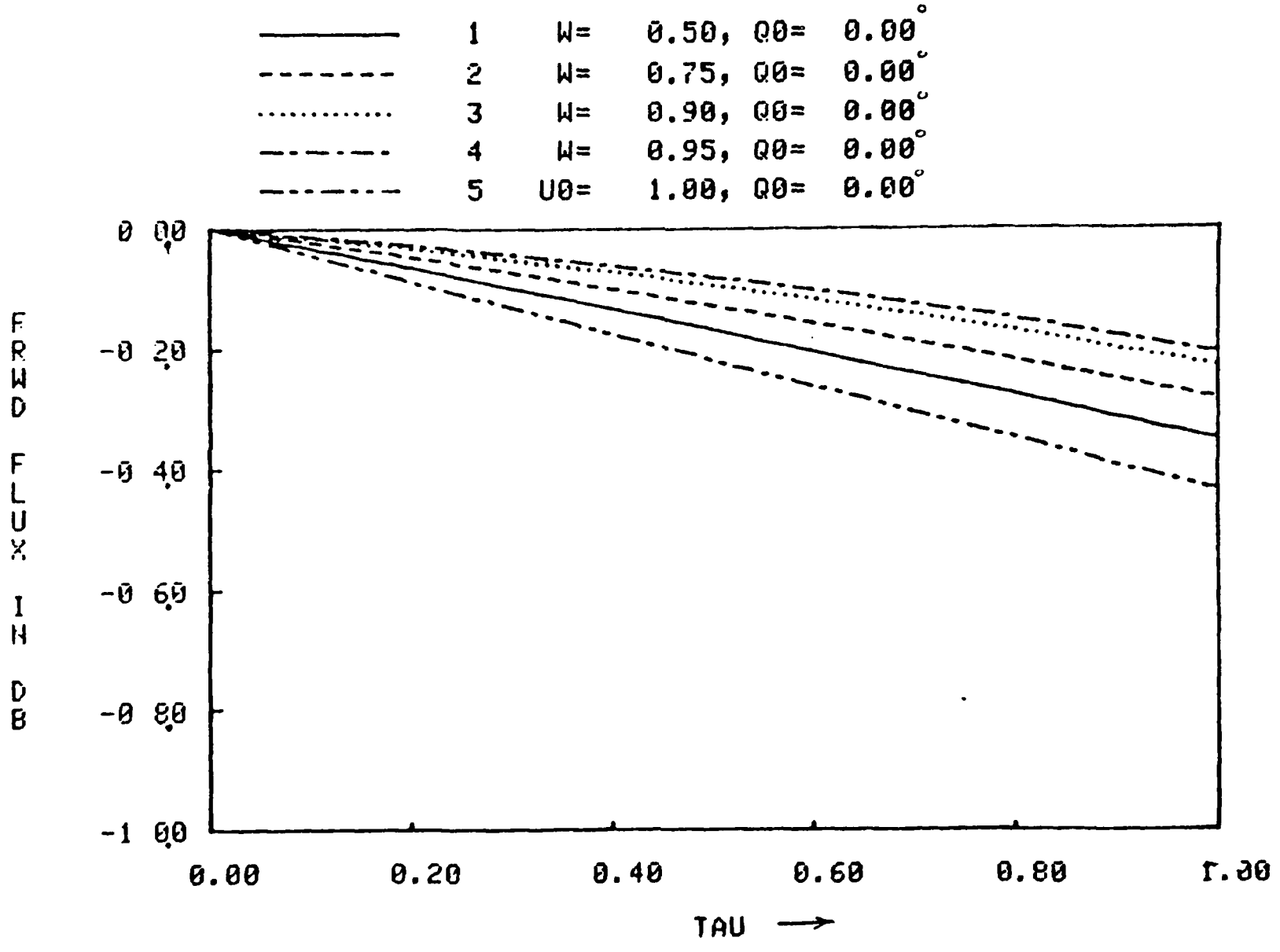

Figure 15.c. FORWARD FLUX VS. DISTANCE FOR SLAB, T0= 1.00, S=1

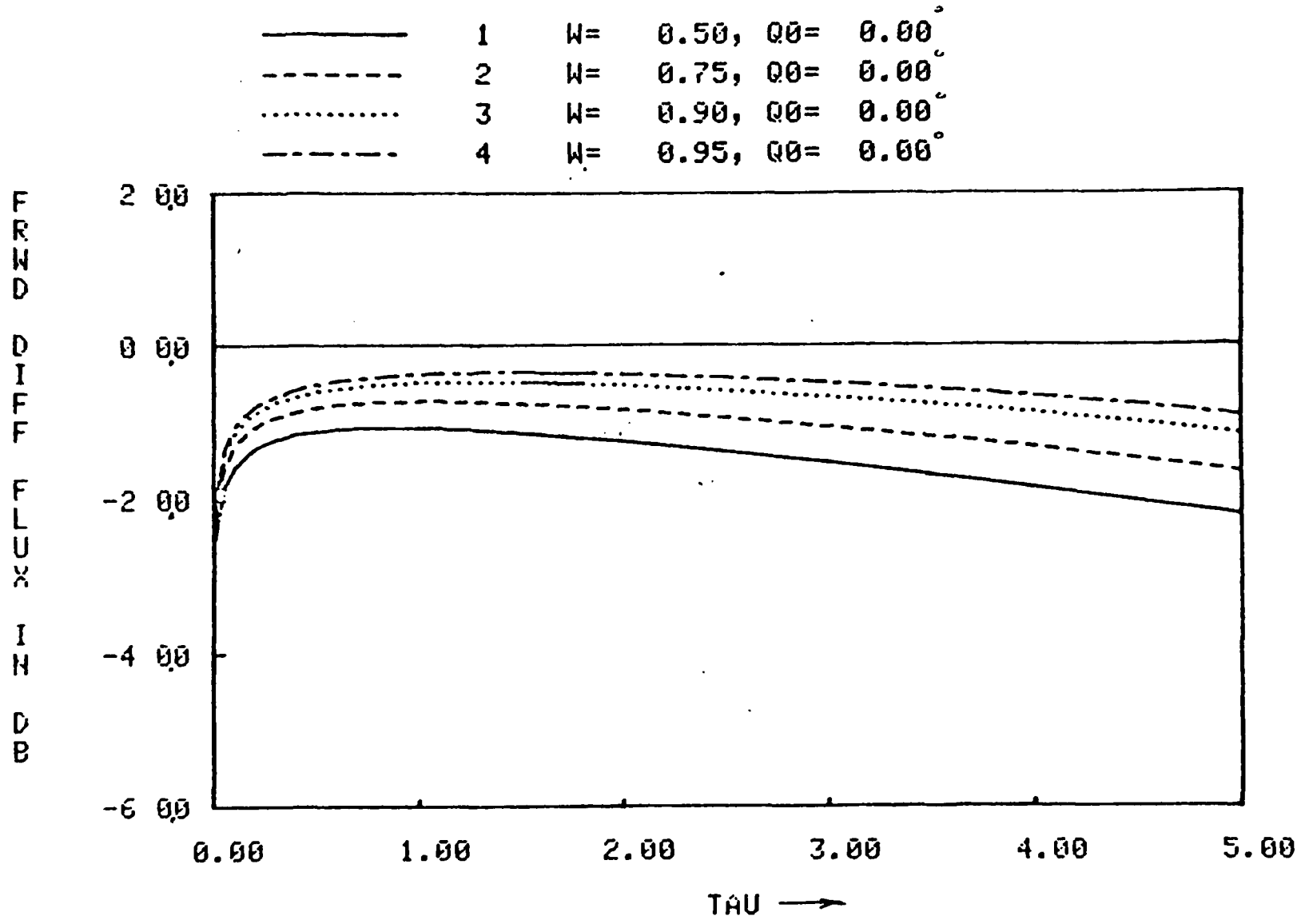

Figure 16.a. FORWARD DIFFUSE FLUX VS. DISTANCE FOR SLAB, T_0= 5.00, S_o=1

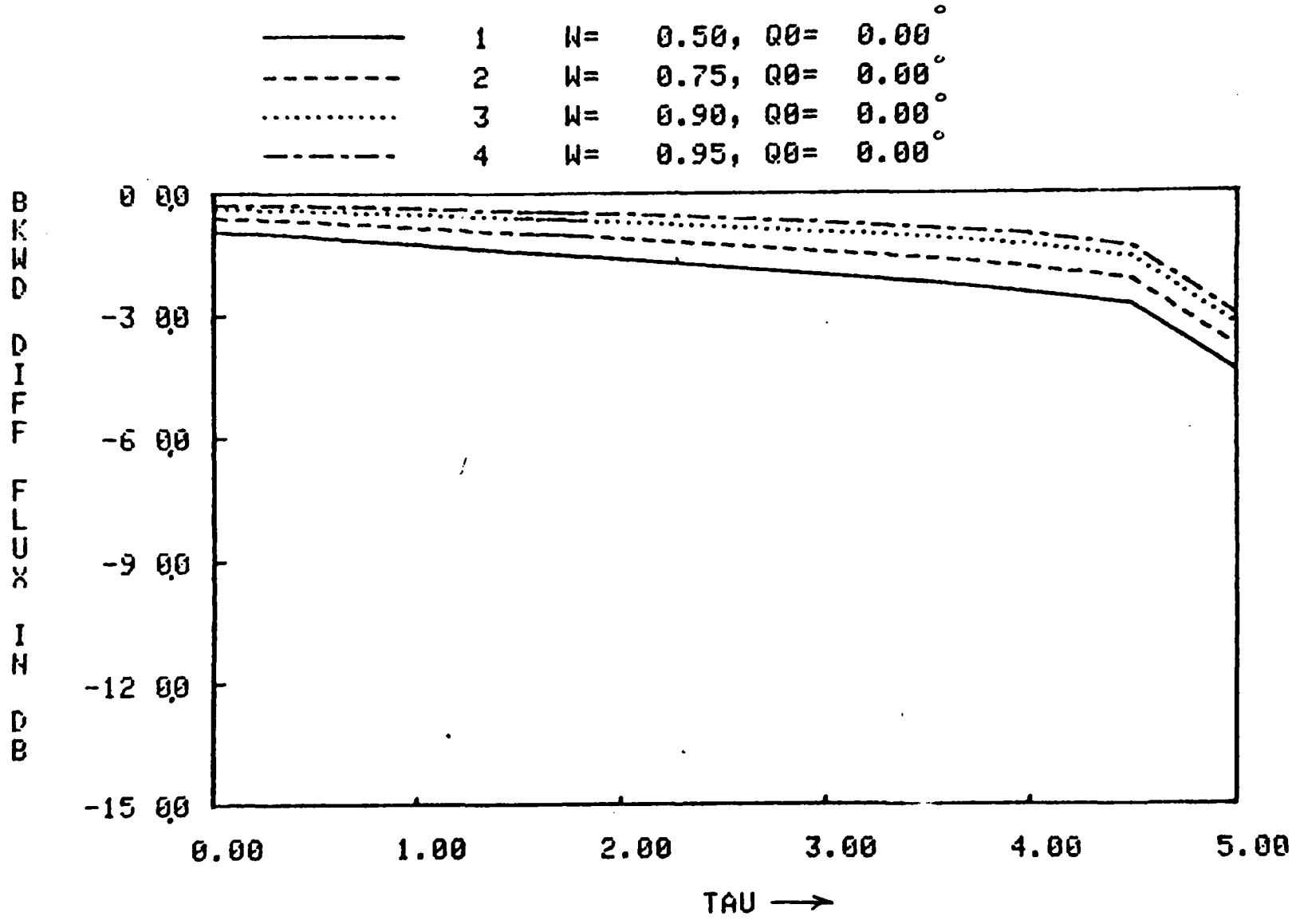

Figure 16.b. BACKWARD DIFFUSE FLUX VS. DISTANCE FOR SLAB, T0= 5.00, S=1

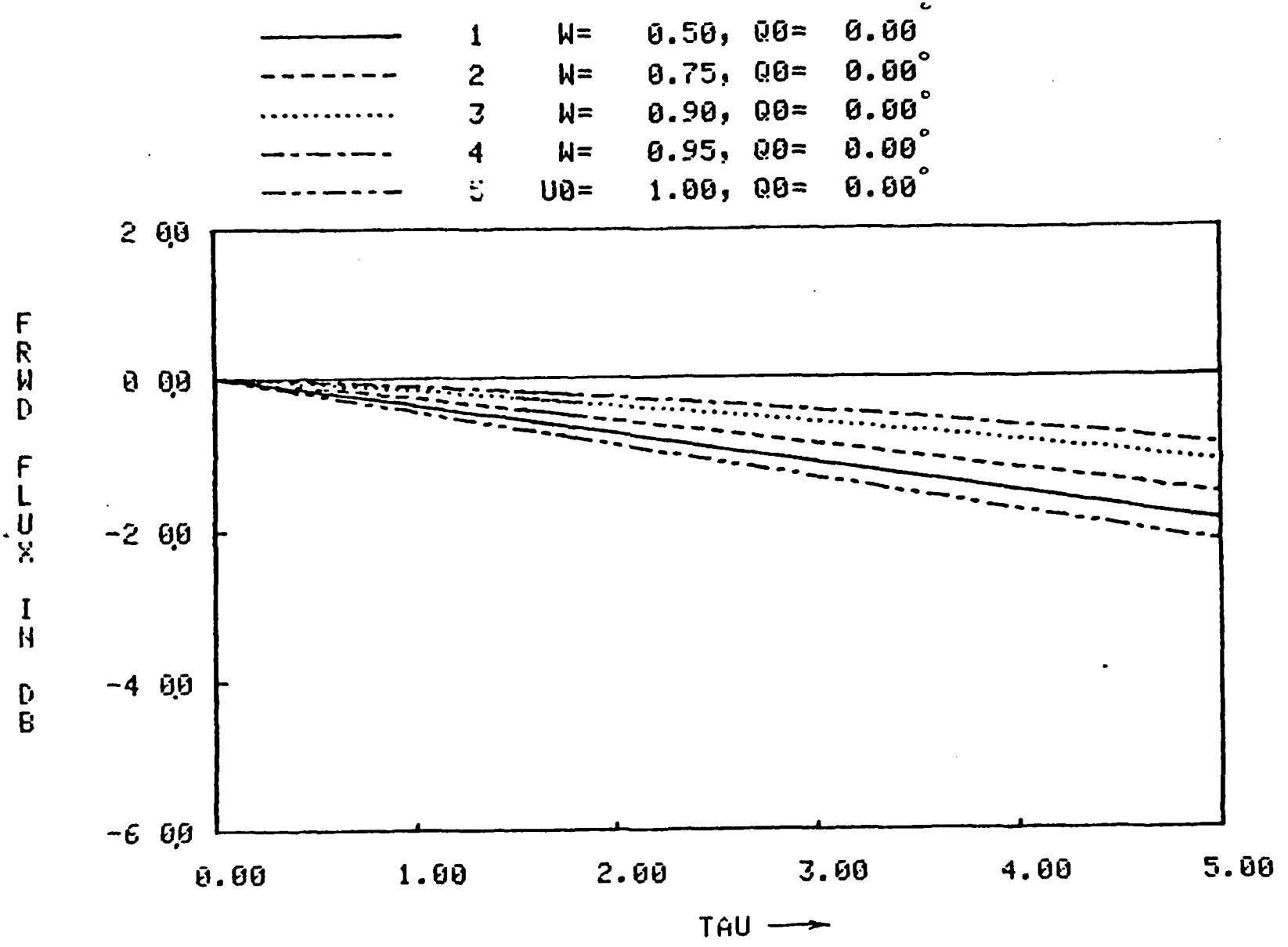

Figure 16.c. FORWARD FLUX VS. DISTANCE FOR SLAB, T0= 5.00, S=1

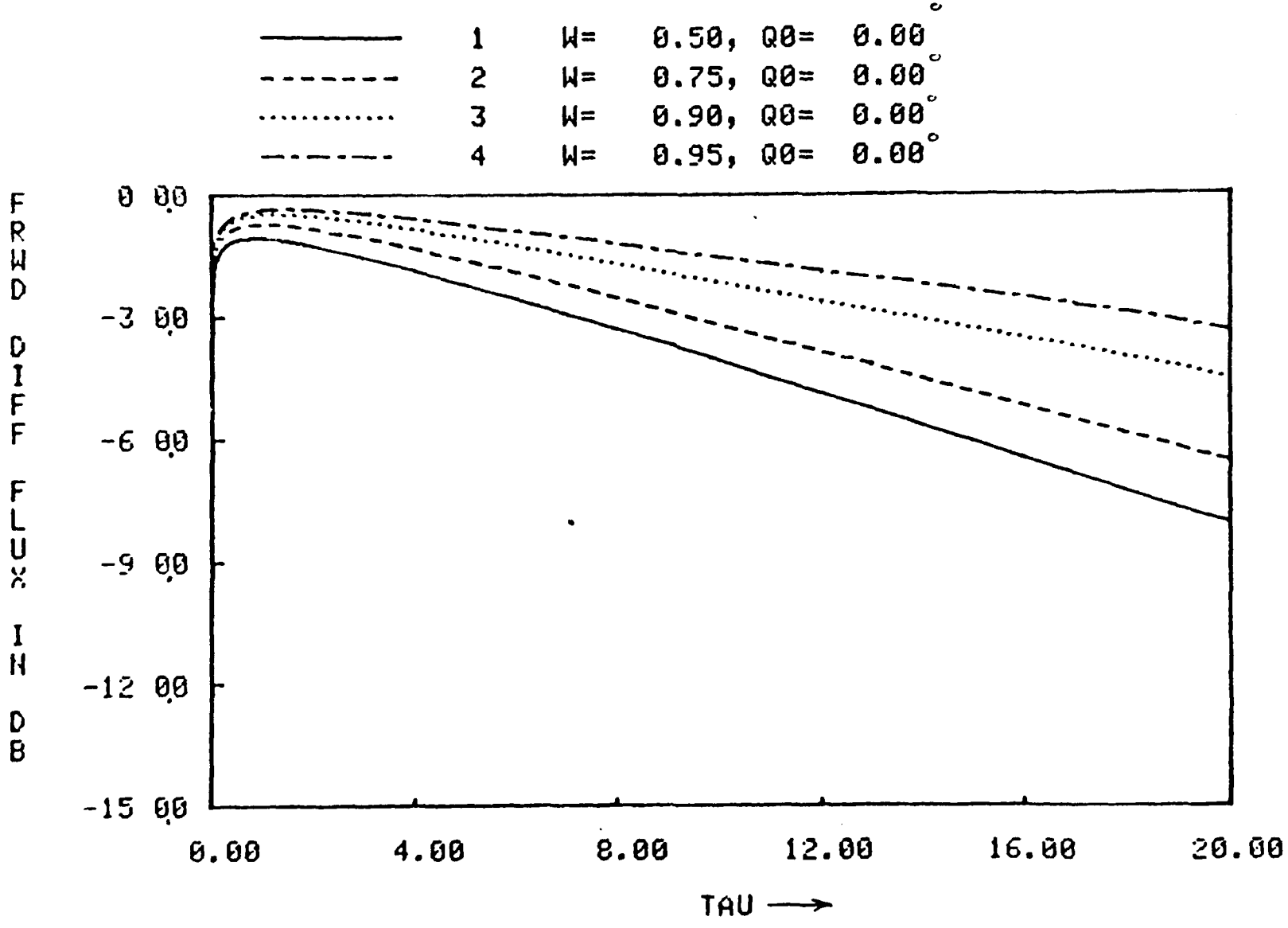

Figure 17.a. FORWARD DIFFUSE FLUX VS. DISTANCE FOR SLAB, T0=20.00, S=1

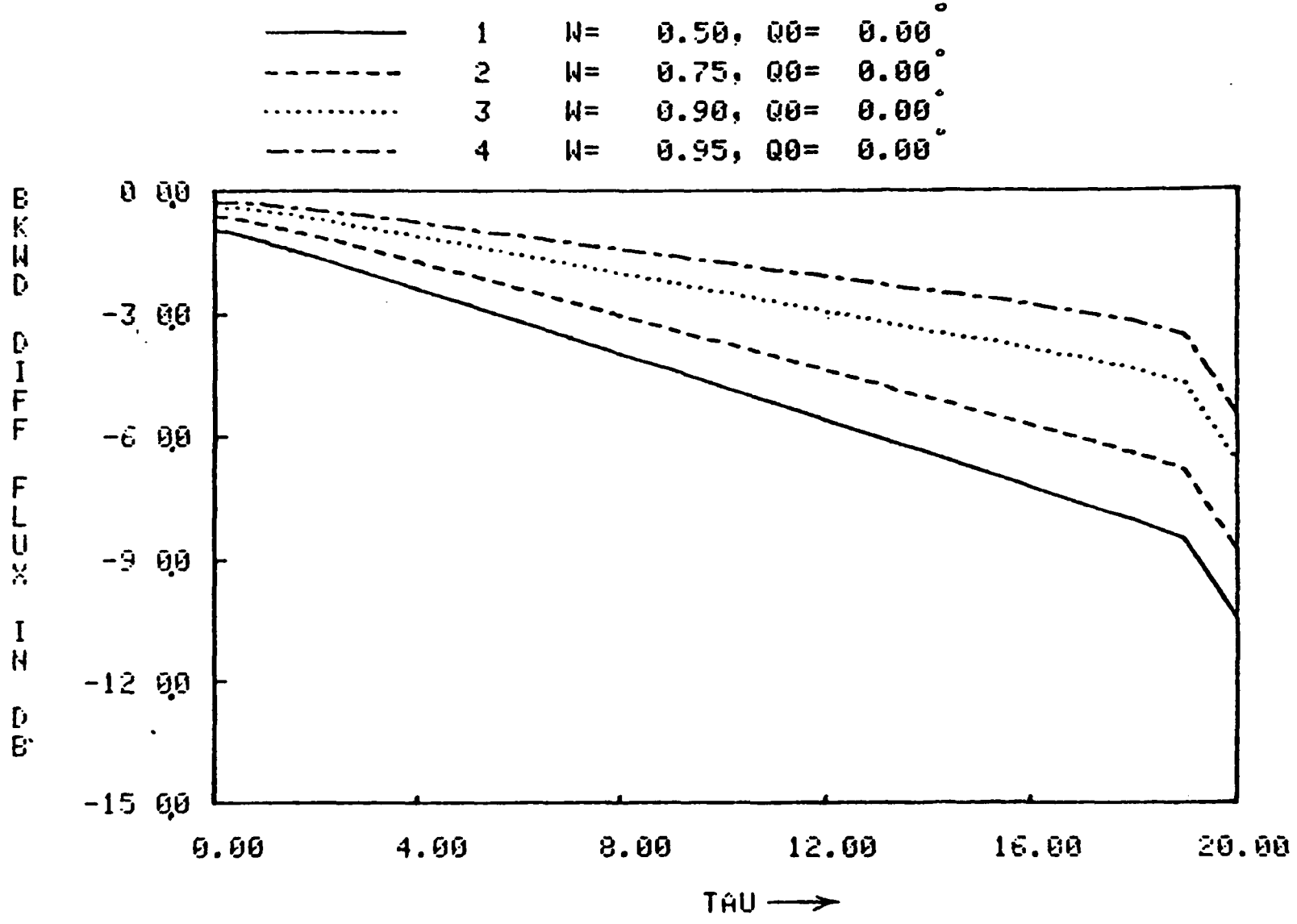

Figure 17.b. BACKWARD DIFFUSE FLUX VS. DISTANCE FOR SLAB, T0=20.00, S=1

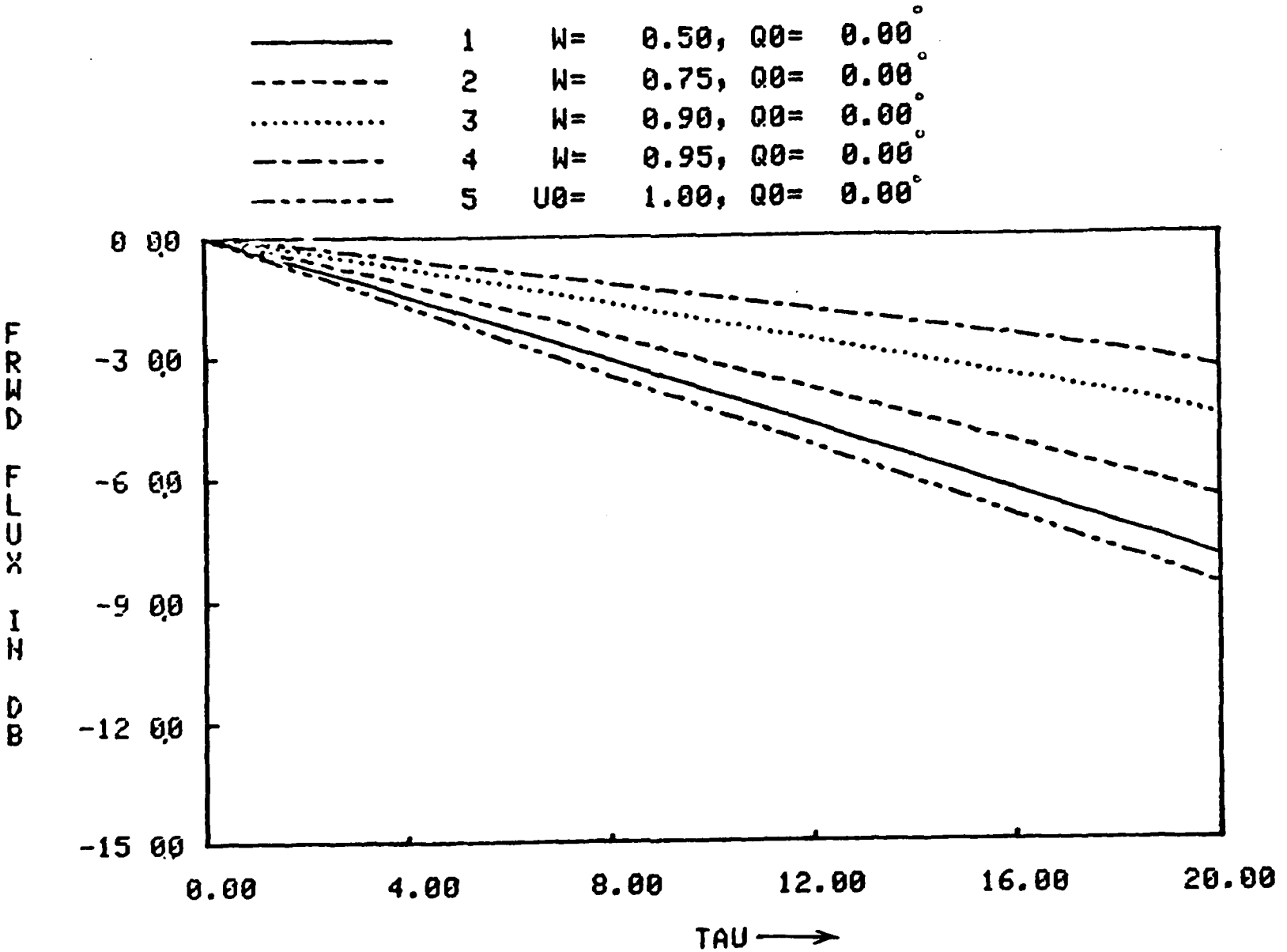

Figure 17.c. FORWARD FLUX VS. DISTANCE FOR SLAB, T0=20.00, S=1

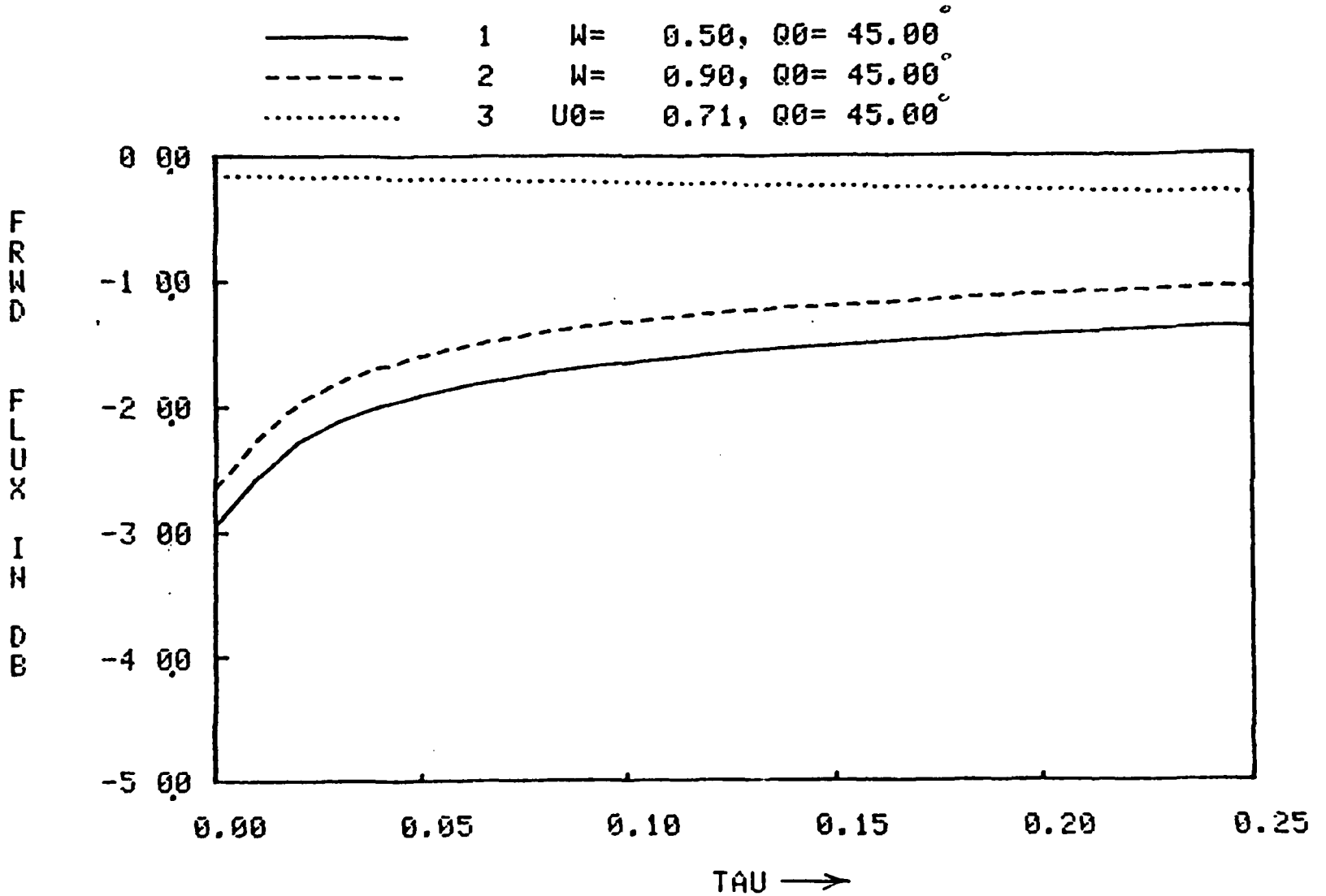

Figure 18.a. FORWARD FLUX VS. DISTANCE FOR SLAB, T0= 0.25, S=1.0

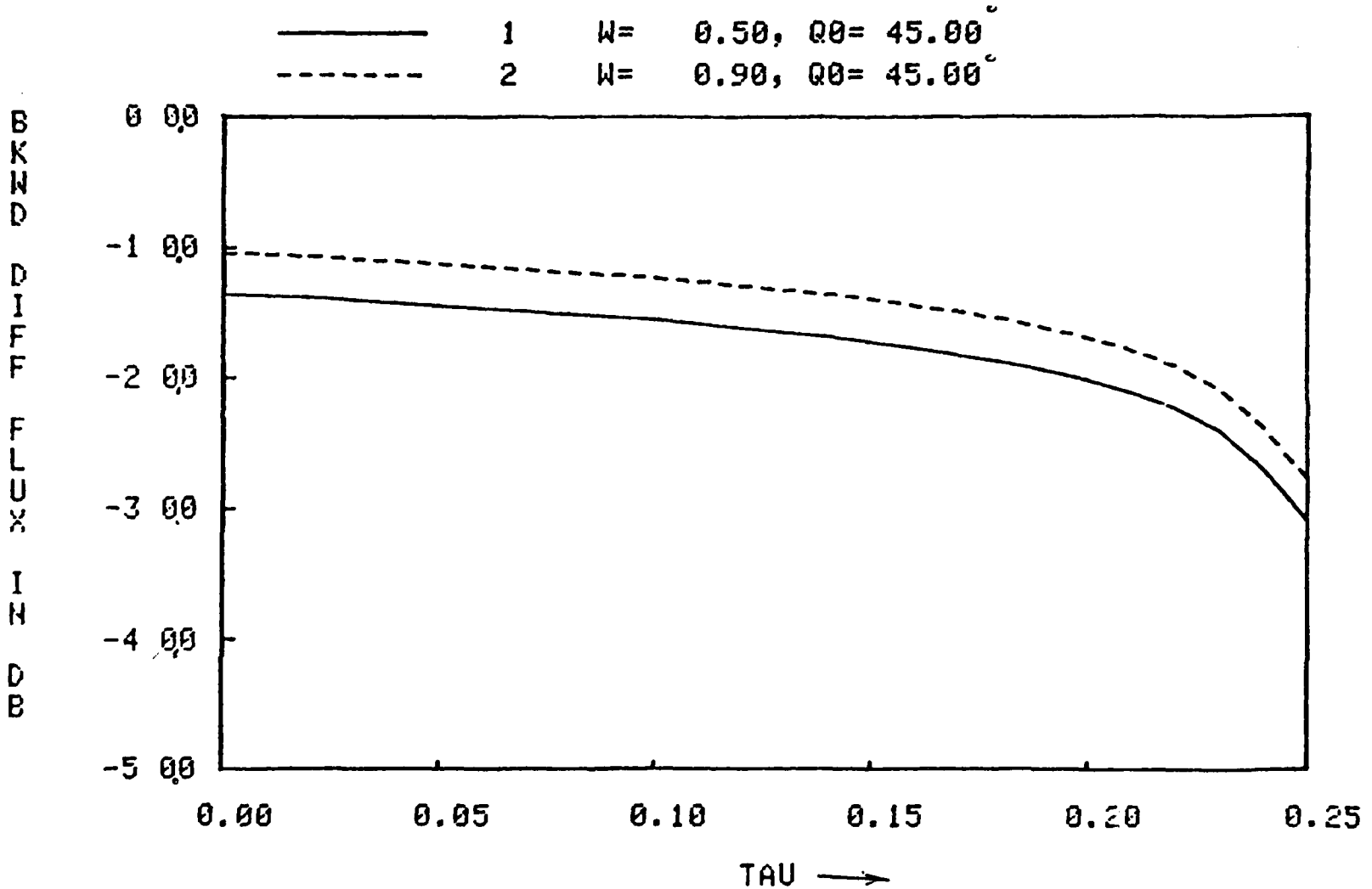

Figure 18.b BACKWARD DIFFUSE FLUX VS. DISTANCE FOR SLAB, T0= 0.25, S_0=1.0

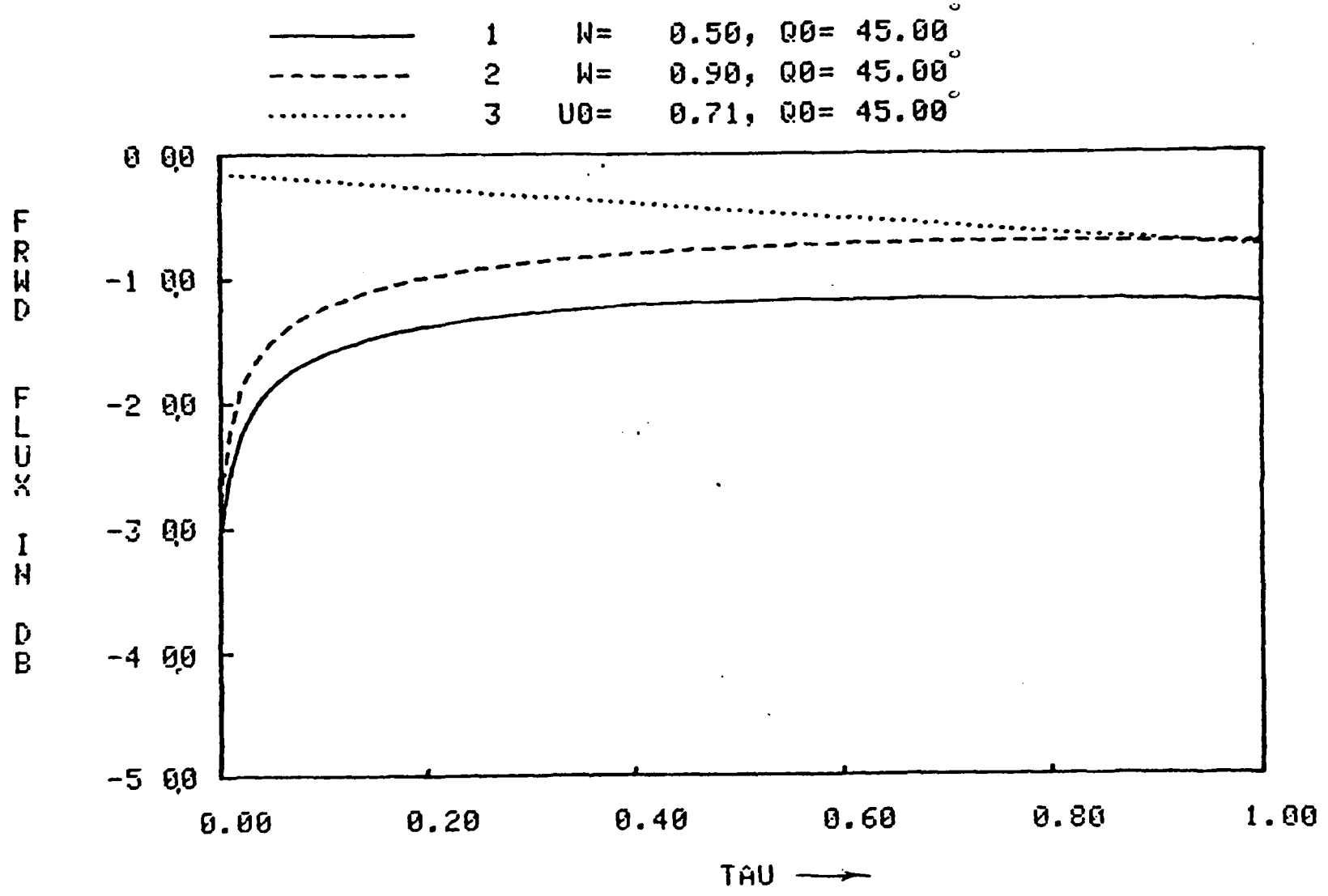

Figure 19.a. FORWARD FLUX VS. DISTANCE FOR SLAB, T0= 1.0, S=1.0

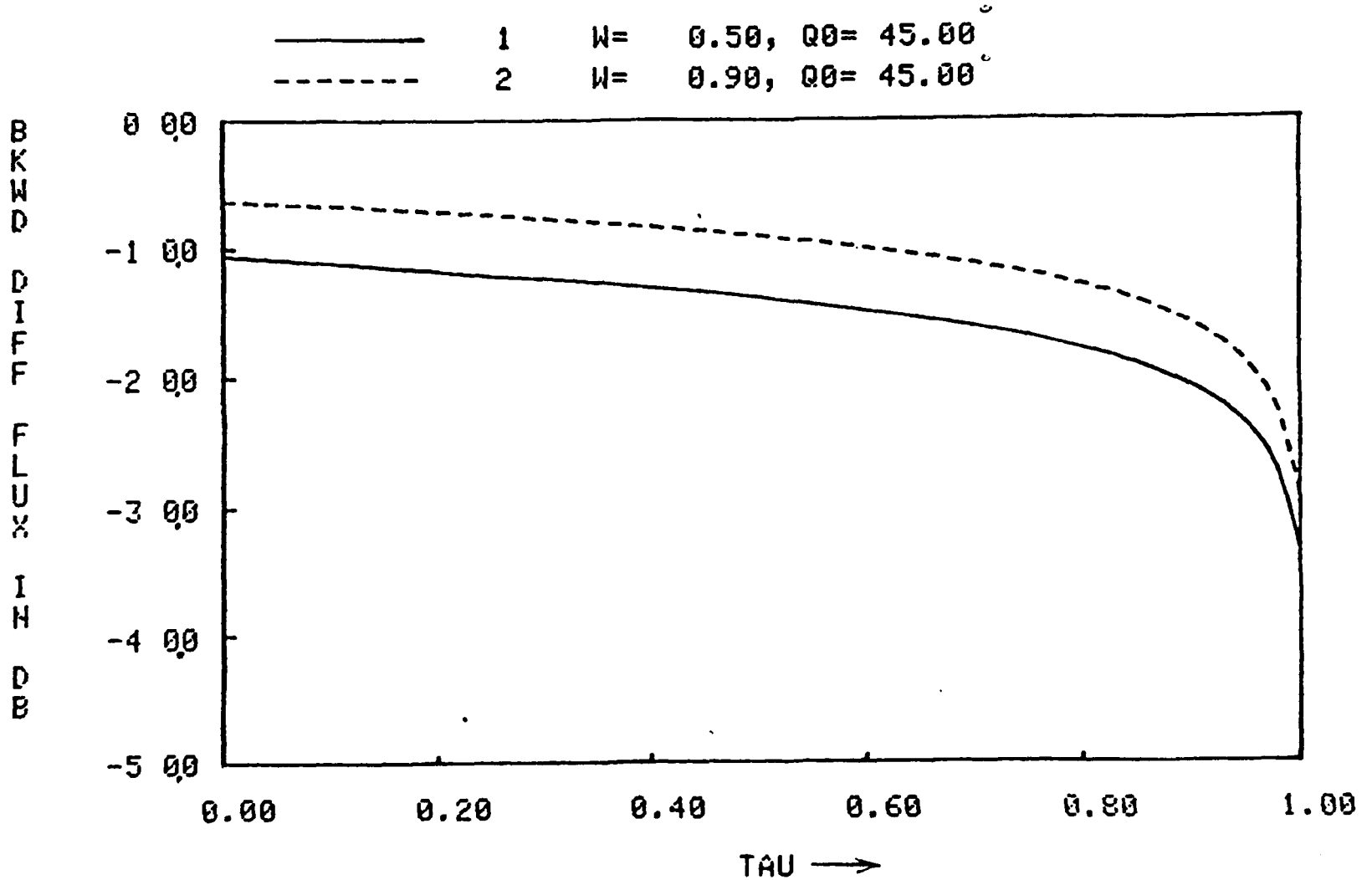

Figure 19.b BACKWARD DIFFUSE FLUX VS. DISTANCE FOR SLAB, T0= 1.0, S_0=1.0

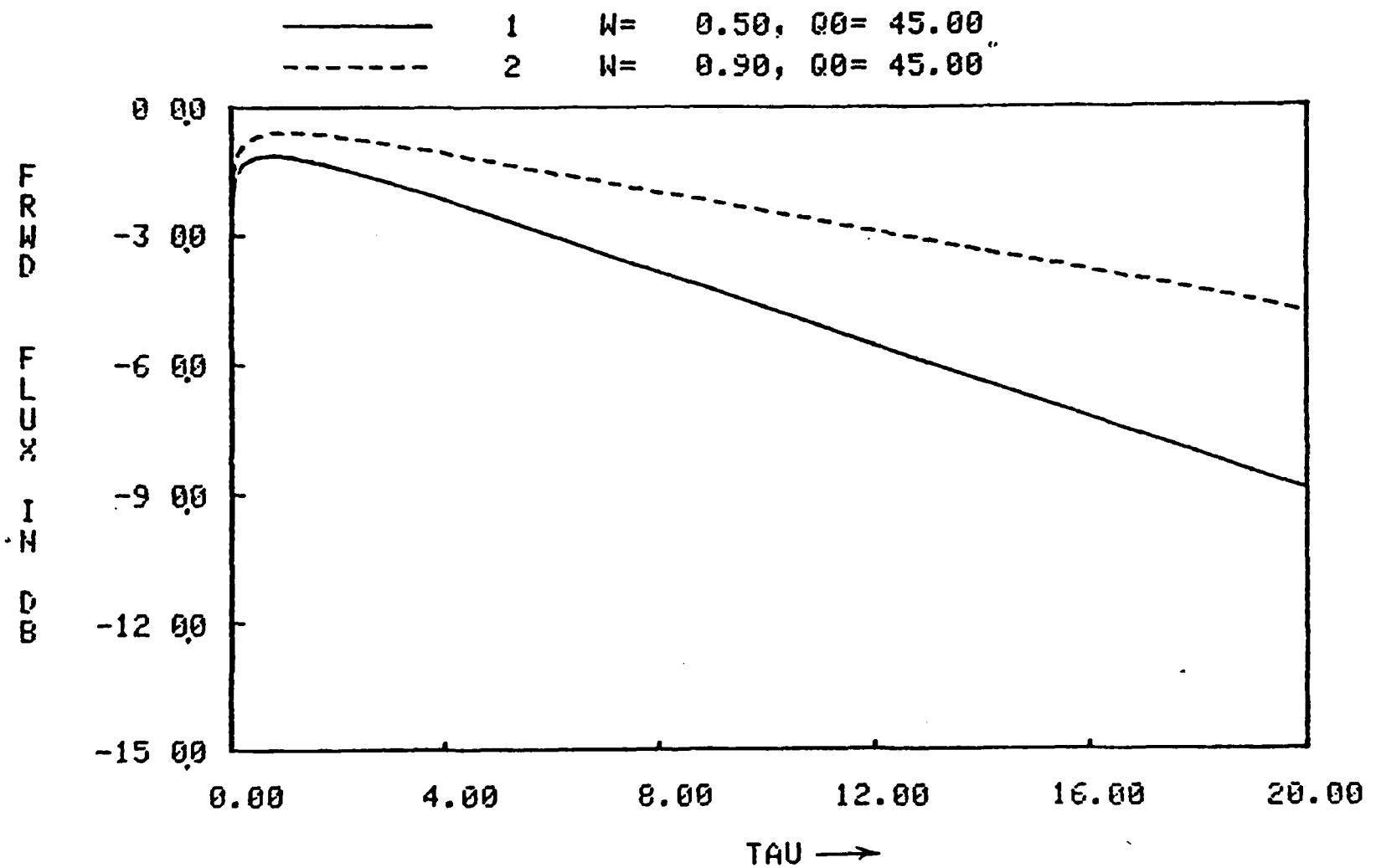

Figure 20.a. FORWARD FLUX VS. DISTANCE FOR SLAB, T0=20.00, S_0=1

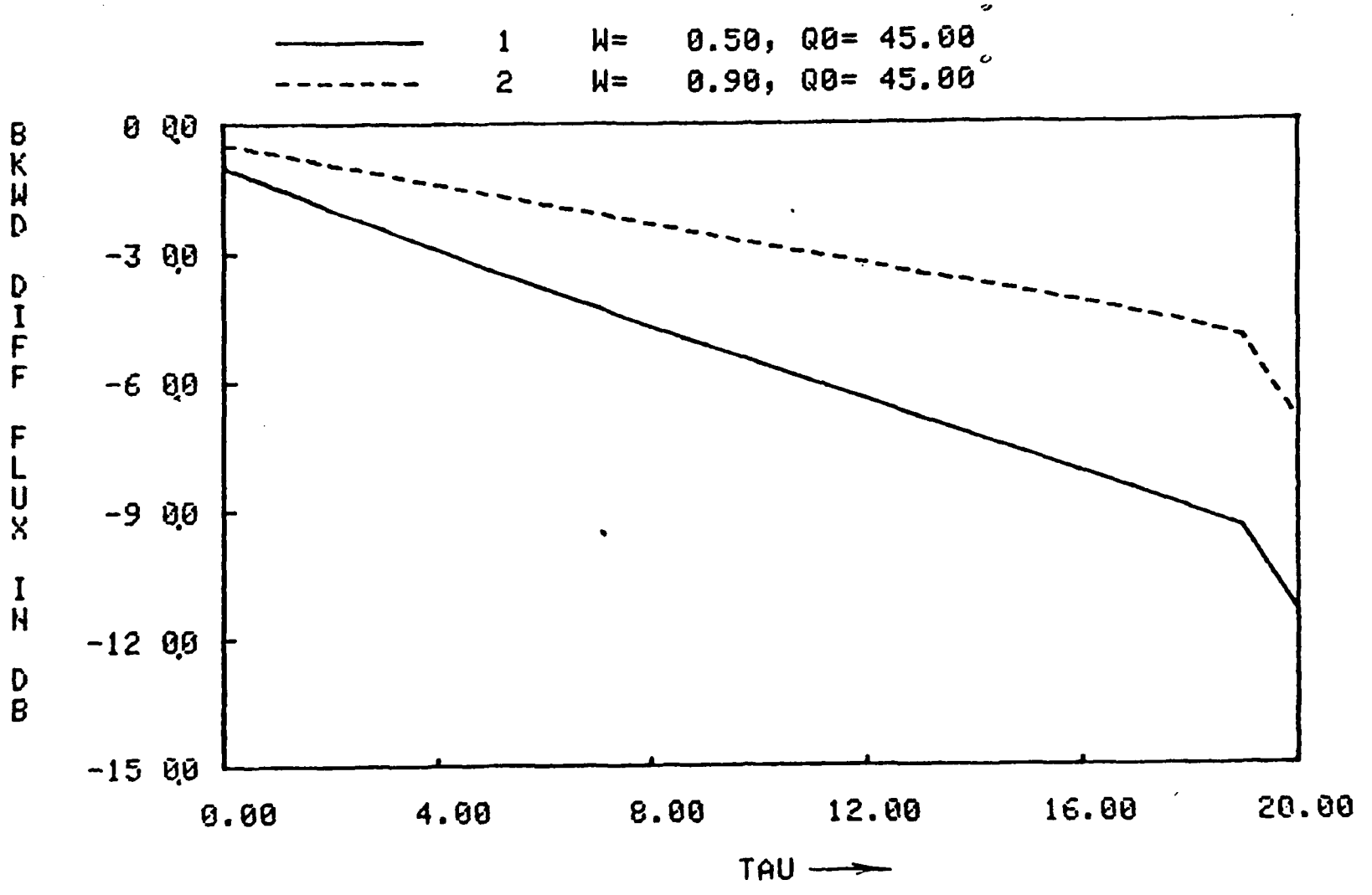

Figure 20.b. BACKWARD DIFFUSE FLUX VS. DISTANCE FOR SLAB, T0=20.00, S=1

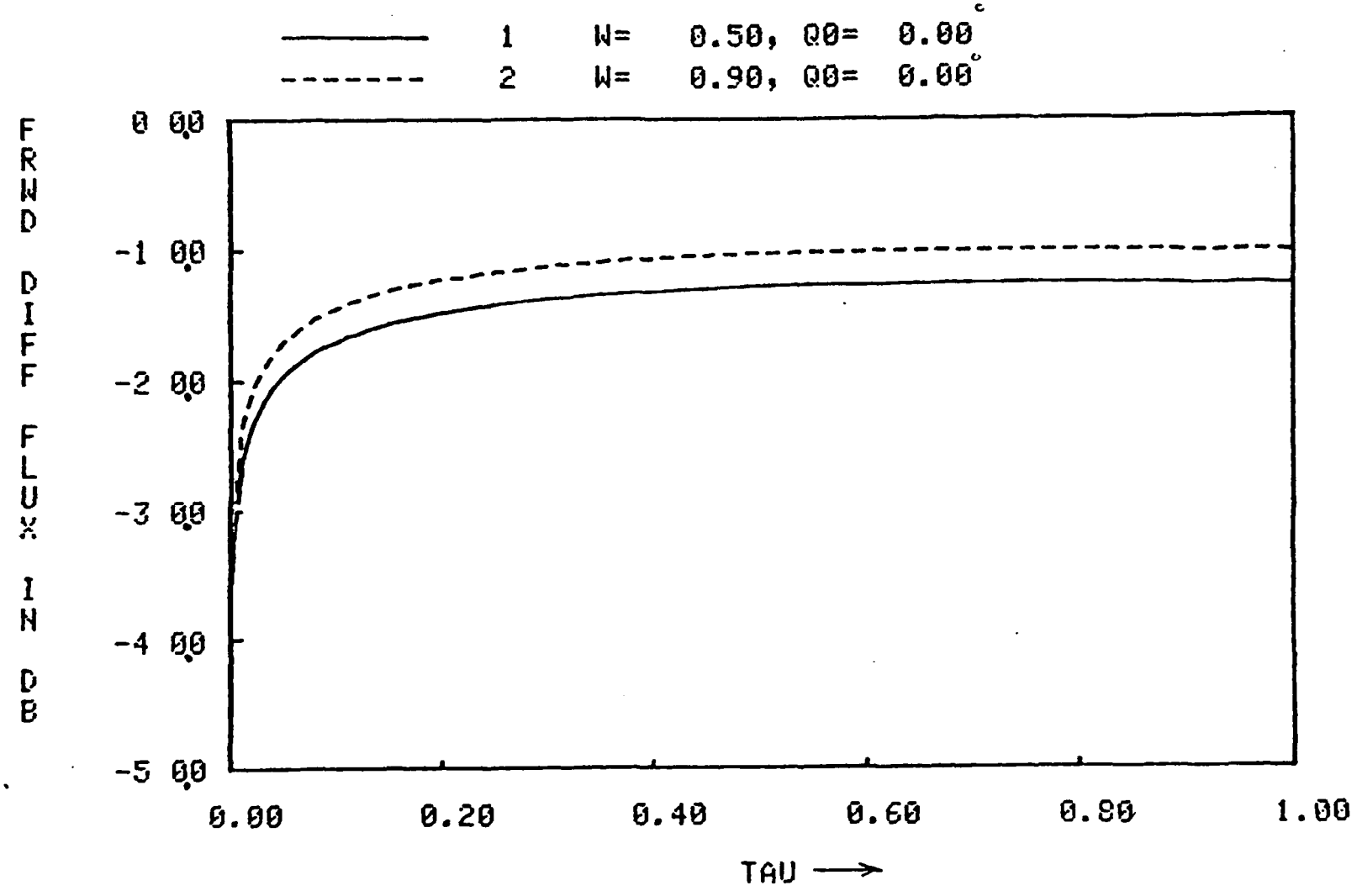

Figure 21.a. FORWARD DIFFUSE FLUX VS. DISTANCE, S=1.0

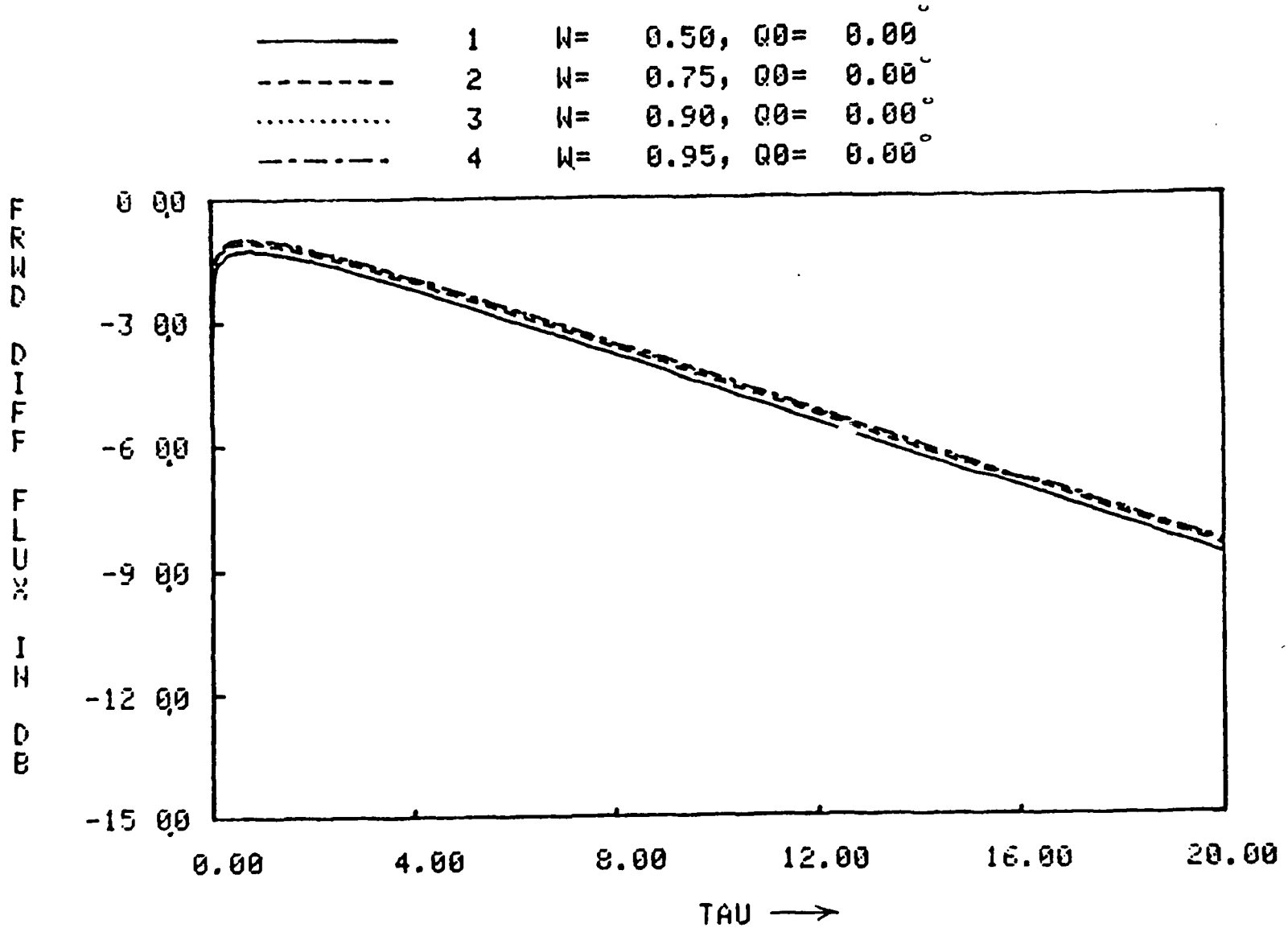

Figure 21.b. FORWARD DIFFUSE FLUX VS. DISTANCE, S=1.0

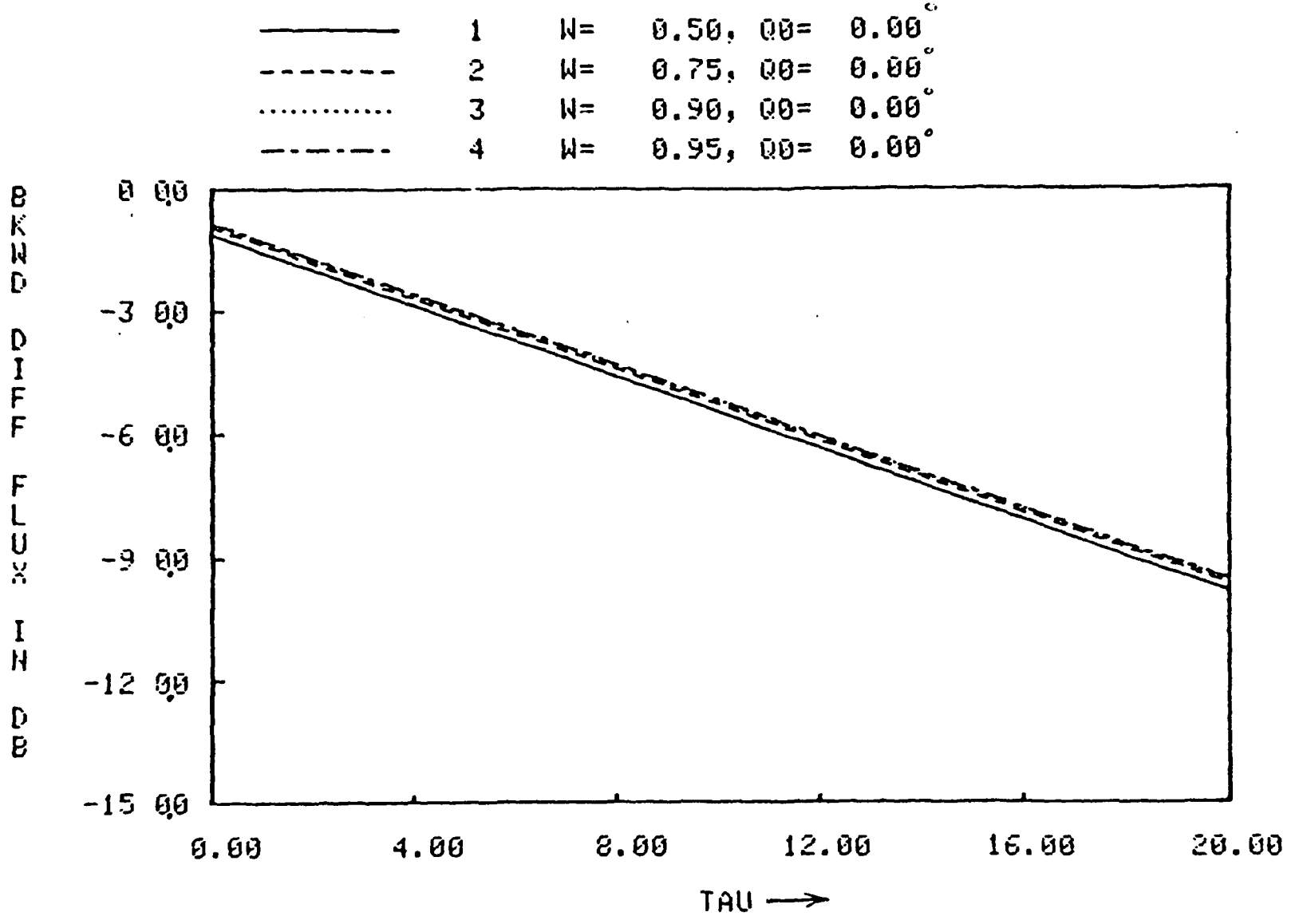

Figure 21.c. BACKWARD DIFFUSE FLUX VS. DISTANCE, 1/2 SPACE, S=1.0

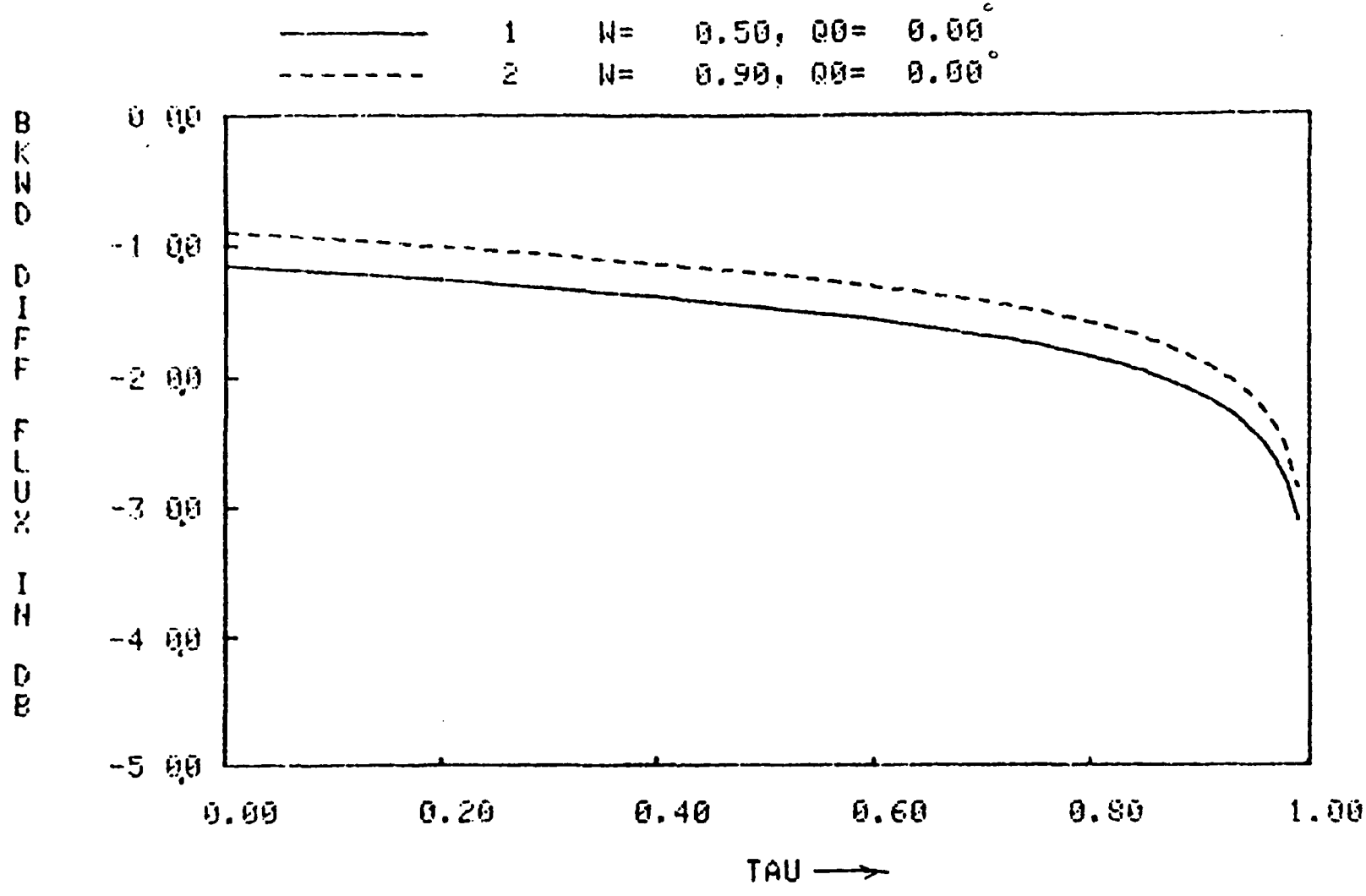

Figure 21.d. BACKWARD DIFFUSE FLUX VS. DISTANCE, SLAB, S=1.0

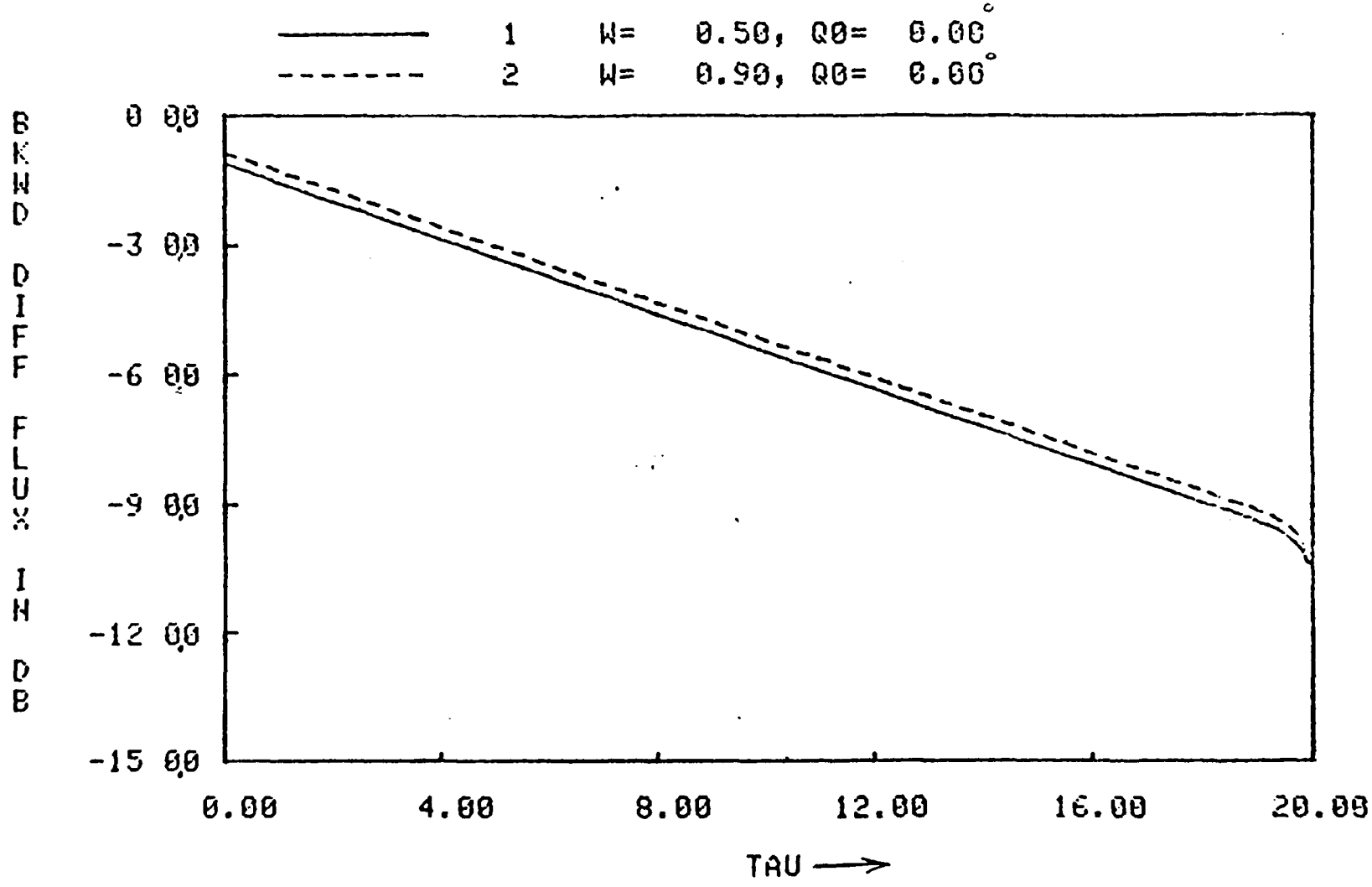

Figure 21.e. BACKWARD DIFFUSE FLUX VS. DISTANCE; SLAB, S=1.0

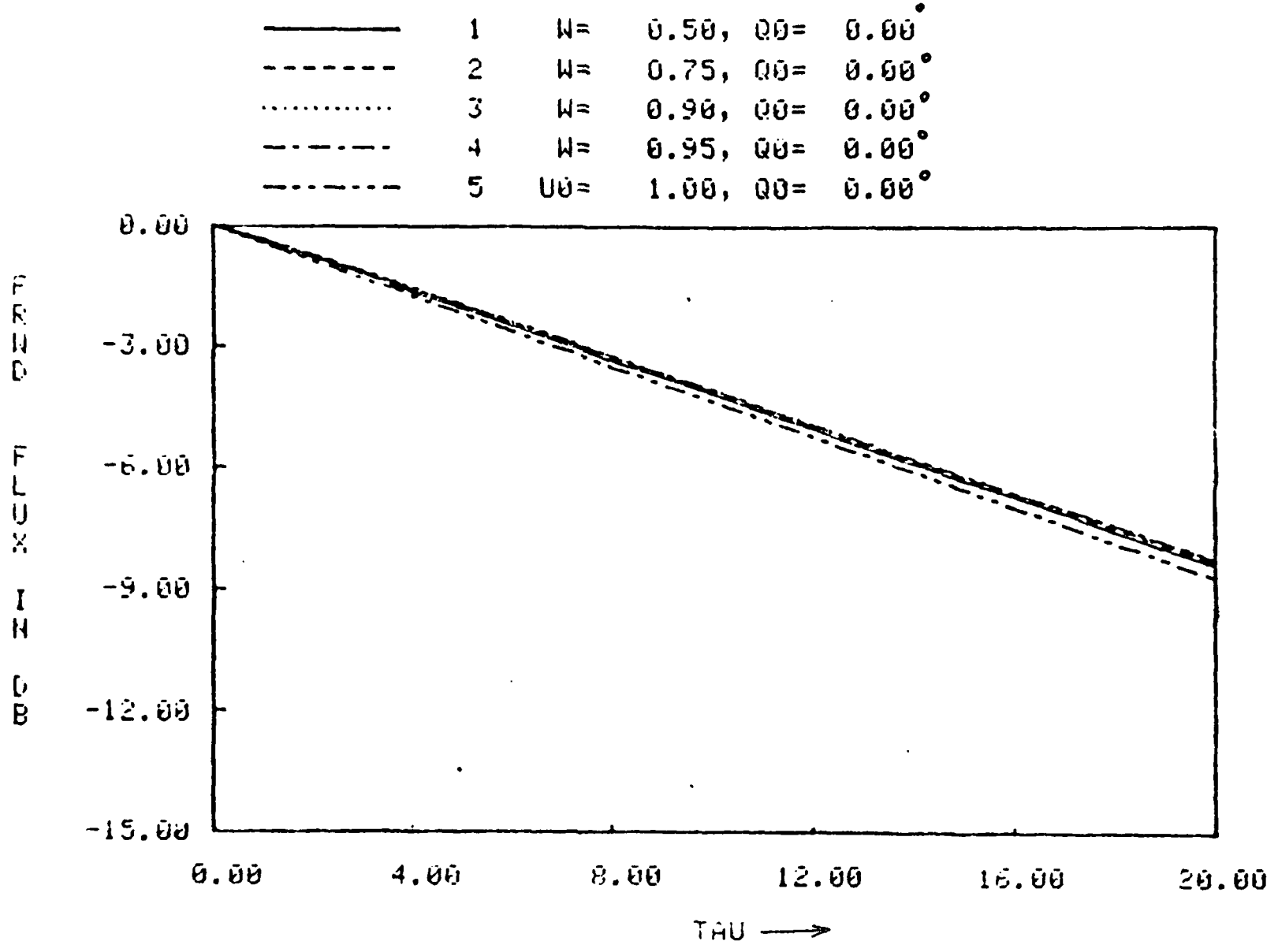

Figure 21.f. FORWARD FLUX VS. DISTANCE, S_0=1.0, τ_0=20.

TABLE 1.

EIGENVALUES FOR W = 0.50, N = 15

	Eigenvalues	Asymptotic Eigenvalue
N=15,W=0.5	0.0024127201	
" "	0.0216888460	
" "	0.0597271820	
" "	0.1153119000	
" "	0.1863812500	
" "	0.2703143700	
" "	0.3637836200	
" "	0.4631488700	
" "	0.5644062200	
" "	0.6634577500	
" "	0.7563703600	
" "	0.8391169500	
" "	0.9085847400	
" "	0.9608198500	
" "	0.9934517000	
" "	1.0443892000	1.0443819000

TABLE 2.

EIGENVALUES FOR W = 0.75, N = 15

	Eigenvalues	Asymptotic Eigenvalue
N=15,W=0.75	0.0024151615	
" "	0.0217681920	
" "	0.0600775240	
" "	0.1162469600	
" "	0.1882330600	
" "	0.2734405900	
" "	0.3684320600	
" "	0.4694660100	
" "	0.5723481100	
" "	0.6727326500	
" "	0.7664521500	
" "	0.8490449300	
" "	0.9171296600	
" "	0.9663557400	
" "	0.9949324100	
" "	1.2894637000	1.2894634000

TABLE 3.

EIGENVALUES FOR W = 0.95, N = 15

	Eigenvalues	Asymptotic Eigenvalue
N=15,W=0.95	0.0024176029	
" "	0.0218328890	
" "	0.0603619480	
" "	0.1170050200	
" "	0.1897284200	
" "	0.2759308300	
" "	0.3720490100	
" "	0.4741962400	
" "	0.5779633500	
" "	0.6787787900	
" "	0.7723188500	
" "	0.8540156400	
" "	0.9206208700	
" "	0.9681477400	
" "	0.9953059400	
" "	2.6351487000	2.6351488000